



HAL
open science

Modeling of fluid flows and heat transfer with interface effects, from molecular interaction to porous media

Meng Liao

► **To cite this version:**

Meng Liao. Modeling of fluid flows and heat transfer with interface effects, from molecular interaction to porous media. Materials. Université Paris-Est, 2018. English. NNT : 2018PESC1054 . tel-02086179

HAL Id: tel-02086179

<https://theses.hal.science/tel-02086179>

Submitted on 1 Apr 2019

HAL is a multi-disciplinary open access archive for the deposit and dissemination of scientific research documents, whether they are published or not. The documents may come from teaching and research institutions in France or abroad, or from public or private research centers.

L'archive ouverte pluridisciplinaire **HAL**, est destinée au dépôt et à la diffusion de documents scientifiques de niveau recherche, publiés ou non, émanant des établissements d'enseignement et de recherche français ou étrangers, des laboratoires publics ou privés.



Université Paris-Est, Laboratoire MSME (UMR CNRS 8208)

Modeling of fluid flows and heat transfer with interface effects, from molecular interaction to porous media

Meng LIAO

Thèse soutenue le Septembre 2018 devant le jury composé de:

Examineur : Benjamin ROTENBERG, CR(HDR), Sorbonne Université

Rapporteur externe : Irina GRAUR, Pr., Université d'Aix-Marseille

Rapporteur externe : Annie LEMARCHAND, DR(HDR), Sorbonne Université

Directeur de thèse : Quy-dong TO, MCF(HDR), Université Paris-Est Marne-la-Vallée

Co-directeur : Céline LÉONARD, Pr., Université Paris-Est Marne-la-Vallée

Co-directeur : Vincent MONCHIET, MCF(HDR), Université Paris-Est Marne-la-Vallée

Abstract

The objectives of the thesis are to study the fluid transport and heat transfer in micro and nano-scale pores. Both experiments and simulations revealed evidence of an enhancement of flow-rate, originated from slip velocity at the solid boundary. On the other hand, the finite thermal resistance at the fluid-solid interface is responsible for the temperature difference between the two phases. These two interface phenomena can have a considerable impact on the permeability and thermal diffusivity of porous media constituted of micro and nano-pores. This contribution focuses on studying the following three issues. First, we examine the slip effects of liquids confined in graphene channel using Green Kubo formalism and Molecular Dynamics method. It is shown that when the solid surface is subject to mechanical uniaxial strain, the friction exhibits anisotropy due to the modification of the potential energy and the dynamics of the fluid molecules. The molecular shapes also play an important factor on the friction discrepancies between two principal directions. The quantification of both effects is addressed. Second, we investigate the rarefied gas regime. In this case, the velocity slip and temperature jump are governed by the collisions between the gas and the solid boundary. Those effects can be determined via the study of scattering kernel and its construction from MD simulation data. To this end, different methods based on statistical learning techniques have been proposed including the nonparametric (NP) kernel and Gaussian mixture (GM) kernel. Finally, the finite element method is used to compute the permeability and the thermal diffusivity of porous media under the influence of the interface effects.

Résumé

Les objectifs de la thèse sont d'étudier le transport de fluide et le transfert de chaleur dans les pores micro et nanométriques. Les expériences et les simulations ont révélé des preuves de l'augmentation du flux provoquée par la vitesse de glissement à la paroi solide. D'autre part, la résistance thermique finie à l'interface fluide-solide est responsable de la différence de température des deux phases. Ces deux phénomènes d'interface peuvent avoir un impact considérable sur la perméabilité et la diffusivité thermique des milieux poreux constitués de micro et nanopores. La contribution se concentre sur l'étude des trois problèmes suivants. Premièrement, nous examinons les effets de glissement des liquides confinés dans un canal de graphène en utilisant le formalisme de Green Kubo et la méthode de la dynamique moléculaire. On montre que lorsque la surface solide est soumise à une contrainte mécanique uniaxiale, la friction présente une anisotropie due à la modification de l'énergie potentielle et de la dynamique des molécules composant le fluide. Les formes moléculaires jouent également un rôle important sur les écarts de frottement entre les deux directions principales. Deuxièmement, nous étudions le régime des gaz raréfiés. Dans ce cas, la vitesse de glissement et le saut de température sont régis par les collisions entre les atomes de gaz et la paroi solide. Ces effets peuvent être déterminés à l'aide d'un modèle statistique qui peut être construit à partir des vitesses incidente et réfléchie des molécules de gaz. A cette fin, différentes méthodes basées sur des techniques d'apprentissage statistique ont été proposées. Enfin, la méthode des éléments finis est utilisée pour calculer la perméabilité et la diffusivité thermique des milieux poreux sous l'influence des effets d'interface.

Acknowledgements

I would like to express my deepest gratitude to:

- All thesis review committee members
- My thesis directors:
Dr. Quy-dong To
Dr. Céline Léonard
Dr. Vincent Monchiet
- My machine learning instructor:
Dr. Wen-lu Yang
- All members in MSME Laboratory
- My parents in China and my Friedrich family in France.

Introduction

Fossil fuels are the main energy supply worldwide today, accounting for more than 80% of the total. In Asia-Pacific where there are many developing countries coal is still the main energy source. Although in Europe, the renewable energy has been set an objective of 20% of renewable energy in the total energy consumption in 2020, in the foreseeable future, hydrocarbons fuel (coal, oil, natural gas) will still be the main source of human energy.

According to the report of the International Panel on Climate Change (IPCC), emissions of CO₂ from fossil fuel combustion and industrial processes contributed about 78% of the total greenhouse gas (GHG) emissions increase from 1970 to 2010, with a similar percentage contribution for the increase during the period 2000 to 2010. Without additional efforts to reduce GHG emissions, global emissions growth is expected to increase. Global mean surface temperature increases in 2100 in baseline scenarios those without additional mitigation range from 3.7 °C to 4.8 °C above the average for 1850–1900 for a median climate response. They range from 2.5 °C to 7.8 °C when including climate uncertainty. In 2005, 195 members of the United Nations Framework Convention on Climate Change (UNFCCC) have signed the climate agreement in Paris. The agreement aims the long-term goal of keeping the increase in global average temperature to well below 2 °C above pre-industrial levels.

There are multiple mitigation pathways in meeting the dual challenge of supplying the energy the world needs to grow and prosper, while also reducing carbon emissions. In the petroleum industry, there is an enhanced oil recovery (EOR) technology, that injects CO₂ underground and increases oil or methane production. This technology has four advantageous: **1.** it sequesters a greenhouse gas (CO₂), **2.** it releases energy via an exothermic reaction, **3.** it retains the mechanical stability of the hydrate reservoir, **4.** produced water can be used to form the emulsion and recycled into the reservoir thus eliminating a disposal problem in arctic settings. In the extraction of non-conventional energy such as shale gas, the natural gas is often found in the micro even nanopores of rock. The rocks involved in this context have very low permeabil-

ities. The porous materials with low permeability are characterized by the presence of pores of very small size, of the order of micrometer even nanometer.

Another area involving nanofluidics is nanomaterial industry, which has recently grown considerably. These nanomaterials are developed for various applications, such as fuel cells, desalination membrane technology. The porous materials involved in this context have very low permeabilities. Due to the microporosity, the specific surface of these materials is very large, and the behaviors at the fluid-solid interface, e.g velocity slip and temperature jump, can have a significant effect on the transport properties of the fluid in micro nanochannels and in micro, nanoporous materials. So whether it is the calculation of natural gas production or the estimation of the escape of CO₂ from a long-term perspective or the diffusivity of fluids in nanodevices, we need to understand how the gas migrate from molecular scale to the meso/macroscopic scale.

The objectives of the thesis are to study the physical mechanisms of slip/jump conditions of fluid flows at the micro/nanoscale and their influences on the effective transport properties at the pore scale. While the interface phenomena in dense fluids are governed by the permanent fluid layers parallel to the wall, the slip/jump effects in gas are related to independent collisions. These two distinct features result in two different ways of modeling and simulation. This work establishes multi-scale framework to study the problem from molecular scale to the pore scale and develops the computation tools to address these issues. The contributions of the present thesis are organized in chapters which are separate published/unpublished papers devoted to the subjects and will be detailed in the following.

Contents

Abstract	i
Résumé	ii
Acknowledgements	iii
Introduction	v
1 Context and literature review	1
1.1 Boundary conditions at the fluid-solid interface	1
1.1.1 Confined liquids in carbon nanochannels	3
1.1.2 Gas flows regimes and collision models	5
1.2 Computation methods and models	8
1.2.1 Molecular dynamics simulations	8
1.2.2 Transport in saturated porous media	13
1.3 Summary of the main contributions of this work	16

2	Strain-induced friction	19
2.1	Introduction	20
2.2	Friction and slip tensors for anisotropic surfaces	22
2.2.1	Green-Kubo expression for the friction tensor	22
2.2.2	Approximation of fluid-wall potential for strained graphene	23
2.2.3	Analytical model for fluid-wall interaction	25
2.3	Molecular Dynamics simulation	28
2.3.1	Choice of systems and potentials	28
2.3.2	System setup	32
2.3.3	Results and discussion	33
2.4	Conclusions	39
3	Non-parametric wall model	42
3.1	Introduction	43
3.2	Study of gas-wall models with Molecular Dynamics method	44
3.2.1	Scattering kernels	44
3.2.2	Expressions for fluxes, average values and accommodation coefficients	47
3.2.3	Boundary conditions for Navier Stokes Fourier (NSF) equations	50
3.2.4	Extension to 13 moments equations	53
3.2.5	Generation of pre-collision velocity	54
3.3	Numerical simulations and results	56

3.3.1	Molecular Dynamics model	56
3.3.2	Determination of accommodation coefficients and construction of non-parametric wall model from collision data	60
3.3.3	Direct computation of interface coefficients	67
3.3.4	Influences of non-equilibrium distributions and discussion	69
3.4	Conclusions	71
4	Helium and Argon Interactions with Gold Surfaces	76
4.1	Introduction	77
4.2	Methods	79
4.2.1	Helium/Au(111) Interaction Energies: the Periodic dlDF + D_{as}^* Approach	79
4.2.2	Momentum and Energy Accommodation Coefficients, Slippage and Temperature Jump	82
4.3	Results and Discussion	87
4.3.1	Helium/Au(111) Interaction Energies	87
4.3.2	Momentum and Energy Accommodation Coefficients, Slippage and Temperature Jump	90
4.4	Conclusions	94
4.4.1	Momentum and Energy Accommodation Coefficients, Slippage and Temperature Jump: Molecular Dynamics Calculations	99
5	Gaussian mixture wall model	102
5.1	Introduction	103

5.2	Description of computation methods	105
5.2.1	Overview of statistical models of collision and their properties	105
5.2.2	Preprocessing of training data and Gaussian mixture model (GM)	109
5.2.3	Evaluation of model performance and comparisons	112
5.3	APPLICATIONS TO REAL GAS-WALL SYSTEMS	115
5.3.1	Construction of scattering kernels from Molecular Dynamics simulation data	115
5.3.2	Accommodation coefficients	118
5.3.3	Collision angles	121
5.3.4	Interfacial friction and thermal conductance	125
5.4	Conclusion	126
6	Homogenization with Finite Element Method	133
6.1	The homogenization problem	134
6.2	Finite elements method	139
6.2.1	Weak form for the Stokes equation	140
6.2.2	Weak form of the convection-diffusivity equation	141
6.2.3	Discretization and interpolation on element	142
6.2.4	Periodic boundary condition	144
6.3	Results and discussion	146
6.3.1	Preliminary works and benchmark	146

6.3.2	Determination of permeability and diffusivity for CH ₄	149
6.4	Conclusion	152
7	Conclusions and perspectives	158
	Bibliography	161

List of Tables

2.1	Interaction LJ parameters for H ₂ O, CO ₂ and CH ₄ interacting with graphene. . .	29
2.2	Potential well depths and equilibrium geometries for the global interaction between one molecule of H ₂ O, CO ₂ , or CH ₄ interacting with graphene or graphite.	31
2.3	Simulation conditions for different liquid systems including N number of liquid molecules, ρ the average liquid density confined between the two graphene sheets, T the temperature and P_{ext} the external pressure.	32
2.4	Friction coefficients for different systems.	36
2.5	The norm of reciprocal vectors for different strains. Note that $q^1 = q^2$	37
3.1	Expected values as functions of the reduced wall temperature $\theta_w = k_B T_w / m$. For CH ₄ , the rotation energy is neglected $d = 0$ and for CO ₂ , $d = 2$	49
3.2	LJ parameters for the interaction of CH ₄ and CO ₂ with the graphite surface. . .	58
3.3	Accommodation coefficients computed by stochastic equilibrium (SE) simulation method using data of Fig. 3.6 and by batch average (BA) simulation method in Fig. 3.3: α_l coefficient is associated to the velocity c_l , α_e is the kinetic energy (the angular velocity of CH ₄ is zero).	63

3.4	The β coefficients of CH ₄ and CO ₂ computed by SN methods and compared with values obtained from accommodation coefficients (SE method, Tab. 3.3) via formula $\beta_{1k} = \alpha_k/(2 - \alpha_k)$, $\beta_2 = \alpha_e/(2 - \alpha_e)$. MB: Maxwell-Boltzmann distribution, CE: Chapman-Enskog distribution, AM: atomic model for wall, NP: the wall is modeled by non-parametric scattering kernel $B(\mathbf{c} \mathbf{c}')$, instead of atomic wall (as in MB-AM method). To increase the precision of the slip coefficients for smooth (isotropic) surface, we average values along β_{1x} and β_{1y} .	69
3.5	β coefficients of R13 equations using Maxwell kernel ($\alpha = 0.3$) and non-parametric scattering kernel.	71
4.1	Equilibrium geometries and well depths of the global interaction potentials of He with Au(111) for the <i>fcc</i> and <i>top</i> adsorption sites presented in Figure 4.3. . .	88
4.2	MAC and EAC results for He, Ar collisions on smooth and rough Au surfaces at 300 K. T_g is the temperature defining the incident velocity distribution of the gas atom (see SI). T_{in} and T_{out} are defined by Eq. (4.14).	91
4.3	Values of β coefficients determined by the direct employment of MD velocities at 100 K, 200 K, and 300 K [Eq. (4.7)], by the use of MAC and EAC parameters [Eqs. (4.6), and (4.11)], and by the NP model. The values of β_{1x} , β_{1y} , and β_2 (MAC) are computed at $T_g = T_w = 300$ K.	92
4.4	dIDF parameters from periodic calculations with He in <i>fcc</i> position and from Ref.[54].	97
4.5	D_{as}^* parameters from He-Au ₁₀ with He in the <i>fcc</i> position and local Hartree-Fock calculations, and from Ref. [54].	99
5.1	The parameters of the He-Au and Ar-Au pairwise interaction potentials [83, 54].	116

5.2	The tangential momentum accommodation coefficient (TMAC) α_1 , the normal momentum accommodation coefficient (NMAC) α_n , and the energy accommodation coefficient (EAC) α_2 , computed using different statistical models: GM, NP, CL, and the atomic (MD) model. The construction of the statistical models NP, GM and CL from MD data is discussed in sec. IIIA. The accommodation coefficients associated to the statistical models are computed based on generation of new data and Eq. (5.18). It is noted that the CL model uses tangential momentum accommodation coefficient (TMAC) and normal energy accommodation coefficient (NEAC) computed by MD as parameters. Consequently, numerical TMAC values of CL model are extremely close to MD results.	120
5.3	The friction coefficient ($\bar{\beta}_1$) and the thermal conductance ($\bar{\beta}_2$) determined by different schemes.	126
6.1	Mass density ρ , heat capacity C_p , dynamic viscosity μ and thermal conductivity C_k of methane under different pressure p at 350K of CH ₄ gas.	149

List of Figures

1.1	Velocity slip (left) and temperature jump (right) conditions at the boundary. . .	1
1.2	Classification of the gas flow regimes and governing equations over the range of Knudsen numbers [166]	5
1.3	Comparison of the Maxwell and Cercignani-Lampis scattering kernels and a real reflection distribution considering an atomic wall. The red arrow indicates the incident direction and the black arrows indicate the possible reflective directions.	8
1.4	The initial state of the fluid and solid particles.	10
1.5	The LJ potential with the depth of the potential well ε , the zero inter-particle potential distance σ	11
1.6	MD periodic condition	12
2.1	Lattice vectors and reciprocal vectors	23

2.2	Comparison of methane-graphene potentials $V(\mathbf{x}, z_O)$ at the first fluid layer, about one molecule diameter from graphene, produced by exact calculation and two analytical approximations (2.11) and (2.12) (a) Exact distribution of potential energy $V(\mathbf{x}, z_O)$ in the first layer. (b) Distribution of potential energy calculated by expression (2.11). (c) Distribution of potential energy calculated by expression (2.12). It is easy to notice that (2.11) can recover the symmetry of the exact potential while (2.12) can not.	25
2.3	Snapshots of the three systems (H_2O , CO_2 and CH_4) in graphene nano-channel under consideration. The shape of three molecules are drawn according to molecules' bond lengths, bond angles and σ_{fw} diameters.	33
2.4	Fluid molecular density for different systems: (a) for H_2O , (b) for CO_2 and (c) for CH_4 . (d) variation of liquid density around the first peaks (first liquid layer).	34
2.5	Time correlation of friction forces along x and y directions for H_2O and graphene.	35
2.6	Friction coefficient, from MD simulations, with strain ranging from 0% to 10%. The quasi-linear relation is observed between friction coefficient and strain. The error bars are calculated for 10 simulations.	36
2.7	Influence of the fluid models on the slip length L_s of water-graphene system. . .	36
2.8	(a) 2D structure factor of oxygen (H_2O) with 10% unilateral strain on graphene sheet. (b) The structure factor of oxygen and hydrogen of water with different q . (c) The structure factor of oxygen (H_2O), carbon (CO_2) and methane (CH_4) at strain-free state.	37
2.9	Coefficient α (two upper figures) and potential energies V_1 (two lower figures) as a function of the strain and the distance z of methane molecule from the graphene sheet.	38

2.10	Factorization of friction coefficient λ to $\langle F^2 \rangle / A$ and τ_t with strain on graphite ranging from 0% to 10%	40
3.1	Simple sketch of the system. The stochastic boundary is indicated by the dashed line and the graphite wall is indicated by the solid line. Snapshots of MD simulations show the local orientation of the smooth (isotropic) and rough (anisotropic) systems.	57
3.2	A collision showing the trajectory of a gas molecule.	58
3.3	Correlation analysis using BA scheme for CH ₄ /CO ₂ -Graphite. Columns (a), (b), (c) represent the velocity (nm/ps) along x , y , z directions respectively and column (d) the kinetic energy for CH ₄ and CO ₂ (the prefactor $m/2$ is removed for simplicity). The horizontal axis shows the incident values and the vertical axis the reflection values. The solid lines represent the fit by least squares linear regression using Eq. (3.13). The diagonal dashed line and the horizontal dashed line indicate the zero accommodation case ($\alpha = 0$) and full accommodation case ($\alpha = 1$), respectively.	61
3.4	Detailed analysis of kinetic energy of CH ₄ beamed on the smooth surface. The tangential kinetic energy component $c_t^2 = c_x^2 + c_y^2$ and the normal kinetic energy component $c_n^2 = c_z^2$ are used for analysis. Subfigures (a), (b), (c), (d) show the correlation between incident energy and reflective energy components.	62
3.5	Energy data scattering observed from (a) MD simulations, (b) parametric ACL model with parameters $\alpha_x = \alpha_y = 0.16$ (constant tangential momentum accommodation coefficient) and $\alpha_z = 0.915$ (constant normal kinetic energy accommodation coefficient)	62

- 3.6 Collision data of incident and reflected velocities for the CH₄/CO₂-Graphite system. Both stochastic reservoir and graphite wall are maintained at 350 K for CH₄ and 600 K for CO₂. Columns (a), (b), (c) represent the velocity (*nm/ps*) along directions *x*, *y*, *z*, respectively, and column (d) the kinetic energy for CH₄ and CO₂ (the prefactor $m/2$ is removed for simplicity). The horizontal axis shows the incident values and the vertical axis the reflection values. The solid lines indicate the linear least square fit of incident and reflected values using Eq. (3.14). The diagonal dashed line and the horizontal dashed line indicate the zero accommodation case ($\alpha = 0$) and full accommodation case ($\alpha = 1$), respectively. 64
- 3.7 Velocity probability density of MD simulations and from some scattering kernels: Dadzie-Meolans (DM) [33], Anisotropic Cercignani-Lampis (ACL) [141] and non-parametric (NP) kernel constructed from MD data. The MD data are from collision simulation of CH₄ (350 K) at anisotropic atomic graphite wall (350 K). Columns (a), (b), (c) represent the velocity (*nm/ps*) at directions *x*, *y*, *z*, respectively, and column (d) the kinetic energy for CH₄ (the prefactor $m/2$ is removed for simplicity). The horizontal axis shows the incident values and the vertical axis the reflection values. 66
- 3.8 Method of computing coefficients β s by non-equilibrium simulation, MB distribution and atomic wall model (AM). (a) $-\hat{\sigma}_{kz}$ and \hat{v}_k of the isotropic graphite wall. (b) $-\hat{\sigma}_{kz}$ and \hat{v}_k of the anisotropic graphite wall. (c) $-\hat{q}_z$ and $\Delta\hat{\theta}$ are calculated by incident and reflective velocities on isotropic and anisotropic graphite wall. 68
- 3.9 Convergence test of CE-NP kernel iteration for rough anisotropic surface. Sub-figures (a): Friction coefficient β_{1x} , (b) Gas temperature (c) Gas velocity. 70
- 3.10 Generation of velocity using non-parametric kernel derived from MD collision clouds 75

- 4.1 Cloud figures of incident (horizontal axis) and reflected (vertical axis) velocity components of 100000 collisions of He and Ar atoms at 300 K projected on smooth and rough Au surfaces at 300 K. The horizontal dashed lines correspond to the full diffusive case, the diagonal ones to the full specular case. The red curves correspond to the linear fit of the velocity cloud. The corresponding MAC and EAC values are given in Tables 4.2. 86
- 4.2 The smooth Au (left) and rough (right) surfaces of gold. The 800 yellow atoms are originated from the initial smooth surface. The 96 blue atoms were deposited in order to form the rough surface composed of 896 atoms. 87
- 4.3 Radial scan of the interaction energies between atomic helium and the Au(111) surface, with the helium atom located at *fcc* (left panel) and *top* (right panel) positions. The interaction energies obtained with the periodic dIDF + D_{as}^* approach are compared with those determined via the vdW-DF2 scheme. The experimentally based value of the well-depth, 7.67 meV, is also indicated (gray dashed line) [149]. 88
- 4.4 Using the NP model, the values of the slip velocity \hat{v}_k , tangential stress $\hat{\sigma}_{kz}$, temperature jump $\Delta\hat{\theta}$ and normal heat flux \hat{q}_z have been determined. All the values have been normalized by the method described in Ref. [84]. The slopes of the lines provide the values of β coefficients. The $T_g = T_w = 300$ K gas velocities have been used to generate the NP kernel for He and Ar. 91
- 4.5 Figure illustrating the supercell model of the gold surface: the $\sqrt{3} \times \sqrt{3}$ supercell is surrounded by blue segments (left) and the 2×2 supercell is surrounded by red segments (right). 97
- 4.6 Au_4 cluster. The Au-Au distance is fixed to 2.8836 Å. The red point indicates the vertical position of He. 98

-
- 4.7 Au₁₀ cluster. The Au-Au distance is fixed to 2.8836 Å. The central red point indicates the *fcc* vertical position of He. 99
- 4.8 Radial scan of *ab initio* dispersion energies as a function of the distance (Z , in Å) between a He atom and the surface of Au₄ and Au₁₀ clusters, with He in the *fcc* position in the Au₁₀ case. 100
- 5.1 Procedure of reconstructing the scattering kernel from MD simulations of collisions. 107
- 5.2 A simple scheme of the incident-reflective velocities, \mathbf{c}' - \mathbf{c} , the incident-reflective vertical angles, γ' - γ , and the deviation angle η 113
- 5.3 Number of Gaussian vs. α_2 determined by statistical models and MD 117
- 5.4 The joint probability density of incident-reflective kinetic energy with unite Å²/ ps^2 (the prefactor $m/2$ is removed for simplicity) determined by the atomic simulations, the Gaussian mixture (GM), the nonparametric (NP), and the Cercignani-Lampis (CL) kernels. The horizontal axis indicates the incident energy \mathbf{c}'^2 and the vertical axis indicates the reflective energy \mathbf{c}^2 . The red line is the least-square linear regression of kinetic data, its slope is equal to $1-\alpha$. When the red line is close to the diagonal dashed line, the reflection is close to be specular (elastic collision). When the red line is close to the horizontal dashed line, the reflection is diffusive. 119
- 5.5 The Kullback Leibler divergence $D_{KL}(Atomic||Kernel)$ of momentum and kinetic energy determined by the atomic simulations, the Gaussian mixture (GM) kernel, the nonparametric (NP) kernel, and the Cercignani-Lampis (CL) kernel. 121

5.6	The probability density of the reflective deviation angle η determined by the atomic simulations, the Gaussian mixture (GM), the nonparametric (NP), and the Cercignani-Lampis (CL) kernels in polar coordinate system. The distance from the curve to the origin, the radius, indicates the probability of associated to angle η , which coincides with the angle coordinate of the system.	122
5.7	The probability density of the incident-reflective vertical angles determined by the atomic simulations, the Gaussian mixture (GM), the nonparametric (NP), and the Cercignani-Lampis (CL) kernels. The horizontal axis indicates the incident angle γ' and the vertical axis indicates the reflective angle γ . The incident and reflective angles range from 0 to 90°	123
5.8	The Kullback-Leibler divergence $D_{KL}(Atomic Kernel)$ derived from Fig. 5.6 and 5.7.	125
5.9	The average relative error of the different schemes, GM, NP, CL, and α , comparing with the atomic simulations considering all the data in Tab. 5.3.	127
5.10	(a) $\bar{\beta}_1$ as a function of α_t . (b) Comparisons between different methods of computing $\bar{\beta}_2$ with the same CL models: the equilibrium method (5.33), the nonequilibrium method 1 in this work (5.36), the nonequilibrium method 2 in literature (5.37).	132
6.1	Description of the homogenization problem	134
6.2	Reference element	142
6.3	Periodic boundary condition	144
6.4	Unit cell of the periodic array of cylinders.	146

6.5 (a) the velocity distribution along x-direction, (b) the temperature distribution, (c) permeability as function of the number of elements, (d) macroscopic diffusivity as function of the number of elements. 147

6.6 Solid line and dash line represent the FEM results, “□” and “△” discrete values represent the FFT results. (a) the permeability along x-direction under a function of the cylinder diameter, (b) conductivity along x-direction (without convection term) as a function of the cylinder diameter, (c) macroscopic diffusivity along x-direction (with convection term) as a function of the ratio the applied pressure gradient. 148

6.7 Variations of Pe and Kn with the dimension of the unit cell, H , for various values of the pressure. 150

6.8 The “●” means “with” the boundary condition, the “○” means without the boundary condition. (a) Variations of the permeability with the porosity Φ , (b) macroscopic diffusivity of a function of the porosity Φ , (c) relative permeability for no-slip/jump condition (with respect to the permeability with slip condition). (d) relative macroscopic diffusivity with no-slip/jump, slip/no jump, no slip/no jump with respect to the permeability with slip and jump condition. . 151

6.9 (a) Average velocity as a function of the applied macroscopic pressure gradient, (b) macroscopic diffusivity as a function of the applied macroscopic pressure gradient. 152

Chapter 1

Context and literature review

1.1 Boundary conditions at the fluid-solid interface

Due to the microporosity, the specific surface of these materials is very large, and the behaviors at the fluid-solid interface, e.g velocity slip and temperature jump, can have significant effect on the transport properties of fluid in micro nanochannels and in micro nanoporous materials. In 1860, Helmholtz and Piotrowski [60] firstly reported the slip phenomena between a moving viscous fluid and a solid. The slip and jump conditions can be modeled using two following quantities: the slip length L_s and the jump length L_t , as illustrated in Fig. 1.1.

The slip length L_s is the extended distance beyond the surface where the velocity is different on two sides of the interface. In 1823, Navier proposed the linear slip model and for a

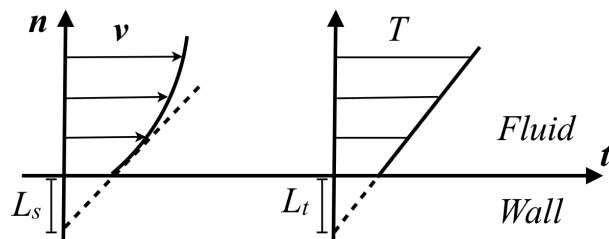


Figure 1.1: Velocity slip (left) and temperature jump (right) conditions at the boundary.

Newtonian fluid, it reads

$$\mathbf{v}_s = L_s \left. \frac{\partial \mathbf{v}}{\partial n} \right|_w \quad \boldsymbol{\tau} = \mu \left. \frac{\partial \mathbf{v}}{\partial n} \right|_w \quad (1.1)$$

where, \mathbf{v}_s is the slip velocity, $\boldsymbol{\tau}$ the tangential stress vector, μ the viscosity, \mathbf{n} the normal unit vector to the wall surface (denoted as w). The friction coefficient, β_1 , is a coefficient which characterizes the frictional property of the fluid-solid interface. Its definition and the relationship with L_s can be written as:

$$\boldsymbol{\tau} = \beta_1 \mathbf{v}_s, \quad L_s = \frac{\mu}{\beta_1} \quad (1.2)$$

Similarly, a characteristic length L_t is used to formulate the jump condition at the solid-fluid interface. The temperature difference between the two phases $T - T_w$ can be evaluated by the formula

$$T - T_w = L_t \left. \frac{\partial T}{\partial n} \right|_w, \quad (1.3)$$

where, the temperature gradient $\left. \frac{\partial T}{\partial n} \right|_w$ is calculated in the fluid phase adjacent to the wall. Another important interfacial thermal coefficient is the Kapitza coefficient β_2 , which is a measure of the interface's resistance (conductance) to the thermal flow

$$q_n = -\beta_2(T - T_w), \quad L_t = \frac{k}{\beta_2}, \quad (1.4)$$

where q_n is the normal heat flux at the interface, k is the conductivity of fluid.

Those interfacial parameters depend strongly on the interaction between the fluid and the solid boundary at the molecular scale. Numerous factors can affect the slip and jump parameters, for example the atomic potential, the temperature, the density, the surface roughness,

the adsorption, the shear rates, etc. In this work, we separately study two distinct fluid phases whose behaviors at the surface are fundamentally different. While in liquid state, it strongly depends on the wetting layers adjacent to the wall, in gaseous state, the gas collisions govern the interface phenomena. As a result, each flow regime is associated to different theoretical considerations, modelings, and simulation methods which will be described as follows.

1.1.1 Confined liquids in carbon nanochannels

It is reported by numerous works that the liquid flows at the nanoscale are different from those at the macro-scale [62, 67, 90, 158]. In the study of Kannam *et al.* [69], the authors reviewed the progress of research on water in carbon nanochannels from 2004 to 2012, and find that the flow enhancement results differ by 1 to 5 orders of magnitude compared to the classical no-slip flow predictions. In 2016, Secchi *et al.* [116] use carbon nanotubes (CNTs) to inject water into a surrounding fluid, and then they accurately measured the slip velocity in the CNTs. They found that when the radius of CNTs ranges from about 10 to 50 nm, the slip length ranges from about 300 to 30 nm. It is noted that the slip length can be determined from equilibrium Molecular Dynamics (EMD) [19, 20, 76] or non-equilibrium Molecular Dynamics (NEMD) simulations. In the study of Falk *et al.* [45], the authors used MD simulations to find that the water-carbon friction in CNTs is sensitive to the curvature, and when the diameter of the CNT goes below a threshold the friction is vanishing i.e. unmeasurable. In a later study, they found that this low friction property can be extended to alcohols, alkanes and octamethylcyclotetrasiloxane (OMCTS) fluids. For some sphere or sphere-like molecules like Ar and CH₄, this low friction phenomenon is also remarkable. In the Ref. [70], the authors used both equilibrium and non-equilibrium MD to simulate the Ar and CH₄ fluids confined in graphene nanochannels. They report that the flow rates are an order of magnitude higher compared to the classical hydrodynamic no-slip boundary condition predictions. They found that the curvature of CNTs can change the interfacial commensurates, affecting considerably the friction coefficient. In another work, Xiong *et al.* [160] also reported that when the water is

confined in a graphene nanochannel, the strain of the graphene wall can also change the surface friction.

In terms of the temperature jump, in 1898, Smoluchowski [124] firstly used experiments to verify the existence of a temperature jump through the measurements of air and hydrogen heat conduction between two surfaces at different temperatures. In 1941, Kapitza [71] performed the measurement of the temperature drop at a liquid (helium)-solid interface. Due to its superfluid nature, when helium is below 2.17 K, the thermal conductivity is extremely high. The author used this property to successfully measure the temperature jump at the interface. Afterward, people also call the thermal resistance coefficient as Kapitza coefficient. In Ref. [132], the authors reviewed the previous study of helium-solid Kapitza resistance and indicated that Kapitza resistance is caused by a combination of mechanisms such as the effects of the helium boundary layer, and of imperfections in or near the interface. Nowadays, MD methods become an important tool to study the heat resistance at the atomic scale. The object of recent studies has expanded from helium at ultra-low temperatures to polyatomic molecular liquids at room temperature [120, 162]. In Ref. [122], the authors thoroughly reviewed the previous experimental and simulation results concerning temperature jumps.

Nevertheless, simulation results of slip/jump documented in literature remain scattered and significantly different from experiments, and the understanding of the interface physics at the nanoscale is still far from complete. In the first part of this work, the friction and slip effects of confined liquids in graphene nanochannels are investigated in chapter 2. In particular, we study how the friction changes with the directions depending the surface strain and how it is affected by the molecular shapes.

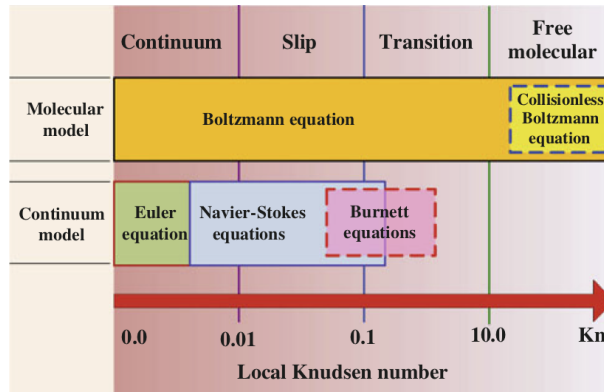


Figure 1.2: Classification of the gas flow regimes and governing equations over the range of Knudsen numbers [166]

1.1.2 Gas flows regimes and collision models

Unlike dense liquids where the fluid-fluid and the fluid-solid interactions are time continuous at the atomic scale, the interaction in dilute gas are distinguished by discrete collision events. The distance traveled between the collisions are called the (mean) free path λ , which is an intrinsic length scale of the fluid. Depending on the Knudsen number, Kn , that is the ratio between the mean free path λ and the characteristic length H of the channel,

$$\text{Kn} = \frac{\lambda}{H}, \quad \lambda = \frac{1}{\sqrt{2}\pi\sigma^2}, \quad (1.5)$$

different flow regimes can be identified. In 1960, Schaaf and Chambre proposed the classification of rarefied gas flows as shown in Fig. 1.2.

Generally, the fluid flow can be divided into four regimes according to the Knudsen number as follows:

1. $\text{Kn} < 10^{-2}$: the continuum regime. The Navier-Stokes and energy equations, and no-slip/no-jump boundary conditions are used.
2. $10^{-2} \leq \text{Kn} < 10^{-1}$: the slip regime. The non-equilibrium effects dominate near the walls. The Navier-Stokes and energy conservation equations are still applicable with the slip/jump boundary conditions.

3. $10^{-1} \leq \text{Kn} < 10$: the transition regime. The rarefaction effects become dominant and the Knudsen layer effect should be considered. The prediction using the Navier-Stokes and energy conservation equations with the slip/jump boundary conditions is no more effective [88, 155].
4. $\text{Kn} \geq 10$: the free molecular regime. The gas molecules are extremely dilute, eg. atmosphere near the satellite orbit. The intermolecular collisions are negligible as compared with the collisions between the gas molecules and wall surfaces.

While the bulk flows of gas can be described by Boltzmann equations, the boundary conditions can be formulated using statistical models of gas-solid collisions, called scattering kernels. In reality, the scattering kernel $B(\mathbf{c}, \mathbf{c}')$ for a wall normal to direction z is the conditional probability distribution $P(\mathbf{c}|\mathbf{c}')$ of reflective velocity $\mathbf{c} \in \Omega^+ = \mathbb{R} \times \mathbb{R} \times \mathbb{R}^+$ for a given incident velocity $\mathbf{c}' \in \Omega^- = \mathbb{R} \times \mathbb{R} \times \mathbb{R}^-$. In literature, collision models are usually based on several parameters called accommodation coefficients. The latter are based on special postulates that there is a linear relation between the post-collision momentum, the pre-collision momentum, and the energy of gas molecules with respect to the wall. For example, the accommodation coefficient α associated to the molecular quantities $Q(\mathbf{c})$ is defined as

$$\langle Q(\mathbf{c}) \rangle = \alpha Q_w + (1 - \alpha) \langle Q(\mathbf{c}') \rangle \quad (1.6)$$

with Q_w is the wall constant and $\langle \rangle$ the average notation. The most popular coefficients are the tangential momentum accommodation coefficients α_t (TMAC) with $Q = c_x$, the normal momentum accommodation α_n coefficient (NMAC) with $Q = c_z$, the energy accommodation coefficient α_e (EAC) where $Q = c^2$, the normal energy accommodation coefficient α_{en} (NEAC) where $Q = c_z^2$, etc. If the postulates are valid, there are connections between the interfacial coefficients β_1, β_2 and the coefficients α_t, α_e [92, 140, 27].

In 1879, Maxwell [92] proposed a collision model where the molecules can reflect either dif-

fusively or specularly with percentage α or $1 - \alpha$

$$B^{MW}(\mathbf{c}, \mathbf{c}') = (1 - \alpha)\delta(c_x - c'_x)\delta(c_y - c'_y)\delta(c_z + c'_z) + \alpha \frac{c_z \exp(-c^2/2\theta_w)}{2\pi\theta_w^2}, \quad (1.7)$$

where δ is the Dirac function for the specular term, θ_w is the variance of the molecular velocity for the molecules at the temperature of the wall, T_w , with $\theta_w = k_B T_w / m$. k_B is the Boltzmann constant and m is the molecular mass. Although the Maxwell wall model is simple and intuitive, its limitations are evident due to the probability discontinuity associated to the Dirac distribution [84] and the use of only one parameter α [140, 24].

The Cercignani-Lampis (CL) kernel [27, 89] is another interesting kernel, which can be written as:

$$B^{CL}(\mathbf{c}, \mathbf{c}') = \frac{c_z}{2\pi\alpha_e\alpha_t(2 - \alpha_t)\theta_w^2} I_0 \left(\frac{\sqrt{1 - \alpha_{en}}c_z c'_z}{\alpha_e\theta_w} \right) \times \exp \left\{ -\frac{[c_x - (1 - \alpha_t)c'_x]^2}{2\alpha_t(2 - \alpha_t)\theta_w} - \frac{[c_y - (1 - \alpha_t)c'_y]^2}{2\alpha_t(2 - \alpha_t)\theta_w} - \frac{[c_z^2 + (1 - \alpha_{en})c'_z]^2}{2\alpha_{en}\theta_w} \right\} \quad (1.8)$$

where I_0 is the modified Bessel function of the first kind and at the 0th order:

$$I_0(x) = \frac{1}{x} \int_0^\pi \exp(x \cos \xi) d\xi. \quad (1.9)$$

The CL model provides a more physical description of the gas-surface collision, since it uses the tangential momentum accommodation coefficient (TMAC) α_t and the normal energy accommodation coefficient (NEAC) α_{en} along direction z .

Although the CL kernel is closer to the atomic wall distribution than the Maxwell kernel in the description of the reflection (see Fig. 1.3), for some anisotropic surfaces like striped surface, the CL kernel can not capture the privileged direction effect. Dadzie and Meolans [34] generalized the Maxwell kernel for an anisotropic surface by attributing 3 accommodation coefficients α_x , α_y , α_z for the 3 reflective directions, respectively. However, the DM model is also composed of specular reflection components like the Maxwell model and is significantly different from the

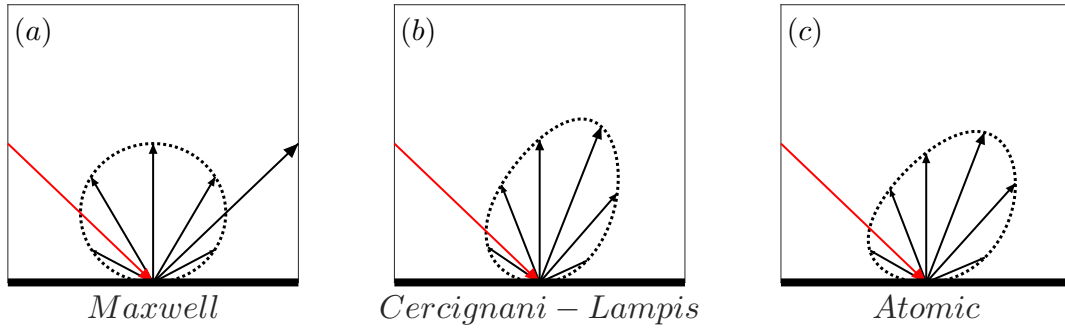


Figure 1.3: Comparison of the Maxwell and Cercignani-Lampis scattering kernels and a real reflection distribution considering an atomic wall. The red arrow indicates the incident direction and the black arrows indicate the possible reflective directions.

atomic models. In 2015, To *et al.* [140] proposed the anisotropic Cercignani-Lampis (ACL) kernel. This new kernel is based on the ingredients of the CL kernel but uses 3 accommodation coefficients

$$B^{ACL}(\mathbf{c}, \mathbf{c}') = \frac{e^{-\frac{[c_x - (1-\alpha_x)c'_x]^2}{2\alpha_x(2-\alpha_x)\theta_w}}}{\sqrt{2\pi\theta_w\alpha_x(2-\alpha_x)}} \frac{e^{-\frac{[c_y - (1-\alpha_y)c'_y]^2}{2\alpha_y(2-\alpha_y)\theta_w}}}{\sqrt{2\pi\theta_w\alpha_y(2-\alpha_y)}} \frac{c_z e^{-\frac{c_z^2 - (1-\alpha_z)c'_z{}^2}{2\alpha_z\theta_w}}}{\alpha_z\theta_w} \times I_0\left(\frac{\sqrt{1-\alpha_e}c_z c'_z}{\alpha_e\theta_w}\right) \quad (1.10)$$

Most of the current scattering kernels are based on a limited number of parameters (maximum 3). Although these parametric models are simple to implement, they rely on many simplifying hypotheses which cannot guarantee the accuracy of the $\mathbf{c}-\mathbf{c}'$ correlation in reality. This requires the reconstruction of more universal scattering kernels, which will be shown in this work.

1.2 Computation methods and models

1.2.1 Molecular dynamics simulations

The Molecular Dynamics Method (MD) is a numerical method based on Newton's second law for studying the physical movements of atoms and molecules. In the 1950s, this method was first introduced by Alder and Wainwright [4] to study the interactions between hard spheres.

Different from the Monte Carlo method based on sampling from a distribution of states (e.g Boltzmann), the MD method consists of studying the trajectory of particles and the spatial evolution of the system over time.

In Newtonian classical mechanics, the dynamics of a particle i can be described by the equation of dynamics and Newton's law:

$$\begin{aligned} \mathbf{v}_i(t) &= \frac{\partial \mathbf{r}_i}{\partial t}, & \mathbf{a}_i(t) &= \frac{\partial \mathbf{v}_i}{\partial t} \\ -\frac{\partial V_{pot}}{\partial \mathbf{r}_i} &= \mathbf{F}_i = m_i \mathbf{a}_i \end{aligned} \quad (1.11)$$

where vectors \mathbf{r}_i , \mathbf{v}_i , \mathbf{a}_i , \mathbf{F}_i are the position, velocity, acceleration and interaction force of particle i , respectively. m_i is the mass of particle i and V_{pot} is the potential energy of the complete system of N particles.

The dynamics equation can be integrated numerically by discretizing time into small intervals in which the velocity is considered constant. At each time step Δt , the force on particle i can be determined via the sum of intermolecular forces from the other particles, and using Eq. (1.11) the current acceleration $\mathbf{a}_i(t)$ can be calculated. Then the position and the velocity of each particle are computed using the Verlet algorithm. By developing the Taylor formula of the position function, we obtain:

$$\begin{cases} \mathbf{r}_i(t + \Delta t) = \mathbf{r}_i(t) + \mathbf{v}_i(t)\Delta t + \frac{1}{2}\mathbf{a}_i(t)\Delta t^2 + \frac{1}{6}\mathbf{b}_i(t)\Delta t^3 + o(\Delta t^3) \\ \mathbf{r}_i(t - \Delta t) = \mathbf{r}_i(t) - \mathbf{v}_i(t)\Delta t + \frac{1}{2}\mathbf{a}_i(t)\Delta t^2 - \frac{1}{6}\mathbf{b}_i(t)\Delta t^3 + o(\Delta t^3) \end{cases} \quad (1.12)$$

According to Eq. (1.12), the current velocity $\mathbf{v}_i(t)$ and the following position $\mathbf{r}_i(t + \Delta t)$ of particle i can be determined by:

$$\begin{cases} \mathbf{r}_i(t + \Delta t) = 2\mathbf{r}_i(t) - \mathbf{r}_i(t - \Delta t) + \mathbf{a}_i(t)\Delta t^2 \\ \mathbf{v}_i(t) = \frac{\mathbf{r}_i(t + \Delta t) - \mathbf{r}_i(t - \Delta t)}{2\Delta t} \end{cases} \quad (1.13)$$

Before simulations, it is necessary to assign the initial positions and velocities to the atoms. In general, the initial configuration of molecules can be given by a crystalline lattice such as simple cubic (SC), body-centered cubic (BCC) or face-centered cubic (FCC) lattices, for example, as shown in Fig 1.4. While the initial conditions are important for solid systems, they have almost no effect on fluid systems. For example, the initial structure of a graphite wall is a hexagon network with several graphene layers and the initial structure of gold wall is a (111) structure.

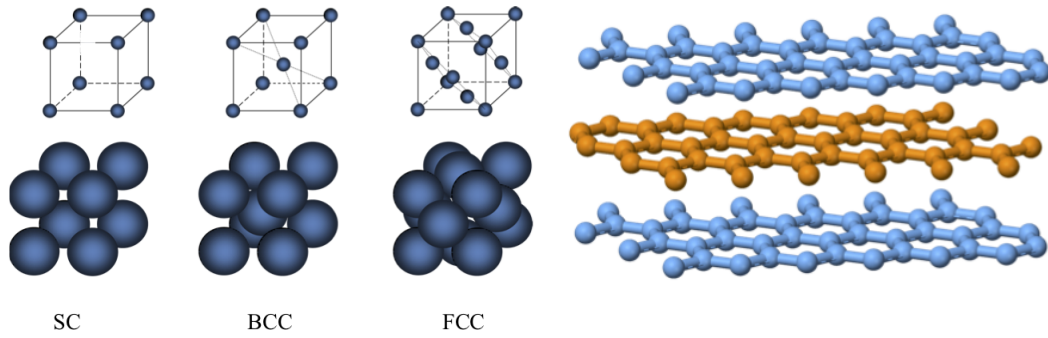


Figure 1.4: The initial state of the fluid and solid particles.

The interatomic potentials play a key role in MD simulations, their choice decides whether the simulation matches the real situation. The 12-6 Lennard-Jones (LJ) potential is the most used potential to model interactions between fluid atoms and between fluid and solid atoms. It is composed of the van der Waals interaction represented by an attractive dispersion term r^{-6} and a repulsive term r^{-12} . The expression of the LJ potential between two particles is given by:

$$V(r_{ij}) = \begin{cases} 4\epsilon \left[\left(\frac{\sigma}{r_{ij}} \right)^{12} - \left(\frac{\sigma}{r_{ij}} \right)^6 \right] & r_{ij} < r_c \\ 0 & r_{ij} \geq r_c \end{cases} \quad (1.14)$$

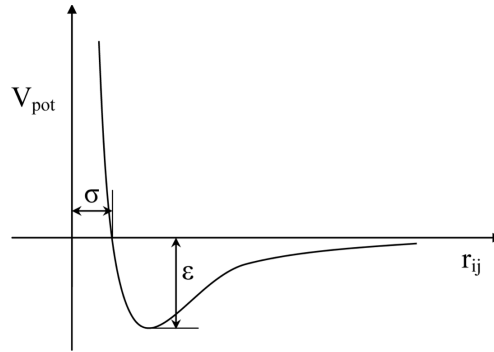


Figure 1.5: The LJ potential with the depth of the potential well ε , the zero inter-particle potential distance σ .

where ε is the depth of the potential well, σ is the distance at which the potential between particles is equal to zero, r_{ij} is the intermolecular distance, r_c is the cut-off distance. The variation of the potential $V(r_{ij})$ with r_{ij} is given in Fig. 1.5. The parameters of this potential can be optimized to reproduce experimental results or can be derived from first principle calculations. The details of the potentials used in this work will be given in the latter chapters.

Due to the limited computing power, MD simulations are limited to at the nanoscale studies. A good choice of the boundary conditions can also reduce simulation time. The periodic boundary conditions are the most used. The simulation domain is considered as a cell that is reproduced periodically in the 3 directions, in a grid that is assumed to be infinite. For example, in the 2D problem of Fig. 1.6, if the boundary conditions are periodic on the x and y-axis, 8 cells are reproduced around the central cell. In the 3D case, if the boundary conditions are also periodic on the z-axis, 26 cells are reproduced around the central cell. During the simulation, when a particle leaves the cell, another particle will come into the cell from the opposite side with the same velocity. The size of the cell must be at least twice larger than the cut-off distance in order to avoid that the particle is influenced by itself.

For further simulations, all intermolecular forces will not be calculated at each step. When calculating the force on one particle, a cut-off distance is chosen (see Eq. (1.14)) and only the intermolecular forces within this distance are calculated. The construction and the man-

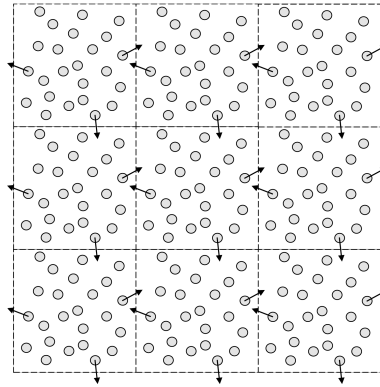


Figure 1.6: MD periodic condition

agement of the interacting atoms can be done efficiently by the Verlet list or cell list techniques.

In simulations, we note the number of particles N , the volume V , the energy E , the temperature T , the pressure P , the chemical potential μ . Since the Newton equations guarantee the conservation of the total energy, the MD simulations in the simplest form correspond to the microcanonical ensemble (NVE) where N , V , E are constants, i.e an adiabatic process with no exchange. However, there are ways to control the temperature T , the pressure P or the particle numbers N to reproduce other statistical ensembles: for examples, thermostat for canonical ensemble (NVT), barostat for isothermal-isobaric ensemble (NPT) or insertion/deletion techniques for grand canonical ensemble (μVT), etc. In our simulations, both NVE and NVT conditions were used. For the latter case, the Nose-Hoover thermostat is applied to the solid wall to control its temperature.

Once the system stabilized, the macroscopic quantities can be computed. The total energy is the sum of the potential and the kinetic energies. For a fluid system of N particles, the expression of the potential energy E_p and the kinetic energy E_c gives:

$$\begin{aligned}
 E_p &= \sum_{i=1}^N E_i^c + V_{pot} \\
 E_c &= \frac{1}{2} \sum_{i=1}^N m_i (\mathbf{v}_i - \bar{\mathbf{v}})^2
 \end{aligned} \tag{1.15}$$

where E_i^e is the external interaction applied to the particle i , V_{pot} is the intermolecular potential of the system, \mathbf{v}_i is the particle velocity and $\bar{\mathbf{v}}$ is the mean fluid velocity. According to the kinetic theory of gases, the temperature is a proportional measure of the average kinetic energy. The relationship between the temperature and the kinetic energy is given by the equation:

$$E_c = \frac{3k_B T}{2} N \quad (1.16)$$

The pressure of the gas in the system depends on the temperature and the intermolecular force:

$$P = \frac{Nk_B T}{V} + \frac{\sum_i^{N'} \mathbf{r}_i \mathbf{f}_i}{dV} \quad (1.17)$$

where \mathbf{r}_i and \mathbf{f}_i are the position and force vector of atom i , respectively, and d represent the dimension number. N' includes periodic ghost atoms outside the central box, and the position and force vectors of ghost atoms are thus included in the summation.

1.2.2 Transport in saturated porous media

The porous medium is made up of cavities which are fulfilled by a single-phase fluid. The fluid can be gas or liquid. In the present study, we are interested in the following two problems: (i) the mass transfer properties of the porous medium given by the permeability tensor, (ii) the heat transfer given by the macroscopic diffusivity tensor. Particularly, we focus on the role of surface effect over these two tensors.

Mass transfer properties

The permeability tensor enters into the well known Darcy law (1856):

$$\mathbf{V} = -\frac{\mathbf{K}_P}{\mu} \mathbf{J}, \quad (1.18)$$

where \mathbf{V} is macroscopic velocity, \mathbf{K}_P is the permeability tensor, μ the dynamic viscosity and \mathbf{J} the macroscopic pressure gradient. In 1941, Klinkenberg [73] provided a phenomenological extension of the Darcy law to account for the wall-slip effect at low pressure. He found that the gas permeability is greater than for a liquid and depends on the nature of the gas.

The determination of the permeability tensor in relation to the microstructure geometry has been provided in the framework of the homogenization methods, considering the method based on volume average [157] or the method based on asymptotic series expansions [111, 7, 8]. It can also be noticed that the correction of the Darcy law due to wall-slip has also been studied in the framework of the asymptotic homogenization by Skjetne and Auriault [123].

Analytic methods have been developed first in the literature for solving the associated unit cell problem. For instance, some works used expansions along eigenfunctions [112, 113, 151] and have later been extended to the problem of Stokes-slip flow [152, 154]. The determination of the permeability has also been performed numerically with finite element method (FEM) [15, 2, 3] for fluid flow passing through a regular array of cylinders. More recently, Monchiet *et al.* [95] adapted the fast Fourier transform (FFT) numerical method to compute the permeability with the wall-slip condition.

Heat transfer properties

The Stokes flow and the heat transfer problems are uncoupled. However, the velocity field computed from the Stokes problem enters in the convection term of the diffusivity equation. The effect of the dispersion effect depends on the value of the Peclet number (Pe). This is a dimensionless number, defined as the ratio between the rate of advection of the physical quantity and the rate of diffusion of the same quantity. In the context of the heat transfer, the Peclet number is defined by:

$$\begin{aligned} \text{Pe} &= \frac{Hv}{\alpha} = \text{Re Pr}, \\ \alpha &= \frac{k}{\rho C_p}, \end{aligned} \tag{1.19}$$

where H is a characteristic length, v a characteristic velocity, C_p the heat capacity, k the thermal conductivity of the fluid, ρ the density, Re the Reynolds number, and Pr the Prandtl number. The dispersion effect on the temperature distribution and on the pore diffusivity becomes significant when Pe is greater than 1.

The effective diffusivity of the porous medium is determined by solving the convection-diffusion equation over the volume of the unit cell:

$$\rho C_p \frac{\partial T}{\partial t} + \mathbf{v} \cdot \nabla (\rho C_p T) = \nabla \cdot (k \nabla T). \quad (1.20)$$

The temperature distribution due to an applied macroscopic temperature gradient is:

$$T = \mathbf{g} \cdot \mathbf{E} + \bar{T} \quad (1.21)$$

where \mathbf{E} is the macroscopic temperature gradient, \bar{T} is the mean (constant) temperature and \mathbf{g} is a localization tensor (having a null volume average over the volume of the unit cell). Once the solution is computed, the effective diffusivity \mathbf{K}_D is given by [17]:

$$\mathbf{K}_D = \langle k \rangle \mathbf{I} + \langle k \nabla^T \mathbf{g} \rangle - \langle (\mathbf{v} - \mathbf{V}) \otimes \mathbf{g} \rangle, \quad (1.22)$$

where $\langle \rangle$ indicates the volume average of the quantity over the volume of the unit cell, \mathbf{I} is the identity for two-order tensors.

From 1996, Kuwahara and Nakayama, using volume averaging, systematically studied laminar as well as turbulent fluid flows through various periodic structures [78, 79, 87, 114]. In 1998, Auriault *et al.* [17] presented the modeling of a temperature field in non-saturated porous media. From 2008, Hooman [63, 64] considered the slip boundary condition and presented analytical solutions based on the Fourier series method for fully developed forced convection in a micro-porous duct of rectangular cross-section. In 2010, Shokouhmand *et al.* [121], considering the conditions of slip and jump at the same time, investigated numerically the convection in circular microchannels filled with porous media. In 2013, Vu *et al.* [150] simulated forced convection

flows of air through ordered networks of cylinders or square rods embedded in microchannels with slip boundary condition. Finally, in a recent study, a FFT method for the computation of thermal diffusivity of porous periodic media was developed [142].

Until now, research on the diffusion in microscopic pores with slip/jump boundary conditions is still scarce. Calculation of the transport properties of the fluid in micropores will be studied systematically in Chapter 6.

1.3 Summary of the main contributions of this work

The main contributions of this thesis are: 1. To understand the physical mechanism of slip/jump conditions of liquid systems at the nanoscale. 2. To study statistical models of gas-solid collisions and their relations to the interface properties. 3. To investigate the thermal diffusion and convection of fluids in porous media taking interface effects into account. The chapters of the thesis are organized as follows:

In Chapter 2, we investigated how the anisotropic strain on a graphene nanochannel affects the fluid-solid slip boundary conditions. Using equilibrium molecular dynamics simulations and Green-Kubo formula, the friction between three molecular liquids, water, methane and carbon dioxide, and an uniaxially strained graphene sheet was computed. We found that the unilateral strain can increase the friction in all the directions but more in the strain direction. We also found that non-spherical molecules like H₂O and CO₂ are more sensitive to the strain and give rise to more pronounced anisotropy effects. An analytical formula was also developed to estimate the friction strength.

In Chapter 3, we used MD to simulate the process of gas molecules CH₄ or CO₂ impacting the graphite solid wall. Using collision data, we calculated the accommodation coefficients for

parametric collision models like Maxwell and Cercignani-Lampis scattering kernels and directly determine the slip/jump boundary conditions. Since the conventional parametric scattering kernels are based on a limited number of accommodation coefficients, their accuracy cannot be improved. To overcome these issues, we adopted nonparametric (NP) statistical methods to construct the kernel. Finally, we found that the boundary conditions determined by the NP model are consistent with the results of full atomic simulations.

In Chapter 4, we determined the pairwise potential between helium and a gold surface by *ab initio* calculations. Then, considering the He-Au potential and the Ar-Au potential provided in the literature, we simulated the gas atom He or Ar impacting the Au solid wall. Numerical evidences show that the adsorption effect between He and Au is very weak. When the reflection occurs on a rough gold surface, although the reflective momentum is more diffused compared with the reflective momentum on smooth surface, the degree of divergence of the reflected energy has not changed and it is basically a specular reflection. This phenomena cannot be estimated by conventional parametric scattering kernel. With the aid of the NP kernel determined in Chapter 3, we can respectively determine the momentum and the kinetic energy of the reflections and use these values to construct statistical slip/jump boundary conditions.

In Chapter 5, we proposed to use unsupervised learning techniques to construct collision models from simulation data. We have chosen to use the Gaussian mixture (GM) method as statistical model for the scattering kernel and the MD collision data of Chapter 4 as training data. The required parameters of the GM model were determined thanks to the Expectation Maximization algorithm. The GM model resembles the CL kernel by the use of multi variate Gaussian functions but it is more robust since the number of parameters is not limited. Physical and statistical based criteria including the accommodation, the slip/jump coefficients, the collision angles etc. were used to judge the quality of the GM model and numerical evidences show that the GM kernel is capable to reproduce faithfully the results of MD simulations.

In Chapter 6, we studied the heat and mass transfer properties of micro and nanoporous media and the role of with slip/jump interface conditions were analyzed. The interface coefficients were taken in the previous Chapters and other values were provided by the literature. The fluid flow problem was studied by solving the Stokes equation with the slip conditions at the interface between the fluid and the solid. Then, the diffusivity problem was considered. Due to the fluid motion, the energy can be transported along with the stream currents. The temperature between the fluid and the solid may also be discontinuous due to the presence of a thin thermal resistant barrier. A finite element code was developed to compute the velocity and temperature distribution fields and the mass and heat transfers of the porous solid at the macroscopic scale.

The last part is dedicated to the Conclusion of the thesis and to the Perspectives.

Chapter 2

Strain-induced friction anisotropy between graphene and molecular liquids

Abstract

In this paper, we study the friction behavior of molecular liquids with anisotropically strained graphene. Due to the changes of lattice and the potential energy surface, the friction is orientation dependent and can be computed by tensorial Green-Kubo formula. Simple quantitative estimations are also proposed for the zero-time response and agree reasonably well with the Molecular Dynamics results. From simulations, we can obtain the information of structures, dynamics of the system and study the influence of strain, molecular shapes on the anisotropy degree. It is found that unilateral strain can increase friction in all directions but the strain direction is privileged. Numerical evidences also show that nonspherical molecules are more sensitive to strain and resulting more pronounced anisotropy effects.

2.1 Introduction

In micro-nanofluidic systems, the fluid-solid interface contributes a significant part in the overall behavior of the system [115, 72, 43]. Generally, the whole system can be modelled by the conventional macroscopic hydrodynamic equations combined with Navier boundary equations for the slip velocity v_s at the wall. For a Newtonian fluid of viscosity η , the latter can be written in two equivalent forms

$$\sigma = \lambda v_s, \quad v_s = L_s \frac{\partial v}{\partial n} \quad (2.1)$$

where $\sigma = \eta \partial v / \partial n$ is the viscous shear stress, $\partial v / \partial n$ the normal derivative of fluid velocity v at the wall. The interface constants, λ the friction coefficient, η the viscosity and L_s the slip length, are related by

$$L_s = \frac{\eta}{\lambda} \quad (2.2)$$

The slip effects which depend on the nature of the fluid solid interaction, are enhanced when the hydrophobicity is involved. Both experiments with advanced techniques and computer simulations have provided supporting evidences of the phenomenon [97, 137, 69]. Atomistic simulations are generally based on either two techniques: Non Equilibrium Molecular Dynamics (NEMD) and Equilibrium Molecular Dynamics (EMD). The former concerns simulations of fluid flow and compute the slip length by comparing with Navier Stokes solution [106, 6, 48, 72]. The latter is founded on the linear response theory and the friction coefficient is determined via Green-Kubo formula [28, 19, 44].

Regarding microfluidics systems involving water and carbon nanotubes (CNTs) or graphene based nano channels, experiments revealed that the water flow rates are many times higher than prediction using no slip boundary conditions [90, 62, 116]. Despite some scattering results in literature, Molecular Dynamics (MD) simulations agree with the exceptionally small fric-

tion found on CNTs and graphene [45, 70, 69]. Most of those results are obtained for pristine graphene or CNTs in laboratory while real graphene can have defects and be affected by other environmental mechanical conditions. Graphene can be subject to mechanical strain due to different reasons, for example lattice mismatch or thermal expansion in graphene/substrate systems. Graphite, that has similar structure as graphene, can be found in profound coal bed, under large compressive stress states. Atomistic simulations have shown that the friction can increase significantly with strain. For example, by MD simulations on graphene/water system, Xiong *et al.* [160] have observed the variation of slip effects by applying isotropic strain on the graphene sheet. Since graphene and graphite have many important applications, it is crucial to understand how the strain affects the slip effect.

The present work investigates graphene (or one graphite layer) and the interaction with different liquids namely water (H_2O), carbon dioxide (CO_2) and methane (CH_4). Those fluids have different molecular shapes and important applications in technology (membrane and nanofluidics systems), energy and environment (carbon dioxide sequestration and methane recovery). Graphene or graphite can be naturally or artificially strained, which result anisotropic friction, i.e the friction along the strain direction is different from the other direction. This type of behavior can be described by a tensorial Green-Kubo expression which will be examined in this paper. The structure and the dynamics of those molecular liquids are also studied to find how they contribute to the friction. Simulation results show that strain has increased the friction but more dominantly along the strain direction. Non spherical molecules are more sensitive to those changes and relaxation time contributes a large part in the friction. Details of these findings will be presented in the following sections.

2.2 Friction and slip tensors for anisotropic surfaces

2.2.1 Green-Kubo expression for the friction tensor

Let us consider the situation where the fluid flowing past a solid surface of area \mathcal{A} where the slip velocity \mathbf{v}_s is linearly proportional to the tangential friction force \mathbf{F}

$$\mathbf{F} = \mathcal{A}\mathbf{\Lambda}\mathbf{v}_s. \quad (2.3)$$

Based on linear response theory, Boquet and Barrat [19, 20] proposed to use the Green-Kubo formalism [76] to compute the friction coefficient. In the general situations, the expression for the friction tensor $\mathbf{\Lambda}$ is the following [13]

$$\mathbf{\Lambda} = \frac{1}{\mathcal{A}k_B T} \int_0^\infty \langle \mathbf{F}(0) \otimes \mathbf{F}(t) \rangle dt \quad (2.4)$$

In (2.4), the ensemble average, notation $\langle \dots \rangle$, of the force correlation function is taken in the equilibrium state and integrated with time. Since the correlation is decaying with time, tensor $\mathbf{\Lambda}$ can be further decomposed into a static term and time decorrelation tensor $\boldsymbol{\tau}_t$, for example

$$\mathbf{\Lambda} = \frac{\langle \mathbf{F}(0) \otimes \mathbf{F}(0) \rangle}{\mathcal{A}k_B T} \boldsymbol{\tau}_t, \quad \boldsymbol{\tau}_t = \langle \mathbf{F}(0) \otimes \mathbf{F}(0) \rangle^{-1} \int_0^\infty \langle \mathbf{F}(0) \otimes \mathbf{F}(t) \rangle dt \quad (2.5)$$

For isotropic-like surfaces, $\mathbf{\Lambda}$ can be replaced with a single friction coefficient λ [19, 20] and $\boldsymbol{\tau}_t$ by the decorrelation time τ_t

$$\lambda = \frac{\langle F(0)^2 \rangle}{\mathcal{A}k_B T} \tau_t, \quad \tau_t = \frac{\int_0^\infty \langle F(0)F(t) \rangle dt}{\langle F(0)^2 \rangle} \quad (2.6)$$

For surfaces with two axes of symmetry, say Ox and Oy , tensor $\mathbf{\Lambda}$ is diagonal in the Oxy system with principal values λ_{xx} and λ_{yy} . In this paper, we shall investigate the behavior of the friction tensor in the modelling of anisotropic surfaces.

Relations between friction coefficient and the fluid structure have been studied in the past. In particular, for FCC (100) crystal surfaces [12] or honeycomb lattice like graphene [45], simple working definitions of the friction coefficient at the solid-liquid interface can be derived. We note that the same theory can be extended to any Bravais lattice structures. Given a surface lying on the plane xOy , the components $\lambda_{\alpha\beta}$ ($\alpha, \beta = x, y$) of the friction tensor can be rewritten in the following form

$$\lambda_{\alpha\beta} = \frac{1}{\mathcal{A}k_B T} \int_0^\infty dt \iint dz dz' d\mathbf{x} d\mathbf{x}' F_\alpha(\mathbf{x}', z') F_\beta(\mathbf{x}, z) \langle \rho(\mathbf{x}, z, 0) \rho(\mathbf{x}', z', t) \rangle \quad (2.7)$$

with $\rho(\mathbf{x}, z, t)$ being the microscopic fluid density at planar coordinate \mathbf{x} and distance z from the wall [57]. In special cases where x and y are already axes of symmetry of the surface, the off-diagonal friction coefficients vanish, $\lambda_{xy} = 0$, and it is sufficient to determine the principal values, λ_{xx} and λ_{yy} , of the friction tensor. The theoretical investigation of those friction coefficients will be detailed in the following section, with application to strained graphene system.

2.2.2 Approximation of fluid-wall potential for strained graphene

Let us assume that by some reason, the graphene sheet is uniformly strained in direction x (armchair) and/or y (zigzag) [160] but still periodic. There are several ways of defining the unit cell and the pair of primitive reciprocal lattice vectors, for example (see Fig. 2.1).

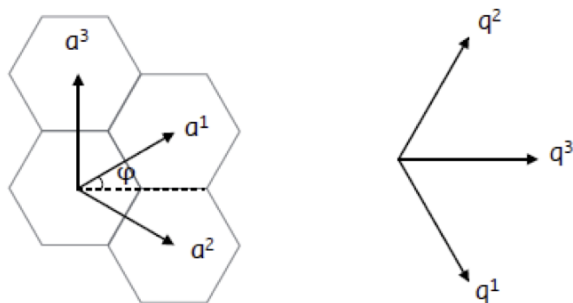


Figure 2.1: Lattice vectors and reciprocal vectors

$$(\mathbf{a}^1, \mathbf{a}^2) \rightarrow (\mathbf{q}^2, \mathbf{q}^1), \quad (\mathbf{a}^1, \mathbf{a}^3) \rightarrow (\mathbf{q}^3, \mathbf{q}^1), \quad (\mathbf{a}^2, \mathbf{a}^3) \rightarrow (\mathbf{q}^3, \mathbf{q}^2), \quad (2.8)$$

with $\mathbf{a}^1, \mathbf{a}^2, \mathbf{a}^3$ being the primitive lattice vectors and $\mathbf{q}^1, \mathbf{q}^2, \mathbf{q}^3$ associated primitive reciprocal lattice vectors

$$\begin{aligned} \mathbf{a}^1 &= l_0(\cos \varphi \mathbf{e}_x + \sin \varphi \mathbf{e}_y), & \mathbf{a}^2 &= l_0(\cos \varphi \mathbf{e}_x - \sin \varphi \mathbf{e}_y), & \mathbf{a}^3 &= 2l_0 \sin \varphi \mathbf{e}_y \\ \mathbf{q}^1 &= q_0 \left(\frac{\mathbf{e}_x}{2 \cos \varphi} - \frac{\mathbf{e}_y}{2 \sin \varphi} \right), & \mathbf{q}^2 &= q_0 \left(\frac{\mathbf{e}_x}{2 \cos \varphi} + \frac{\mathbf{e}_y}{2 \sin \varphi} \right), & \mathbf{q}^3 &= \frac{q_0 \mathbf{e}_x}{\cos \varphi}. \end{aligned} \quad (2.9)$$

The quantity φ is half angle between \mathbf{a}^1 and \mathbf{a}^2 , l_0 is the distance between hexagon centers as shown in Fig. 2.1 and $q_0 = 2\pi/l_0$. In all cases, the following properties must hold

$$\mathbf{q}^i \cdot \mathbf{a}^i = 0, \quad \mathbf{q}^i \cdot \mathbf{a}^j = \pm 2\pi \quad (2.10)$$

We consider first the case of monatomic fluid and note that results for molecules can be obtained approximately by superpositions as suggested in Ref. [46]. The analytical expression of friction force $\mathbf{F}(\mathbf{x}, z)$ of a fluid atom with the wall is derived from the potential $V(\mathbf{x}, z)$. To the first order Fourier series approximation (see Appendix B), we can write

$$V(\mathbf{x}, z) = V_0(z) - V_1(z)[\cos(\mathbf{q}^1 \cdot \mathbf{x}) + \cos(\mathbf{q}^2 \cdot \mathbf{x})] - \alpha(z)V_1(z) \cos(\mathbf{q}^3 \cdot \mathbf{x}). \quad (2.11)$$

Depending on the choice of the unit cell, the original Fourier series contains only two of three terms $\cos(\mathbf{q}^1 \cdot \mathbf{x})$, $\cos(\mathbf{q}^2 \cdot \mathbf{x})$ or $\cos(\mathbf{q}^3 \cdot \mathbf{x})$. Here we adopt an expression that can account for the periodicity of the potential along all directions $\mathbf{a}^1, \mathbf{a}^2$ and \mathbf{a}^3 and the anisotropy effect via the parameter $\alpha(z)$. Comparing with the expression of Ref. [45]:

$$V(\mathbf{x}, z) = V_0(z) - V_1(z)[\cos(\mathbf{q}^1 \cdot \mathbf{x}) + \cos(\mathbf{q}^2 \cdot \mathbf{x})], \quad (2.12)$$

the present expression is able to recover the symmetry of the graphene structure, which is important for the isotropy/anisotropy analysis (see Fig. 2.2). For given z the values of $V_0(z), V_1(z)$

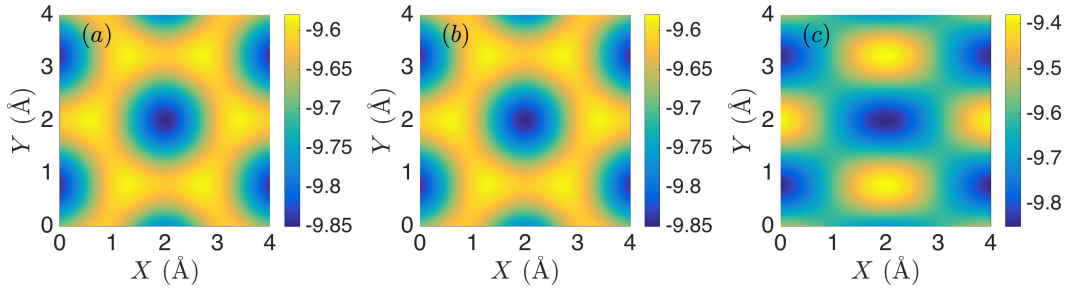


Figure 2.2: Comparison of methane-graphene potentials $V(\mathbf{x}, z_O)$ at the first fluid layer, about one molecule diameter from graphene, produced by exact calculation and two analytical approximations (2.11) and (2.12) (a) Exact distribution of potential energy $V(\mathbf{x}, z_O)$ in the first layer. (b) Distribution of potential energy calculated by expression (2.11). (c) Distribution of potential energy calculated by expression (2.12). It is easy to notice that (2.11) can recover the symmetry of the exact potential while (2.12) can not.

and $\alpha(z)$ are determined by fitting the exact results at 3 representative points, for example

$$\begin{aligned}
 V(\mathbf{0}, z) &= V(\mathbf{a}^1, z) = V(\mathbf{a}^2, z) = V(\mathbf{a}^3, z) = V_0(z) - (\alpha(z) + 2)V_1(z), \\
 V(\mathbf{a}^1/2, z) &= V_0(z) + \alpha(z)V_1(z), \\
 V(\mathbf{a}^3/2, z) &= V_0(z) - (\alpha(z) - 2)V_1(z).
 \end{aligned} \tag{2.13}$$

2.2.3 Analytical model for fluid-wall interaction

After constructing the analytical expression for the potential, we can differentiate the latter with respect to x and y to derive the tangential force components

$$\begin{aligned}
 F_x &= f_x(z)[\sin(\mathbf{q}^1 \cdot \mathbf{x}) + \sin(\mathbf{q}^2 \cdot \mathbf{x}) + 2\alpha(z)\sin(\mathbf{q}^3 \cdot \mathbf{x})], \quad F_y = f_y(z)[\sin(\mathbf{q}^1 \cdot \mathbf{x}) - \sin(\mathbf{q}^2 \cdot \mathbf{x})] \\
 f_x(z) &= \frac{V_1(z)q_0}{2\cos\varphi}, \quad f_y(z) = \frac{-V_1(z)q_0}{2\sin\varphi}
 \end{aligned} \tag{2.14}$$

Here $V_1(z)(1 + \alpha(z))/2$ and $V_1(z)$ are the energy barriers along direction \mathbf{a}^1 (or \mathbf{a}^2) and \mathbf{a}^3 . As a result, we can rewrite (2.7) in the form

$$\begin{aligned}
 \lambda_{xx} &= \frac{1}{\mathcal{A}k_B T} \int_0^\infty dt \int dz dz' f_x(z) f_x(z') \iint d\mathbf{x} d\mathbf{x}' [\sin(\mathbf{q}^1 \cdot \mathbf{x}') + \sin(\mathbf{q}^2 \cdot \mathbf{x}') + 2\alpha \sin(\mathbf{q}^3 \cdot \mathbf{x}')] \\
 &[\sin(\mathbf{q}^1 \cdot \mathbf{x}) + \sin(\mathbf{q}^2 \cdot \mathbf{x}) + 2\alpha \sin(\mathbf{q}^3 \cdot \mathbf{x})] \langle \rho(\mathbf{x}, z, 0) \rho(\mathbf{x}', z', t) \rangle
 \end{aligned} \tag{2.15}$$

and a similar expression for λ_{yy} . Following the approach presented in Ref. [12], we make use of the Fourier transform and obtain the simple expression for λ_{xx}

$$\begin{aligned} \lambda_{xx} = & \frac{q_0^2}{4 \cos^2 \varphi \mathcal{A} k_B T} \int_0^\infty dt \int dz dz' V_1(z) V_1(z') \times \\ & \times \Re \{ \langle \rho_{\mathbf{q}^1}(z)(0) \rho_{-\mathbf{q}^1}(z')(t) \rangle + 2\alpha(z)\alpha(z') \rho_{\mathbf{q}^3}(z)(0) \rho_{-\mathbf{q}^3}(z')(t) \} \end{aligned} \quad (2.16)$$

and for λ_{yy}

$$\lambda_{yy} = \frac{q_0^2}{4 \sin^2 \varphi \mathcal{A} k_B T} \int_0^\infty dt \int dz dz' V_1(z) V_1(z') \Re \{ \langle \rho_{\mathbf{q}^1}(z)(0) \rho_{-\mathbf{q}^1}(z')(t) \rangle \} \quad (2.17)$$

In deriving (2.16,2.17), we assume that the fluid is homogeneous in the plane xOy and the symmetry between \mathbf{q}^1 and \mathbf{q}^2 . The notation \Re stands for the real part and $\rho_{\mathbf{q}}$ is given by the expression

$$\rho_{\mathbf{q}}(z, t) = \int d\mathbf{x} e^{-i\mathbf{q}\cdot\mathbf{x}} \rho(\mathbf{x}, z, t) \quad (2.18)$$

It is clear that for perfect graphene surface where $\varphi = \pi/6$, $\alpha(z) = 1$ and the roles of $\mathbf{q}^1, \mathbf{q}^2, \mathbf{q}^3$ can be interchanged, one can show that $\lambda_{xx} = \lambda_{yy}$. This property can not be obtained using potential (2.12), as done in previous works. When only the first fluid layer at coordinate z_0 is considered, one can obtain the simple relations

$$\begin{aligned} \langle F_x(0) F_x(t) \rangle & \simeq \frac{q_0^2 V_1^2(z_0)}{4 \cos^2 \varphi} N(z_0) [\mathcal{F}(\mathbf{q}^1, z_0, t) + 2\alpha^2(z_0) \mathcal{F}(\mathbf{q}^3, z_0, t)] \\ \langle F_y(0) F_y(t) \rangle & \simeq \frac{q_0^2 V_1^2(z_0)}{4 \sin^2 \varphi} N(z_0) \mathcal{F}(\mathbf{q}^1, z_0, t) \end{aligned} \quad (2.19)$$

where $\mathcal{F}(\mathbf{q}, z_0, t)$ is the planar intermediate scattering function of $N(z_0)$ molecules

$$\mathcal{F}(\mathbf{q}, z_0, t) = \frac{1}{N(z_0)} \langle \rho_{\mathbf{q}}(z_0)(0) \rho_{-\mathbf{q}}(z_0)(t) \rangle \quad (2.20)$$

Substituting $t = 0$ in the above equation yields the zero-time behavior and the relation with the planar structure factor $S(\mathbf{q}^k, z_0)$ and the layer density $\rho_s(z_0) = N(z_0)/\mathcal{A}$

$$\begin{aligned}\langle F_x^2(0) \rangle / \mathcal{A} &\simeq \frac{q_0^2 V_1^2(z_0)}{4 \cos^2 \varphi} \rho_s(z_0) [S(\mathbf{q}^1, z_0) + 2\alpha^2(z_0) S(\mathbf{q}^3, z_0)] \\ \langle F_y^2(0) \rangle / \mathcal{A} &\simeq \frac{q_0^2 V_1^2(z_0)}{4 \sin^2 \varphi} \rho_s(z_0) S(\mathbf{q}^1, z_0)\end{aligned}\quad (2.21)$$

The 2D structure factor $S(\mathbf{q}, z_0)$ of the layer of the first liquid layer can be calculated by using the following expression [45]:

$$S(\mathbf{q}, z_0) = \frac{1}{N(z_0)} \left\langle \left(\sum_{j=1}^N \cos(\mathbf{q} \cdot \mathbf{r}_j) \right)^2 + \left(\sum_{j=1}^N \sin(\mathbf{q} \cdot \mathbf{r}_j) \right)^2 \right\rangle \quad (2.22)$$

In (2.22), N is the number of fluid molecules in the first fluid layer, \mathbf{r}_j is the coordinates of the j th fluid atoms. Although using equation (2.21) can reproduce correctly some important phenomena and tendencies, it considerably underestimates $\langle F_x^2 \rangle$ and $\langle F_y^2 \rangle$ by an order of magnitude. In reality, the first liquid layer is not truly localized in a plane, as considered by the theory, but rather spreads over a finite thickness. Using $V(z_0)$ to represent the whole depth and the presence of many liquid layers can be responsible for those differences. To improve these issues, a possible treatment is to use the assumption of independent multi liquid layer at z_0, z_1, \dots , which results the equations

$$\begin{aligned}\langle F_x^2(0) \rangle &\simeq \frac{q_0^2}{4 \cos^2 \varphi} \sum_i N(z_i) V_1^2(z_i) [S(\mathbf{q}^1, z_i) + 2\alpha^2(z_i) S(\mathbf{q}^3, z_i)], \\ \langle F_y^2(0) \rangle &\simeq \frac{q_0^2}{4 \sin^2 \varphi} \sum_i N(z_i) V_1^2(z_i) S(\mathbf{q}^1, z_i),\end{aligned}\quad (2.23)$$

in which calculation of structure factor must be done at different levels. In the present paper, we propose using a simpler approximate formula

$$\begin{aligned}\langle F_x^2(0) \rangle &\simeq \frac{q_0^2}{4 \cos^2 \varphi} [S(\mathbf{q}^1, z_0) + 2\alpha^2(z_0) S(\mathbf{q}^3, z_0)] \int dz \rho(z) V_1^2(z), \\ \langle F_y^2(0) \rangle &\simeq \frac{q_0^2}{4 \sin^2 \varphi} S(\mathbf{q}^1, z_0) \int dz \rho(z) V_1^2(z).\end{aligned}\quad (2.24)$$

This expression is also computationally simple while keeping all the important ingredients as before. As noted previously, the above analysis is applied to monatomic fluid model. For fluids composed of molecules, as example H₂O or CO₂, the full expression $\langle F_\alpha^2(0) \rangle$ is the following

$$\langle F_\alpha^2(0) \rangle = \sum_i \langle (F_\alpha^{(i)}(0))^2 \rangle + \sum_{i \neq j} \langle F_\alpha^{(i)}(0) F_\alpha^{(j)}(0) \rangle \quad (2.25)$$

where the summations are done over the different atoms composing the molecule of the fluid. In a more recent work [46], numerical evidences have shown that we can neglect the cross correlation between the friction of different atom species. As a result, we can compute separately the friction of each species and then simply superpose,

$$\langle F_\alpha^2(0) \rangle \simeq \sum_i \langle (F_\alpha^{(i)}(0))^2 \rangle \quad (2.26)$$

The accuracy of those simplifications will be examined in comparison with the exact results from MD simulation presented in the next section.

2.3 Molecular Dynamics simulation

2.3.1 Choice of systems and potentials

To study the friction theory presented previously and the influence of molecular sizes and shapes, and interactions, we considered different liquids confined between two strained graphene sheets. Those liquids are water (H₂O, triangular shape), carbon dioxide (CO₂, rod like shape) and methane (CH₄, spherical particle), which are present abundantly in nature and involved in many technological, energetic and environmental problems. For example, the water-graphene interaction arises in fast transport nanofluidic systems with applications in desalinated membrane industry. Carbon dioxide sequestration and methane recovery are directly related to exploitation of natural gas reserve in coal bed while reducing green house effect. The presence

of underground water is also an issue that must be taken into account. In summary, the study of those systems from the atomic scale is of both theoretical and technological importances.

The choice of the different pairwise and many-body interaction potentials is crucial with a strong impact on the MD results. The fluid-wall interactions are modeled by Lennard-Jones (LJ) potentials whose parameters are given in Table 2.1.

For the graphene sheet, denoted as G, we have used the adaptive intermolecular reactive bond order (AIREBO) potential [130] for the interaction between the carbon atoms. In addition to the classical reactive empirical bond-order (REBO) functional form, LJ and 4-body torsional interactions are taken into account.

The model TIP4P-2005 [1] has been used for water, constituting of four rigid sites, three fixed point charges and one LJ center. The H-O-H bond angle 104.52° and the O-H bond length 0.9572 \AA are maintained using SHAKE algorithm [109]. It is worthy emphasizing that unlike many previous works on water/graphene systems, we take into account the realistic interaction between G-H based on Ref. [66] with LJ parameters provided in Table 2.1. Numerical results in the later section also show that the friction coefficients change significantly and become closer to the experimental values in Ref. [116] with the use of G-H interaction.

		Fluid-Fluid		Fluid-Wall		
		$\sigma_{ff}[\text{\AA}]$	$\epsilon_{ff}[\text{meV}]$		$\sigma_{fw}[\text{\AA}]$	$\epsilon_{fw}[\text{meV}]$
H ₂ O	O-O	3.159	8.0	O-G	3.38	4.664
				H-G	2.7	2.487
CO ₂	O-O	3.033	6.938	C-G	3.059	2.418
	C-C	2.757	2.424	O-G	3.197	4.091
	C-O	2.892	4.101			
CH ₄		3.73	12.75		3.55	5.547

Table 2.1: Interaction LJ parameters for H₂O, CO₂ and CH₄ interacting with graphene.

For CO₂-CO₂ interaction, we have used EPM2 model [58] which consists of 12-6 LJ sites in conjunction with partial charges centered on each of sites. The O-C-O bond angle 180° and the C-O bond length 1.16 Å are maintained constant by rigid body algorithm. For CO₂-Graphene interaction, we have used LJ potential computed using Lorentz-Berthelot rules: $\sigma_{AB} = (\sigma_A + \sigma_B)/2$ and $\epsilon_{AB} = \sqrt{\epsilon_A \epsilon_B}$ with LJ parameters of graphene from Ref. [147]: $\sigma_G = 3.36$ Å, $\epsilon_G = 2.413$ meV (see Table 2.1).

The CH₄ molecules are modeled as united spherical particles with the TraPPE force field [91] and the fluid-wall potential is also determined by Lorentz-Berthelot rules with the same σ_G and ϵ_G as for the CO₂-Graphene interaction. All LJ parameters in CH₄-Graphene model are presented in Table 2.1.

Since interaction potentials between the fluid molecules and graphene sheets are important for the derivation of meaningful results, we carry out some verifications. The global interaction potential between a fluid molecule and the graphene sheet have been recomputed from the pairwise LJ using parameters of Table 2.1. The corresponding potential well-depths and equilibrium distances have then been compared with bibliographic entries. For some liquids, experimental data only exist for the molecule-graphite interaction. In that cases, we have also computed the global interaction potentials with graphite. The graphene slab is composed of 256 atoms and the graphite surface contains 8000 atoms divided in 5 layers. Periodic boundary conditions in the x and y directions are applied in both cases. The C-C distance has been fixed to 2.46 Å for both structures. The geometries of H₂O, CH₄ and CO₂ are fixed to those of the MD simulations. The corresponding results are displayed in Table 2.2.

For H₂O-Graphene, the potential parameters have been derived by Hugues *et al.* [66] from extensive plane-wave DFT calculations using the revPBE-vdW-DF functional in order to produce an efficiently implemented polarisable force-field (GRAPPA). The potential well depth and equilibrium geometry, obtained for the adsorption conformation where both H water atoms

	V_{eq} [meV]	Ref.	Z_{eq} [Å]	Ref.
H ₂ O-Graphene	130.37	139.92 ^a	3.28	3.19 ^a
CO ₂ -Graphene	158.70		3.13	
CO ₂ -Graphite	177.21	178.2 ^b	3.11	3.2±0.1 ^b
CH ₄ -Graphene	102.68		3.49	
CH ₄ -Graphite	118.59	130±0.1 ^b	3.47	3.45 ^b

^a Reactive force field [66]. ^b Best estimate [149].

Table 2.2: Potential well depths and equilibrium geometries for the global interaction between one molecule of H₂O, CO₂, or CH₄ interacting with graphene or graphite.

pointed towards a carbon atom of graphene, compare well with the results of coupled-cluster (DFT/CC) calculations [108].

For CO₂ and CH₄, only their interactions with graphite have been previously reported to the best of our knowledge. The best estimate potentials have been reported from averaged interaction potential as deduced from analyses of experimental data and calculations by Vidali *et al.* [149]. The corresponding potential well depth and equilibrium geometry of the CO₂-graphite system agree with the present values obtained for the parallel bridge conformation, that has been confirmed to be the lowest energy conformation by Xu *et al.* [161] with DFT calculations for the CO₂-(4×4) six-ring aromatic surface system.

The present LJ potential for CH₄-G leads to a hollow lowest energy conformation, i.e. the CH₄ molecule preferentially adsorbs towards the center of a C ring, which is one of the lowest energy adsorption site found also by Xu *et al.* [161] for the CH₄-(4×4) six-ring aromatic surface system. The recomposed global interaction potential of CH₄ with graphite also presents potential well depth and equilibrium geometry in good agreement with the Vidali *et al.* [149] best estimations.

From the present analysis, we can conclude that the LJ parameters given in Table 2.1 allow to reproduce the global interactions of the different molecules with graphene and the corresponding pairwise potentials can be safely used in MD simulations devoted to interface effects.

2.3.2 System setup

All our molecular dynamic simulations and friction calculations are done in equilibrium state using LAMMPS (Large-scale Atomic/Molecular Massively Parallel Simulator) package [102]. The systems, periodic in x, y , are first relaxed for 5×10^6 time step at zero lateral external pressure in order to reach the natural reference state. Next, the simulation box is deformed in x or y direction in accordance with the desired strain for graphene. In the present work, we keep the direction y (zigzag) undeformed while the strain in direction x (armchair) is varied from 0% to 10%. The systems undergo equilibration process again and only after 5×10^6 time step, we start to compute the auto correlation function based on data of the next 10×10^6 time step. During the whole simulation, an external uniform pressure P_{ext} is applied to graphene sheet to equilibrate the liquid pressure inside the channel. Additionally, to avoid drifting, one atom of the lower graphene sheet is fixed. The simulation time step is 1 fs. The temperature of the graphene is maintained by Nose Hoover thermostat and the equations of motions of liquid atoms are integrated using Verlet algorithm. In order to obtain the liquid density for fluids, we list different temperature and different external pressure for the different systems in Tab 2.3. To improve the reliability, the results are averaged over at least 10 independent runs of the same system.

Liquids	N	ρ [nm ⁻³]	T [K]	P_{ext} [bar]
H ₂ O	1001	33.1	298	1
CH ₄	720	16.7	148	520
CO ₂	352	15.9	250	100

Table 2.3: Simulation conditions for different liquid systems including N number of liquid molecules, ρ the average liquid density confined between the two graphene sheets, T the temperature and P_{ext} the external pressure.

Since the immobile graphene nanochannel may lead to non-physical results, flexible graphene sheets have been used in all simulations. The periodic boundary conditions are adopted in x

and y . The dimension of the graphene surface A is $42.6 \text{ \AA} \times 24.6 \text{ \AA}$ and the height of nano-channels has been adjusted by external pressure and temperature of the given fluid. A snapshot of our systems can be seen in Fig. 2.3.

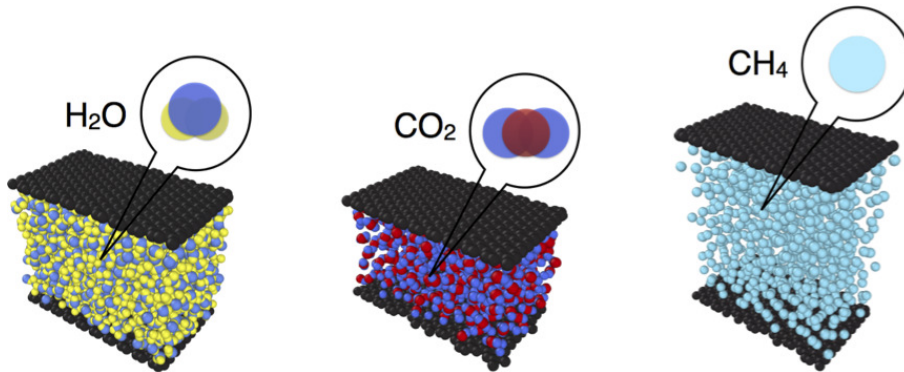


Figure 2.3: Snapshots of the three systems (H_2O , CO_2 and CH_4) in graphene nano-channel under consideration. The shape of three molecules are drawn according to molecules' bond lengths, bond angles and σ_{fw} diameters.

In water-graphene simulations, the system is composed of 1001 water (H_2O) molecules between two graphene sheets. For simulations involving methane (CH_4) in graphene channel, 720 liquid molecules are considered. Regarding carbon dioxide-graphene system, there are 352 CO_2 molecules in the simulation box.

2.3.3 Results and discussion

The variation of the liquid density with respect to distance from the graphene surface can be seen in Fig. 2.4. We find that for spherical particles like CH_4 , the density profile is almost insensitive to the applying strain whereas for the most aspherical molecules, i.e CO_2 which adopts a rod shape, the influence is more visible. Specifically, both the first and the second peaks corresponding to the first and second liquid layers decrease. The effect is more pronounced for CO_2 simulations for which the second peak shifts slightly towards the bulk. For all three different fluids, the positions of the first peak are however in agreement with the fluid-wall LJ distance, σ_{fw} .

From the density profile, intuitively, one can suppose that less liquid molecules are present near the wall smaller will be friction of strained graphene. However, this prediction is disproved by detailed results presented in the following. The anisotropy effect, which can not be shown from the density profile, must also be studied.

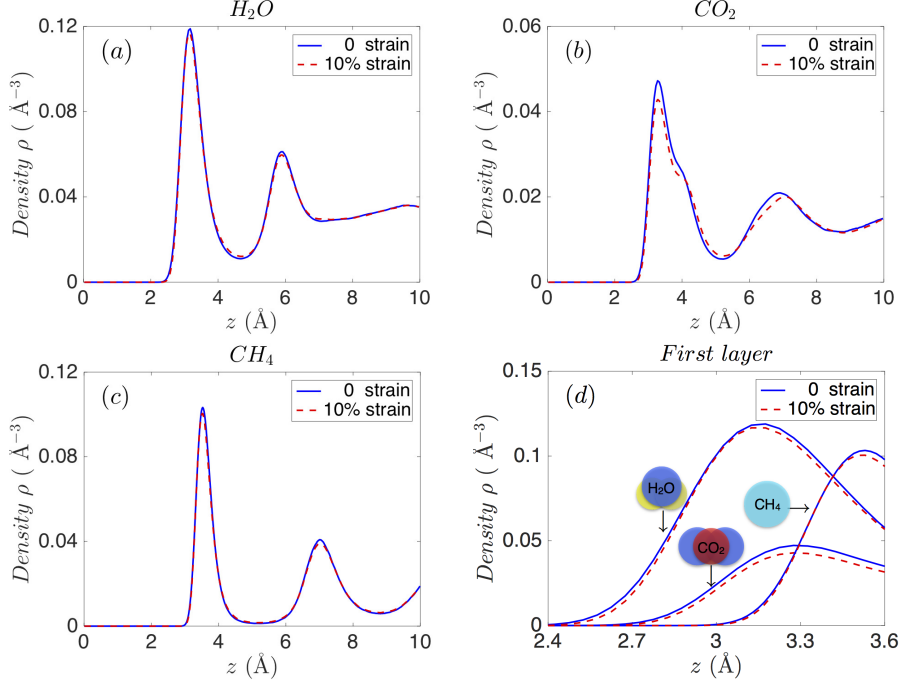


Figure 2.4: Fluid molecular density for different systems: (a) for H_2O , (b) for CO_2 and (c) for CH_4 . (d) variation of liquid density around the first peaks (first liquid layer).

The exact value of friction tensor can be computed using the time correlation presented in Fig. 2.5. To obtain the friction coefficients by the Green Kubo expression, the correlations $\langle F_\alpha(0)F_\beta(t) \rangle$ are accumulated continuously until convergence. For given t , at least 800000 samples are collected for the ensemble average. Finally, results are averaged again over 10 independent simulations. The difference in behavior between strained and natural graphene can be observed, especially along direction x . All curves show an exponentially decaying behavior but they are quantitatively different. The zero-time value $\langle F^2(0) \rangle$ at $t = 0$, representing the static friction intensity, is significantly higher for strained graphene and the correlation decays more slowly in that case. We will see later that the correlation time increases with the strain value. The same behavior can also be observed for friction along y but the change is less pronounced

since the graphene has zero strain along y . The anisotropy effect due to unequal strain can also be seen from the x, y correlation behaviors which are identical for natural graphene and very different for strained graphene.

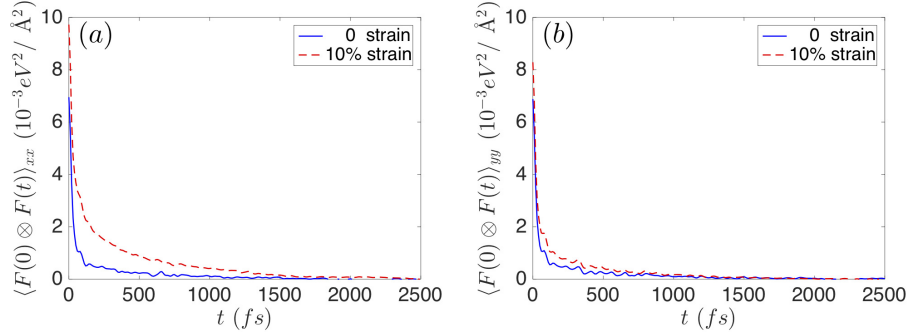


Figure 2.5: Time correlation of friction forces along x and y directions for H_2O and graphene.

Fig. 2.6 and Tab. 2.4 shows the friction coefficient results for different fluid types at different strains. The isotropic behavior can be clearly seen for all types of liquid at zero strain and the anisotropy effect starts to increase as the strain increases. The friction increases for both directions but the increase is more important for direction x . It is interesting to note that the relation between λ_{xx} and λ_{yy} , and the applying strain is quasi-linear up to strain as large as 10%. The difference between λ_{xx} and λ_{yy} is more significant for non-spherical molecules like H_2O and CO_2 , and is reduced for spherical molecules like CH_4 . Due to the direct connection between slip length and friction, the slip effect is minimum, maximum along x, y direction, respectively. The sensitiveness of non-spherical molecules suggests that it is possible to enhance or reduce the transport performance using engineering strain in one or two directions. However, it is less effective to use this method for spherical molecules.

The viscosity for the TIP4P/2005 water model is 0.855 mPa.s at 298 K and 1 bar [52]. In order to compare our results with other researches, we converted all friction coefficients λ of water to the slip lengths L_s using relation (2.2). At the strain-free state, the present L_s value is 30.5 nm which is consistent with the value of about 30 nm obtained by Thomas *et al.* [135] and which is also close to the theoretical value of Myers, i.e. 35 nm [96]. In the recent experiment of Secchi *et al.* [116], measurements on very large radius (33 nm to 50 nm) CNTs show that L_s varies

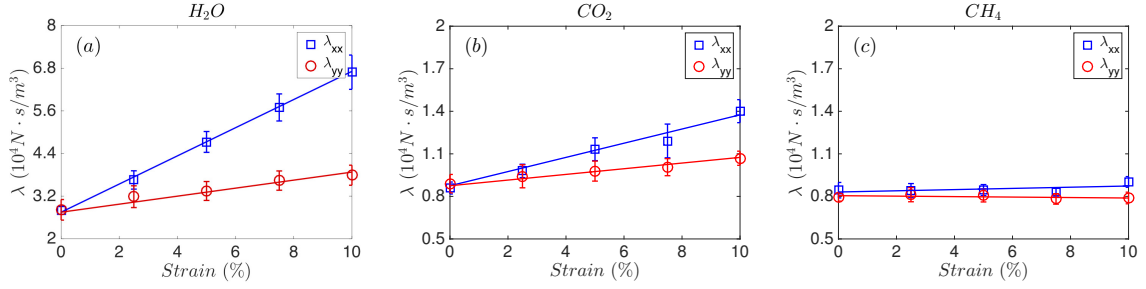


Figure 2.6: Friction coefficient, from MD simulations, with strain ranging from 0% to 10%. The quasi-linear relation is observed between friction coefficient and strain. The error bars are calculated for 10 simulations.

$\varepsilon(\%)$		0	2.5	5	7.5	10
H ₂ O	λ_{xx} ($10^4 N \cdot s/m^3$)	2.81	3.66	4.73	5.70	6.69
	λ_{yy} ($10^4 N \cdot s/m^3$)	2.80	3.19	3.35	3.64	3.79
CO ₂	λ_{xx} ($10^4 N \cdot s/m^3$)	0.859	0.980	1.13	1.19	1.40
	λ_{yy} ($10^4 N \cdot s/m^3$)	0.890	0.942	0.978	1.00	1.07
CH ₄	λ_{xx} ($10^4 N \cdot s/m^3$)	0.844	0.840	0.844	0.830	0.902
	λ_{yy} ($10^4 N \cdot s/m^3$)	0.794	0.812	0.807	0.782	0.789

Table 2.4: Friction coefficients for different systems.

from 45 nm to 17 nm, which is comparable with the present results. It can be concluded that accounting for the G-H interaction and the flexibility of the graphene sheet are very important. The present results show that the typical L_s values are two times smaller than those resulting from simulations neglecting these aspects. More importantly, they are closer to experimental results. For example in Fig. 2.7, at all strain values, the present L_s along direction x is significantly smaller than the isotropic results (same strain along x and y directions) of Xiong *et al.* [160].

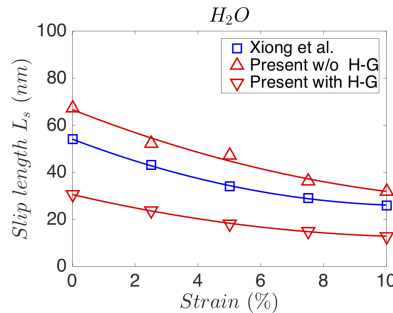


Figure 2.7: Influence of the fluid models on the slip length L_s of water-graphene system.

Since the friction increase due to strain can be approximately decomposed by Eqs (2.5, 2.24), we

shall look at the influence of different terms in the overall behavior, including the static terms $\langle F_x(0) \rangle$, $\langle F_y(0) \rangle$ depending on the structure factor $S(\mathbf{q})$ and the integral involving potential strength and the decorrelation time τ_x , τ_y . Fig. 2.8(a) shows that the quasi-isotropic structure is observed at the first fluid layer at the maximal strain 10%. The changes of structure factor due to strain can be considered negligible Fig. 2.8(b), less than 2%. This remarks suggests that the contribution of $S(\mathbf{q})$ on the anisotropy is not significant. The norm of reciprocal vectors \mathbf{q}^1 , \mathbf{q}^2 and \mathbf{q}^3 at different strain states are presented in Table 2.5.

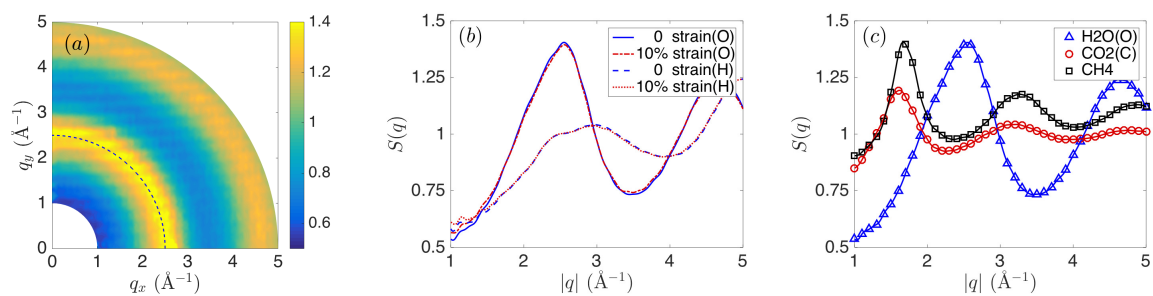


Figure 2.8: (a) 2D structure factor of oxygen (H_2O) with 10% unilateral strain on graphene sheet. (b) The structure factor of oxygen and hydrogen of water with different q . (c) The structure factor of oxygen (H_2O), carbon (CO_2) and methane (CH_4) at strain-free state.

$\varepsilon(\%)$	0	2.5	5	7.5	10
$q^1[\text{\AA}^{-1}]$	2.950	2.932	2.915	2.900	2.885
$q^3[\text{\AA}^{-1}]$	2.950	2.878	2.809	2.744	2.682

Table 2.5: The norm of reciprocal vectors for different strains. Note that $q^1 = q^2$.

Fig. 2.9 represents the dependence of coefficients α and V_1 in terms of the distance z of a methane molecule from the graphene sheet. As can be seen, both strain and z can affect α and V_1 , but the strain mainly contributes to the linear change of α while the potential energies coefficient V_1 is very sensitive to z . The variation of $V_1(z)$ in the range, $z \in [2.2, 3.6](\text{\AA})$, better agrees with exponential form $V_1(z) = 3.031 \times 10^4 \exp\{-5.797z\}(\text{eV})$ for strain free case and $V_1(z) = 2.104 \times 10^4 \exp\{-5.67z\}(\text{eV})$ for 10% strain. It suggests that using the representative value at z_0 may not yield the best estimation. In this paper we consider the potential form of V_1 when calculating the static term in (2.24).

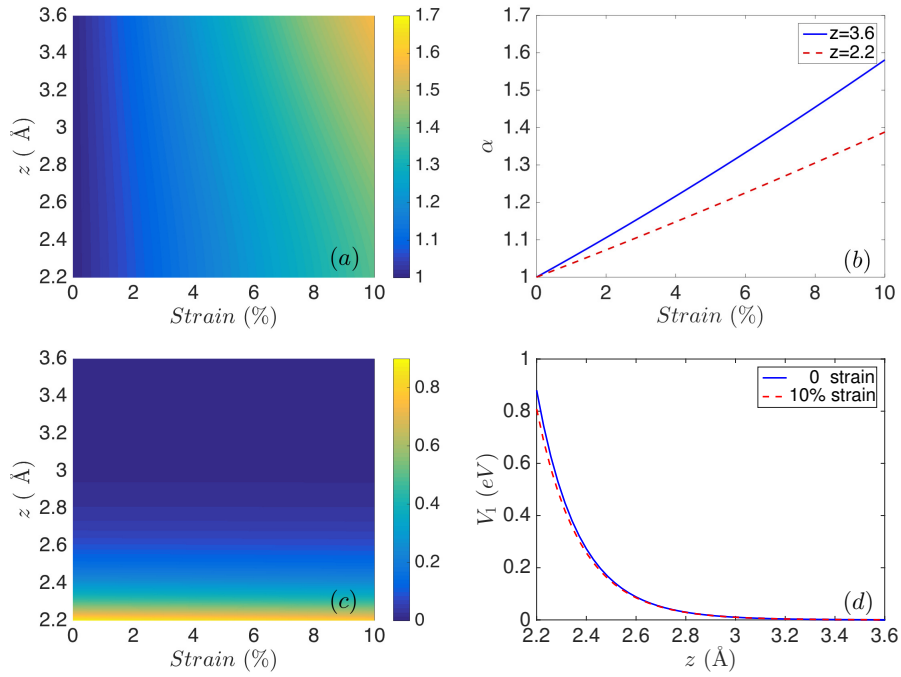


Figure 2.9: Coefficient α (two upper figures) and potential energies V_1 (two lower figures) as a function of the strain and the distance z of methane molecule from the graphene sheet.

In Fig.2.10, we can find that the static forces $\langle F_x^2 \rangle / A$, $\langle F_y^2 \rangle / A$, and the decorrelation time depend on the strain. It is noted that the spherical molecules (CH_4) are less sensitive to the unilateral strain, which agrees with the friction results shown in Fig. 2.6. The variation of those quantities for H_2O and CO_2 is much more significant. The theoretical results from (2.24) have well predicted the variation trend and the value of $\langle F_x^2 \rangle / A$ with strain. For $\langle F_y^2 \rangle / A$, there are still difference between theoretical and simulation results. The simulation results show slight changes of $\langle F_y^2 \rangle / A$ while it is more visible according to the theoretical prediction. The discrepancies could be clearly understood from the analysis of the assumptions: i) the use of a time independent potential energy surface obtained from static graphene ii) the superposition hypothesis for molecules in Eq. (26) iii) the fact that we only account for the structure factor in the first liquid layer. The first assumption, adopted in most theoretical works [12, 46, 45], corresponds to situations where flexibility of the graphene sheet is negligible, e.g at small temperature or at large strain. Physically, stretching membrane reduces the out-of-plane vibration amplitude, which agrees with the reduced difference between MD solution and the theory at

large strain for both $\langle F_x^2 \rangle / A$ and $\langle F_y^2 \rangle / A$. The second superposition hypothesis have been tested for large alkanes [46] and proved to yield good estimates. Finally, the assumption that allows reducing the static part of (2.16) to (2.24) is relatively strong but necessary to obtain important connections to the molecular distribution and the interaction strength, appeared as two separated contributions. In (2.24), although we does consider the variation of potential with depth for the whole slab, but only the structure factor of the first liquid layer is used for calculation. As a result, potential improvements to the model can be done from the analysis of second and third liquid layers based on the same procedure, in order to reduce further the gap between simulation and theory results.

Regarding the decorrelation time, numerical evidences have shown that it plays important role in the increase of the friction due to strain. Indeed, while the static term $\langle F_x^2 \rangle / A$ is responsible for 10% increase, the decorrelation time can be doubled for H₂O. It suggests that the motion of molecules has been affected by the changes of the environment. From atomistic viewpoint, the changes of lattice distances induce changes in the potential energy landscape and the diffusion mechanism of molecules. Spherical molecules like CH₄ are less affected, but molecules like H₂O and CO₂ tend to have less mobility along x than along y .

2.4 Conclusions

In the present paper, we have considered the friction between different liquids and an anisotropic surface, e.g graphene subject to anisotropic engineering strain. Due to the changes of the lattice structure, the potential field of strained graphene has lost its six fold symmetry and is responsible for anisotropic friction behavior between the liquid and the surface. Depending on the molecular shape and interaction strength, the anisotropy degree may vary from one fluid species to another. Using LAMMPS software, one can compute the friction tensor via time correlation integral and access to structure via post process routine. Simple predictive estimation is proposed from a constructed surface potential for strained graphene.

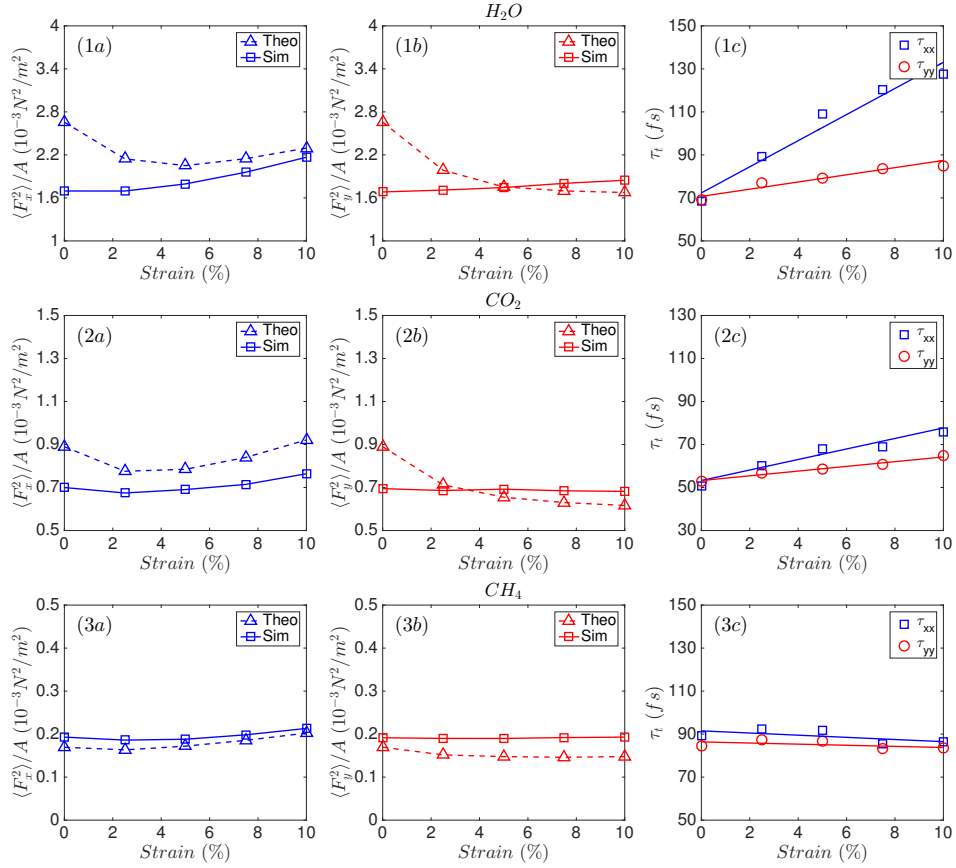


Figure 2.10: Factorization of friction coefficient λ to $\langle F^2 \rangle / A$ and τ_t with strain on graphite ranging from 0% to 10%

The authors study three different liquids with distinct molecular shape, namely water, carbon dioxide and methane. Numerical evidences show that the strain induced anisotropy effect is significant, especially for non spherical molecules. When strain increases, the friction and the anisotropy degree also increase. For example, the friction coefficient can rise 100% for water and 50% for carbon dioxide at 10% strain along x . The friction ratio between two directions increases from 1 to 1.6 for water and from 1 to 1.3 for carbon dioxide. However, for spherical molecules like methane, the variation of friction is insignificant. Investigation on the structure and dynamics of those liquids has revealed that the relaxation time increases considerably with strain and contributes an important part in the increase of the friction.

The contribution of this work helps better understanding and modelling the friction between

liquids and anisotropic surfaces. Those surfaces can exist naturally, for example in the form of orthorhombic crystal systems or cubic systems subject to misfit strain etc.. The study also contributes practical aspects to answer energetic and environmental challenges, specifically it is closely related to carbon dioxide sequestration process via Enhanced coal bed methane recovery method.

Chapter 3

Non-parametric wall model and methods of identifying boundary conditions for moments in gas flow equations

Abstract

In this paper, we use Molecular Dynamics (MD) simulation method to study gas-wall boundary conditions. Discrete scattering information of gas molecules at the wall surface are obtained from collision simulations. The collision data can be used to identify the accommodation coefficients for parametric wall models such as Maxwell, Cercignani-Lampis scattering kernels. Since these scattering kernels are based on a limited number of accommodation coefficients, we adopt non-parametric statistical methods to construct the kernel to overcome these issues. Different from parametric kernels, the non-parametric kernels require no parameter (i.e accommodation coefficients) and no predefined distribution. We also propose approaches to derive directly the Navier friction and Kapitza thermal resistance coefficients as well as other interface coefficients associated to moment equations from the non-parametric kernels. The methods are applied

successfully to systems composed of CH_4 or CO_2 and graphite, which are of interest to the petroleum industry.

3.1 Introduction

The study of transport properties in porous media plays an important role in many applications such as soil mechanics, geohydrology and the storage of nuclear waste. Along with the development of unconventional reservoirs (shale gas) extraction technology, like hydraulic fracturing, more attention has been paid to the transport of gas molecules in carbon pores. As a result, modeling the gas behavior and its interaction with the boundary is of significant interest.

Due to the size of the pore, gaseous molecules, here methane (CH_4) and carbon dioxide (CO_2) in this study, can travel with few collisions, resulting in high Knudsen number (Kn), a similar situation as the rarefaction effect. It is known that when $\text{Kn} > 0.01$, predictions based on the continuum Navier-Stokes-Fourier (NSF) equations and classical no-slip, no-jump conditions are no longer in agreement with experiences and atomistic simulation results [73, 168]. In order to capture these phenomena, more advanced continuum equations and boundary conditions are necessary [143, 127].

Unlike liquids where the friction and thermal resistance are characterized by layers of interacting molecules adsorbed at the wall [85, 11, 19], the gas molecules collide infrequently and their residence time near the wall can be neglected. The exchange of momentum and energy between the gas and the wall can be understood from ensemble of independent gas-wall collisions. In most cases, the collisions are usually modeled with scattering kernels based on several accommodation coefficients [92, 27, 26, 163, 33, 65, 140]. Other class of wall models for rough surfaces [146, 164, 82] were analytically derived from corrugation parameter and potential well depth. Although these parametric models are simple to code, they rely on many oversimplification hypotheses which cannot guarantee the accuracy of the collisions for the whole velocity range.

These problems can have consequences on the boundary conditions at the continuum level and simulation results based on these scattering kernels.

The paper presents a systematic study of gas-wall collision models based on Molecular Dynamics (MD) simulations. The systems in consideration are composed of methane CH_4 (considered as monatomic gas) or carbon dioxide CO_2 (rigid linear molecule) interacting with a graphite wall constituted of carbon atoms. By beaming independently gas molecules onto the surface and recording the reflected flux, we can determine the accommodation coefficients. More importantly, we can reconstruct numerically a non-parametric (NP) wall model. Different from parametric models in literature, this scattering kernel is able to capture the reflection process in a more realistic way. Originated from non-parametric statistics, the NP scattering kernel requires no parametrization (i.e accommodation coefficients) and no predefined analytical form. Interestingly, it can be used to determine directly the parameters of any phenomenological boundary conditions, including those for NSF or moment equations. While these equations are valid for a limited range of Kn in the transition regime, the NP wall model can be directly implemented in particle methods like DSMC (Direct Simulation Monte Carlo) or MD to simulate flows at any Kn number. The development of gas-wall boundary conditions for continuum equations from a non-parametric kernel is the major contribution of the present work, which will be detailed in the subsequent sections.

3.2 Study of gas-wall models with Molecular Dynamics method

3.2.1 Scattering kernels

In kinetic theory, the state of monatomic gas at any location \boldsymbol{x} at time t is entirely determined from the local number density $n(\boldsymbol{x}, t)$ and the probability density function $f(\boldsymbol{x}, \boldsymbol{c}, t)$ of velocity \boldsymbol{c} .

The evolution of the latter is governed by the Boltzmann equation and the boundary conditions

$$c_z(nf)^+(\mathbf{c}) = \int_{\Omega^-} B(\mathbf{c}|\mathbf{c}')|c'_z|(nf)^-(\mathbf{c}')d\mathbf{c}', \quad \mathbf{c}' \in \Omega^-, \quad \mathbf{c} \in \Omega^+. \quad (3.1)$$

In the above expression, we assume that the boundary is normal to the z direction, and time t and space \mathbf{x} variables are dropped for simplicity. Eq. (3.1) connects the incoming flux $c'_z(nf)^-(\mathbf{c}')$ and the outgoing flux $c_z(nf)^+(\mathbf{c})$ via the scattering kernel $B(\mathbf{c}|\mathbf{c}')$. The two velocities \mathbf{c} and \mathbf{c}' belong to dual half-spaces Ω^- and Ω^+ in \mathbb{R}^3 , respectively, defined below

$$\mathbf{c}' \in \Omega^- = \mathbb{R}^2 \times \mathbb{R}^-, \quad \mathbf{c} \in \Omega^+ = \mathbb{R}^2 \times \mathbb{R}^+. \quad (3.2)$$

For fluid in equilibrium, the distribution of velocity is equal to the Maxwell-Boltzmann distribution

$$f_{eq}(\mathbf{c}) = f_M(\mathbf{c}) = \frac{1}{\sqrt{2\pi\theta}^3} \exp\left[-\frac{\mathbf{c}^2}{2\theta}\right], \quad \theta = k_B T/m, \quad (3.3)$$

where k_B is the Boltzmann constant, m the atomic mass, and T the temperature. For rigid gas molecules, in addition to translational velocity of the center of mass, we must account for the rotational velocity $\boldsymbol{\omega}$. The scattering kernel must be replaced by $B(\boldsymbol{\omega}, \mathbf{c}|\boldsymbol{\omega}', \mathbf{c}')$ and the probability density by $f(\boldsymbol{\omega}, \mathbf{c})$. The two half-spaces Ω^- and Ω^+ are also extended to include the rotational velocity $\boldsymbol{\omega}$, e.g $\Omega^- = \mathbb{R}^5 \times \mathbb{R}^-$ for incident molecules and $\Omega^+ = \mathbb{R}^5 \times \mathbb{R}^+$ for reflected molecules. It is possible to include the orientation distribution in the scattering kernel but this will not be considered in the present work. At equilibrium, this density function is given by

$$f_{eq}(\boldsymbol{\omega}, \mathbf{c}) = f_M(\mathbf{c})f_M^\omega(\boldsymbol{\omega}), \quad f_M^\omega(\boldsymbol{\omega}) = \frac{1}{\sqrt{2\pi\theta^\omega}^d} \exp\left[-\frac{\boldsymbol{\omega}^2}{2\theta^\omega}\right], \quad \theta^\omega = k_B T/I. \quad (3.4)$$

The quantity I represents the moment of inertia and the power d the rotational degree of freedom, $d = 2$ for linear molecules and $d = 3$ otherwise. It is noted that for linear molecules, the

rotation around its proper axis is not considered.

The scattering kernel $B(\boldsymbol{\omega}, \mathbf{c}|\boldsymbol{\omega}', \mathbf{c}')$ which is the probability of finding molecules bouncing with velocity $(\boldsymbol{\omega}, \mathbf{c})$ with given colliding velocities $(\boldsymbol{\omega}', \mathbf{c}')$ can be determined by Molecular Dynamics collision simulation. Gas molecules are beamed at given velocities $(\boldsymbol{\omega}', \mathbf{c}')$ onto the surface in consideration and the velocity distribution of reflecting molecules associated to $(\boldsymbol{\omega}', \mathbf{c}')$ is recorded. Next the arriving velocities $(\boldsymbol{\omega}', \mathbf{c}')$ are also varied to cover the incident velocity space. Generally, if the number of realizations is sufficiently large, we have a large set of discrete points which can represent the true probability density $B(\boldsymbol{\omega}, \mathbf{c}|\boldsymbol{\omega}', \mathbf{c}')$.

We are also concerned about the use of the kernel as wall boundary conditions in other simulation methods (for example Molecular Dynamics, Direct Simulation Monte Carlo or Lattice Boltzmann). If we use the discrete form of $B(\boldsymbol{\omega}, \mathbf{c}|\boldsymbol{\omega}', \mathbf{c}')$, output results must be obtained from the interpolation of known points. This method is accurate but less computationally convenient. The scattering kernel can be analytically modeled using some physical parameters for example Tangential Momentum Accommodation Coefficients (TMAC) or Energy Momentum Accommodation Coefficients (EAC), etc... Some notable scattering models are Maxwell-Yamamoto (MY) [163], Cercignani-Lampis (CL) [27] etc... which can be used for atomistic gas flow simulations and accommodation coefficients can be used to derive velocity slip and temperature jump coefficients for NSF equations. To account for the special reflection mechanism of the anisotropic surface, one can use Dadzie-Meolans (DM) kernel [34] or anisotropic Cercignani-Lampis (ACL) kernel [140] with three different coefficients associated to the three directions x, y, z .

The MD collision point cloud can be fitted by analytical scattering models and the model parameters can be identified. However, the data can be scattered and there is no truly efficient fitting algorithm, for example, one can use the mean square of the difference between the two probability densities or methods based on accommodation parameters. We note that

constant accommodation coefficients are only meaningful for analytical scattering kernel listed previously. For realistic gas surface interaction, those coefficients are usable in approximative sense and can oversimplify the true behavior.

3.2.2 Expressions for fluxes, average values and accommodation coefficients

Given molecular quantities Q as function of velocities $\mathbf{c}, \boldsymbol{\omega}$, the average value \bar{Q} and the flux Φ_Q across a plane normal to z can be computed as

$$\bar{Q} = \int Q(\mathbf{c}, \boldsymbol{\omega}) f d\mathbf{c} d\boldsymbol{\omega}, \quad \Phi_Q = n \int Q(\mathbf{c}, \boldsymbol{\omega}) c_z f d\mathbf{c} d\boldsymbol{\omega}. \quad (3.5)$$

Given the fact that all the physical quantities such as density n , temperature T , stress $\boldsymbol{\sigma}$, velocity v , and heat flux \mathbf{q} are either average value or flux of molecular quantities, it is possible to investigate their relations at the boundary by examining the gas wall collisions. With respect to the wall normal to the z direction, we define influx Φ_Q^- and outflux Φ_Q^+ of atomic quantity $Q(\mathbf{c}, \boldsymbol{\omega})$ at the wall via the expressions

$$\Phi_Q^- = \int_{\Omega^-} |c_z| (nf)^- Q(\mathbf{c}, \boldsymbol{\omega}) d\mathbf{c} d\boldsymbol{\omega}, \quad \Phi_Q^+ = \int_{\Omega^+} |c_z| (nf)^+ Q(\mathbf{c}, \boldsymbol{\omega}) d\mathbf{c} d\boldsymbol{\omega}. \quad (3.6)$$

From atomistic viewpoint, Φ_Q^-, Φ_Q^+ can be computed by counting the number of atoms N crossing the control plane in a given time t

$$\Phi_Q^- = \frac{1}{t} \sum_{incident} Q(\mathbf{c}, \boldsymbol{\omega}) = \frac{N}{t} \langle Q \rangle_i = \nu \langle Q \rangle_i, \quad \Phi_Q^+ = \nu \langle Q \rangle_o, \quad (3.7)$$

where the subscript i stands for input (incident), o for output (reflection), ν collision rate. Here the notation $\langle Q \rangle$ is the average of molecular quantities Q that cross the control plane in Molecular Dynamics simulations. By breaking each relation in (3.5) into two integrals in

half-spaces Ω^- and Ω^+ as follows

$$\begin{aligned} n\bar{Q} &= \int_{\Omega^-} \frac{Q(\mathbf{c}, \boldsymbol{\omega})}{|c_z|} |c_z| (nf)^- d\mathbf{c} d\boldsymbol{\omega} + \int_{\Omega^+} \frac{Q(\mathbf{c}, \boldsymbol{\omega})}{|c_z|} |c_z| (nf)^+ d\mathbf{c} d\boldsymbol{\omega}, \\ \Phi_Q &= - \int_{\Omega^-} Q(\mathbf{c}, \boldsymbol{\omega}) |c_z| (nf)^- d\mathbf{c} d\boldsymbol{\omega} + \int_{\Omega^+} Q(\mathbf{c}, \boldsymbol{\omega}) |c_z| (nf)^+ d\mathbf{c} d\boldsymbol{\omega}, \end{aligned} \quad (3.8)$$

and making use of (3.7) and (3.6), the flux Φ_Q and the average value \bar{Q} at the wall can also be expressed as

$$n\bar{Q} = \Phi_{Q/|c_z|}^+ + \Phi_{Q/|c_z|}^- = \nu \langle Q/|c_z| \rangle_{i+o}, \quad \Phi_Q = \Phi_Q^+ - \Phi_Q^- = \nu \langle Q \rangle_{o-i}, \quad (3.9)$$

with notation $\langle Q \rangle_{\alpha \pm \beta} := \langle Q \rangle_\alpha \pm \langle Q \rangle_\beta$. The relation between the average value \bar{Q} , and fluxes $\Phi_{Q/|c_z|}^+$ and $\Phi_{Q/|c_z|}^-$ is useful because it is more convenient to compute \bar{Q} with MD simulations. Choosing $Q = 1$ in (3.9) and noting that $\bar{Q} = \langle Q \rangle_i = \langle Q \rangle_o = 1$, we have the equalities

$$\nu = n \frac{1}{\langle 1/|c_z| \rangle_{i+o}}, \quad \Phi_1 = 0. \quad (3.10)$$

Substituting ν/n from the first expression in (3.10) back into (3.9) for the general Q , we can derive that

$$\bar{Q} = \frac{\langle Q/|c_z| \rangle_{i+o}}{\langle 1/|c_z| \rangle_{i+o}}, \quad \Phi_Q = \frac{n \langle Q \rangle_{o-i}}{\langle 1/|c_z| \rangle_{i+o}}. \quad (3.11)$$

We remark that the second relation of (3.10) is equivalent to the no atom accumulation condition at the wall, i.e the influx is equal to the outflux. If the leaving atoms are fully thermalized by the wall, the phase density f^+ should be replaced by the equilibrium distribution $f_{eq}(\boldsymbol{\omega}, \mathbf{c})$ at the wall temperature T_w . The outgoing flux $\Phi_{Q_w}^+$ associated to this distribution is given by the expression

$$\Phi_{Q_w}^+ = \int_{\Omega^+} |c_z| n f_{eq}(\boldsymbol{\omega}, \mathbf{c}) Q d\mathbf{c} d\boldsymbol{\omega} = \nu \langle Q \rangle_w, \quad (3.12)$$

where the subscript w is for outgoing flux at the wall temperature T_w . Since $f_{eq}(\boldsymbol{\omega}, \mathbf{c})$ is known from (3.4) and ν is estimated by setting $Q = 1$, we can compute the expected values for thermal wall $\langle Q \rangle_w$. They are functions of the reduced wall temperature $\theta_w = k_B T_w / m$ and given in Tab 3.1. It is noted that for the special case where $d = 0$, the tabulated values are consistent with previous works for monatomic gas [125].

Component	Velocity	Energy
Tangential (x, y)	$\langle c_x \rangle_w = 0$	$\langle c_x^2 \rangle_w = \theta_w$
Normal (z)	$\langle c_z \rangle_w = \frac{1}{2} \sqrt{2\pi\theta_w}$	$\langle c_z^2 \rangle_w = 2\theta_w$
Total	$\langle c \rangle_w = \frac{3}{4} \sqrt{2\pi\theta_w}$	$\langle c^2 + \frac{I}{m} \omega^2 \rangle_w = (4 + d)\theta_w$

Table 3.1: Expected values as functions of the reduced wall temperature $\theta_w = k_B T_w / m$. For CH_4 , the rotation energy is neglected $d = 0$ and for CO_2 , $d = 2$.

As a result, the accommodation coefficient of quantity Q is equivalent to the expression

$$\alpha_Q = \frac{\Phi_Q^- - \Phi_Q^+}{\Phi_Q^- - \Phi_{Q_w}^+} = \frac{\langle Q \rangle_{i-o}}{\langle Q \rangle_{i-w}} \quad \text{or} \quad \langle Q \rangle_o = (1 - \alpha_Q) \langle Q \rangle_i + \alpha_Q \langle Q \rangle_w. \quad (3.13)$$

The above expression which is independent of the collision rate ν , is useful for the determination of the accommodation coefficients using MD method. Usually, the value for $\langle Q \rangle_w$ is known explicitly (see Tab I) and the coefficient can be computed based on Eq. (3.13). Most analytical wall models in literature are based on constant accommodation coefficients, which are independent of the input data nf^- . These assumptions may not be true for a general kernel $B(\boldsymbol{\omega}, \mathbf{c} | \boldsymbol{\omega}', \mathbf{c}')$ and this is the major disadvantage of using accommodation coefficients to model realistic surfaces.

When accommodation coefficients are not properly defined, different methods can be used to compute those coefficients and result differently. For example, in Ref.[125], the authors

proposed using the least-squares formula

$$\alpha_Q = 1 - \frac{\sum_{collision} (Q_i - \langle Q \rangle_i)(Q_o - \langle Q \rangle_o)}{\sum_{collision} (Q_i - \langle Q \rangle_i)^2}, \quad (3.14)$$

from the collision clouds. They found that results are very different from those obtained by Eq. (3.13).

These observations pose some problems on theories based on the existence of the constant accommodation coefficients for general surfaces. However, interface phenomena like slip velocity and temperature jumps do exist. Modeling those effects and identifying the parameters without using accommodation coefficients will be considered in the following.

3.2.3 Boundary conditions for Navier Stokes Fourier (NSF) equations

In this subsection, we present a new method to directly determine the macroscopic velocity and temperature jump coefficients via collision simulations. This completely avoids the intermediate modeling and simulations based on scattering kernels. As we know, all available analytical models have limitations. First, they only allow at most three accommodation coefficients. If we choose to model momentum accommodation effect along one direction, we have to sacrifice the energy accommodation along this direction. Accommodation effects for high order moment are also unavailable. Secondly, using constant accommodation coefficients, like most analytical wall models in literature can be a strong assumption. Numerical evidence in the latter section shows that in some cases, the true behavior deviates significantly from that hypothesis.

The approach proposed here is independent of scattering model and can be applied to any surfaces. It can also be extended to deal with general boundary conditions involving higher order moments. In slip regimes, the usual macroscopic boundary conditions for velocities v_x, v_y

and reduced temperature jump $\theta - \theta_w$ are given in the following forms

$$v_k = -\frac{2 - \alpha_k}{\alpha_k} \frac{\sigma_{kz}}{nm\sqrt{2\theta/\pi}}, \quad \theta - \theta_w = -\frac{2 - \alpha_e}{2\alpha_e} \frac{q_z}{nm\sqrt{2\theta/\pi}}, \quad k = x, y, \quad (3.15)$$

where σ_{xz}, σ_{yz} are the (minus) shear stress components and q_z the normal heat flux at the wall. Constants α_k are the tangential accommodation coefficients associated to the tangential translational molecular velocities, and α_e is the energy accommodation coefficient associated to its kinetic energy. The above equation where the thermal transpiration is neglected can be derived from the scattering models. In this paper, we propose a more general phenomenological form for the boundary conditions

$$\beta_{1k}v_k = -\frac{\sigma_{kz}}{nm\sqrt{2\theta/\pi}}, \quad \beta_2(\theta - \theta_w) = -\frac{q_z}{2nm\sqrt{2\theta/\pi}}, \quad k = x, y, \quad (3.16)$$

where β_{1x}, β_{1y} and β_2 are the dimensionless friction and Kapitza coefficients, depending on the gas-wall couple. It is clear that we recover the original equation if the coefficients β_{1k} and β_2 are connected to the accommodation coefficients α_k and α_e via the relation

$$\beta_{1k} = \frac{\alpha_k}{2 - \alpha_k}, \quad \beta_2 = \frac{\alpha_e}{2 - \alpha_e}, \quad k = x, y, \quad (3.17)$$

It is noted that the two expressions in (3.16) can also be used for the cases where the accommodation coefficients are not constant.

Using Eqs. (3.7-3.11), we shall derive schemes to determine β_{1k} and β_2 from MD simulations. The velocity defined as $v_k = \overline{c_k}$ (i.e $Q = c_k$) can be computed by the expression

$$v_k = \frac{\langle c_k/|c_z| \rangle_{i+o}}{\langle 1/|c_z| \rangle_{i+o}}. \quad (3.18)$$

The (minus) shear stress $\sigma_{kz} = \Phi_{mC_k}$ (i.e $Q = mC_k$) can also be computed in the following way

$$-\sigma_{kz} = m\nu(\langle C_k \rangle_i - \langle C_k \rangle_o) = mn \frac{\langle c_k \rangle_i - \langle c_k \rangle_o}{\langle 1/|c_z| \rangle_i + \langle 1/|c_z| \rangle_o} = mn \frac{\langle c_k \rangle_{i-o}}{\langle 1/|c_z| \rangle_{i+o}}, \quad (3.19)$$

where $C_k = c_k - v_k$ is the peculiar velocity. Comparing Eqs. (3.18,3.19) with (3.16), we can derive the interface coefficients β_{ik} via the expression

$$\beta_{1k} = \frac{\langle c_k \rangle_{i-o} / \sqrt{2\theta/\pi}}{\langle c_k / |c_z| \rangle_{i+o}}. \quad (3.20)$$

Next, the reduced temperature $\theta = \overline{C^2 + (I/m)\omega^2} / (3 + d)$ and the heat flux $q_z = \Phi_{(mC^2 + I\omega^2)/2}$ are given by the equation

$$\theta = \frac{\langle (C^2 + (I/m)\omega^2) / |c_z| \rangle_{i+o}}{(3 + d)\langle 1/|c_z| \rangle_{i+o}}, \quad -q_z = mn \frac{\langle (C^2 + (I/m)\omega^2) / 2 \rangle_{i-o}}{\langle 1/|c_z| \rangle_{i+o}}, \quad (3.21)$$

where d is the number of rotation degrees of freedom of gas molecule, $d = 2$ for CO_2 . Comparing Eqs. (3.21) with (3.16), we can calculate the Kapitza coefficient

$$\beta_2 = \frac{(3 + d)\langle (C^2 + (I/m)\omega^2) / 2 \rangle_{i-o} / (4\theta/\pi)}{[\langle (C^2 + (I/m)\omega^2) / |c_z| \rangle_{i+o} - (3 + d)\theta_w \langle 1/|c_z| \rangle_{i+o}] / \sqrt{2\theta/\pi}}. \quad (3.22)$$

We note that for monatomic gas, it is sufficient to remove the terms $I\omega^2$ and d in the above expression and obtain

$$\beta_2 = \frac{3\langle C^2/2 \rangle_{i-o} / (4\theta/\pi)}{[\langle C^2 / |c_z| \rangle_{i+o} - 3\theta_w \langle 1/|c_z| \rangle_{i+o}] / \sqrt{2\theta/\pi}}. \quad (3.23)$$

To facilitate the comparison between the numerical results, we normalize stress and heat flux computed by MD method with suitable quantities and rewrite the phenomenological law in the following way

$$\beta_{1k} = \frac{-\hat{\sigma}_{kz}}{\hat{v}_k}, \quad \beta_2 = \frac{-\hat{q}_z}{\Delta\hat{\theta}}, \quad k = x, y. \quad (3.24)$$

Here, the hat notation is used for the normalized quantities,

$$\hat{\sigma}_{kz} = \frac{\sigma_{kz}}{nm\zeta^2}, \quad \hat{v}_k = \frac{v_k}{\zeta}, \quad \hat{q}_z = \frac{q_z}{2nm\zeta^3}, \quad \Delta\hat{\theta} = \frac{\theta - \theta_w}{\zeta^2}, \quad \zeta = \sqrt{2\theta/\pi}. \quad (3.25)$$

3.2.4 Extension to 13 moments equations

Without being limited to NSF equations, the method presented previously can be applied to higher order model. Given any macroscopic boundary conditions in terms of moments, the present method can be used to derive the coefficients associated to boundary conditions. As an example, we consider the boundary conditions of R13 equations written for isotropic surfaces in dimensionless form[144, 143]

$$\beta_1 = \frac{-\hat{\sigma}_{xz}}{\hat{\kappa}_1}, \quad \beta_2 = \frac{-\hat{q}_z}{\hat{\kappa}_2}, \quad \beta_3 = \frac{-\hat{m}_{xxz}}{\hat{\kappa}_3}, \quad \beta_4 = \frac{\hat{m}_{zzz}}{\hat{\kappa}_4}, \quad \beta_5 = \frac{\hat{R}_{xz}}{\hat{\kappa}_5}, \quad (3.26)$$

with

$$\begin{aligned} \hat{m}_{ijl} &= \frac{m_{ijl}}{nm\zeta^3}, \quad \hat{R}_{ij} = \frac{R_{ij}}{nm\zeta^2}, \\ \hat{\kappa}_1 &= \sqrt{\frac{2}{\pi\theta}} \left(Pv_x + \frac{1}{2}m_{xzz} + \frac{1}{5}q_x \right) / (nm\zeta^2), \\ \hat{\kappa}_2 &= \sqrt{\frac{2}{\pi\theta}} \left(2P(\theta - \theta_w) - \frac{1}{2}Pv^2 + \frac{1}{2}\theta\sigma_{zz} + \frac{R}{15} + \frac{5}{28}R_{zz} \right) / (2nm\zeta^3), \\ \hat{\kappa}_3 &= \sqrt{\frac{2}{\pi\theta}} \left(\frac{1}{14}R_{xx} + \theta\sigma_{xx} - \frac{1}{5}\theta\sigma_{zz} + \frac{1}{5}P(\theta - \theta_w) - \frac{4}{5}Pv_x^2 - \frac{R}{150} \right) / (nm\zeta^3), \\ \hat{\kappa}_4 &= \sqrt{\frac{2}{\pi\theta}} \left(\frac{2}{5}P(\theta - \theta_w) - \frac{1}{14}R_{zz} - \frac{3}{5}Pv^2 - \frac{7}{5}\theta\sigma_{zz} + \frac{R}{75} \right) / (nm\zeta^3), \\ \hat{\kappa}_5 &= \sqrt{\frac{2}{\pi\theta}} \left(P\theta v_x - \frac{11}{5}\theta q_x - \frac{1}{2}\theta m_{xzz} - Pv^2 v_x + 6Pv_x(\theta - \theta_w) \right) / (nm\zeta^4). \end{aligned} \quad (3.27)$$

The quantities P, R, R_{ij} and m_{ijl} are defined from the moments

$$\begin{aligned}
 P &= nm\theta + \frac{1}{2}\sigma_{zz} - \frac{1}{120}\frac{R}{\theta} - \frac{1}{28}\frac{R_{zz}}{\theta}, & R_{ij} &= mn\overline{C^2(C_i C_j - C^2/3\delta_{ij})} - 7\theta\sigma_{ij}, \\
 R &= mn(\overline{C^4} - 15\theta^2), & m_{ijl} &= mn\overline{C_i C_j C_l - C^2(C_i\delta_{jl} + C_j\delta_{il} + C_l\delta_{ij})}/5, \\
 k &= x, y, & i, j, l &= x, y, z.
 \end{aligned} \tag{3.28}$$

These original boundary conditions are derived for Maxwell molecules and Maxwell scattering kernel where all the coefficients are identical $\beta_1 = \beta_2 = \dots = \beta_5 = \alpha/(2 - \alpha)$ with α being the accommodation coefficient. Moments R, R_{ij} and m_{ijl} are connected to stress, heat flux, velocity, temperature and their derivatives via a regularization procedure [126, 129, 143].

Although the derivation conditions are rather restrictive, we shall assume that they are valid and determine the coefficients $\beta_1, \beta_2, \dots, \beta_5$. We shall base directly on the moment definitions Eqs. (3.28) which are independent of the regularization methods and also relax the conditions that all coefficients $\beta_1, \beta_2, \dots, \beta_5$ must be identical. We note that in Ref. [126], these authors already consider that $\beta_1, \beta_2, \dots, \beta_5$ can be different and take empirical values allowing matching with a more accurate method. In these cases, those coefficients are used to fix the Knudsen layer effect that the R13 equation fails to capture completely. This empirical approach seems to be incompatible with the rigorous mathematical derivation of R13 equations.

3.2.5 Generation of pre-collision velocity

Molecular Dynamics simulation requires generating velocities of atoms that cross the control plane and collide with the wall. The (unnormalized) distribution of the latter is $|c_z|f^-(\mathbf{c}, \boldsymbol{\omega})$ with $c_z < 0$ as seen in the previous section. In this paper, we use three types of distribution

- The Maxwell Boltzmann (MB) distribution

$$\text{For molecular gas } |C_z|f^-(\mathbf{c}, \boldsymbol{\omega}) = |C_z|f_M(\mathbf{C})f_M^\omega(\boldsymbol{\omega}).$$

$$\text{For monatomic gas } |c_z|f^-(\mathbf{c}) = |c_z|f_M(\mathbf{C}). \quad (3.29)$$

The parameters of the distribution are the mean velocity \mathbf{v} and the reduced temperature θ . Using this distribution, we can model equilibrium system where the fluid is stationary $\mathbf{v} = 0$ and the temperature is uniform $\theta = \theta_w$ or non-equilibrium system by assuming that the gas adjacent to the wall is in local equilibrium with temperature and velocity different from the wall, i.e $\mathbf{v} \neq 0$, $\theta \neq \theta_w$.

- The Chapman-Enskog (CE) distribution [29, 53]

$$|c_z|f^-(\mathbf{c}) = |C_z|f_{CE}(\mathbf{C}). \quad (3.30)$$

In addition to temperature θ and mean velocity \mathbf{v} , there are also parameters associated to heat flux q_k and shear stress σ_{ik} . This distribution is for non-equilibrium monatomic gas.

- The R13 distribution [129, 144]

$$|c_z|f^-(\mathbf{c}) = |C_z|f_{R13}(\mathbf{C}). \quad (3.31)$$

The last two distributions CE and R13 are for monatomic gases with expressions given in Appendix A. The generation of the input velocity is done via the Acceptance-Rejection approach. For example, in Ref. [49], a scheme to generate distributions in the form $f(\mathbf{c}) = f_M(\mathbf{C})\Gamma(\mathbf{C})$ where $\Gamma(\mathbf{C})$ is a polynomial of \mathbf{C} , is proposed. The distribution to be treated in this paper is slightly different since we are limited to the half-space $c_z < 0$ and there is a function $|c_z|$ standing before $f_M(\mathbf{C})$ due to the flux definition (see Appendix A).

3.3 Numerical simulations and results

3.3.1 Molecular Dynamics model

We study the collision of gas molecules, methane (CH_4) and carbon dioxide (CO_2) on a graphite wall (C atoms). The system contains two parts: the reservoir and the collision zone. The MD simulation is only done in the collision zone and the pre-collision velocity of gas molecules is generated directly at the stochastic boundary between the reservoir and the collision zone. Two graphite wall models will be considered. The first is a smooth wall model composed of 3 graphene layers with dimensions $17.04 \text{ \AA} \times 17.22 \text{ \AA}$ (336 carbon atoms). The second is a rough model where a narrower band of graphene with surface $8.52 \text{ \AA} \times 17.22 \text{ \AA}$ is added on the smooth surface (392 carbon atoms). Due to the surface geometry and symmetry, the scattering behavior of the smooth model is close to being isotropic and that of the rough model is anisotropic. We define the x and y directions as respectively “armchair” and “zigzag” directions, and the z direction as the normal direction to the graphite plane. During the simulation, the lowest sheet is fixed and the second layer is maintained at constant temperature (350 K for CH_4 model and 600 K for CO_2 model) by Nose-Hoover thermostat with the relaxing temperature parameter equals to 100 time steps. The two final layers are free to interact with the gas molecules. We use periodic boundary conditions for x, y directions, and we fix the height of box along z direction. The gas-wall truncation distance is set to 15 \AA from the upper layer, and the stochastic boundary is located at the truncation distance from the graphite wall. A simple sketch of the system and snapshots of MD simulations are shown in Fig. 3.1.

All MD simulations are performed with LAMMPS (Large-scale Atomic/Molecular Massively Parallel Simulator) package [102]. A typical simulation of 10^5 collisions takes roughly 50 hours on an architecture of 92 Intel(R) Xeon(R) processors 2-3 GHz. The adaptive intermolecular reactive bond order (AIREBO) potential [130] is used for the interaction between the graphite carbon atoms. The CH_4 molecule is modeled as a united atom and its interaction with graphite

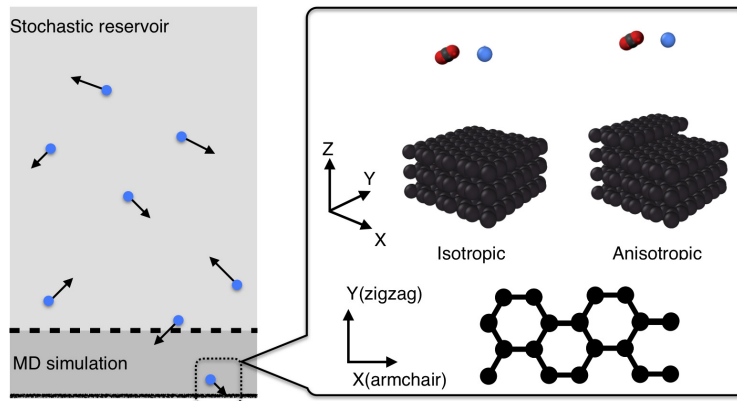


Figure 3.1: Simple sketch of the system. The stochastic boundary is indicated by the dashed line and the graphite wall is indicated by the solid line. Snapshots of MD simulations show the local orientation of the smooth (isotropic) and rough (anisotropic) systems.

atoms is governed by the Lennard Jones (LJ) potential

$$V = 4\epsilon \left[\left(\frac{\sigma}{r} \right)^{12} - \left(\frac{\sigma}{r} \right)^6 \right], \quad (3.32)$$

where r is the distance between two atoms under consideration and σ and ϵ the parameters of the LJ model. Regarding the CO_2 molecules, we don't consider the contribution of the internal degrees of freedom (bending/stretching) and use the rigid model [167]. The interaction of each site with the graphite atoms is also of LJ type with parameters taken from Ref. [85] (see Table 3.2). After equilibrating the graphite system at the given temperature (10^6 time steps of 1 fs), gas molecules are inserted one by one in the collision zone. Only after one collision event, i.e a molecule interacts with the wall and goes out of the collision zone, another molecule is inserted in the zone from a random position at the stochastic boundary (for CH_4 and CO_2) and with a random orientation (for CO_2). The residence time is considered negligibly small with respect to the flying time outside this zone and the velocities at the entrance and the outlet are collected (see Fig. 3.2).

Some comments can be made about the models for CH_4 and CO_2 used in the present work. Both rigid molecule models don't account for the vibrational internal degrees of freedom. The bending mode of CO_2 associated with a wavenumber of 667 cm^{-1} [86] is the most concerned

by an excitation due to collisions with the solid surface since this mode is the lowest energetic. The CO_2 molecule collides with a surface at 600 K, i.e. $k_B T = 417 \text{ cm}^{-1}$. Using Boltzmann statistics, it can be estimated that only 20% of the CO_2 molecules may be concerned by such an excitation. The lowest energetic vibrational mode of CH_4 is the angle deformation mode associated with a wavenumber at 1306 cm^{-1} [86] and this molecule collides a surface at 350 K ($k_B T = 243 \text{ cm}^{-1}$). The Boltzmann statistics indicate that only 5% of the molecules would be excited. From these estimates and for simplification, CO_2 and CH_4 are kept rigid.

	$\sigma[\text{\AA}]$	$\epsilon[\text{meV}]$
$\text{CH}_4 - \text{C}$ (Graphite)	3.550	5.547
$\text{C} (\text{CO}_2) - \text{C}$ (Graphite)	3.059	2.418
$\text{O} (\text{CO}_2) - \text{C}$ (Graphite)	3.197	4.091

Table 3.2: LJ parameters for the interaction of CH_4 and CO_2 with the graphite surface.

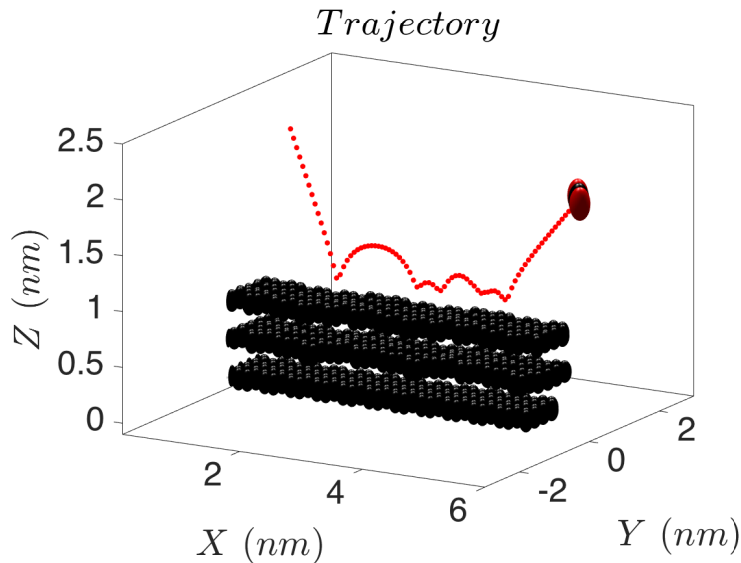


Figure 3.2: A collision showing the trajectory of a gas molecule.

We implement 3 simulation schemes to study gas-wall models and determine the model coefficients. They are different in terms of the gas state (equilibrium/non-equilibrium) and the associated velocity generator.

- **Batch average (BA) scheme:** We repeat the same incident velocity (ω', \mathbf{c}') many times and

record the reflected velocity $(\boldsymbol{\omega}, \mathbf{c})$ which is a distribution. To generate samples, the incident velocity is taken from equilibrium distribution and the reflected velocity is averaged. By this way [101], we can examine the accommodation coefficients via their definition (Eq. (3.13)). In Fig. 3.3, We have plotted the input quantities $\langle Q \rangle_i$ against output quantities $\langle Q \rangle_o$, where $Q = c_x, c_y, c_z$ or $c^2 + I\omega^2/m$. In the ideal case, the data population should concentrate along a straight line and its slope corresponds to the constant accommodation coefficient α_Q (see section III.B for details).

- **Stochastic equilibrium (SE) scheme:** The reservoir is considered to be in equilibrium. The pre-collision velocity $(\boldsymbol{\omega}', \mathbf{c}')$ for each collision is generated using equilibrium distribution at zero mean velocity and at the same temperature as the graphite wall. By this way, we obtain numerical estimates of the density $B(\boldsymbol{\omega}, \mathbf{c}|\boldsymbol{\omega}', \mathbf{c}')$. The accommodation coefficients can be extracted using (3.14) (see section III.B for details).

- **Stochastic non-equilibrium (SN) scheme:** The non-equilibrium gas is considered. Depending on the problems, we use Maxwell-Boltzmann (MB), Chapman Enskog (CE) or R13 distribution as discussed in the previous section. The surface can be modeled atomistically (AM) as described from the beginning of the present section III.A. It can also be modeled statistically using the non-parametric (NP) model $B(\boldsymbol{\omega}, \mathbf{c}|\boldsymbol{\omega}', \mathbf{c}')$. The latter is constructed by the scattering results on the atomic model, which is detailed at the end of section III.B.

The simulation results will be analyzed using the theory we have proposed in the previous section.

3.3.2 Determination of accommodation coefficients and construction of non-parametric wall model from collision data

As mentioned previously, the accommodation coefficients are parameters based on Eq. (3.13). To verify this assumption, it is sufficient to study incident fluxes of constant velocity. Using BA scheme for the couples CH₄/CO₂-Graphite (smooth and rough surfaces), we set up 100 sampling groups and each group contains 500 collisions with the same incident velocity. These 100 incident velocities are drawn from equilibrium distribution at the same temperature as the wall. Then, we average the reflected values in the group for later analysis. Theoretically, if the ratio between the input and the output values are constant, the collision data will form a straight line. In Fig. 3.3, we find a strong correlation between the input and the output velocities. For the tangential velocity, despite some slight curvature the relation between the input and output is visibly linear for most of the data. However, the linear regression works less well for the normal velocity and especially for the kinetic energy. These data suggest that Eq. (3.13) is not valid for these cases and linear coefficients obtained by fitting (see Tab. 3.3) are not representative.

Parametric studies based on varying the number of samples per input velocity from 20 to 1000 show that the scattering of energy data is always present. Given the fact that the results for c_x and c_y are clearly correlated, the energy data merit more detailed investigation to understand the origin of the deviation. We still use the same data and decompose the kinetic energy into tangential and normal components c_n^2, c_t^2 . In Fig. 3.4(a) and (b), we can see that the tangential and normal kinetic energy data $\langle c_t'^2 \rangle$ vs. $\langle c_t^2 \rangle$, $\langle c_n'^2 \rangle$ vs. $\langle c_n^2 \rangle$ are strongly correlated. However, like the data $\langle c_x' \rangle$ vs. $\langle c_x \rangle$ and $\langle c_z' \rangle$ vs. $\langle c_z \rangle$ in Fig. 3.3, their slopes are different. There is a strong contrast between the tangential reflection c_t^2 which is more specular-like (energy mostly conserved after collision) and the normal reflection c_n^2 which is more diffusive-like (energy close to the walls' after collision). On the other hand, in Fig. 3.4(c) and (d), the data $\langle c_t'^2 \rangle$ vs. $\langle c_n^2 \rangle$ and $\langle c_n'^2 \rangle$ vs. $\langle c_t^2 \rangle$ are scattered and the correlation is weak. It is suggested that the

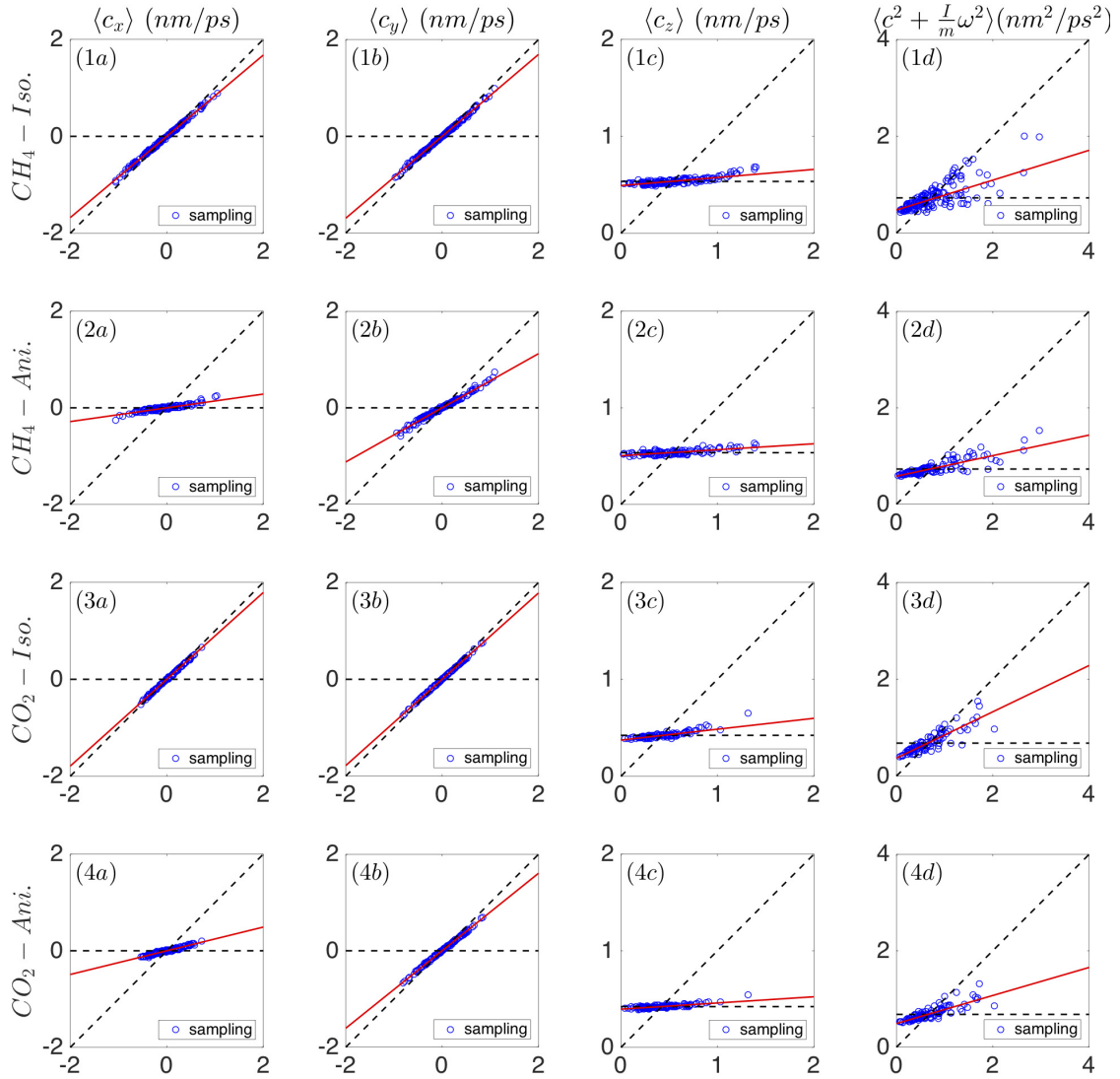


Figure 3.3: Correlation analysis using BA scheme for CH_4/CO_2 -Graphite. Columns (a), (b), (c) represent the velocity (nm/ps) along x , y , z directions respectively and column (d) the kinetic energy for CH_4 and CO_2 (the prefactor $m/2$ is removed for simplicity). The horizontal axis shows the incident values and the vertical axis the reflection values. The solid lines represent the fit by least squares linear regression using Eq. (3.13). The diagonal dashed line and the horizontal dashed line indicate the zero accommodation case ($\alpha = 0$) and full accommodation case ($\alpha = 1$), respectively.

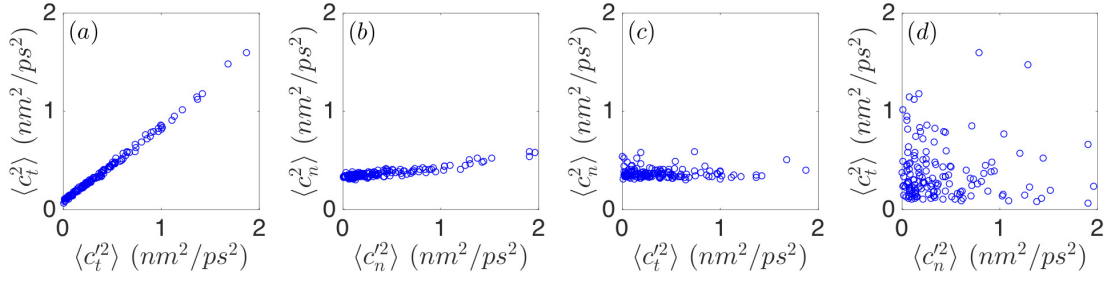


Figure 3.4: Detailed analysis of kinetic energy of CH_4 beamed on the smooth surface. The tangential kinetic energy component $c_t^2 = c_x^2 + c_y^2$ and the normal kinetic energy component $c_n^2 = c_z^2$ are used for analysis. Subfigures (a), (b), (c), (d) show the correlation between incident energy and reflective energy components.

combination of different tangential and normal reflection behaviors can be responsible for the scattering of the total energy data c^2 . As a final remark, the energy data scattering exists in literature models, especially for parametric models like ACL/CL or DM which are not based on a constant energy accommodation coefficient. Indeed, Fig 3.5 shows that the parametric kernel ACL/CL with suitable parameters has produced the same pattern, i.e energy data scattering, as the MD results.

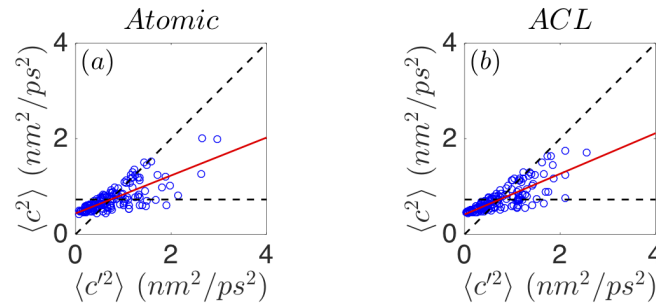


Figure 3.5: Energy data scattering observed from (a) MD simulations, (b) parametric ACL model with parameters $\alpha_x = \alpha_y = 0.16$ (constant tangential momentum accommodation coefficient) and $\alpha_z = 0.915$ (constant normal kinetic energy accommodation coefficient)

Next, with the SE scheme, we simulated 10^5 collisions on graphite surfaces. The input velocities are taken from equilibrium distribution and results are presented in Fig. 3.6. From these figures we can analyze the correlation between incident and reflected velocities on graphite wall then we can compute the accommodation coefficients from Eq. (3.14) issued from [125]. It is noted that due to the equilibrium state, Eq. (3.13) takes the form $0/0$ and cannot be used

to determine the accommodation coefficients in this case. We find that for smooth graphite surface, the incident and reflected velocity data have significant correlation in x and y directions. Despite its crystalline nature, the surface behavior is isotropic and no visible difference is observed between directions x and y . The accommodation coefficients calculated by the least-squares method [125] in Tab. 3.3 also confirm this remark. However, the influence of periodic roughness affects the anisotropy of the surface (second row figures) and the magnitude of the accommodation coefficients. We can see that the scattering is more diffusive along both directions but more pronounced for x direction. In all cases, the correlation between c_z and c'_z as well as the correlation between c^2 and c'^2 are very weak, and close to the diffusive wall.

Gas	Surface	Scheme	$\alpha_x(c_x)$	$\alpha_y(c_y)$	$\alpha_z(c_z)$	$\alpha_e(c^2 + \frac{I}{m}\omega^2)$
CH ₄	Isotropic	SE	0.158	0.160	0.915	0.559
		BA	0.162	0.154	0.916	0.691
	Anisotropic	SE	0.839	0.440	0.948	0.775
		BA	0.857	0.438	0.938	0.787
CO ₂	Isotropic	SE	0.102	0.104	0.885	0.515
		BA	0.105	0.109	0.888	0.521
	Anisotropic	SE	0.737	0.196	0.942	0.682
		BA	0.755	0.197	0.936	0.709

Table 3.3: Accommodation coefficients computed by stochastic equilibrium (SE) simulation method using data of Fig. 3.6 and by batch average (BA) simulation method in Fig. 3.3: α_l coefficient is associated to the velocity c_l , α_e is the kinetic energy (the angular velocity of CH₄ is zero).

We note that all analytical surface models in literature are based on the accommodation coefficients. Thus, we can construct scattering kernels which can serve as boundary conditions for atomistic method like MD or DSMC. The main advantage of these kernels is the simplicity in implementation but their drawbacks are their differences from the real surface behavior. This can be explained from the fact that they rely on the existence of the limited number of constant accommodation coefficients. To reconstruct $B(\boldsymbol{\omega}, \mathbf{c}|\boldsymbol{\omega}', \mathbf{c}')$, we don't use any parameter and make no assumption on the distribution form except for the decomposition of each

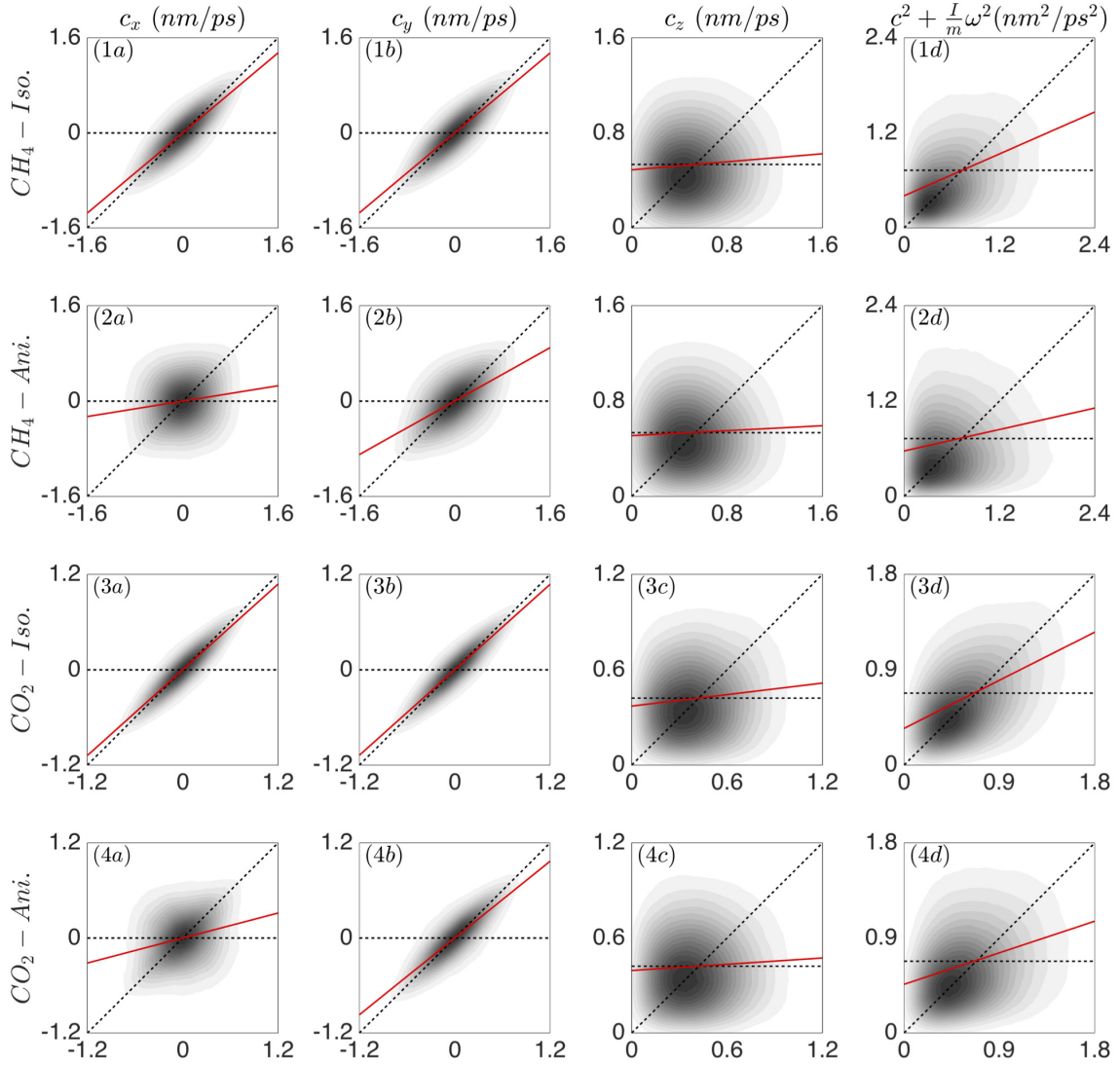


Figure 3.6: Collision data of incident and reflected velocities for the CH₄/CO₂-Graphite system. Both stochastic reservoir and graphite wall are maintained at 350 K for CH₄ and 600 K for CO₂. Columns (a), (b), (c) represent the velocity (nm/ps) along directions x , y , z , respectively, and column (d) the kinetic energy for CH₄ and CO₂ (the prefactor $m/2$ is removed for simplicity). The horizontal axis shows the incident values and the vertical axis the reflection values. The solid lines indicate the linear least square fit of incident and reflected values using Eq. (3.14). The diagonal dashed line and the horizontal dashed line indicate the zero accommodation case ($\alpha = 0$) and full accommodation case ($\alpha = 1$), respectively.

components

$$B(\boldsymbol{\omega}, \mathbf{c}|\boldsymbol{\omega}', \mathbf{c}') = \prod_{i=1}^3 B_i(c_i|c'_i) B_i^\omega(\omega_i|\omega'_i). \quad (3.33)$$

The above relation reduces the realization of $B(\boldsymbol{\omega}, \mathbf{c}|\boldsymbol{\omega}', \mathbf{c}')$ to the realizations of independent univariate densities $B_i(c_i|c'_i)$ and $B_i^\omega(\omega_i|\omega'_i)$. We note that, theoretically, the construction of $B(\boldsymbol{\omega}, \mathbf{c}|\boldsymbol{\omega}', \mathbf{c}')$ doesn't depend on the above assumption. However, the usual non-parametric estimates of multivariate density require a very large number of samples to be accurate (the curse of dimensionality) and more advanced learning methods are needed to solve this issue.

Without losing generality, we take the case of translation velocity c_i . The probability density function (PDF) of reflective velocity with given incident velocity $P(c_i|c'_i)$ can be determined by joint PDF of reflective-incident velocity $P(c_i, c'_i)$ and marginal PDF of incident velocity $P(c'_i)$ with relation:

$$B_i(c_i|c'_i) = P(c_i|c'_i) = \frac{P(c_i, c'_i)}{P(c'_i)}. \quad (3.34)$$

The discrete collision data can be used to estimate the joint probability $P(c_i, c'_i)$ by histogram or kernel density estimation method. After determining $B_i(c_i|c'_i)$, we can use it to generate the outgoing velocities at any given incident velocities. This can be done via the use of conditional cumulative distribution function (CDF) $F(c_i|c'_i)$.

To illustrate the robustness of the non-parametric model, we take the case of anisotropic surface and plot the probability density of input and output velocities of different kernels together with the MD data in Fig. 3.7. The considered kernels are Dadzie-Meolans (DM) [33] and anisotropic Cercignani-Lampis (ACL) [141], and non-parametric kernel constructed numerically from MD simulations (see Appendix B). The accommodation parameters of ACL kernel (α_x associated to c_x , α_y to c_y and α_z to c_z^2) and DM kernels (α_x and α_y are the same as ACL kernels and α_z is associated to c_z) are determined by SE simulations using Eq. (3.14). One can find that the DM kernel that includes mirror-reflected mechanisms is very different from the true collision

data, the probability density shows a strong discontinuity. The ACL kernel performs better but the non-parametric kernel is the most faithful to the MD data. Such differences can have significant influences on the results based on the kernel.

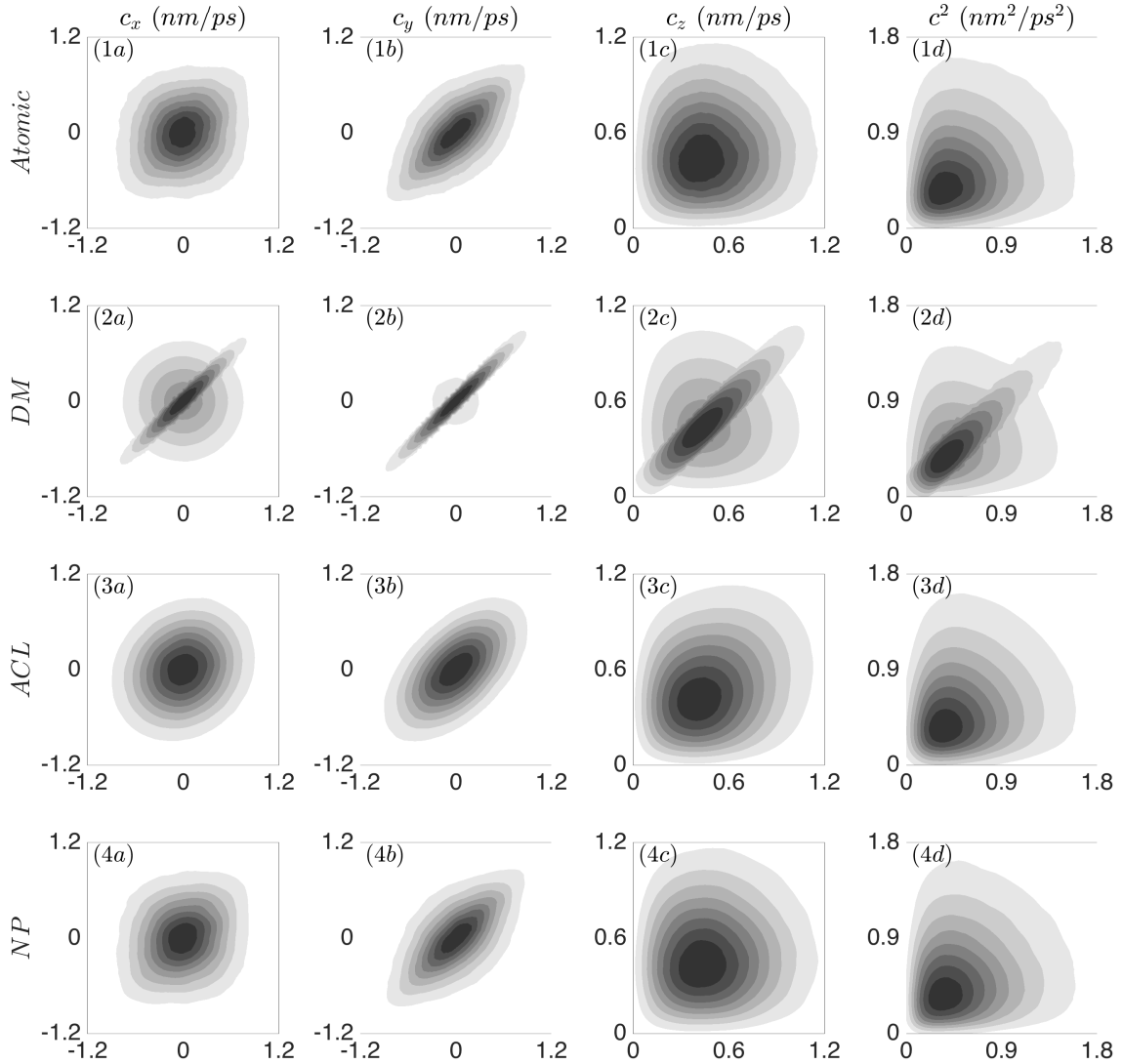


Figure 3.7: Velocity probability density of MD simulations and from some scattering kernels: Dadzie-Meolans (DM) [33], Anisotropic Cercignani-Lampis (ACL) [141] and non-parametric (NP) kernel constructed from MD data. The MD data are from collision simulation of CH_4 (350 K) at anisotropic atomic graphite wall (350 K). Columns (a), (b), (c) represent the velocity (nm/ps) at directions x , y , z , respectively, and column (d) the kinetic energy for CH_4 (the prefactor $m/2$ is removed for simplicity). The horizontal axis shows the incident values and the vertical axis the reflection values.

3.3.3 Direct computation of interface coefficients

The methods of determining the accommodation parameters like SE and BA depend on the existence of these constant coefficients. The BA gas beam experiments show that the postulates are rather restrictive (see e.g. Fig. 3.3, column d). Deriving those coefficients by fitting may correspond values in average sense without connection to the boundary conditions (3.16). Nevertheless, the slip and jump phenomena still exist and it is of interest to identify the coefficients associated to these effects. In this situation, one must make use of the non-equilibrium state of the gas near the wall. In principle, the more realistic the gas distribution is, the better interface coefficients we obtain. Before using more sophisticated distribution like Chapman-Enskog or R13 density, we shall examine the workability of a simpler distribution, MB at different temperatures and mean velocities. For β_{1x}, β_{1y} associated to the friction coefficients, we use Maxwellian with the same temperature as the wall but non zero mean velocity. The latter is a vector lying in the bisector plane (making angle $\pi/4$ with respect to axis x and y) with variable magnitude. For β_2 related to the Kapitza coefficient, we use Maxwellian with zero mean velocity but different temperatures. Specifically, the temperature ranges from 250 K to 450 K for CH_4 , from 500 K to 700 K for CO_2 and mean velocities range from -0.05nm/ps to 0.05nm/ps for both CH_4 and CO_2 . At this stage, we have two wall models:

- Atomic wall model (AM)
- Non-parametric wall model (NP)

for comparisons. To examine the connection between the quantities in the boundary models, results for the slip velocities, the temperature jump, stress and heat flux obtained by Eqs. (3.18-3.23) are plotted together in Fig. 3.8.

We see a clear linear relation between $-\hat{\sigma}_{kz}$ and \hat{v}_z as well as between $-\hat{q}_z$ and $\Delta\hat{\theta}$ in Fig. 3.8. The slopes of fitted lines represent the value of the dimensionless friction coefficient β_{1k} (subfigures *a* and *b*) and the dimensionless thermal coefficient β_2 (subfigure *c*). The friction coefficient of the x direction increases 8 times from smooth wall to rough wall, compared with the

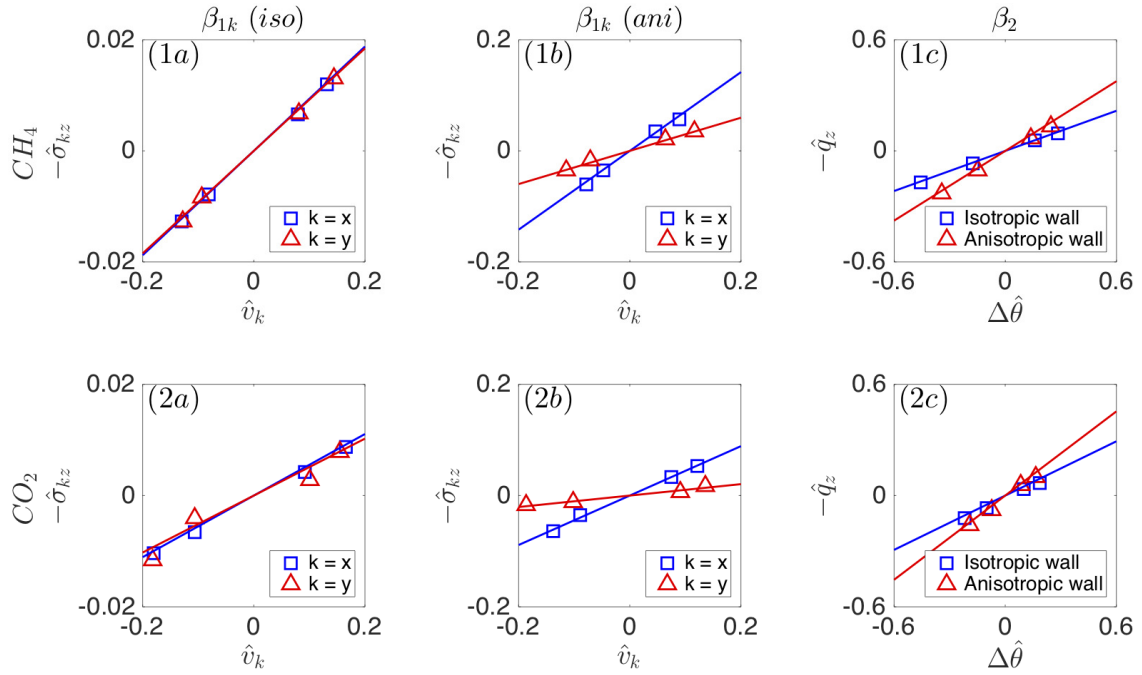


Figure 3.8: Method of computing coefficients β_s by non-equilibrium simulation, MB distribution and atomic wall model (AM). (a) $-\hat{\sigma}_{kz}$ and \hat{v}_k of the isotropic graphite wall. (b) $-\hat{\sigma}_{kz}$ and \hat{v}_k of the anisotropic graphite wall. (c) $-\hat{q}_z$ and $\Delta\hat{\theta}$ are calculated by incident and reflective velocities on isotropic and anisotropic graphite wall.

3 times increase in the y direction. It's also interesting to see that the β_2 coefficient of smooth wall is smaller than the rough wall's (about 2 times). These tendencies coincide with reality that rough surface friction and thermal resistance are larger than the smooth surface ones. For comparison with theoretical models where the accommodation coefficients are connected to the interface equations Eqs. (3.17), the results of CH_4 and of CO_2 are plotted in Tab. 3.4.

In terms of friction coefficient β_{1k} , the results of the non-equilibrium method with MB distribution are very close to those obtained with the methods based on equilibrium distribution. This is reasonable since the BA method also shows that the accommodation model works well for this case. For thermal coefficient β_2 , the SN method seems to agree better with the coefficient derived from SE method than the BA method. This observation can be explained from the scattering data in the BA method, meaning that the theoretical definition of the thermal accommodation coefficient is no longer valid. In this case, an effective coefficient which reproduces the thermal jump effect can be determined.

Surface	Method	CH ₄			CO ₂		
		β_{1x}	β_{1y}	β_2	β_{1x}	β_{1y}	β_2
Isotropic	SE (α)	0.087	0.087	0.388	0.054	0.054	0.347
	SN (MB-AM)	0.093	0.093	0.361	0.053	0.053	0.488
	SN (MB-NP)	0.095	0.095	0.382	0.052	0.052	0.469
	SN (CE-NP)	0.094	0.094	0.336	-	-	-
Anisotropic	SE (α)	0.722	0.282	0.632	0.584	0.108	0.518
	SN (MB-AM)	0.709	0.299	0.627	0.444	0.103	0.756
	SN (MB-NP)	0.720	0.298	0.644	0.459	0.102	0.728
	SN (CE-NP)	0.646	0.280	0.553	-	-	-

Table 3.4: The β coefficients of CH₄ and CO₂ computed by SN methods and compared with values obtained from accommodation coefficients (SE method, Tab. 3.3) via formula $\beta_{1k} = \alpha_k/(2 - \alpha_k)$, $\beta_2 = \alpha_e/(2 - \alpha_e)$. MB: Maxwell-Boltzmann distribution, CE: Chapman-Enskog distribution, AM: atomic model for wall, NP: the wall is modeled by non-parametric scattering kernel $B(\mathbf{c}|\mathbf{c}')$, instead of atomic wall (as in MB-AM method). To increase the precision of the slip coefficients for smooth (isotropic) surface, we average values along β_{1x} and β_{1y} .

3.3.4 Influences of non-equilibrium distributions and discussion

Essentially based on the same procedure as previous subsection, we study the influence of the near wall distribution and the surface models on the interface coefficients. We focus on the monatomic gas CH₄, NP wall model and the following non-equilibrium distributions:

- Chapman-Enskog distribution
- R13 distribution

To generate CE and R13 distributions, we use the Acceptance-Rejection approach described in Appendix A. In addition to temperature and mean velocity, the CE and R13 distributions require input fluxes and moments which are generally unknown. We carry out the following iterations:

- Step n
 - Generation of input distribution using CE (or R13) distribution with average moments of the previous steps $n - 1$.
 - Compute the output distribution using the kernel $B(\mathbf{c}|\mathbf{c}')$.
 - Calculate the average moments at the wall from input and output distributions.

- Next step.

The loop stops when all the average moments converge (see e.g Fig. 3.9). The input distribution at the first step $n = 1$ can be initialized with MB distribution as the previous SN/MB scheme, i.e all fluxes (heat fluxes, stress, etc...) are set zero. The latter quantities become non-zero after the initialization ($n \geq 2$) and we can effectively use the CE and R13 generator. Numerical tests show that while the average moments at convergence depend on the initialized values, the value of β coefficients are insensitive to them.

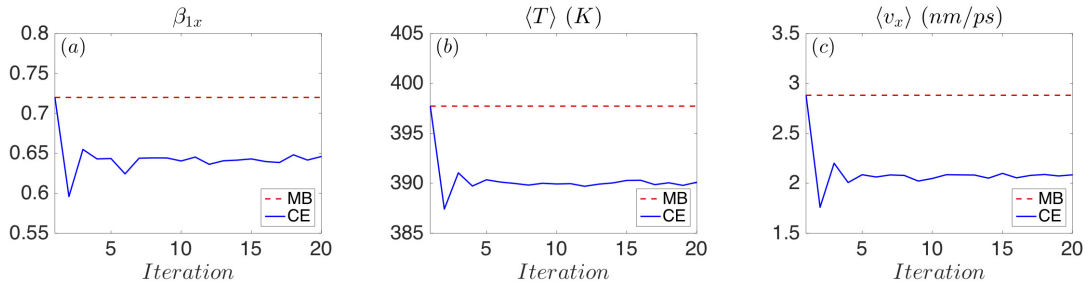


Figure 3.9: Convergence test of CE-NP kernel iteration for rough anisotropic surface. Subfigures (a): Friction coefficient β_{1x} , (b) Gas temperature (c) Gas velocity.

About 10^7 collisions with scattering kernel are simulated. In Tab. 3.4, we find that all the methods yield results close to each other, especially for isotropic surface. For anisotropic surface and friction coefficient along x , the method based on CE shows some discrepancies with the rest (although the coefficient is of the same range of order). The visible differences can be explained from the influences of heat flux and shear stress at convergence. By examining in detail the convergence of β_{1x} in Fig. 3.9, we find the final parameter is different from the first iteration one. It is suggested that the presence of the roughness perturbs considerably the phase density. Due to the realistic kernel $B(\mathbf{c}|\mathbf{c}')$, the output is not necessarily of the same distribution class as the input. This raise questions on the use of CE distribution near the wall, especially the component c_x along the roughness directions. Another possible reason is that there may be a considerable coupling between different moments which must be taken into account in the phenomenological equations. The complete answer can only be found from flow

simulations using the same surface model, but with different input distributions.

Next we consider another non-equilibrium distribution associated to R13 moment equations. The boundary conditions are originally derived for Maxwell scattering kernel with one accommodation coefficient (isotropic surface) and all β coefficients being identical. In order to test the R13 generator, we use first the Maxwell kernel with $\alpha = 0.3$ and obtain interface coefficients. From Tab. 3.4, we find that these coefficients are overall in good agreement with the theory prediction $\beta = \alpha/(2 - \alpha) = 0.176$. Most of the computed coefficients are within less than 1% error from the analytical value. This is a good starting point to proceed with our graphite surface.

We use NP model for our graphite surface. The results show that coefficients β_1, β_2 agree with the computed values for NSF equations listed in Tab. 3.5. Coefficients $\beta_3, \beta_4, \beta_5$ correspond to boundary conditions for higher order terms. As the overall remark, all coefficients β are different, showing that the use of Maxwell kernel cannot capture correctly the boundary conditions at the wall. In this case, the present approach can provide an alternative and reliable solution for any surface.

Surface	Kernel	β_1	β_2	β_3	β_4	β_5
Test	Maxwell	0.177	0.177	0.160	0.173	0.161
Graphite	NP	0.097	0.373	0.024	0.028	0.129

Table 3.5: β coefficients of R13 equations using Maxwell kernel ($\alpha = 0.3$) and non-parametric scattering kernel.

3.4 Conclusions

It is known that gas flows at high Knudsen number are present in micro-nanopore underground. To accurately obtain macroscopic transport behavior (permeability for example), we must use relevant gas model and boundary conditions at the pore scale. The present paper is devoted to the construction of gas-wall interaction models and to the determination of boundary con-

ditions for continuum equations such as Navier-Stokes-Fourier or R13 equations.

Based on MD simulation of independent collisions of CH₄ and CO₂ rigid molecules on graphite surface, we collect data of pre- and post-collision and numerically recover the scattering kernel for the gas-wall couples. Specifically, it can be used to construct non-parametric models capable of generating a distribution of post-collision velocity, given the pre-collision velocity. The effective accommodation coefficients can also be obtained from the scattering kernel using a different fitting procedure.

In the general case, a method is proposed to directly compute the parameters of any phenomenological boundary conditions without using the concept of accommodation coefficients. The approach relies on the general scattering kernel issued from MD with suitable input gas distribution, which is similar to the theoretical method of Grad [53]. Such an approach is of interest since it can capture more accurately the distribution of reflection velocity. There are still some drawbacks to the current version which will be improved in the future, for example, the use of rigid gas molecule model and the assumptions of independence between the velocity components. Another interesting subject which has not been treated in this work is the Knudsen layer effect. We note that by simulating flows using non-parametric kernel, one can obtain correction coefficients to the microslip obtained by the present paper.

Appendix

A. Generation of non-equilibrium distribution

Generating pre-collision velocity of particle requires first the PDF of initial velocity. The Maxwell-Boltzmann distribution is used for a equilibrium dilute gas at temperature T . In order to generate the pre-collision velocity, we rewrite the flux associated to the normalized

MB distribution $f_M^*(\tilde{\mathbf{C}})$ as:

$$f_M^*(\tilde{\mathbf{C}}) = 2 \frac{|\tilde{C}_z|}{\pi} \exp(-\tilde{\mathbf{C}}^2), \quad \tilde{C}_z < 0, \quad (3.35)$$

where $\tilde{\mathbf{C}} = \mathbf{C}/\sqrt{2\theta}$ and $\theta = k_B T/m$. This distribution is constituted of three independent distributions: two normal distributions along x, y and a Rayleigh distribution along z . Then we can calculate the flux associated to Chapman-Enskog distribution $f_{CE}^*(\tilde{\mathbf{C}})$ by the relation:

$$f_{CE}^*(\tilde{\mathbf{C}}) = \Gamma_{CE}(\tilde{\mathbf{C}}) f_M^*(\tilde{\mathbf{C}}), \quad \tilde{C}_z < 0, \quad (3.36)$$

where

$$\begin{aligned} \Gamma_{CE}(\tilde{\mathbf{C}}) = 1 & + \left(\tilde{q}_x \tilde{C}_x + \tilde{q}_y \tilde{C}_y + \tilde{q}_z \tilde{C}_z \right) \left(\frac{2}{5} \tilde{\mathbf{C}}^2 - 1 \right) \\ & + 2 \left(\tilde{\sigma}_{xy} \tilde{C}_x \tilde{C}_y + \tilde{\sigma}_{xz} \tilde{C}_x \tilde{C}_z + \tilde{\sigma}_{yz} \tilde{C}_y \tilde{C}_z \right) \\ & + \tilde{\sigma}_{xx} \tilde{C}_x^2 + \tilde{\sigma}_{yy} \tilde{C}_y^2 + \tilde{\sigma}_{zz} \tilde{C}_z^2, \end{aligned} \quad (3.37)$$

with

$$\tilde{\sigma}_{ij} = \frac{\sigma_{ij}}{p}, \quad \tilde{q}_i = \frac{q_i}{p\sqrt{\theta/2}}, \quad p = mn\theta, \quad i, j = x, y, z. \quad (3.38)$$

Similarly, the R13 distribution can be calculated from MB distribution by the relation:

$$f_{R13}^*(\tilde{\mathbf{C}}) = \Gamma_{R13}(\tilde{\mathbf{C}}) f_M^*(\tilde{\mathbf{C}}), \quad \tilde{C}_z < 0, \quad (3.39)$$

where

$$\begin{aligned}
\Gamma_{R13}(\tilde{\mathbf{C}}) &= 1 + \varphi_{13}(\tilde{\mathbf{C}}) + \varphi_{R1}(\tilde{\mathbf{C}}) + \varphi_{R2}(\tilde{\mathbf{C}}), \\
\varphi_{13}(\tilde{\mathbf{C}}) &= \left(\tilde{q}_x \tilde{C}_x + \tilde{q}_z \tilde{C}_z \right) \left(\frac{2}{5} \tilde{C}^2 - 1 \right) + 2\tilde{\sigma}_{xz} \tilde{C}_x \tilde{C}_z + \tilde{\sigma}_{xx} \tilde{C}_x^2 + \tilde{\sigma}_{yy} \tilde{C}_y^2 + \tilde{\sigma}_{zz} \tilde{C}_z^2, \\
\varphi_{R1}(\tilde{\mathbf{C}}) &= \frac{1}{3} \left(\tilde{m}_{xxx} \tilde{C}_x^3 + \tilde{m}_{zzz} \tilde{C}_z^3 \right) + \tilde{m}_{xxz} \tilde{C}_x^2 \tilde{C}_z + \tilde{m}_{xzz} \tilde{C}_x \tilde{C}_z^2 + \tilde{m}_{xyy} \tilde{C}_x \tilde{C}_y^2 + \tilde{m}_{zyy} \tilde{C}_z \tilde{C}_y^2, \\
\varphi_{R2}(\tilde{\mathbf{C}}) &= \left(\tilde{R}_{xx} \tilde{C}_x^2 + \tilde{R}_{yy} \tilde{C}_y^2 + \tilde{R}_{zz} \tilde{C}_z^2 + 2\tilde{R}_{xy} \tilde{C}_x \tilde{C}_y \right) \left(\frac{\tilde{C}^2}{7} - \frac{1}{2} \right) + \frac{\tilde{R}}{30} \left(\tilde{C}^4 - 5\tilde{C}^2 + \frac{15}{4} \right),
\end{aligned} \tag{3.40}$$

with

$$\tilde{m}_{ijl} = \frac{m_{ijl}}{p\sqrt{\theta/2}}, \quad \tilde{R}_{ij} = \frac{R_{ij}}{p\theta}, \quad \tilde{R} = \frac{R}{p\theta} \quad i, j, l = x, y, z. \tag{3.41}$$

Since the CE and R13 distributions have analytical PDF expression, we can generate random velocities corresponding to these distributions by the Acceptance-Rejection method. The specific steps are as follows:

1. Find $B_{CE} = \max(|\sigma_{ij}|, |q_i|)$ for distribution CE, $B_{R13} = \max(|\sigma_{ij}|, |q_i|, |m_{ijk}|, |R_{ij}|, |R_{ij}|)$ for distribution R13 .
2. Set amplitude parameter $A_{CE} = 1 + 30B_{CE}$ and $A_{R13} = 1 + 60B_{R13}$.
3. Generate a normalized velocity $\tilde{\mathbf{C}}_{MB}$ obeying MB distribution (Eq. (3.35)), and a uniform random number $U(0, 1)$.
4. If $\Gamma_{CE}(\tilde{\mathbf{C}}_{MB}) \geq AU$, accept $\tilde{\mathbf{C}}_{MB}$ as normalized CE distribution velocity $\tilde{\mathbf{C}}_{CE}$, and if $\Gamma_{R13}(\tilde{\mathbf{C}}_{MB}) \geq AU$, accept $\tilde{\mathbf{C}}_{MB}$ as normalized R13 distribution velocity $\tilde{\mathbf{C}}_{R13}$; else reject this velocity and return to step 3;
5. The real velocity is $\mathbf{c} = \sqrt{2\theta}\tilde{\mathbf{C}}_{MB} + \mathbf{v}$, \mathbf{v} is the mean velocity.

During the Acceptance-Rejection process, the function $\Gamma(\tilde{\mathbf{C}})$ can be negative. This velocity is rejected in this case.

B. Method for generating non-parametric kernel

Different from parametric scattering models, like CL or Maxwell, the non-parametric wall model is not specified a priori but is instead determined from data. Using the discrete incident-reflection velocities data, we can generate the reflective velocities at any given incident velocities. The implementation of Eq. (3.34) is as follows:

1. Discretize the velocity space c'_i and c_i to a series of velocity points with sufficient small interval. Choose a volume $\Delta c'_i$ and let us call class c'_i the collisions in the volume centered at c'_i .
2. Use sliding window method to count the number of collision ΔN in class c'_i .
3. Calculate discrete CDF of every class c'_i as $F(x|c'_i) = \frac{\Delta N(c_i \leq x)}{\Delta N}$.
4. Generate a uniform random number U between 0 to 1, then the reflective velocity is $c_i \sim F^{-1}(U|c'_i)$.

The procedure is shown in Fig. 3.10. The reflective rotation velocity can be obtained by the same procedure.

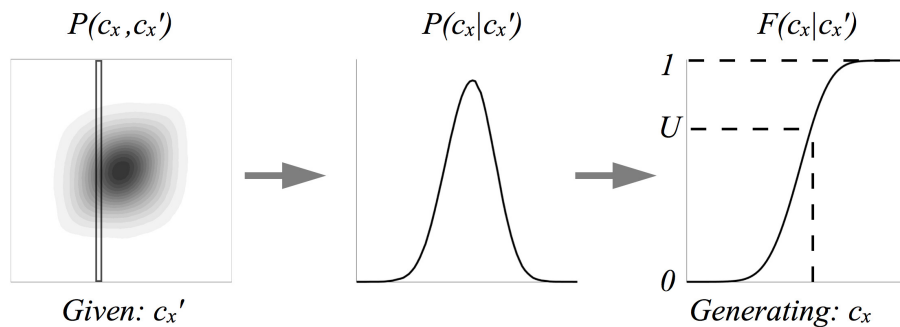


Figure 3.10: Generation of velocity using non-parametric kernel derived from MD collision clouds

Chapter 4

Helium and Argon Interactions with Gold Surfaces: *Ab Initio*-Assisted Determination of the He-Au Pairwise Potential. Application to Accommodation Coefficients Determination

Abstract

Global potentials for the extremely weak interaction between the He atom and gold surfaces are determined from *ab initio* calculations and validated with experimental-based determinations of well-depth values. Dispersionless density functional periodic calculations are combined with effective pairwise functional parameters for the dispersion. These parameters are obtained from time-dependent DFT response theory using localized Hartree-Fock orbitals, as applied on He-Au_n clusters. This He-Au pairwise potential is used in Molecular Dynamics simulations

of gas-gold surface collisions from which incident and reflected gas atom velocities allow the determination of energy and momentum accommodation coefficients. Boundary quantities such as slip velocity and thermal resistance are derived from these coefficients, but also from a new methodology based on a non-parametric kernel avoiding the atomic description of the gold surface. Similar collision simulations are performed for Ar for comparison. A model of a rough gold surface is also investigated.

4.1 Introduction

In the domain of Micro-Electro-Mechanical-Systems (MEMS), the study of fluid micro-flows is essential. Slippage and thermal resistance quantities are fundamental to characterize such micro-flows and are dependent on the fluid and micro-channel surface natures. Helium and argon are usual gases for the experimental studies. Gold is also a common coating of MEMS channel surfaces because it is a soft material which presents a strong resistance to oxidation and a reasonably high thermal conductivity. As an illustrative example, Hadj Nacer *et al.* [55, 56] have experimentally studied the flows of different gases (helium, argon, carbon dioxide, and nitrogen) through micro-tubes with different coatings including gold to extract accommodation coefficients.

The Tangential Momentum Accommodation Coefficient (TMAC) is an interesting quantity allowing the characterization of a fluid-surface interface. It is usually employed in fluid mechanics to evaluate the slip length of the fluid speed at the interface. Depending on its value (comprised in between 0 and 1) the collision of the fluid particles on the surface is characterized as being diffusive (TMAC = 1) or specular (TMAC = 0). The first definition of this parameter was established by Maxwell [92]. Since many years ago, several methodologies based on Molecular Dynamics (MD) simulations have been developed to evaluate the value of this parameter from particle velocities and different works have been devoted to determine these coefficients [101, 100, 81, 139, 140], as well as the so-named Energy Accommodation Coefficient (EAC).

The latter can be used to evaluate the temperature jump at a surface and in some models is connected to all the Momentum Accommodation Coefficients (MAC) [140]. The present work presents MAC and EAC values, as obtained from the method proposed by Spijker et al.[125] This method is based on the fit of impacting and reflected velocities of the gas atoms on the solid wall. In this work, this treatment has been applied to both He and Ar atoms in order to demonstrate the effect of the interaction potential and atomic masses. The effect of the roughness of the solid wall has also been explored. In order to be more general and to provide useful quantities for Navier-Stokes based macroscopic flow simulations, interface coefficients such as slippage and thermal resistance parameters have been derived from gas velocities, and from MAC and EAC for comparison. Our new non-parametric (NP) kernel approach has also been applied to verify its efficiency with the peculiar case of helium gas. This approach avoids a full atomic description of the surface without losing its specificity since it is not restricted to the use of just a few parameters [84].

Contrary to most of the works on MAC and EAC determinations, using Lorentz-Berthelot rules for the Lennard-Jones parameters, we use *ab initio* potentials. Following our theoretical work on the interface properties of argon with gold [54], we propose to extend the present study to the helium-gold couple. Helium is the lightest rare-gas atom. Its reduced size and weight imply special physical and chemical properties, as compared with heavier rare gases. Then, a peculiar behavior is expected for the interface of helium on gold. The present work addresses both an *ab initio*-assisted determination of pair He-Au potential and its employment in MD simulations for the determination of interface coefficients of the helium fluid interacting with gold surfaces. The results will also be compared with those obtained for the Ar-Au couple.

In a previous work, the Ar-Au pair potential was derived from calculations on the Ar+Au₂ complex mixing dispersionless density functional theory (dlDF) and a density functional theory (DFT)-based determination of dispersion coefficients (D_{as}) [54] using symmetry-adapted

perturbation theory (SAPT). The He-Au interaction is much weaker than the Ar-Au one. The best estimate of the He-Au diatomic molecule well-depth value is 1.897 meV from state-of-the-art *ab initio* calculations [50]. The previous empirical potentials based on the works of Zaremba and Kohn [165] indicate that the adsorption energy of a helium atom on a Au(111) surface might be about 10 meV [30, 31, 149, 134] with a wide range of values for the equilibrium geometry values, i.e. from 2.5 to 3.98 Å. The best experimental estimate of the well-depth was reported in the review by Vidali *et al.* [149], being 7.67 meV from scattering measurements. These energy values are an order of magnitude smaller than the Ar-Au(111) ones [54]. In the present work, a new strategy based on the $dIDF + D_{as}$ approach is proposed to produce an accurate He-Au pairwise potential.

The present work is organized as follows: in the next section, we describe the derivation of the He-Au pairwise potential from *ab initio* determinations and the application of the He-Au and Ar-Au potentials in molecular dynamics simulations of gas atom - gold surface collisions. EAC and MAC parameters, and boundary quantities are then derived from the gas velocities. Next, in Section 3, we present the results and especially, the comparison between Ar and He concerning the interaction potentials with gold and the interface quantities. Finally, the main conclusions are provided in Section 4.

4.2 Methods

4.2.1 Helium/Au(111) Interaction Energies: the Periodic $dIDF + D_{as}^*$ Approach

The present section is devoted to the *ab initio*-assisted determination of He-Au pairwise potential. In a first step, He-Au(111) interaction potential has been computed using the $dIDF +$

D_{as}^* approach, from where the pairwise potential coefficients have been extracted so that the He-Au potential has the form:

$$E_{\text{int}}(R) = \left(A + B R + \frac{C}{R} \right) e^{(-\alpha R - \gamma R^2)} + \sum_{n=6,8} \frac{\sqrt{C_n^{\text{He}} C_n^{\text{Au}}}}{R^n} f_n \left(\sqrt{\beta_{\text{He}} \beta_{\text{Au}}} R \right). \quad (4.1)$$

where R is the distance between a helium atom and a gold atom, A , B , C , α , and γ are the parameters associated with the dispersionless part of the potential, the other parameters concern the dispersion part of the potential, and f_n is the damping function of Tang and Toennies [133],

$$f_n(R) = 1 - e^{-\beta R} \left(1 + R + \dots + \frac{(\beta R)^n}{n!} \right) \quad (4.2)$$

Our approach can be viewed as a complementary extended version of the dispersionless density functional (dlDF) + D_{as} treatment proposed by Pernal et al.,[98] with D_{as} being a general-purpose effective pairwise functional for the dispersion [98, 105, 104]. The idea underlying the scheme (denoted then as the periodic dlDF + incremental D_{as}^* approach[36]) is the partition of the global interaction energy into dispersionless as well as dispersion contributions. The dispersionless contribution is obtained through the periodic dispersionless dlDF approach [36]. Next, dispersion contributions are calculated via time-dependent density functional response theory, using the localized Hartree-Fock method,[38] on a surface cluster model Au_{10} or Au_4 , allowing the D_{as} function parametrization (denoted as D_{as}^* parametrization). The D_{as}^* function is then employed to extrapolate the adsorbate/cluster dispersion contribution to the extended adsorbate/surface system.

As mentioned above, our pairwise potential model uses different functions for the dispersionless and dispersion energy contributions. It accounts for the typical exponential growth of the dominant dispersionless contribution, the exchange-repulsion but also including a Gaussian-

type ‘cushion’ to describe weakly attractive tails stemming from other dispersionless terms

$$E_{\text{int}}^{\text{disp-less}}(\{\mathbf{R}_{\text{He-Au}}\}) = \sum_{\text{Au}} \left(A + B R_{\text{He-Au}} + \frac{C}{R_{\text{He-Au}}} \right) e^{(-\alpha R_{\text{He-Au}} - \gamma R_{\text{He-Au}}^2)}, \quad (4.3)$$

where $R_{\text{He-Au}}$ stands for the distance between the adsorbate and one gold atom of the surface. The sum in the second term runs over all the gold atoms of the surface. For the dispersion part, the D_{as}^* function has the typical C_6/C_8 expansion with the damping functions of Tang and Toennies f_n ($n = 6, 8$)[133]

$$E_{\text{int}}^{\text{disp}}(\{\mathbf{R}_{\text{He-Au}}\}) = - \sum_{\text{Au}} \sum_{n=6,8} \frac{\sqrt{C_n^{\text{He}} C_n^{\text{Au}}}}{R_{\text{He-Au}}^n} f_n \left(\sqrt{\beta_{\text{He}} \beta_{\text{Au}}} R_{\text{He-Au}} \right). \quad (4.4)$$

where the Au sum applies on all the gold atoms of the cluster Au_4 or Au_{10} .

It has been found that an appropriate tuning of dispersion model parameters is achieved using rather small cluster models composed of four and ten gold atoms (see section 3.1). In fact, one basic conclusion from accurate studies of van der Waals-dominated adsorbate/surface systems (see e.g., Refs. [35, 37]) is that, although the dispersion is long-range, dispersion parameters show excellent transferability properties upon increasing the size of the surface cluster models.

For comparison purposes, a vdW-corrected DFT-based treatment has also been applied for the determination of the He-Au(111) interaction potential. Specifically, within the framework of the non-local vdW density functionals developed by Langreth and co-workers, we have chosen the second-generation vdW-DF2 treatment [80].

The details concerning all the electronic structure calculations can be found in the Supporting Information (SI).

4.2.2 Momentum and Energy Accommodation Coefficients, Slippage and Temperature Jump

The MAC coefficient α_k and the EAC coefficient α_e are defined by the relations [72]

$$\alpha_k = \frac{\langle c'_k \rangle - \langle c_k \rangle}{\langle c'_k \rangle - \langle c_{wk} \rangle}, \quad \alpha_e = \frac{\langle c'^2 \rangle - \langle c^2 \rangle}{\langle c'^2 \rangle - \langle c_w^2 \rangle}, \quad k = x, y, z, \quad (4.5)$$

where c'_k , c_k and c_{wk} are the k -components of the incident, reflected and wall-thermalized gas atom velocities, respectively. The latter is drawn from the equilibrium distribution at the wall temperature T_w . The notation $\langle \rangle$ stands for the average over the number of collisions, or equivalently the number of molecules crossing a control plane parallel to the wall. Since $\langle c_{wk} \rangle$ and $\langle c_w^2 \rangle$ can be computed from the equilibrium distribution, they are known quantities as a function of T_w . The calculation of $\langle c'_k \rangle$ and $\langle c_k \rangle$ depends on their distributions, or on the choice of incident velocities c'_k and the associated reflected velocities c_k . If α is close to 1, the collisions are characterized as being diffusive and if α is close to 0, they are characterized as being specular instead. Theoretically, the accommodation coefficients are related to the slip and jump coefficients via the expressions

$$\beta_{1k} = \frac{\alpha_k}{2 - \alpha_k}, \quad \beta_2 = \frac{\alpha_e}{2 - \alpha_e}, \quad k = x, y. \quad (4.6)$$

where β_{1k} is the dimensionless Navier tangential friction coefficient, depending on tangential accommodation coefficients α_k , β_2 is the dimensionless temperature resistance coefficient or Kapitza coefficient, depending on the energy accommodation coefficient α_e . These coefficients appear in the following sets of boundary conditions for Navier-Stokes-Fourier equations

$$\beta_{1k} v_k = -\frac{\sigma_{kz}}{n} \sqrt{\frac{\pi}{2k_B T m_g}}, \quad \beta_2 (T - T_w) = -\frac{q_z}{n} \sqrt{\frac{m_g \pi}{8k_B^3 T}}, \quad k = x, y. \quad (4.7)$$

where m_g is the mass of the gas atom, T the average temperature near the wall, and k_B the Boltzmann constant. As can be observed from Eq. 4.7, when the number density n and tem-

perature T are kept fixed, the slip velocity v_k is proportional to the shear component of the pressure tensor σ_{kz} and the temperature jump $T - T_w$ is proportional to the normal heat flux component q_z .

In an ideal case, the accommodation coefficients are constant and can be determined by Equation 4.5. Specifically, we can beam independently gas atoms onto the solid surface and average incident and reflected velocities to calculate MAC and EAC values. When the incident velocity set has the same mean velocity and temperature as the wall, the zero denominator is prone to numerical issues. In this case, Spijker et al. [125] proposed to analyze the correlation between input (incident) and output (reflection) data. In practice, it consists in computing the best least-square linear fit of all (c'_k, c_k) points obtained after a large number of collisions

$$\begin{aligned}\alpha_k &= 1 - \frac{\sum(c'_k - \langle c'_k \rangle)(c_k - \langle c_k \rangle)}{\sum(c'_k - \langle c'_k \rangle)^2} \quad k = x, y, z, \\ \alpha_e &= 1 - \frac{\sum(c'^2 - \langle c'^2 \rangle)(c^2 - \langle c^2 \rangle)}{\sum(c'^2 - \langle c'^2 \rangle)^2}.\end{aligned}\tag{4.8}$$

For realistic surfaces, however, the accommodation coefficients might not be constant and cannot be used to model the gas-wall interaction. In this case, Liao et al.[84] proposed to use a non-parametric approach to construct the relationship between the incident and the reflected velocity distributions. From the given collision data obtained from MD simulations, it is possible to construct a NP scattering kernel $B(\mathbf{c}|\mathbf{c}')$:

$$B(\mathbf{c}|\mathbf{c}') = P(\mathbf{c}|\mathbf{c}') = \prod_k B_k(c_k|c'_k), \quad k = x, y, z\tag{4.9}$$

where c'_k and c_k are the incident and reflective velocity components, respectively. Here, $B(\mathbf{c}|\mathbf{c}')$ is the usual conditional probability density $P(\mathbf{c}|\mathbf{c}')$ of \mathbf{c} for given \mathbf{c}' and is decomposed in 3 independent realizations $B_k(c_k|c'_k)$ depending on directions $k = x, y, z$, respectively. By (4.9), we assume that the reflective velocity component depends only on the incident velocity component of the same direction and neglect the influence of the incident velocity component associated

with different directions. Such decomposition avoids the curse of dimensionality, easing the construction of the kernel $B(\mathbf{c}|\mathbf{c}')$ from the available collision data. Using the NP kernel, we can generate new velocity data, i.e generating a random output c_k for a given input c'_k . This kernel can serve to set boundary conditions in the Boltzmann equation and particle-based simulation methods, including Direct Simulation Monte Carlo (DSMC) and MD treatments.

It is also possible to directly determine the boundary coefficients for Navier-Stokes-Fourier equations β_{1k}, β_2 without using intermediate accommodation coefficients. It is sufficient to use suitable input velocities, as example, non-equilibrium gas velocity distribution. Usually, to identify β_{1k} , we use the distribution with the same temperature as the wall but with different mean tangential velocity. To compute β_2 , the input distribution has zero mean tangential velocity but different temperatures are used. Output velocities can be generated via the fast NP scattering kernel or via realistic but more time-consuming collisions with the atomic wall. From the two input and output distributions, the stream velocity v_k and temperature T can be computed as

$$v_k = \frac{\langle c_k/|c_z| + c'_k/|c'_z| \rangle}{\langle 1/|c_z| + 1/|c'_z| \rangle}, \quad T = \frac{m_g \langle c^2/|c_z| + c'^2/|c'_z| \rangle}{3k_B \langle 1/|c_z| + 1/|c'_z| \rangle}, \quad (4.10)$$

and the heat flux $-q_z/n$ and shear stress $-\sigma_{kz}/n$ as

$$-\frac{\sigma_{kz}}{n} = \frac{m_g \langle c'_k - c_k \rangle}{\langle 1/|c_z| + 1/|c'_z| \rangle}, \quad -\frac{q_z}{n} = \frac{m_g \langle c'^2/2 - c^2/2 \rangle}{\langle 1/|c_z| + 1/|c'_z| \rangle}, \quad (4.11)$$

and use them to calculate the interface coefficients. The above expressions are obtained from the consideration of MD collision simulations and the kinetic theory where physical quantities are moments of phase density functions. To simplify the calculation, we normalized the values in Eq. (4.10) and (4.11) as follow:

$$\hat{\sigma}_{kz} = \frac{\sigma_{kz}}{nm_g\zeta^2}, \quad \hat{v}_k = \frac{v_k}{\zeta}, \quad \hat{q}_z = \frac{q_z}{2nm_g\zeta^3}, \quad \Delta\hat{\theta} = \frac{k_B(T - T_w)}{m_g\zeta^2}, \quad \zeta = \sqrt{\frac{2k_B T}{m_g\pi}}. \quad (4.12)$$

So the slip and jump coefficients are rewritten as:

$$\beta_{1k} = \frac{-\hat{\sigma}_{kz}}{\hat{v}_k}, \quad \beta_2 = \frac{-\hat{q}_z}{\Delta\hat{\theta}}, \quad k = x, y. \quad (4.13)$$

In what follows, the different methods briefly described above will be applied to study the accommodation coefficients and the slip/jump coefficients.

The gas atom velocities were obtained from Molecular Dynamics simulations of collisions of He or Ar on a gold surface, using the He-Au, Ar-He pairwise potentials derived above and in Ref.[54], respectively. The technical details are given in the Supporting Information. After each collision, the atomic velocity components are collected such that α_k is derived from the least-square linear fit of the clouds of points (c'_k, c_k) [125] (see equations (4.8)). Each sum is over all the collisions. Some velocity clouds are shown in Figure 4.1 for He or Ar colliding on gold surfaces.

We examine the dependences of α_k with both the gas temperature and the nature of the rare-gas atom. The gas temperature was computed from the average of the kinetic energies of the gas atoms before (T_{in}) and after the collision (T_{out}) with the gold surface at 300 K,

$$T_{in} = \frac{\langle c'^2 \rangle m_g}{4k_B}, \quad T_{out} = \frac{\langle c^2 \rangle m_g}{4k_B}. \quad (4.14)$$

The resulting MAC and EAC values are presented in Table 4.2.

In order to investigate the effect of the roughness of the surface on the MAC and EAC values, a rough surface was created by projecting gold atoms on a Au(111) surface (see SI). A surface example is illustrated by Figure 4.2 for which 96 Au atoms have been trapped after projection. The corresponding MAC and EAC values for different gas temperatures are given in Table 4.2.

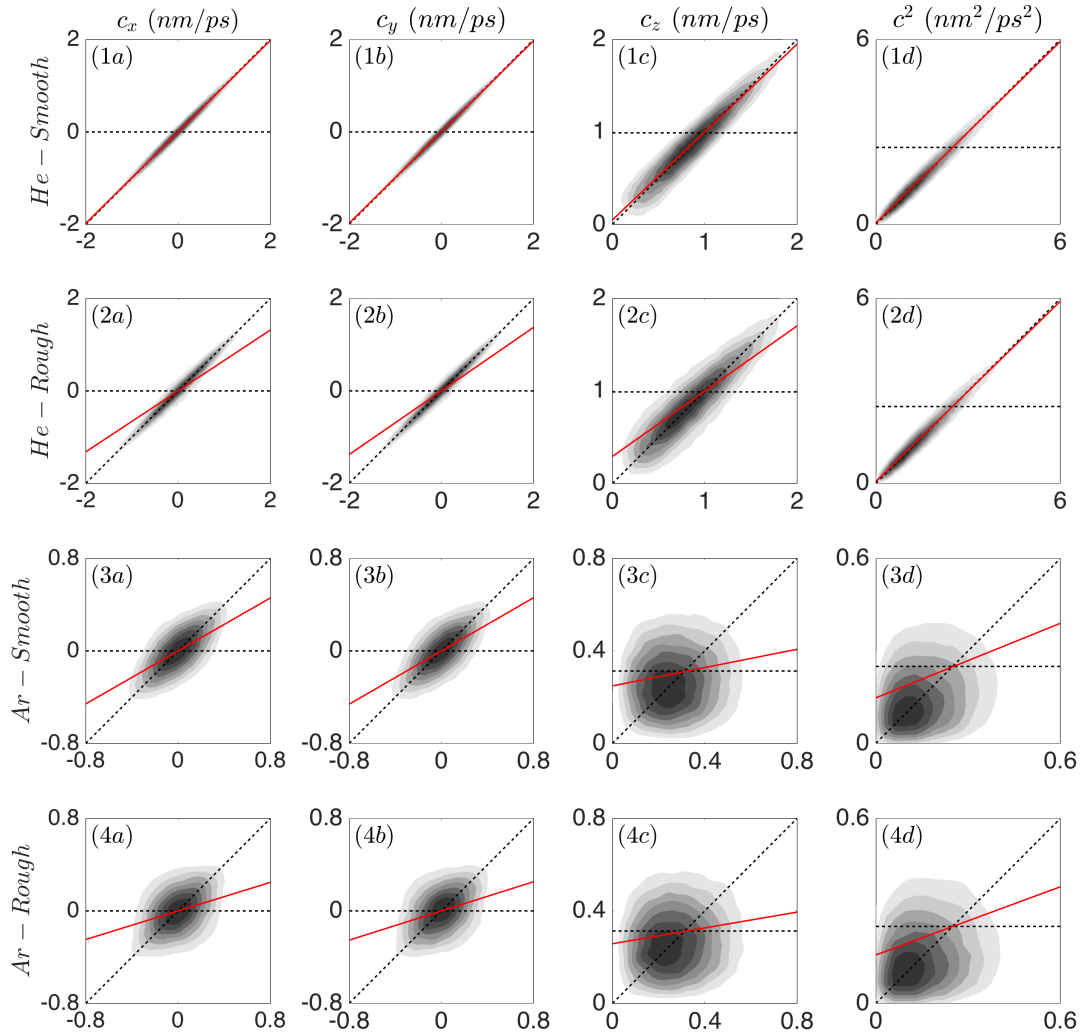


Figure 4.1: Cloud figures of incident (horizontal axis) and reflected (vertical axis) velocity components of 100000 collisions of He and Ar atoms at 300 K projected on smooth and rough Au surfaces at 300 K. The horizontal dashed lines correspond to the full diffusive case, the diagonal ones to the full specular case. The red curves correspond to the linear fit of the velocity cloud. The corresponding MAC and EAC values are given in Tables 4.2.

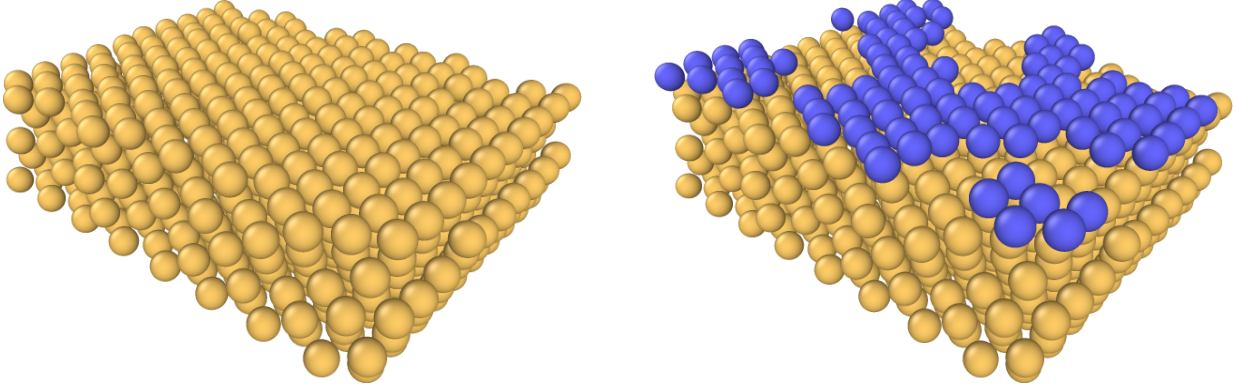


Figure 4.2: The smooth Au (left) and rough (right) surfaces of gold. The 800 yellow atoms are originated from the initial smooth surface. The 96 blue atoms were deposited in order to form the rough surface composed of 896 atoms.

In the NP model, we delimit the He velocity range from -4 to 4 nm/ps, and the Ar velocity range from -2 to 2 nm/ps. These ranges cover over 99.999% the gas velocities at 300 K. We use the kernel density estimation to estimate the joint probability density of velocities and to generate random reflection velocity for a given incident velocity. Then, we discretized the incident velocity space into 100 intervals, and the reflective velocity space into 1000 intervals. Next, we take a bandwidth of 0.2 nm/ps and use the Parzen-window method to calculate the numerical cumulative distribution function of the reflective velocities under different incident velocities. The probability of a reflective velocity not belonging to a category is determined by interpolation.

4.3 Results and Discussion

4.3.1 Helium/Au(111) Interaction Energies

The interaction energies obtained with our potential model (referred to as $\text{dlDF}+D_{as}^*$) are compared to those determined via the vdW-DF2 scheme in Figure 4.3. Dispersionless energies obtained from periodic dlDF calculations are indicated with green points while those extracted from the pairwise potential model are shown with green lines. Total interaction energies ob-

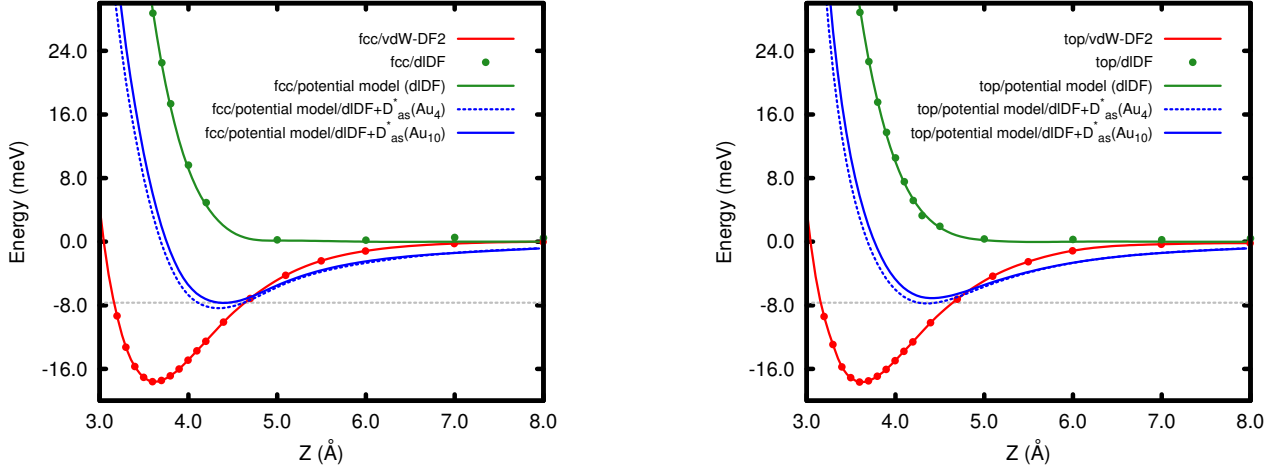


Figure 4.3: Radial scan of the interaction energies between atomic helium and the Au(111) surface, with the helium atom located at *fcc* (left panel) and *top* (right panel) positions. The interaction energies obtained with the periodic dIDF + D_{as}^* approach are compared with those determined via the vdW-DF2 scheme. The experimentally based value of the well-depth, 7.67 meV, is also indicated (gray dashed line) [149].

Table 4.1: Equilibrium geometries and well depths of the global interaction potentials of He with Au(111) for the *fcc* and *top* adsorption sites presented in Figure 4.3.

Site	Method	R_e (Å)	V_e (meV)
<i>top</i>	vdW-DF2	3.6205	-17.674
	dIDF+ D_{as}^* (Au ₄)	4.3519	-7.770
	dIDF+ D_{as}^* (Au ₁₀)	4.4124	-7.102
<i>fcc</i>	vdW-DF2	3.6193	-17.619
	dIDF+ D_{as}^* (Au ₄)	4.3410	-8.360
	dIDF+ D_{as}^* (Au ₁₀)	4.3994	-7.701

tained using the Au₄ cluster model to tune the dispersion parameters are compared with those extracted using the Au₁₀ cluster model. The experimentally based value of the well-depth is also indicated (gray dashed line). As shown in Figure 4.3 and Table 4.1, the well-depth values calculated with the dlDF+D_{as}^{*} treatment are very close to those based on experimental measurements [149]. It can also be seen that the vdW-DF2 approach[80] provides well-depth values as twice as large. The reason of this overestimation can be understood according to previous studies of He-surface interactions (e.g. see Ref. [36, 35, 37]). Semi-local DFT treatments tend to provide short-range dispersionless contributions which are attractive while the benchmarking at Coupled-Cluster level indicates that short-range intra-monomer correlation contributions are repulsive. Concerning the equilibrium geometry, compared with the wide range of values reported in the literature (i.e. from 2.5 to 3.98 Å[30, 31, 149, 134]), the dlDF+D_{as}^{*} approach might produce an overestimated value.

The total interaction energies presented in Figure 4.3 and the data of Table 4.1 indicate that the D_{as}^{*} parametrization extracted from the Au₁₀ cluster model provides dispersion energies which are very close to those using the Au₄ cluster instead (to within about 1 meV for the total energy). The particular position of the He atom in the Au_n clusters, considering both *top* or *fcc* positions, was found to be almost irrelevant for the D_{as}^{*} function parametrization (to within about 0.5 meV for the the Au₁₀ cluster case). However, the *fcc* site provides the most stable minimum using the dlDF+D_{as}^{*} approach, and the corresponding parameters derived from the Au₁₀ cluster results were used for the definition of the pairwise potential needed for the MD calculations.

Figure 4.3 results confirm that the He-surface interaction is a special case for which 'standard' DFT methods such as vdW-DF2 cannot be used, contrary to the results we obtained for Ar [54]. The current version of the dlDF+D_{as}^{*} approach is a cost-efficient alternative. At a variance with our previous work on the Ar/gold interaction, [54] the dispersionless pairwise potential

has been extracted from periodic calculations while the dispersion has been determined from TD-DFT linear response theory, using localized Hartree-Fock orbitals, instead of SAPT(DFT) calculations.

The D_{as}^* and dispersionless He-Au coefficients are presented in Tables S2 and S1 of SI, respectively. For comparison and further need, the corresponding Ar-Au coefficients are also included. These parameters provide a pairwise potential well-depth value of 0.78723 meV and an equilibrium geometry of 4.8720 Å for the He-Au pair. These values can be compared with those determined for the Ar-Au pair: 11.360 meV and 4.2848 Å, respectively [54]. As expected from the very different polarizabilities of He and Ar atoms, the He-Au D_{as}^* parameters render an interaction which is much less attractive than the Ar-Au interaction. The fact that the dispersionless part has to be expressed by more parameters in the He-Au case also indicates the difficulty to accurately reproduce such an interaction.

4.3.2 Momentum and Energy Accommodation Coefficients, Slippage and Temperature Jump

The first inspection of Table 4.2 indicates that the MAC values are, at least, an order of magnitude lower for He than for Ar. The collisions of He on gold are then much more specular than the Ar ones. This result is expected from the difference of pairwise potentials as well as the mass difference between He and Ar.

For both atomic species, α_x and α_y values are almost identical as expected from the study of a smooth isotropic surface. Contrary to the general behavior, α_x and α_y increase with T_g for He colliding with the smooth gold surface, whereas α_z for He and all α component values for Ar decrease with T_g . However, this result may not be significant since α_x and α_y values for

Table 4.2: MAC and EAC results for He, Ar collisions on smooth and rough Au surfaces at 300 K. T_g is the temperature defining the incident velocity distribution of the gas atom (see SI). T_{in} and T_{out} are defined by Eq. (4.14).

Gas	Surface	T_g (K)	α_x	α_y	α_z	α_e	T_{in} (K)	T_{out} (K)
He	smooth	100	0.007	0.007	0.144	0.038	99.844	104.698
		200	0.010	0.010	0.073	0.023	199.693	201.602
		300	0.011	0.012	0.049	0.018	299.536	299.712
		400	0.016	0.016	0.043	0.020	399.390	397.231
	rough	100	0.380	0.341	0.354	0.044	99.844	105.727
		200	0.347	0.320	0.309	0.025	199.696	202.202
		300	0.341	0.311	0.294	0.025	299.536	299.430
		400	0.336	0.286	0.273	0.025	399.381	396.747
Ar	smooth	100	0.524	0.536	0.940	0.763	99.845	234.667
		200	0.478	0.476	0.864	0.676	199.689	261.217
		300	0.427	0.423	0.801	0.597	299.531	298.060
		400	0.385	0.391	0.748	0.531	399.383	341.999
	rough	100	0.792	0.785	0.951	0.800	99.845	243.593
		200	0.734	0.726	0.888	0.721	199.691	265.816
		300	0.691	0.683	0.829	0.632	299.535	299.214
		400	0.661	0.648	0.784	0.560	399.388	339.517

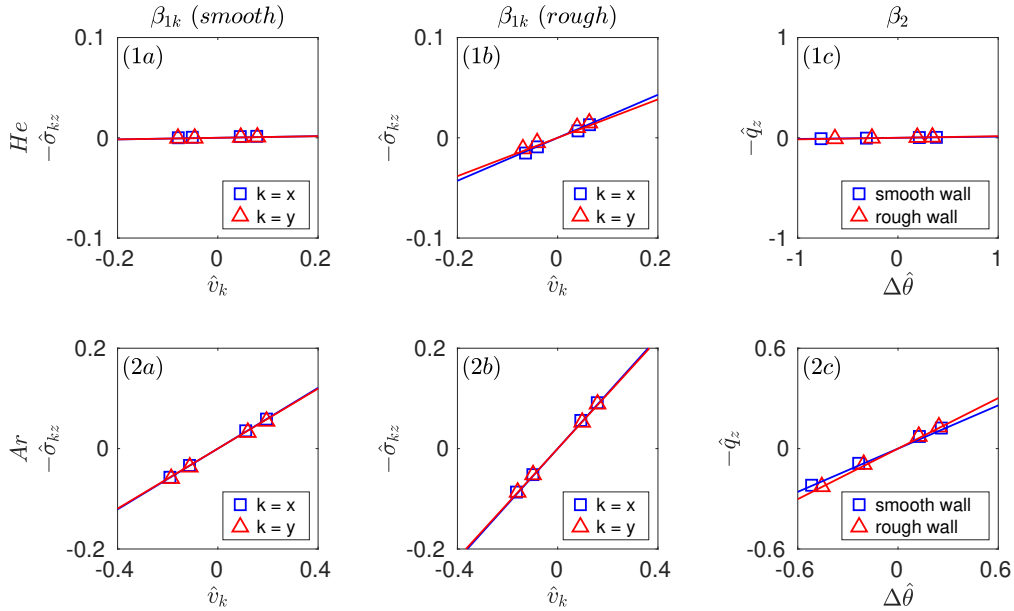


Figure 4.4: Using the NP model, the values of the slip velocity \hat{v}_k , tangential stress $\hat{\sigma}_{kz}$, temperature jump $\Delta\hat{\theta}$ and normal heat flux \hat{q}_z have been determined. All the values have been normalized by the method described in Ref. [84]. The slopes of the lines provide the values of β coefficients. The $T_g = T_w = 300$ K gas velocities have been used to generate the NP kernel for He and Ar.

Table 4.3: Values of β coefficients determined by the direct employment of MD velocities at 100 K, 200 K, and 300 K [Eq. (4.7)], by the use of MAC and EAC parameters [Eqs. (4.6), and (4.11)], and by the NP model. The values of β_{1x} , β_{1y} , and β_2 (MAC) are computed at $T_g = T_w = 300$ K.

Surface	Method	He			Ar		
		β_{1x}	β_{1y}	β_2	β_{1x}	β_{1y}	β_2
smooth	Atomic	0.007	0.007	0.012	0.276	0.281	0.445
	M/EAC	0.006	0.006	0.009	0.272	0.269	0.425
	NP	0.008	0.008	0.012	0.303	0.299	0.431
rough	Atomic	0.227	0.242	0.015	0.568	0.571	0.486
	M/EAC	0.206	0.185	0.013	0.528	0.520	0.462
	NP	0.215	0.191	0.016	0.555	0.546	0.503

He are smaller than 0.02. The roughness increases the $\alpha_{x,y}$ values for both He and Ar gases, indicating that the collisions are more diffusive than with a smooth surface. However, the collisions of He are always more specular than those of Ar in any situation, as confirmed by the results presented in Figure 4.1. Due to the smaller size of the He atoms, the effect of the surface roughness is more important for He than for Ar. The rough surface has no reason to be isotropic, and the anisotropy appears in the fact that α_x is always larger than α_y for both He and Ar atomic species and all T_g values for the rough surface. The coefficient α_z remains almost constant for Ar on both surface types but it increases with roughness for He. It must be noticed that the c_z collision clouds of Figure 4.1 are more diffusive than the clouds of the other velocity components for both Ar and He. This behavior has also been found for CO₂ and CH₄ colliding on graphene [84]. It can be seen as an indication that the normal component of the velocity is the main responsible component of the thermal exchange with the surface, i.e. of the displacements of the solid atoms due to the collision.

The gas temperatures after collision are dependent on the gas atom nature. The difference with respect to the target temperature before collision is much more marked for Ar than for He, in agreement with the most diffusive nature of the Ar collisions with gold. However, for both atom types, the gas atoms gain thermal energy when they are colder than the surface and lose a part of it after collision with a colder surface, in agreement with α_e variations. The

coefficient α_e decreases with T_g for both atomic species and it is larger for Ar than for He, demonstrating once again that the He collisions are almost specular while the Ar collisions are almost diffusive. The roughness of the surface causes an increase of the α_e value for Ar, but it has almost no effect in the α_e value for He.

From Figure 4.1, it can be observed that although the reflective velocities are closer to the diffuse case on the rough surface, the value of reflective energy still corresponds to the specular case. The results of Table 4.2 also show that the temperature change in the He flow is very small after the collision (below 6%). These evidence indicate that the diffusivity degree in velocity components is mainly due to the conversion of kinetic energy during the collision. As apparent from the pairwise potentials, the Ar atom interacts more strongly with the Au surface than the He atom. This conclusion can also be observed from the kinetic energy diffusivity in Figure 4.1 and the temperature change in Table 4.2.

The β coefficients obtained by the NP model are the slope coefficients, as presented in Figure 4.4. The NP kernel was originally developed for CH₄ and CO₂ on graphite surface, for which the adsorption effect is more remarkable. For the He/Ar-Au systems, the adsorption effect is weaker. Therefore, if we calculate the reflective energy using the reflective velocities produced by the NP model, its diffusivity degree will be overestimated. The alternative way is to directly generate the reflective energy, i.e using $P(c^2|c'^2)$, in order to evaluate the term $\langle c'^2/2 - c^2/2 \rangle$ in Eq. (4.11) for the normal heat flux. We took the β value determined by the atomic wall as our benchmark and, comparing the mean error of NP model with the mean error of MAC (3.3% vs. 11.9%), we found that the performance of the NP model is better. From the β values presented in Table 4.3, we can conclude that the roughness of the Au surface can significantly affect the friction coefficient of He and Ar noble gases at room temperature. However, the effect of surface roughness on thermal resistance is very limited.

Especially due to the reproduction of the roughness in the surface, our results can be compared with just a few data from the literature. Experimentally, it is as difficult to produce a perfectly smooth surface as to control its roughness. Karniadakis *et al.* [72] have reported a thermal momentum accommodation coefficient value of 0.073 for the He-Al pair. This value is consistent with the experimentally-determined EAC value 0.017 by Thomas and Schofield [136] at 320.15 K, confirming the very weak nature of the interaction of He with metal surfaces and the quality of the present He-Au pairwise potential.

Hadj Nacer *et al.* [55] measured slip coefficients from He and Ar gas flows in a silicon micro-channel covered with gold. They obtained β_1 values of 1.305 ± 0.018 and 1.342 ± 0.019 for He and Ar, respectively. These values are much higher than those presented in Table 4.3 for the rough surface, indicating that the present surface is not rough enough. In the experimental work of Hadj Nacer *et al.*[55], the roughness of the gold coating, realized by vapor deposition, was evaluated at 0.87 nm. This value corresponds roughly to 6 times the gold atom bulk radius. The addition of only one more gold atom height on the smooth surface, as in the present rough surface, is certainly not sufficient to model this coating.

Trott *et al.* [145] have measured thermal accommodation coefficients from gas heat flux between plates at different temperatures. For the steel plates made coated with gold cleaned by plasma treatment, they obtained $EAC = 0.85$ for Ar and 0.31 for He, respectively at 296 K. These results are consistent with the α_e values presented in Table 4.2 if we consider once again that the experimental surface is rougher than the simulated one. It can also be noticed, the final experimental roughness also depends on the steel surface quality before coating.

4.4 Conclusions

In summary, the extremely weak He-Au pairwise interaction potential has been derived from *ab initio* determinations for the first time. For this purpose, dispersionless density functional periodic calculations were combined with effective pairwise functional parameters for the dis-

persion. These parameters were obtained from time-dependent DFT response theory using localized Hartree-Fock orbitals on He-Au_n clusters. The global interaction He-Au(111) potential reproduces accurately the best estimate of the well depth value (about 8 meV) while the “standard” vdW-DFT method greatly overestimates the attractive interaction. Next, the *ab initio* pairwise potential was used in Molecular Dynamics simulations of collisions of a He atom with a smooth Au(111) surface as well as a rough Au surface. The gas velocities recorded before and after the collision were employed to determine accommodation coefficients. These coefficients are the key ingredients to model interface phenomena such as slippage or temperature jump, having further applications such as, for example, in macroscopic gas flow simulations based on Navier-Stokes equations.

Different methodologies were applied and compared for the derivation of interface quantities: the use of atomistic velocities, of accommodation coefficients, and of an NP kernel constructed from a reduced number of simulations. The results obtained with the three methods compare very well, with the NP kernel approach having clearly a better performance than the treatment based on using accommodation coefficients. Our results allow to conclude that He gas flow has almost no friction effect on a smooth surface, but the friction is more pronounced on a rough one. However, in both surface cases, the temperature transfer is almost inexistent. The collisions of He on gold are then almost elastic.

For comparison purposes, Molecular Dynamics simulations using the same computational setup were carried out for Ar using the *ab initio*-based pairwise potential reported in our previous work [54]. As expected from the force field strength difference, the collisions of Ar with the gold surfaces are more diffusive than for He, and the friction effect and temperature jump are more pronounced for Ar flows on the rough gold surface. These results confirm the quality of the *ab initio*-based He-Au and Ar-Au pairwise potentials. It can also be concluded that improved simulations must consider surfaces with a much more pronounced roughness than that modeled

in this work.

Appendix: Support information

Figures of the clusters and of the slabs used for the determination of the He-Au pairwise potential, electronic structure computational details, fitting analyses, Molecular Dynamics computational details.

This Supporting Material contains computational details concerning the *ab initio* determination of the interaction between atomic helium and a gold surface or a gold cluster, and the Molecular Dynamics simulations used for the determination of the boundary quantities.

Helium/Au(111) Interaction Energies: Electronic Structure Calculations

Details of Periodic Calculations

The CRYSTAL14 code[42, 41] was used for all the periodic calculations applying the periodic dlDF implementation.[36] The augmented polarized correlation-consistent triple- ζ basis of Woon and Dunning, Jr.[159] (aug-cc-pVTZ) was adopted for atomic helium while, for Au atoms, we used energy-consistent relativistic 19-valence-electron pseudopotentials in combination with the valence basis set reported in Ref. [40]. The Au(111) surface was modeled considering a $(\sqrt{3} \times \sqrt{3})R30^\circ$ supercell (see Figure 4.5). The slab model of the Au(111) surface had a thickness of 3 layers. This supercell was large enough to parametrize the dispersionless function (see above), which is short-range in nature. The lattice constant was fixed to the value of 4.0786 Å.

The fitting of the *ab initio* data obtained from the above calculations by equation (3) was performed with a standard deviation of 0.07934 meV for the *fcc* site. The resulting parameters

Table 4.4: dlDF parameters from periodic calculations with He in *fcc* position and from Ref.[54].

	A (eV)	B (eV.Å ⁻¹)	C (eV.Å)	α (Å ⁻¹)	γ (Å ⁻²)
He-Au	-2.9755	0.47351	4.8980	-2.576	0.8204
He-Ar	16.230×10^3	-	-	3.356	-

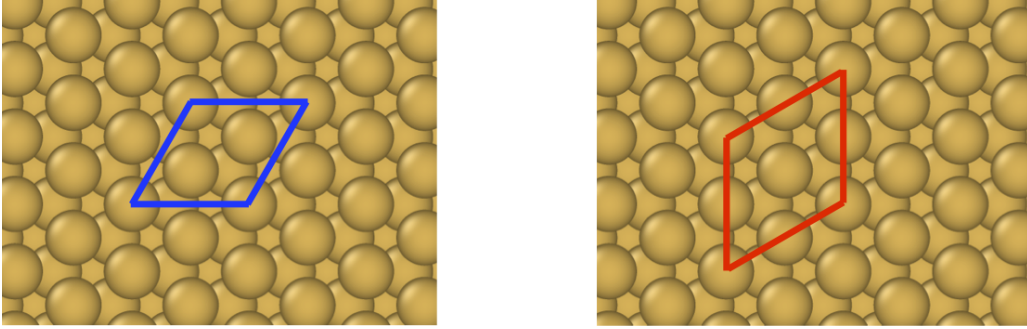


Figure 4.5: Figure illustrating the supercell model of the gold surface: the $\sqrt{3} \times \sqrt{3}$ supercell is surrounded by blue segments (left) and the 2×2 supercell is surrounded by red segments (right).

are given in Table 4.4. For comparison and need in the Molecular Dynamics calculations, Ar-Au parameters are also given.

The vdW-DF2 calculations have been performed using the Vienna *Ab initio* Simulation Package,[75, 74] based on the projector augmented-wave method.[18, 74] Plane wave basis sets with a kinetic energy cutoff of 479 eV and PAW-PBE pseudopotentials were employed. The total energy calculations used a Γ -centered $8 \times 8 \times 1$ k -point mesh, and the Methfessel-Paxton smearing method at the first order with $\sigma = 0.01$ eV. The Au(111) surface was modeled using a repeated slab of 3 atomic layers. A 2×2 supercell (see Figure 4.5) and vacuum spacing of 25 Å was used to minimize the interactions between the periodic images along the three directions of the slab. Structural relaxation effects of the gold atom positions were not included.

Details of Cluster Calculations: Dispersion He/Au_n ($n = 4, 10$) Interaction

Similarly to the dispersion-corrected second-order Möller-Plesset perturbation theory (MP2C) method,[93] the dispersion energies were evaluated via time-dependent density functional response theory (TD-DFT), using the localized Hartree-Fock method.[38] The necessary Kohn-Sham orbitals and orbital energies were calculated using the localized Hartree-Fock method by Della Sala and Görling.[38] In all surface cluster calculations, correlation consistent basis sets were employed using the MOLPRO package [156]. The cluster geometries can be found in Figures 4.6 and 4.7. The augmented polarized correlation-consistent triple- ζ basis of Woon and Dunning, Jr.[159] (aug-cc-pVTZ) was adopted for the cluster He atoms, while the aug-cc-pVTZ-PP basis set was employed for gold atoms,[99] including a small-core (19-valence-electron) relativistic pseudopotential [47].

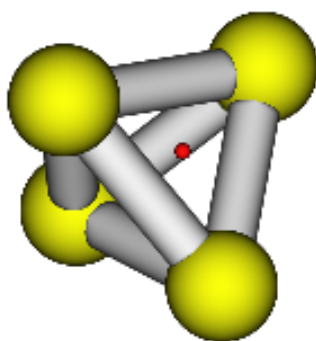


Figure 4.6: Au₄ cluster. The Au-Au distance is fixed to 2.8836 Å. The red point indicates the vertical position of He.

A comparison of the *ab initio* dispersion energies to the energies calculated from the D_{as}^* function (equation (4)) are also presented in Figure 4.8. The parameters of this function were calculated by fitting of *ab initio* energies for both Au₄ and Au₁₀ clusters. As examples of the good accuracy of the fits, the relative root-mean-squares were of 1.32 % for He-Au₁₀ and of 7.25 % for He-Au₄ for He in the *fcc* position. For the Molecular Dynamics calculations, the parameters of Table 4.5, derived from He-Au₁₀ with He in the *fcc* position, were used.

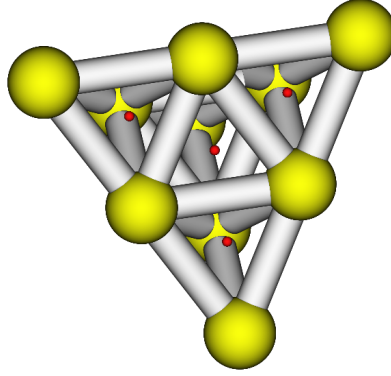


Figure 4.7: Au₁₀ cluster. The Au-Au distance is fixed to 2.8836 Å. The central red point indicates the *fcc* vertical position of He.

Table 4.5: D_{as}^* parameters from He-Au₁₀ with He in the *fcc* position and local Hartree-Fock calculations, and from Ref. [54].

	C_6 (J.nm ⁶ .mol ⁻¹)	C_8 (J.nm ⁸ .mol ⁻¹)	β (bohr ⁻¹)
He	0.64419	0.095935	0.5387
Au	1.3062	0.16699	1.905
	$C_6 = \sqrt{C_6^{RG}C_6^{Au}}$ (eV.Å ⁶)	$C_8 = \sqrt{C_8^{RG}C_8^{Au}}$ (eV.Å ⁸)	$\beta = \sqrt{\beta_{RG}\beta_{Au}}$ (Å ⁻¹)
He-Au	9.5073	131.18	3.618
Ar-Au	76.785	1066.9	3.051

4.4.1 Momentum and Energy Accommodation Coefficients, Slip-page and Temperature Jump: Molecular Dynamics Calculations

The different MD calculations were performed using the LAMMPS package [102, 103]. The He-Au pair potential derived above was tested. For the Ar-Au pair, the dIDF+ D_{as} pairwise potential determined in Ref.[54] has been used. The parameters can be found in Tables 4.5 and 4.4. The z direction is orthogonal to the solid surface. The (111) surface is composed of 800 gold atoms with periodic boundary conditions along the directions of the x and y axes. The slab is composed of 5 layers. The innermost layer is kept fixed while the second and following layers are maintained at constant temperature using a Nosé-Hoover thermostat (NVT ensemble). The

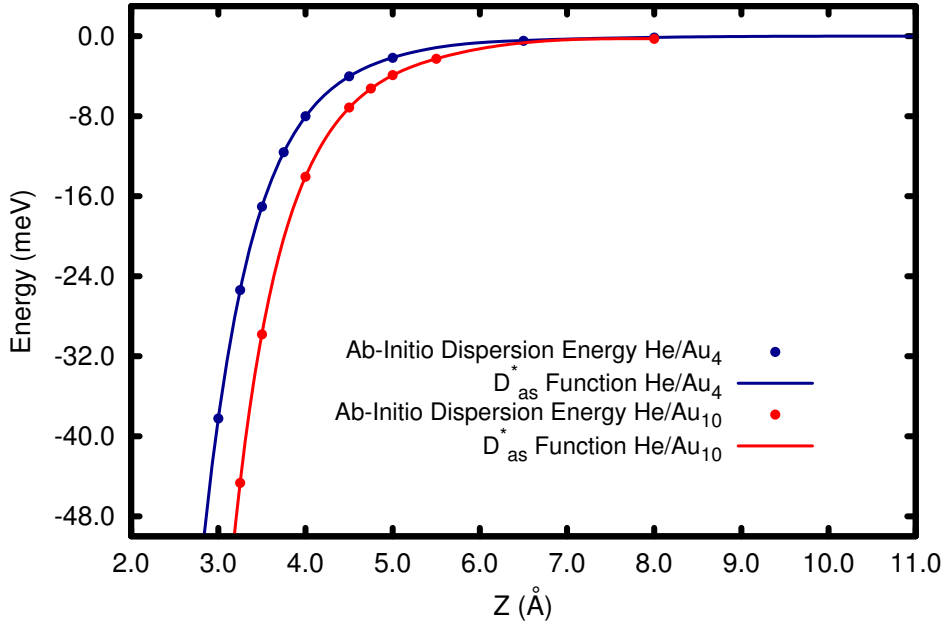


Figure 4.8: Radial scan of *ab initio* dispersion energies as a function of the distance (Z , in Å) between a He atom and the surface of Au₄ and Au₁₀ clusters, with He in the *fcc* position in the Au₁₀ case.

embedded-atom-method potential (EAM) of Sheng *et al.* [119] has been chosen to describe the interaction between the gold atoms due to its capability to reproduce the experimental values of surfaces and bulk solid gold. The cut-off distance was set at 12 Å for both Au-He and Au-Ar interactions for which all the gold atoms have been considered. Before simulating the collision process, the thermal equilibrium of the gold solid wall at 300 K was guaranteed after 10^7 time steps of 0.001 ps.

The rare gas atoms are projected at $R > R_{coll} = 8$ Å above the surface. One collision is assumed to be finished once the atoms pass back the $R = R_{coll}$ limit with positive velocity component along z -direction. The atom is reinserted at the same position but with an initial velocity that is drawn from equilibrium distribution: c'_x and c'_y follow the normal distribution $\mathcal{N}(v, \sigma^2)$ with $v = 0$ mean and standard deviation $\sigma = \sqrt{k_B T_g / m_g}$, and $-c'_z$ the Rayleigh distribution $\mathcal{R}(\sigma)$ with the same parameter σ . In order to compute β_1 coefficients, non-zero mean velocities

$v_x = v_y = 0.5, 0.25,$ and -0.5 \AA/ps are imposed.

For each test, 100000 collisions were performed, using a time step of 0.0001 ps for He and 0.001 ps for Ar. Hence, the ratio between the time steps used for He and Ar atoms has a similar value to that of the corresponding atomic masses.

The rough gold surface was constructed from an initial smooth surface composed of 5 layers of 160 atoms each. Then 100 atoms are projected randomly in space above the smooth surface. Not all of them finished being attached to the surface. Finally, the resulting slab is thermostated during 10^7 time steps of 0.001 ps. The lower layer atoms are fixed and the temperature of the others is controlled via a Nosé-Hoover thermostat as in the smooth surface case.

Chapter 5

Prediction of thermal conductance and friction coefficients at solid-gas interface from statistical learning of collisions

Abstract

In this paper, we present the construction of statistical models of gas-wall collision based on data issued from Molecular Dynamics (MD) simulations. The Gaussian Mixture (GM) model, an unsupervised learning technique, is chosen for this purpose. The model shares some similarities with the well-known Cercignani-Lampis model in kinetic theory but it is more robust due to the unlimited number of Gaussian functions used and the ability to deal with correlated data of high dimensions. Applications to real wall-gas systems confirm the good performance of the model. The trained GM model predicts physical and statistical properties including accommodation, friction and thermal conductance coefficients in excellent agreement with the MD model.

5.1 Introduction

Velocity slip and temperature jump are important interface phenomena which are frequently encountered in micro-nanofluidic systems [72]. The common way to model the imperfect boundary conditions is to use the following phenomenological relations

$$\beta_1 v_k = -\sigma_{kz}, \quad \beta_2 (T - T_w) = -q_z, \quad k = x, y, \quad (5.1)$$

Here the wall is assumed to be stationary at temperature T_w and normal to direction z . The slip velocity v_k is proportional to the (minus) shear stress σ_{kz} and the temperature jump $T - T_w$ is proportional to the heat flux q_z . The constants, β_1 and β_2 , are respectively the Navier isotropic friction and Kapitza thermal conductance coefficients. For gas flow problems, it is well-known that the interface phenomena become significant when the mean free path λ is comparable to the channel height H , starting from $\lambda/H \geq 0.01$. The origin of the Knudsen layer effect comes from two sources: the finite actual velocity/temperature jump at the boundary and the deviation from the bulk solution within the distance λ from the wall. In this paper, we do not consider the variation of the velocity/temperature in the Knudsen layer and assume that the linear relations Eq. (5.1) are valid at the solid boundary [138]. Since both the bulk and interfacial transport properties of gases are governed by collisions at the atomic scale [29], they are expected to be proportional to the collision rate. It is thus natural to non-dimensionalize the boundary coefficients β_1 and β_2 as follows

$$\bar{\beta}_1 = \frac{\beta_1}{n} \sqrt{\frac{\pi}{2k_B T m}}, \quad \bar{\beta}_2 = \frac{\beta_2}{n} \sqrt{\frac{m\pi}{8k_B^3 T}}, \quad k = x, y, \quad (5.2)$$

In Eq. (5.2), n is the gas density at the wall, m the atomic mass of the monatomic gas and k_B the Boltzmann constant. The other reason to non-dimensionalize the interfacial coefficients is that $\bar{\beta}_1$ and $\bar{\beta}_2$ are connected to tangential momentum accommodation coefficient α_1 and

energy accommodation coefficients α_2 [72]

$$\bar{\beta}_1 = \frac{\alpha_1}{2 - \alpha_1}, \quad \bar{\beta}_2 = \frac{\alpha_2}{2 - \alpha_2} \quad (5.3)$$

The origin of the accommodation coefficients comes from the collision models of gas atoms with the solid boundary [92, 140, 27]. These constants appear in the linear relation between the pre-collision and post-collision momenta and energy of gas atoms with respect to the wall. However, MD simulations showed that the linearity postulate is not always valid. Errors from the linear regression procedure to obtain α_1 and especially α_2 are observed [101, 84]. It is suggested that the more effective way to model slip and jump phenomena is to directly use coefficients $\bar{\beta}_1$ and $\bar{\beta}_2$ to quantify them from realistic collision data whenever possible. On the other hand, the formulation based on coefficients $\bar{\beta}_1, \bar{\beta}_2$ can avoid the errors due to the use of (5.3) and the intermediate accommodation coefficients. It is noted that while Eqs. (5.3) are widely used, they are derived under restrictive conditions, e.g the Chapman-Enskog distribution [29], an approximate solution of the Boltzmann equation, and the Maxwell or Cercignani-Lampis wall model [126, 53]. As a result, if we want to extend or investigate the validity (5.3) in general situations, more accurate methods (see e.g Refs. [117, 118]) should be adopted.

In the framework of probabilistic modeling, there are numerous ways of reconstructing the (collision) behavior of the system based on the available (collision) data, which are realizations via Molecular Dynamics simulations. One of the method, proposed in our previous work is to use the nonparametric (NP) techniques to estimate the probability density functions (PDF) and generate new collision data [84]. To avoid the sparsity of the data in high dimension, the reflection process was assumed to be independent for each velocity components (c'_x, c_x) , (c'_y, c_y) and (c'_z, c_z) and the model can be constructed with a good accuracy [61]. Although such modeling is relatively general, the uncorrelation hypothesis can be strong and oversimplify the true behavior. This motivates us to investigate the use of unsupervised learning techniques and their performance with high dimension data. Specifically, the present work considers the Gaus-

sian Mixture (GM) model, which is a popular technique and has proved to be successful in many data science applications. The GM are probabilistic models using linear combination of multiple multidimensional gaussians to estimate the probability density of data. Like all collision models (or scattering kernels) in kinetic theory, the construction of GM are based on parameters which can be determined from collision data for each gas-solid couple under consideration. While the existing collision models are limited by a finite number of parameters (e.g accommodation coefficients), the GM models are not. On the other hand, the GM models require a special algorithm, i.e Expectation Maximization (EM) algorithm to tune the parameters.

The paper is organized as follows. In Sect. 5.2, we present a literature review of statistical models of collisions, the general principles to construct them from MD data and their properties. GM model is then introduced with the EM algorithm to tune the model parameters. Criteria based on both statistical and physical parameters including accommodation coefficients, interfacial coefficients, reflection angles, and Kullback-Leibler divergence will be used to evaluate the performance of the model. Applications to real material systems (Ar and He gases vs Au surface) are presented in Section III, confirming the superiority of the GM model when compared with nonparametric and parametric models of literature. Finally, some remarks and conclusions are given.

5.2 Description of computation methods

5.2.1 Overview of statistical models of collision and their properties

The collision model, also called scattering kernel in kinetic theory, serves as boundary conditions for Boltzmann equations and aims at describing how gas atoms are reflected after collision with the wall at temperature T_w . It is defined by the conditional probability distribution, $P(\text{output} = \mathbf{c} | \text{input} = \mathbf{c}', \text{temperature} = T_w)$ or denoted shortly $P(\mathbf{c} | \mathbf{c}')$ of velocity \mathbf{c} for a given incoming velocity \mathbf{c}' . In addition to the usual PDF properties like non-negativeness and

normalization, $P(\mathbf{c}|\mathbf{c}')$ is also expected to satisfy the physical reciprocity conditions [25, 22, 128]:

$$P_{eq}(\mathbf{c}')P(\mathbf{c}|\mathbf{c}') = P_{eq}(-\mathbf{c})P(-\mathbf{c}'|-\mathbf{c}), \quad \mathbf{c} \in \mathbb{R}^2 \times \mathbb{R}^+, \quad \mathbf{c}' \in \mathbb{R}^2 \times \mathbb{R}^- \quad (5.4)$$

where, $P_{eq}(\mathbf{c}')$ is the distribution associated to the equilibrium gas at the same temperature as the wall $T = T_w$ and motionless with respect to the wall (zero mean velocity)

$$P_{eq}(\mathbf{c}') = \sqrt{\frac{2\pi}{\theta}} |c'_z| M_B(\mathbf{c}'), \quad M_B(\mathbf{c}') = \frac{e^{-\mathbf{c}'^2/2\theta}}{(2\pi\theta)^{3/2}}, \quad \theta = k_B T/m \quad (5.5)$$

This condition implies that the incidence-reflection is microscopically reversible when the wall is in equilibrium state.

It can be shown that all popular collision models in literature can be classified as parametric models, in most cases, taking from one to three accommodation coefficients as parameters. For example, in the Maxwell model [92] where the gas atom can be reflected either specularly or diffusively with percentage $1 - \alpha$ and α , only one accommodation coefficient is used. In the anisotropic Cercignani-Lampis (ACL) model [140, 27], three different accommodation coefficients associated to tangential momentums along x, y directions and normal kinetic energy along z direction are used. While the Maxwell model exhibits discontinuities in the probability space due to the portion of the mirror reflections (Dirac distribution), the smooth PDF from ACL model agrees better with MD simulations. However, like all parametric models, they are subject to common limitations: the requirement of the existence of a limited number of constant accommodation coefficients and the lack of flexibility in the case of complex collision data. Since the flow solution depends both on the gas-gas and gas-wall collision, those limitations may have consequences on the determination of boundary conditions' coefficients β_1 and β_2 in Navier-Stokes-Fourier equations as mentioned earlier and can cause errors in other simulation methods, e.g direct simulation Monte Carlo (DSMC) [16], MD [106, 6], moment equations [129, 53], etc. based on the collision model. It suggests that to achieve better accuracy, we need to rely on the whole data range and to not be limited by the number of model parameters.

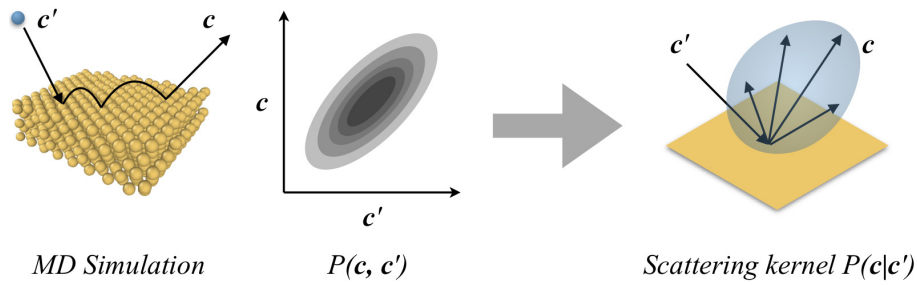


Figure 5.1: Procedure of reconstructing the scattering kernel from MD simulations of collisions.

The procedure of reconstructing the scattering kernel from MD simulations of collisions is shown in Fig. 5.1. The gas atoms are inserted with velocity \mathbf{c}' at a plane beyond the cut-off distance and interact with the well thermostated solid atoms before escaping by crossing the same plane with velocity \mathbf{c} . Each couple of input and output velocities $(\mathbf{c}, \mathbf{c}')$ recorded is thus a realization of the joint PDF $P(\mathbf{c}, \mathbf{c}')$. In principle, if we can estimate accurately $P(\mathbf{c}, \mathbf{c}')$, we can derive accurately the scattering kernel via the equation

$$P(\mathbf{c}|\mathbf{c}') = \frac{P(\mathbf{c}, \mathbf{c}')}{P(\mathbf{c}')}, \quad (5.6)$$

where $P(\mathbf{c}')$ is the distribution of input variable \mathbf{c}' . While $P(\mathbf{c}|\mathbf{c}')$ is a unique function of \mathbf{c} and \mathbf{c}' , the joint PDF $P(\mathbf{c}, \mathbf{c}')$ depends on the input distribution $P(\mathbf{c}')$ via (5.6). In the special case where the input distribution is the equilibrium distribution, $P(\mathbf{c}') = P_{eq}(\mathbf{c}')$, the joint PDF becomes the equilibrium joint PDF $P(\mathbf{c}, \mathbf{c}') = P_{eq}(\mathbf{c}, \mathbf{c}')$. The reciprocity condition (5.4) is equivalent to the symmetry condition of $P_{eq}(\mathbf{c}, \mathbf{c}')$ in hyperspace

$$P_{eq}(\mathbf{c}, \mathbf{c}') = P_{eq}(-\mathbf{c}', -\mathbf{c}) \quad (5.7)$$

As a result, to model the scattering kernel via $P_{eq}(\mathbf{c}, \mathbf{c}')$ and the associated collision data, it is necessary that the above constraints are satisfied.

We remark that in many parametric scattering kernels [33, 140, 27], the reflection process

occurs independently in x , y , and z directions. Under this assumption, both $P(\mathbf{c}|\mathbf{c}')$ and $P_{eq}(\mathbf{c}, \mathbf{c}')$ can be decomposed as:

$$P(\mathbf{c}|\mathbf{c}') = \prod_{k=1}^3 P(c_k|c'_k), \quad P_{eq}(\mathbf{c}, \mathbf{c}') = \prod_{k=1}^3 P_{eq}(c_k, c'_k), \quad k = x, y, z \quad (5.8)$$

A typical example is the well-known Cercignani-Lampis kernel and its associated joint PDF at equilibrium $P_{eq}^{CL}(\mathbf{c}, \mathbf{c}')$

$$\begin{aligned} P^{CL}(\mathbf{c}|\mathbf{c}') &= \frac{e^{-\frac{[c_x - (1-\alpha_t)c'_x]^2}{2\alpha_t(2-\alpha_t)\theta_w}}}{\sqrt{2\pi\theta_w\alpha_t(2-\alpha_t)}} \frac{e^{-\frac{[c_y - (1-\alpha_t)c'_y]^2}{2\alpha_t(2-\alpha_t)\theta_w}}}{\sqrt{2\pi\theta_w\alpha_t(2-\alpha_t)}} \frac{c_z e^{-\frac{c_z^2 + (1-\alpha_e)c_z'^2}{2\alpha_e\theta_w}}}{\alpha_e\theta_w} \times \\ &I_0\left(\frac{\sqrt{1-\alpha_e}c_z c'_z}{\alpha_e\theta_w}\right) \\ P_{eq}^{CL}(\mathbf{c}, \mathbf{c}') &= \frac{e^{-\frac{(c_x^2 - 2(1-\alpha_t)c_x c'_x + c_x'^2)}{2\alpha_t(2-\alpha_t)\theta_w}}}{2\pi\theta_w\sqrt{\alpha_t(2-\alpha_t)}} \frac{e^{-\frac{(c_y^2 - 2(1-\alpha_t)c_y c'_y + c_y'^2)}{2\alpha_t(2-\alpha_t)\theta_w}}}{2\pi\theta_w\sqrt{\alpha_t(2-\alpha_t)}} \frac{|c_z c'_z| e^{-\frac{(c_z^2 + c_z'^2)}{2\alpha_e\theta_w}}}{\alpha_e\theta_w^2} \times \\ &I_0\left(\frac{\sqrt{1-\alpha_e}c_z c'_z}{\alpha_e\theta_w}\right), \end{aligned} \quad (5.9)$$

have this property. In particular, they are based on two parameters α_t, α_e , combination of multivariate Gaussian functions, and I_0 as modified Bessel function of first kind and zeroth order. Additionally, the joint PDF $P_{eq}^{CL}(\mathbf{c}, \mathbf{c}')$ also satisfies the symmetry condition (5.7).

It is interesting to note that a general class of 1D nonparametric collision model can also be constructed based on Eq. (5.8) and collision data. The uncorrelation hypothesis reduces the model from 3D (or 6D in data space \mathbf{c}', \mathbf{c}) to 1D (or 2D in each of 3 data spaces $c'_x, c_x, c'_y, c_y, c'_z, c_z$), which greatly simplifies the kernel construction. Using kernel density estimation (KDE) techniques, the constructed collision model has good performances when determining velocity slip and temperature jump coefficients like for the CH₄-graphite or Ar-Au systems [84, 83]. However, for nearly perfect elastic-reflection system like the He-Au system [83], the independent assumption of Eq. (5.8) can overestimate the reflective energy and can cause errors in the thermal conductance coefficient. In what follows, we shall explore the GM model, a popular and general purpose machine learning technique, which is not subject to above limitations. The

model shares some similarities with the CL kernel which is among the best parametric models, by the presence of smooth multivariate Gaussian functions but it is much more powerful and flexible by means of superposition and unlimited number of the parameters used. Furthermore, the algorithms to identify those parameters from data are well developed in literature and in commercial software. Thus the efforts to construct an accurate collision model will be significantly minimized.

5.2.2 Preprocessing of training data and Gaussian mixture model (GM)

As mentioned earlier, the data are collected from MD simulations of independent gas-wall collisions at a given temperature T_w . The pre-collision velocity is drawn from equilibrium distribution, i.e $P(\mathbf{c}') = P_{eq}(\mathbf{c}')$ and $P(\mathbf{c}, \mathbf{c}') = P_{eq}(\mathbf{c}, \mathbf{c}')$ and we can fit the GM model with data, the realizations of $P_{eq}(\mathbf{c}, \mathbf{c}')$. To achieve the best performance of the method, we propose to precondition the data in the following way

- Symmetrization of the data: For each realization $(\mathbf{c}, \mathbf{c}')$, a virtual copy $(-\mathbf{c}', -\mathbf{c})$ is also added to the existing data. This step will double the size of the training data and ensure the symmetry of $P_{eq}(\mathbf{c}, \mathbf{c}')$ as shown in (5.7).
- Transformation of the random variables \mathbf{c} and \mathbf{c}' : This is because of the support constraints $c_z > 0$ and $c'_z < 0$ are not compatible with gaussian functions. Specifically, while c_x, c_y, c'_x, c'_y have Gaussian distributions, c_z, c'_z have Rayleighian distributions. In this case, we propose to adopt a transformation \mathcal{T} that changes the distributions of c_z, c'_z to the same type as c_x, c_y, c'_x, c'_y .

For example

$$\mathcal{T}(U) = \sqrt{2\theta} \operatorname{erf}^{-1} \left[1 - 2 \exp \left(-\frac{U^2}{2\theta} \right) \right], \quad \mathcal{T}^{-1}(U) = \sqrt{-2\theta \ln \left[\frac{1}{2} - \frac{1}{2} \operatorname{erf} \left(\frac{U}{\sqrt{2\theta}} \right) \right]},$$

$$\mathbf{x}_R = \begin{bmatrix} c_x \\ c_y \\ \mathcal{T}(c_z) \end{bmatrix}, \quad \mathbf{x}_I = \begin{bmatrix} c'_x \\ c'_y \\ \mathcal{T}(c'_z) \end{bmatrix}, \quad \mathbf{c} = \begin{bmatrix} x_{R1} \\ x_{R2} \\ \mathcal{T}^{-1}(x_{R3}) \end{bmatrix}, \quad \mathbf{c}' = \begin{bmatrix} x_{I1} \\ x_{I2} \\ -\mathcal{T}^{-1}(x_{I3}) \end{bmatrix} \quad (5.10)$$

where \mathbf{x}_R and \mathbf{x}_I are two vector which are used to record the reflective value or incident value respectively. We note that to map the Gaussian to the Rayleigh distribution, we compute the CDFs of Gaussian distribution and of Rayleigh distribution

$$F^G(\mathcal{T}) = \frac{1}{2} \left[1 + \operatorname{erf} \left(\frac{\mathcal{T}}{\sqrt{2\theta}} \right) \right], \quad F^R(U) = 1 - \exp[-U^2/(2\theta)]. \quad (5.11)$$

and use the relation $F^G(\mathcal{T}) = F^R(U)$ to recover the transformation (5.10) concerning c_z, c'_z .

The GM model is a probabilistic model that assumes all the data points are generated from a mixture of Gaussian distributions [131]. More importantly, it is general enough to estimate complex PDF function. Specifically, the GM estimator of $P(\mathbf{x}_R, \mathbf{x}_I)$ can be written as a superposition of M Gaussian functions with weights $\varphi_1, \varphi_2, \dots, \varphi_M$ as follows

$$P(\mathbf{x}_R, \mathbf{x}_I) \simeq P^{GM}(\mathbf{x}_R, \mathbf{x}_I) = \sum_{m=1}^M \varphi_m p_m(\mathbf{x}_R, \mathbf{x}_I), \quad p_m(\mathbf{x}_R, \mathbf{x}_I) = \mathcal{N}(\mathbf{X} | \boldsymbol{\mu}_m, \boldsymbol{\Sigma}_m) \quad (5.12)$$

Each Gaussian $p_m(\mathbf{x}_R, \mathbf{x}_I)$ has its own parameters $\boldsymbol{\mu}_m$ and $\boldsymbol{\Sigma}_m$ as mean vector and covariance matrix

$$\mathcal{N}(\mathbf{X} | \boldsymbol{\mu}_m, \boldsymbol{\Sigma}_m) = \frac{1}{(2\pi)^{d/2}} \frac{1}{|\boldsymbol{\Sigma}_m|^{1/2}} \exp \left[-\frac{1}{2} (\mathbf{X} - \boldsymbol{\mu}_m)^T \boldsymbol{\Sigma}_m^{-1} (\mathbf{X} - \boldsymbol{\mu}_m) \right],$$

$$\mathbf{X} = \begin{bmatrix} \mathbf{x}_R \\ \mathbf{x}_I \end{bmatrix}, \quad \boldsymbol{\mu}_m = \begin{bmatrix} \boldsymbol{\mu}_{mR} \\ \boldsymbol{\mu}_{mI} \end{bmatrix}, \quad \boldsymbol{\Sigma}_m = \begin{bmatrix} \boldsymbol{\Sigma}_{mRR} & \boldsymbol{\Sigma}_{mRI} \\ \boldsymbol{\Sigma}_{mIR} & \boldsymbol{\Sigma}_{mII} \end{bmatrix}, \quad (5.13)$$

where d is the dimension of variables \mathbf{X} . Comparing with the parametric CL model (5.9), the bivariate gaussians also appear in the independent reflection process x and y where the covariance parameters $(1 - \alpha_t)$ are connected to the tangential momentum accommodation coefficients. In the case $M = 1$, the GM model also shares some strong similarities with Nocilla [32] model based on a drifted Maxwellian for reflected velocities. However, the application of the GM model on the preprocessed collision data rather than the original data, as mentioned previously has fully eliminated the negative reflective velocity c_z that the drifted Maxwellian can not. Furthermore, as seen in (5.12,5.13), the GM model is much more general. Constituted of multiple multivariate Gaussian functions, it does not rely on independent reflection hypothesis and contains numerous parameters to fit with data. Those are φ_m , $\boldsymbol{\mu}_m$ and $\boldsymbol{\Sigma}_m$ with $m = 1, 2, \dots, M$ which can be effectively determined using the EM algorithm. (see Appendix 1) [23, 39, 59].

The scattering kernel is the conditional probability function of reflective velocity $P(\mathbf{x}_R|\mathbf{x}_I)$ given incident velocity and this function can also be written as a mixture form[131, 107]:

$$P^{GM}(\mathbf{x}_R|\mathbf{x}_I) = \sum_{m=1}^M \tilde{\varphi}_m(\mathbf{x}_I) p_m(\mathbf{x}_R|\mathbf{x}_I). \quad (5.14)$$

with the following weights

$$\tilde{\varphi}_m(\mathbf{x}_I) = \frac{\varphi_m p_m(\mathbf{x}_I)}{\sum_{m=1}^M \varphi_m p_m(\mathbf{x}_I)}. \quad (5.15)$$

The marginal and the conditional distributions appearing in equations (5.14) and (5.15) are calculated with the formula

$$p_m(\mathbf{x}_I) = \int p_m(\mathbf{x}_R, \mathbf{x}_I) d\mathbf{x}_R = \mathcal{N}(\mathbf{x}_I | \boldsymbol{\mu}_{mI}, \boldsymbol{\Sigma}_{mII}), \quad (5.16)$$

and

$$\begin{aligned}
p_m(\mathbf{x}_R|\mathbf{x}_I) &= \frac{p_m(\mathbf{x}_R, \mathbf{x}_I)}{p_m(\mathbf{x}_I)} = \mathcal{N}(\mathbf{x}_R|\boldsymbol{\mu}_{mR|I}, \boldsymbol{\Sigma}_{mR|I}), \\
\boldsymbol{\mu}_{mR|I} &= \boldsymbol{\mu}_{mR} + \boldsymbol{\Sigma}_{mRI}\boldsymbol{\Sigma}_{mII}^{-1}(\mathbf{x}_I - \boldsymbol{\mu}_{mI}), \\
\boldsymbol{\Sigma}_{mR|I} &= \boldsymbol{\Sigma}_{mRR} - \boldsymbol{\Sigma}_{mRI}\boldsymbol{\Sigma}_{mII}^{-1}\boldsymbol{\Sigma}_{mIR}.
\end{aligned} \tag{5.17}$$

In the next section, we will study the performance of the GM model in comparison with the NP and CL kernels.

5.2.3 Evaluation of model performance and comparisons

Generally, the criteria to judge the quality of a statistical model is the accuracy of fitting with the given data and more importantly, the ability to generate new data predicting quantities consistent with the realistic system. For evaluation, we propose to compute physical based parameters including accommodation coefficients, the reflective deviation angle and boundary conditions coefficients $\bar{\beta}_1$ and $\bar{\beta}_2$ at the interface using the GM model and compare with the same parameters issued from NP, CL kernels and the realistic MD simulations.

As mentioned earlier, accommodation coefficients appear in parametric collision models as constants. However, for realistic atomistic systems, these constants may not be properly defined. In literature, there exist several methods to identify those coefficients but they cannot guarantee the uniqueness of the obtained results (see examples in Appendix 2). Among those works, we consider the method based on correlation analysis [125, 84]. In this case, the accommodation coefficients are defined via the correlation parameters of the data

$$\begin{aligned}
\alpha_1 &= 1 - \frac{\langle c'_x c_x \rangle - \langle c'_x \rangle \langle c_x \rangle}{\langle c'^2_x \rangle - \langle c'_x \rangle^2}, & \alpha_2 &= 1 - \frac{\langle c'^2 c^2 \rangle - \langle c'^2 \rangle \langle c^2 \rangle}{\langle c'^4 \rangle - \langle c'^2 \rangle^2} \\
\alpha_n &= 1 - \frac{\langle |c'_z| c_z \rangle - \langle |c'_z| \rangle \langle c_z \rangle}{\langle c'^2_z \rangle - \langle c'_z \rangle^2}, & \alpha_e &= 1 - \frac{\langle c'^2_z c^2_z \rangle - \langle c'^2_z \rangle \langle c^2_z \rangle}{\langle c'^4_z \rangle - \langle c'^2_z \rangle^2}
\end{aligned} \tag{5.18}$$

While α_1 and α_2 are the tangential momentum accommodation coefficient (TMAC) and the energy accommodation coefficient (EAC), respectively (see equation (5.3)), α_e is the normal momentum accommodation coefficients (NMAC) and α_{e_e} is the normal energy accommodation coefficients (NEAC). Those expressions are derived from the linear regression of collision data (c'_x, c_x) , (c'^2, c^2) , $(|c'_z|, c_z)$ and (c'^2_z, c^2_z) , respectively. Being special composite parameters depending on the moments of $P(\mathbf{c}, \mathbf{c}')$, they can be sensitive to the choice of $P(\mathbf{c}, \mathbf{c}')$ and $P(\mathbf{c}')$. In what follows, we assume that those parameters are obtained from the equilibrium distribution $P_{eq}(\mathbf{c}, \mathbf{c}')$ which is also the basis of our model. For the sake of simplicity, we continue to call them accommodation coefficients despite knowing that from definition (5.18), they are more statistical than physical quantities.

In addition to the correlation analysis of velocities in association with the accommodation coefficients described above, we also examine in details the statistical relations between the incident γ' , reflection γ and deviation η angles as defined in Fig. 5.2.

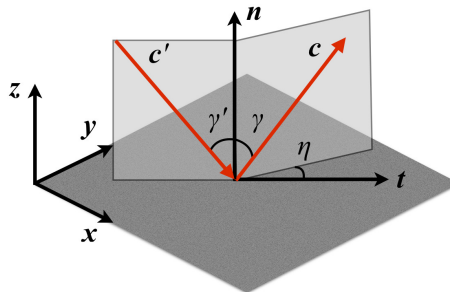


Figure 5.2: A simple scheme of the incident-reflective velocities, \mathbf{c}' - \mathbf{c} , the incident-reflective vertical angles, γ' - γ , and the deviation angle η .

Other physical parameters to be checked are the interfacial coefficients $\bar{\beta}_1$ and $\bar{\beta}_2$. From the kinetic consideration of the terms involved in equations (5.1) and (5.2), $\bar{\beta}_1$ and $\bar{\beta}_2$ can be computed by the expressions

$$\bar{\beta}_1 = \frac{\sqrt{\pi/2\theta}\langle c'_x - c_x \rangle}{\langle c'_x/|c'_z| + c_x/|c_z| \rangle}, \quad \bar{\beta}_2 = \frac{\sqrt{9\pi/32\theta}\langle c'^2 - c^2 \rangle}{\langle c'^2/|c'_z| + c^2/|c_z| \rangle - 3\theta_w \langle 1/|c'_z| + 1/|c_z| \rangle} \quad (5.19)$$

Because of the non-equilibrium origin of the expressions, those coefficients cannot be determined using the equilibrium distribution for the gas at the same temperature and the same velocity as the wall, i.e $P(\mathbf{c}') \neq P_{eq}(\mathbf{c}'|\theta = \theta_w, \langle c'_x \rangle = 0)$, otherwise we shall encounter numerical issues. Instead, for the determination of $\bar{\beta}_1$, the equilibrium distribution with a non zero mean velocity $\langle c'_x \rangle \neq 0$ and the temperature of the wall $\theta = \theta_w$ is used as the input gas distribution $P(\mathbf{c}') = P_{eq}(\mathbf{c}'|\theta = \theta_w, \langle c'_x \rangle \neq 0)$ and for $\bar{\beta}_2$, we used the equilibrium distribution with zero mean velocity $\langle c'_x \rangle = 0$ and a temperature different from the wall temperature $\theta \neq \theta_w$ or $P(\mathbf{c}') = P_{eq}(\mathbf{c}'|\theta \neq \theta_w, \langle c'_x \rangle = 0)$. We also highlight the importance of transforming the variables c_z and c'_z in the data preconditioning step before training the GM model. This step guarantees the vanishing probability at $c'_z = 0$ and $c_z = 0$ like the Rayleigh distribution and the convergence of the rational moments containing $1/c'_z$ and $1/c_z$. Unlike the previous analysis of accommodation coefficients and reflective angle based on the existing collision data at equilibrium, this method requires new realizations, i.e using the new input $P(\mathbf{c}')$ to generate new data $P(\mathbf{c}', \mathbf{c})$ with the wall model $P(\mathbf{c}|\mathbf{c}')$ (parametric/nonparametric kernels, GM model or atomic wall).

Another criteria to evaluate the statistical performance of different scattering kernels is based on the relative entropy, the Kullback-Leibler divergence (D_{KL}) [77]. This quantity is a measure of the differences between the probabilities P and Q . Defined as the expectation of the logarithmic difference, its discrete form is written as:

$$D_{KL}(P||Q) = \sum_j P(\mathbf{x}_j) \log \frac{P(\mathbf{x}_j)}{Q(\mathbf{x}_j)}, \quad (5.20)$$

To compute $P(\mathbf{x}_j)$ and $Q(\mathbf{x}_i)$, we divide the data space into n bins and choose a Parzen-window size h , then the probability density of data generated by MD simulation or a scattering kernel is estimated. The density in each bin can be written as:

$$P(\mathbf{x}_j) = \frac{N_j}{\sum_j N_j}, \quad (5.21)$$

where, \mathbf{x}_j represents the center of bin j , N_j is the number of data in the window of length h centered on \mathbf{x}_j . We note that the above formula can be applied to any distribution of random variables \mathbf{x} , for example velocity, kinetic energy, collision angles etc..

5.3 APPLICATIONS TO REAL GAS-WALL SYSTEMS

5.3.1 Construction of scattering kernels from Molecular Dynamics simulation data

Based on the same systems as Refs. [83, 54], we shall carry out more detailed analysis of the MD simulation results, in order to construct and evaluate statistical models of collisions. We simulate the process of He or Ar gas atoms impacting smooth/rough Au atomic surface and investigated the gas-solid friction and thermal conductance. The rough surface is generated by depositing randomly atoms on the smooth surface. The He or Ar molecules are inserted one by one in the collision zone, only after the molecule interacts with the wall and goes out of the collision zone, another molecule is inserted in the zone from a random position with a random velocity. The MD simulations are performed by LAMMPS (Large-scale Atomic/Molecular Massively Parallel Simulator)[103]. Each collision simulation was run with one gas atom at a time. The simulation parameters will be described briefly as follows as follows:

- temperature of the Au surface: 300 K, controlled by the Nosé-Hoover thermostat
- to compute β_1 we apply a average velocity to the incident gas atom: ranging from -0.5 Å/ps to 0.5 Å/ps (with a step of 0.25 Å/ps)
- to compute β_2 we apply a initial temperature to the incident gas: ranging from 100 K to 400 K (with a step of 100 K)

Pair	$A[\text{eV}]$	$B[\text{eV}\text{\AA}^{-1}]$	$C[\text{eV}\text{\AA}]$	$\alpha[\text{\AA}^{-1}]$	$\gamma[\text{\AA}^{-2}]$	$C_6[\text{eV}\text{\AA}^6]$	$C_8[\text{eV}\text{\AA}^8]$	$\beta[\text{\AA}^{-1}]$
He-Au	-2.9755	0.47351	4.8980	-2.576	0.8204	9.5073	131.18	3.618
Ar-Au	1.623×10^4	-	-	3.356	-	76.785	1066.9	3.051

Table 5.1: The parameters of the He-Au and Ar-Au pairwise interaction potentials [83, 54].

The highly optimized version of multibody EAM potential [119] is employed for the description of the interaction between the Au atoms. The Au-Ar and Au-He pairwise potentials, which are recently determined from ab-initio studies [83, 54], are implemented in LAMMPS and adopted in this work. The functional form of the pair potentials $V_{g-\text{Au}}(R)$ is given by

$$V_{g-\text{Au}}(R) = \left(A + BR + \frac{C}{R} \right) e^{(-\alpha R - \gamma R^2)} + \sum_{n=6,8} \frac{C_n}{R^n} f_n(\beta R). \quad (5.22)$$

where R is the distance between the gas atom ('g' standing for He or Ar) and a gold atom (Au). The parameters A , B , C , α , and γ are associated with the repulsive part and the remaining parameters correspond to the attractive part of the potential. The function f_n is the damping function of Tang and Toennies [133],

$$f_n(x) = 1 - e^{-x} \left(1 + x + \dots + \frac{x^n}{n!} \right). \quad (5.23)$$

The numerical values of the pairwise potential parameters are given in Tab.5.1

In this paper, to construct the scattering kernel, we use the velocity data of the MD simulations under the equilibrium state, in which the temperature of gas flow is equal to the temperature of the atomic wall (300 K) and the mean velocity of the flow equals to 0. We can calculate the accommodation coefficients for the CL kernel using Eq. (5.18). For the NP kernel, we followed the model of Ref. [83], the He velocities range from -40 to 40 $\text{\AA}/\text{ps}$, and the Ar velocities range from -20 to 20 $\text{\AA}/\text{ps}$. The incident and reflective velocity spaces were discretized into 100 and 1000 intervals, respectively, the Parzen-window size $h = 1$ $\text{\AA}/\text{ps}$. The probability that a reflective velocity does not belong to a category is determined by interpolation. In the GM model, the number of mixtures M is a free parameter which needs to be chosen before the learning. To avoid the risk of overfitting or underfitting, there is an optimal value of M for

a given MD data size. We tested the number of Gaussian functions from $M = 1$ to 512 with different initial covariance matrices and mean vectors. To find the optimal M we calculate the energy accommodation coefficient α_2 using the reflective velocity generated by GM model and Eq. (5.18). In Fig.5.3, we found that when M is equal to 64 (2^6), the performance of the GM model is the best and much better than CL and NP models. So the GM model with $M = 64$ has a good accuracy and a reasonable computation time and is used in the present study.

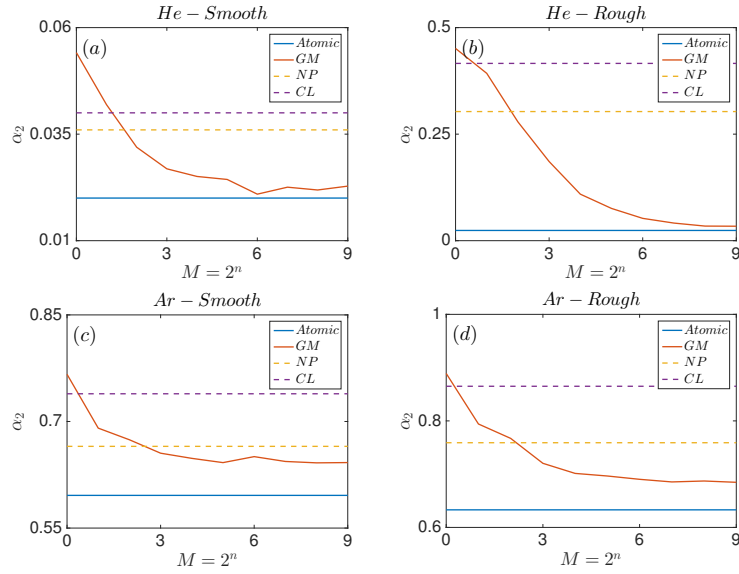


Figure 5.3: Number of Gaussian vs. α_2 determined by statistical models and MD

We then used each kernel, CL, NP and GM, to generate new incident-reflective velocities (about 10^5 data points) based on incident velocities under equilibrium or non-equilibrium states. We investigated the characteristics of the scattering kernels according to the following aspects:

- the accommodation coefficients and the momentum/energy distribution
- the incident, reflective, and deflection angles
- the surface friction and the thermal conductance

5.3.2 Accommodation coefficients

We decomposed the velocity into the normal and the tangential components and then studied the correlations between the incident-reflective velocities and the kinetic energy. Using Eq. (5.18), we can calculate TMAC (α_1), NMAC (α_n), and EAC (α_2) from incident-reflective velocity data. Tab. 5.2 presents TMAC, NMAC and EAC of He/Ar gas on the smooth/rough Au surface using the atomic wall and the different statistical models of collision (GM, NP, CL). From this table, we find that TMAC and NMAC obtained by the different kernels are very close to the atomic simulation results. However, significant differences are observed for the coefficient EAC. The result of the GM kernel is consistent with the atomic model, but the NP and CL kernels considerably overestimate EAC, especially for the He-Au rough surface system. We note that, unlike Ar, He is a special gas which has a very small atomic mass and its interaction with the gold surface is very weak (see ref. [83]). These points can explain the nearly perfect elastic collision of an helium atom on a Au wall, even for the rough atomic surface. In other words, while the atomic motion can change its direction after collisions due to the surface corrugation (e.g via the influences of the atomic roughness, the thermal motion, and the energy landscape), the atomic kinetic energy is almost conserved.

Using the density estimator presented in Eq. (5.21), we can estimate the joint probability of the incident-reflective velocities, and of the kinetic energy. The kinetic energy distributions determined by the atomic wall use and by different scattering kernels are plotted in Fig. 5.4. The energy clouds of the atomic and GM models are visibly narrower than those of the CL and NP kernels. From the column figures of both atomic and GM surface, we can see that roughness does not significantly change EAC (16.7% for He, 5.9% for Ar). However, this trend cannot be captured by both NP and CL kernels.

These phenomenas are further illustrated in Fig. 5.5. The KL divergence D_{KL} between different statistical models and the atomic model was calculated. We can notice that for tangential and

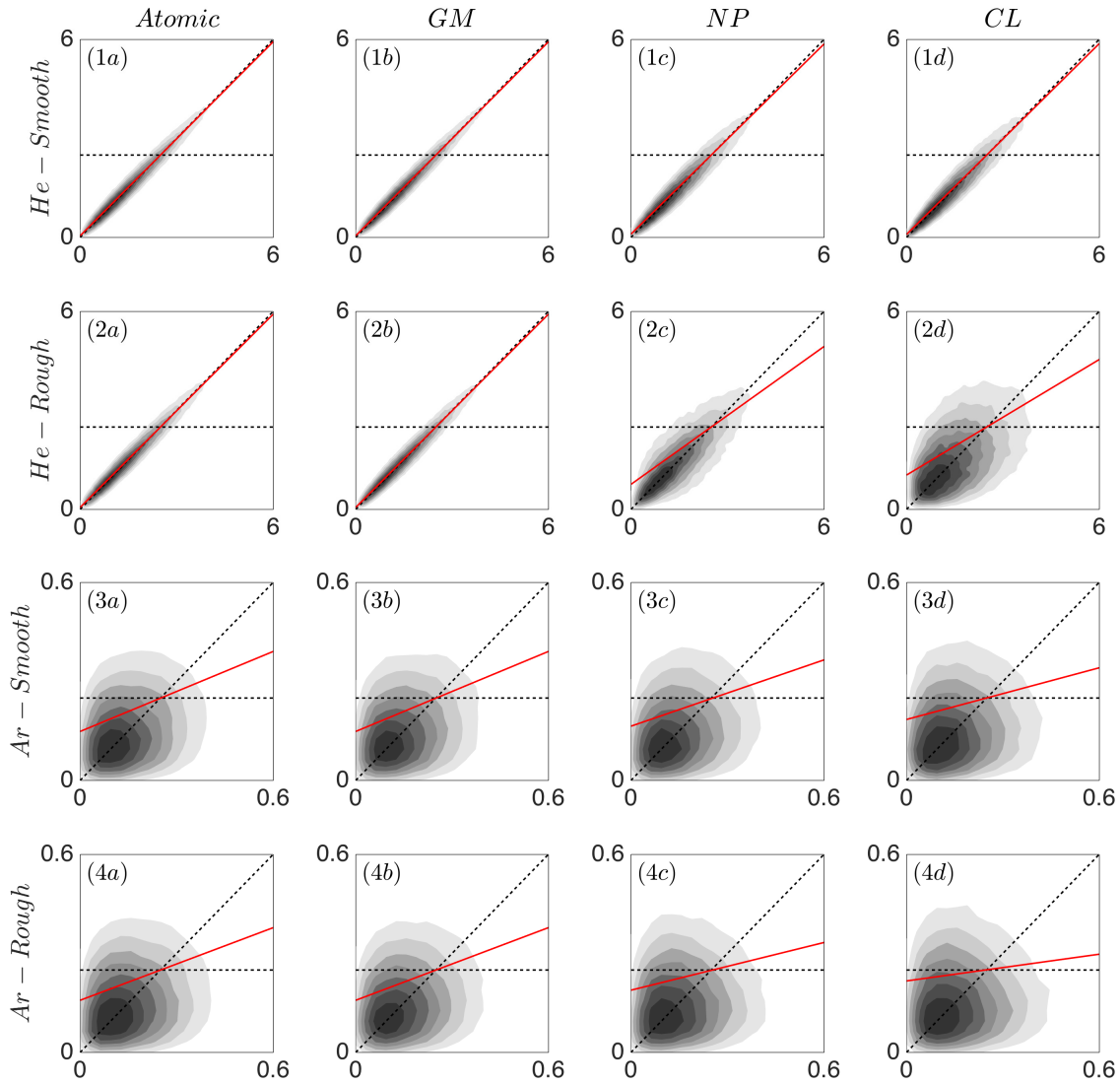


Figure 5.4: The joint probability density of incident-reflective kinetic energy with unite $\text{\AA}^2/\text{ps}^2$ (the prefactor $m/2$ is removed for simplicity) determined by the atomic simulations, the Gaussian mixture (GM), the nonparametric (NP), and the Cercignani-Lampis (CL) kernels. The horizontal axis indicates the incident energy \mathbf{c}'^2 and the vertical axis indicates the reflective energy \mathbf{c}^2 . The red line is the least-square linear regression of kinetic data, its slope is equal to $1-\alpha$. When the red line is close to the diagonal dashed line, the reflection is close to be specular (elastic collision). When the red line is close to the horizontal dashed line, the reflection is diffusive.

Gas	Surface model	Smooth			Rough		
		α_1	α_n	α_2	α_1	α_n	α_2
He	Atomic	0.012	0.052	0.020	0.326	0.293	0.024
	GM	0.012	0.052	0.021	0.327	0.297	0.031
	NP	0.015	0.058	0.040	0.323	0.295	0.303
	CL	0.012	0.055	0.036	0.325	0.317	0.416
Ar	Atomic	0.425	0.803	0.596	0.688	0.831	0.633
	GM	0.425	0.798	0.597	0.686	0.835	0.643
	NP	0.450	0.823	0.665	0.701	0.844	0.759
	CL	0.424	0.814	0.739	0.689	0.841	0.865

Table 5.2: The tangential momentum accommodation coefficient (TMAC) α_1 , the normal momentum accommodation coefficient (NMAC) α_n , and the energy accommodation coefficient (EAC) α_2 , computed using different statistical models: GM, NP, CL, and the atomic (MD) model. The construction of the statistical models NP, GM and CL from MD data is discussed in sec. IIIA. The accommodation coefficients associated to the statistical models are computed based on generation of new data and Eq. (5.18). It is noted that the CL model uses tangential momentum accommodation coefficient (TMAC) and normal energy accommodation coefficient (NEAC) computed by MD as parameters. Consequently, numerical TMAC values of CL model are extremely close to MD results.

normal momentums, the D_{KL} of the GM and NP kernels is at the same level. For the CL kernel, although the D_{KL} for c_x and c_z are larger than those of the other two kernels, its good performance in determining TMAC and NMAC (Tab. 5.2) indicates that CL kernel is still a good kernel to generate a single velocity component. Meanwhile, Fig. 5.5b presents anomalies for the kinetic energy. The energy D_{KL} of NP and CL kernels are close to 1 for the He/rough Au case, meaning that the incident-reflective kinetic energy distributions determined by the NP and CL kernels differ greatly from the results of the atomic simulations. Considering the good performance of CL and NP kernels for the momentum reflection, and less for the kinetic energy, it is suggested that the independent assumption of Eq. (5.8) may oversimplify the true behavior especially for nearly perfect elastic systems like He/Au. This deficiency has been properly covered by the GM model. We note that the EAC value difference between the statistical models is due to the correlation parameter

$$\langle c'^2 c^2 \rangle = \int c'^2 c^2 P_{eq}(\mathbf{c}, \mathbf{c}') d\mathbf{c} d\mathbf{c}'$$

As a result, the accuracy of $P_{eq}(\mathbf{c}, \mathbf{c}')$ governs the accuracy of the correlation parameter and EAC. While it is not trivial to connect the elastic collision phenomena to the property of the probability function $P_{eq}(\mathbf{c}, \mathbf{c}')$ or $P(\mathbf{c}|\mathbf{c}')$, we can conclude mathematically that using the decomposition postulate (5.8) like CL and NP models oversimplifies the real behavior of $P_{eq}(\mathbf{c}, \mathbf{c}')$. In other words, due to the exchange between the velocity components in order to conserve the energy, each of post-collision velocity components is expected to depend on all the pre-collision components.

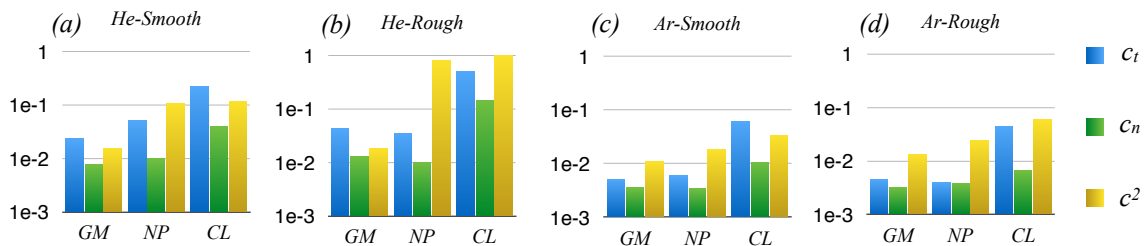


Figure 5.5: The Kullback Leibler divergence $D_{KL}(Atomic||Kernel)$ of momentum and kinetic energy determined by the atomic simulations, the Gaussian mixture (GM) kernel, the nonparametric (NP) kernel, and the Cercignani-Lampis (CL) kernel.

5.3.3 Collision angles

To further study the performance of each scattering kernel, the probability densities of deviation angle η and incident-reflective vertical angles $\gamma'-\gamma$ determined by atomic simulations and scattering kernels were analyzed. The geometric definitions of η , γ' , γ are illustrated in Fig. 5.2.

Angle η can be calculated from velocity components c'_x , c'_y , c_x , c_y and measures the deviation of the gas atom reflection from the incident direction in xy-plane. The incident angle γ' and reflective angle γ depend on the incident, \mathbf{c}' , and reflective, \mathbf{c} , velocities, respectively. By calculating the correlation between γ' and γ , we can understand the aberration of the reflection in the normal direction.

Figure 5.6 shows the probability of the reflective direction on the tangential plane obtained from

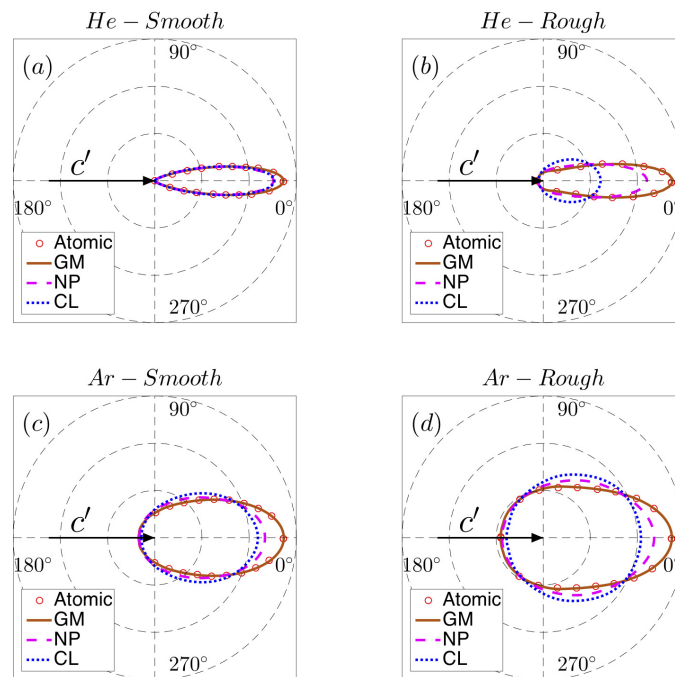


Figure 5.6: The probability density of the reflective deviation angle η determined by the atomic simulations, the Gaussian mixture (GM), the nonparametric (NP), and the Cercignani-Lampis (CL) kernels in polar coordinate system. The distance from the curve to the origin, the radius, indicates the probability of associated to angle η , which coincides with the angle coordinate of the system.

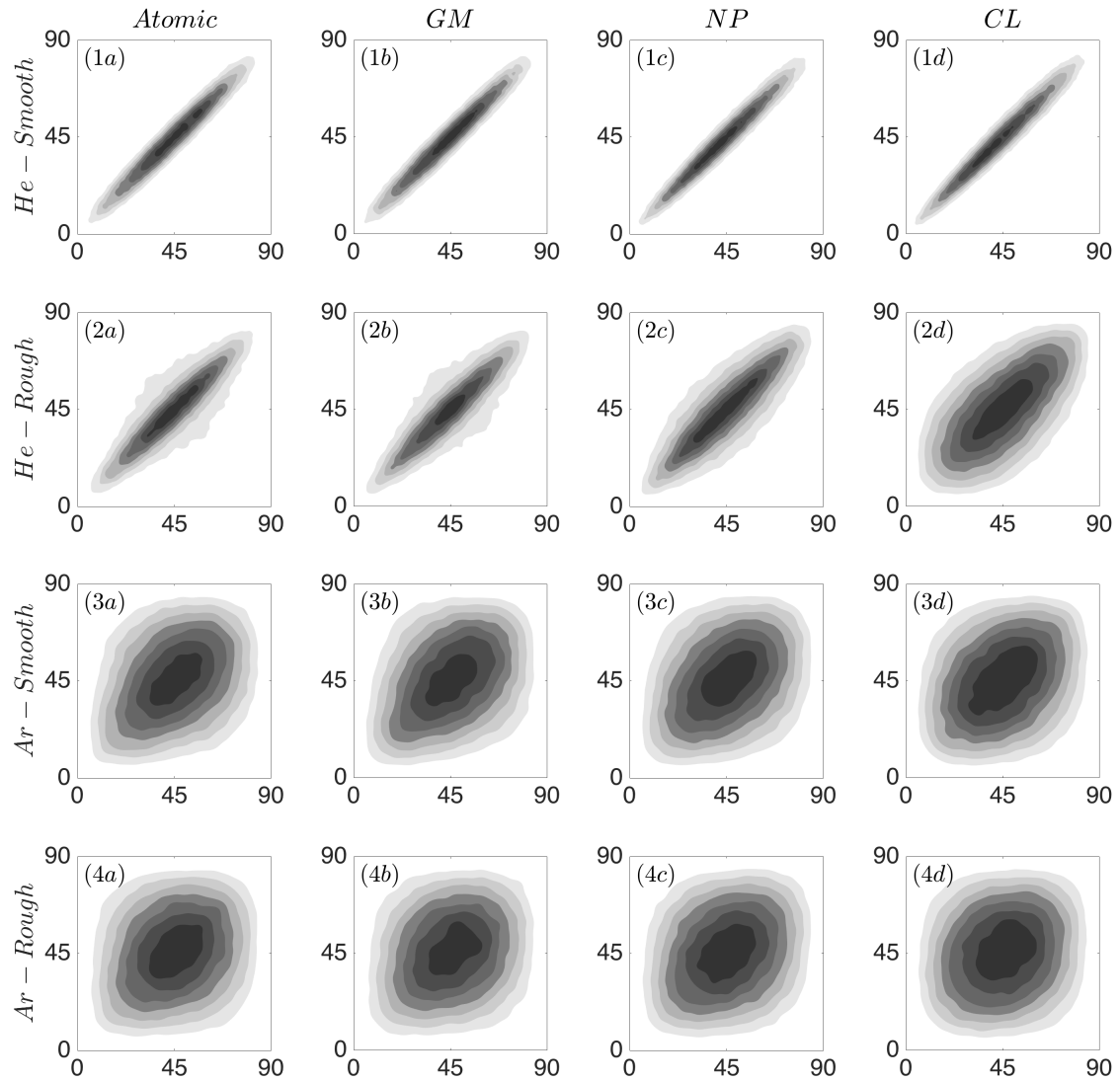


Figure 5.7: The probability density of the incident-reflective vertical angles determined by the atomic simulations, the Gaussian mixture (GM), the nonparametric (NP), and the Cercignani-Lampis (CL) kernels. The horizontal axis indicates the incident angle γ' and the vertical axis indicates the reflective angle γ . The incident and reflective angles range from 0 to 90°

atomic simulation data, GM, NP and CL kernels under equilibrium state. Numerical results show that the rough surface can increase the deviation of the reflective direction with respect the incident direction in xy-plane, especially the percentage of backscattering ($\pi/2 < \eta < 3\pi/2$). As the result, the overall scattering is more diffusive and the probability contour is shifted towards and envelope the origin. In contrast, the contour of reflection on smooth surfaces is narrower. From analysis of gas atoms, the adhesion between Au wall and Ar gas atoms is stronger than for the He-Au system, so that the reflection direction has a greater probability of deviating from the specular direction. From Fig. 5.6, we can find that both CL and NP kernels overestimate the diffusivity of the reflective direction. Only the probability contour of the GM kernel is identical with the one of the the atomic simulations.

Figure 5.7 shows the joint probability density of γ' and γ . When the deviation angle is small, the data population becomes narrow and shrinks toward the diagonal line. Through these cloud figures, we can also confirm that the roughness of the wall surface and the bonding properties between the gas and the wall affect the reflective direction of the gas atom. To quantitatively compare the differences between the three types of kernels and the atomic simulations, we calculate the KL divergence between the scattering kernels and the atomic wall results. The KL divergence of the reflective angle probability is presented in Fig. 5.8. The results of the figure confirm the differences observed in Figures 5.6 and 5.7. The KL divergence of the CL kernel is over 3 times larger than that of the GM kernel, especially for He-Au rough surface system. Basically, the CL kernel incorrectly estimates the distribution of the reflection direction. The results of the NP kernel for the Ar-Au system are better than the CL kernel ones, the corresponding KL divergence is under 2 times larger than the GM kernel ones in terms of tangential deviation angle η . We can clearly see that the GM kernel has a great advantage in predicting the distribution of the reflection directions.

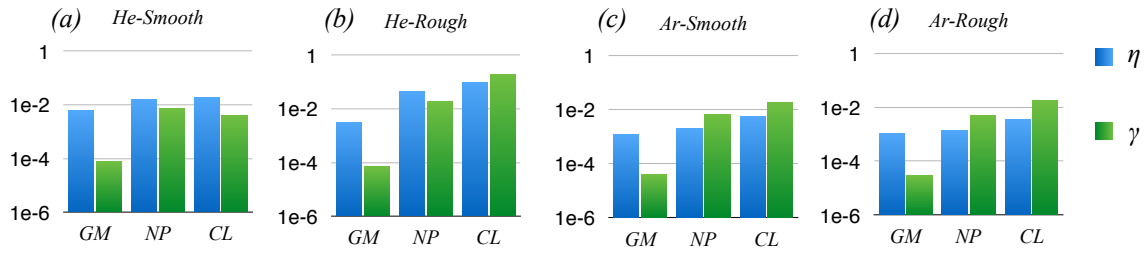


Figure 5.8: The Kullback-Leibler divergence $D_{KL}(Atomic||Kernel)$ derived from Fig. 5.6 and 5.7.

5.3.4 Interfacial friction and thermal conductance

The surface friction and thermal conductance properties can be characterized by the velocity slip coefficient, $\bar{\beta}_1$, and the temperature jump coefficient, $\bar{\beta}_2$, respectively. These two coefficients can be determined by the accommodation coefficients determined previously and relation (5.3) or by a direct method based on equation (5.19) and the non-equilibrium collision simulation data. This step permits to test the ability of the GM model in terms of generating new data and reproducing these important physical properties for real systems. We note that if the final objective is to construct kernels usable in kinetic simulation methods, this step is crucial and guarantees the reliability of the results.

The results for both coefficients are reported in Tab. 5.3. The coefficient $\bar{\beta}_1$ depends on the accommodation momentums and is sensitive to the surface roughness. It means that the friction significantly increases $\bar{\beta}_1$. These effects are observed for both Ar/Au et He/Au systems. From smooth surface to rough surface, the $\bar{\beta}_1$ value increases about 34 times for He-Au system and about 2 times for Ar-Au system. In contrast, the contribution of the surface roughness to the increase of the thermal conductance is relative small, about 20% for He and 9% for Ar.

The numerical tests confirm again the superior performance of the GM model. This is the statistical model that produces the best results when compared with the atomic model (see Fig. 5.9). It is surprising to find that the simple analytical relation between β and α (Eq. (5.3)) works relatively well and yields values of the same order as MD and GM models. It is less

Gas	Scheme	Smooth		Rough	
		$\bar{\beta}_1$	$\bar{\beta}_2$	$\bar{\beta}_1$	$\bar{\beta}_2$
He	Atomic	0.0069	0.0123	0.236	0.015
	GM	0.0064	0.0120	0.240	0.020
	NP	0.0087	0.0194	0.194	0.176
	CL	0.0060	0.0186	0.205	0.252
	$\alpha/(2 - \alpha)$	0.0060	0.0100	0.195	0.012
Ar	Atomic	0.276	0.445	0.571	0.485
	GM	0.283	0.442	0.555	0.484
	NP	0.301	0.459	0.559	0.548
	CL	0.273	0.518	0.530	0.644
	$\alpha/(2 - \alpha)$	0.270	0.424	0.524	0.463

Table 5.3: The friction coefficient ($\bar{\beta}_1$) and the thermal conductance ($\bar{\beta}_2$) determined by different schemes.

accurate than the GM model but better than other models in terms of evaluating the thermal coefficient $\bar{\beta}_2$. In Appendix 2, we also carry out theoretical investigation of CL models. Specifically, we compute analytically the slip and jump coefficients $\bar{\beta}_1$ and $\bar{\beta}_2$ for the CL model with parameters α_t, α_e using the same approaches as the MD model. Results show that the obtained expressions for $\bar{\beta}_1$ and $\bar{\beta}_2$ in terms of α_t, α_e are different but the numerical differences are very small for the whole admissible range $(0, 1)$ of α_t and α_e . However as discussed previously, the coefficients α_1 and α_2 defined by Eq. (5.18) are more of statistical nature and furthermore α_2 is not associated to any parametric statistical models in literature (except for the Maxwell model). This fact will limit the application of those coefficients in particle and/or statistical based simulation methods like MD or DSMC. In contrary, the GM model is not subject to this limitation.

5.4 Conclusion

In this paper, we present the application of unsupervised learning techniques in the construction of wall-gas models and the computation of interfacial properties like friction and thermal

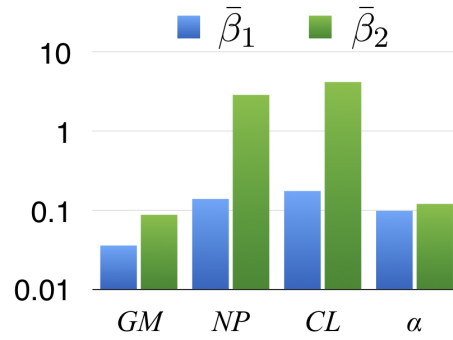


Figure 5.9: The average relative error of the different schemes, GM, NP, CL, and α , comparing with the atomic simulations considering all the data in Tab. 5.3.

conductance. The data obtained from the Molecular Dynamics simulations of gas-wall collision is used to train the scattering kernels, i.e statistical collision models that predict the post-collision velocity from a given pre-collision velocity. Due to the common similarities with the well-known Cercignani-Lampis (CL) model in kinetic theory and the good overall performance in general data treatment, the GM model is chosen for this purpose.

Unlike CL and other parametric scattering kernels in literature, the GM model is flexible with unlimited number parameters and supported by EM algorithm, a robust technique to identify those parameters from data. We also propose to use physical and statistical based criteria e.g accommodation coefficients, friction and thermal conductance, collision angles to evaluate the performance of the GM model. Applications to real gas-wall systems including He-Au and Ar-Au confirm the accuracy of the model. All the coefficients obtained/predicted by the GM model are close to MD results. The overall accuracy of the trained GM model assessed by KL divergence is also superior to other models. The constructed model is useful both for theoretical studies of boundary conditions and for the gas simulation methods like MD and DSMC by saving considerable computation cost devoted to the atomic wall.

Appendix

1. Expectation maximization algorithm

Expectation maximization (EM) algorithm is an iterative method to find the maximum likelihood of parameters in statistical models, which is introduced by Dempster *et. al.* [39]. The parameter set of the GM model is noted as $\Theta = (\theta_1, \theta_2, \dots, \theta_M)$ and the m^{th} parameter is $\theta_m = (\varphi_m, \boldsymbol{\mu}_m, \boldsymbol{\Sigma}_m)$. Noting samples as \mathbf{X} , i.e. \mathbf{X}_i corresponds to the i^{th} training data of total N training data, the likelihood can be written as

$$\begin{aligned}\mathcal{L}(\mathbf{X}|\Theta) &= \prod_{i=1}^N p(\mathbf{X}_i|\Theta), \\ p(\mathbf{X}_i|\Theta) &= \sum_{m=1}^M \varphi_m \mathcal{N}(\mathbf{X}_i|\boldsymbol{\mu}_m, \boldsymbol{\Sigma}_m)\end{aligned}\quad (5.24)$$

To determine the parameter Θ , we can maximize the log-likelihood function:

$$\begin{aligned}\Theta &= \arg \max_{\Theta} \log \mathcal{L}(\mathbf{X}|\Theta) \\ &= \arg \max_{\Theta} \sum_{i=1}^N \log p(\mathbf{X}_i|\Theta),\end{aligned}\quad (5.25)$$

and the sum of log-likelihood function in Eq. (5.25) can be replaced by the expectation of log-likelihood function:

$$\Theta = \arg \max_{\Theta} \mathbb{E}(\log p(\mathbf{X}_i|\Theta)). \quad (5.26)$$

Then, we can use an iterative algorithm to determine the parameter Θ of the GM model. The EM algorithm can be concluded in four steps: initial state, E-step, M-step and convergence test:

1. Initial state: take the initial value $\theta_m^{(0)} = (\varphi_m^{(0)}, \boldsymbol{\mu}_m^{(0)}, \boldsymbol{\Sigma}_m^{(0)})$ for each Gaussian distribution in the GM model.

2. E-step: use the parameters of the $(r-1)^{th}$ iteration to calculate the mixture weights w_{im} of each sample \mathbf{X}_i for the $(r)^{th}$ iteration:

$$w_{im} = \frac{\varphi_m^{(r-1)} \mathcal{N}(\mathbf{X}_i | \boldsymbol{\mu}_m^{(r-1)}, \boldsymbol{\Sigma}_m^{(r-1)})}{\sum_m \varphi_m^{(r-1)} \mathcal{N}(\mathbf{X}_i | \boldsymbol{\mu}_m^{(r-1)}, \boldsymbol{\Sigma}_m^{(r-1)})}. \quad (5.27)$$

3. M-step: use the w_{im} calculated by E-step to determine the new parameters $\boldsymbol{\mu}_m^{(r)}$, $\boldsymbol{\Sigma}_m^{(r)}$ and $\varphi_m^{(r)}$:

$$\begin{aligned} \boldsymbol{\mu}_m^{(r)} &= \frac{\sum_i w_{im} \mathbf{X}_i}{\sum_i w_{im}} \\ \boldsymbol{\Sigma}_m^{(r)} &= \frac{\sum_i w_{im} (\mathbf{X}_i - \boldsymbol{\mu}_m^{(r)}) (\mathbf{X}_i - \boldsymbol{\mu}_m^{(r)})^T}{\sum_i w_{im}} \\ \varphi_m^{(r)} &= \frac{1}{n} \sum_{i=1}^n w_{im}. \end{aligned} \quad (5.28)$$

4. convergence test: conclude the iterative process if the following conditions are met:

$$\left| 1 - \frac{\mathbb{E}(\log p(\mathbf{X}_i | \Theta^{(r)}))}{\mathbb{E}(\log p(\mathbf{X}_i | \Theta^{(r-1)}))} \right| < \varepsilon, \quad (5.29)$$

where, ε is a threshold. Repeat the steps 2 to 4 until the expectation of the log-likelihood function converge.

The advantage of the EM algorithm is that it guarantees local convergence, but the drawback is that the algorithm is sensitive to the initial state. In practice, the k-means algorithm [23] and the iterative pairwise replacement algorithm (IPRA) [131] have a good performance in giving an initial state for the GM model. In addition, we can also use multiple random initial states and then compare the distributions of GMs obtained with different initial states.

2. Comparisons of interfacial coefficients associated to the CL model by different methods

We consider the CL kernel whose analytical expression is given by (5.9) and examine the coefficients $\alpha_1, \alpha_2, \bar{\beta}_1, \bar{\beta}_2$ computed from the correlation analysis and by the non-equilibrium method.

Using the equilibrium distribution $P_{eq}^{CL}(\mathbf{c}, \mathbf{c}')$, the moments $f(\mathbf{c}, \mathbf{c}')$ in correlation analysis can be calculated by

$$\langle f(\mathbf{c}, \mathbf{c}') \rangle = \int f(\mathbf{c}, \mathbf{c}') P_{eq}^{CL}(\mathbf{c}, \mathbf{c}') d\mathbf{c} d\mathbf{c}' \quad (5.30)$$

which yields the explicit expressions

$$\begin{aligned} \langle c_x \rangle = \langle c'_x \rangle = 0, \quad \langle c_x c'_x \rangle = (1 - \alpha_1) \theta_w, \quad \langle c_x^2 \rangle = \langle c'^2_x \rangle = \theta_w, \quad \langle c_z^2 \rangle = \langle |c'^2_z| \rangle = 2\theta_w, \\ \langle c^2 \rangle = \langle c'^2 \rangle = 4\theta_w, \quad \langle c^2 c'^2 \rangle = 4\theta_w^2 (\alpha_t^2 - 2\alpha_t - \alpha_e + 6), \quad \langle c^4 \rangle = \langle c'^4 \rangle = 24\theta_w^2. \end{aligned} \quad (5.31)$$

Substituting the above results in (5.18), we obtain coefficients α_1, α_2

$$\alpha_1 = \alpha_t, \quad \alpha_2 = \frac{1}{2} [\alpha_e + \alpha_t (2 - \alpha_t)] \quad (5.32)$$

and the associated interfacial coefficients, $\bar{\beta}_1, \bar{\beta}_2$

$$\bar{\beta}_1 = \frac{\alpha_t}{2 - \alpha_t}, \quad \bar{\beta}_2 = \frac{\alpha_e + \alpha_t (2 - \alpha_t)}{2 + (1 - \alpha_e) + (1 - \alpha_t)^2}, \quad (5.33)$$

under assumption of the validity of the relation $\bar{\beta}_i = \alpha_i / (2 - \alpha_i)$ with $i = 1, 2$.

Regarding the non-equilibrium method, we impose the input distribution $P(\mathbf{c}')$ at a differ-

ent temperature or velocity from the wall and use the scattering kernel to compute $P(\mathbf{c})$

$$P(\mathbf{c}) = \int P^{CL}(\mathbf{c}|\mathbf{c}')P(\mathbf{c}')d\mathbf{c}' \quad (5.34)$$

To determine $\bar{\beta}_1$ and $\bar{\beta}_2$ with (5.19), we need to compute the moments

$$\langle f(\mathbf{c}') \rangle = \int f(\mathbf{c}')P(\mathbf{c}')d\mathbf{c}', \quad \langle f(\mathbf{c}) \rangle = \int f(\mathbf{c})P(\mathbf{c})d\mathbf{c} \quad (5.35)$$

yielding the final results (after considering $\theta \simeq \theta_w$)

$$\bar{\beta}_1 = \frac{\alpha_t}{2 - \alpha_t}, \quad \bar{\beta}_2 = \frac{3}{2} \left[\frac{\alpha_e + \alpha_t(2 - \alpha_t)}{(1 - \alpha_e) + 2(1 - \alpha_t)^2 + 3} \right]. \quad (5.36)$$

We also noted that in literature, there also exists different expressions of coefficients $\bar{\beta}_1, \bar{\beta}_2$ (see Ref. [140, 128])

$$\bar{\beta}_1 = \frac{\alpha_t}{2 - \alpha_t}, \quad \bar{\beta}_2 = \frac{\alpha_e + \alpha_t(2 - \alpha_t)}{4 - \frac{2}{5}[3\alpha_e + 2\alpha_t(2 - \alpha_t)]}. \quad (5.37)$$

Despite using non equilibrium gas distribution as input distribution, the derivation of these equations is different from the non equilibrium method used in the present work. It is based on the moment balance at the wall and the temperature, velocity and stress and heat flux are parameters of input distribution (Chapman-Enskog) and are not computed from both input and output distributions as in (5.19).

A general remark can be made here that while all the methods agree in terms of slip effects (coefficient $\bar{\beta}_1$), analytical expressions for the interfacial conductance are different (coefficient $\bar{\beta}_2$). It is suggested that these discrepancies are due to the fact that the EAC coefficient is undefined for the CL wall kernel [84], except for the diffusive wall $\alpha_e = \alpha_t = 1$. Nevertheless, the discrepancies between the methods are not significant, maximum 6% at the extreme contrast cases $\alpha_t = 1, \alpha_e = 0$ or $\alpha_t = 0, \alpha_e = 1$ (see Fig. 5.10).

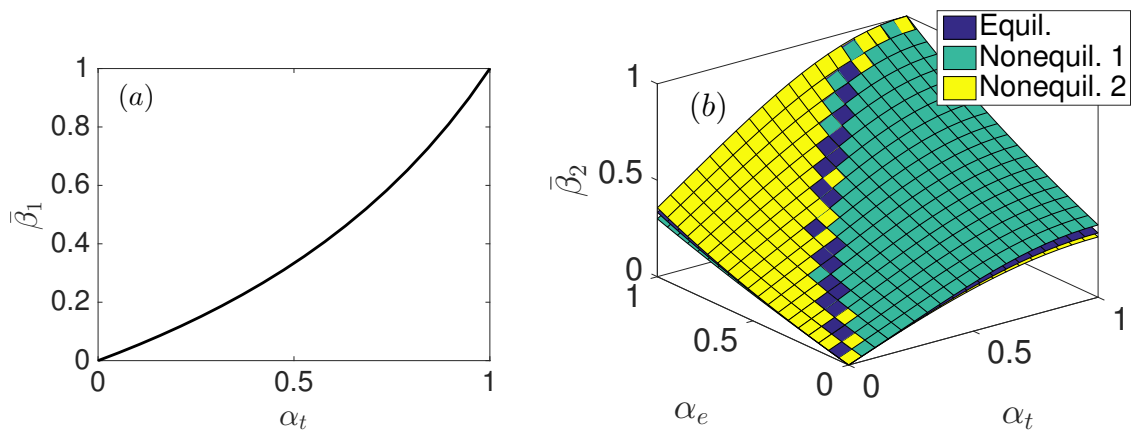


Figure 5.10: (a) $\bar{\beta}_1$ as a function of α_t . (b) Comparisons between different methods of computing $\bar{\beta}_2$ with the same CL models: the equilibrium method (5.33), the nonequilibrium method 1 in this work (5.36), the nonequilibrium method 2 in literature (5.37).

Chapter 6

Computation of the permeability and diffusivity of an array of cylinders with wall-slip and temperature jump.

The object of this chapter is to study the surface effect on the heat and mass properties of a regular array of cylinders. We determine (i) the permeability tensor and (ii) the effective diffusivity. The effective properties are determined in the framework of the periodic homogenization and asymptotic expansion methods initiated by Auriault et Sanchez-Palencia [9, 14, 110]. The permeability is obtained by solving the Stokes flow around the cylinders with the wall-slip condition at the surface of the solids. This problem has been already studied by [153], however, the velocity distribution is needed to compute the effective diffusivity. The latter is obtained by solving a convection-diffusivity problem with an imperfect interface between the solid and the fluid which involves a jump of the temperature. After a description of the local problem with dimensionless variables (section 6.1, we propose a FE implementation of the local problem in section (6.2). The surface effects are then illustrated by an application to CH_4 gas flow in an array of graphite cylinders.

6.1 The homogenization problem

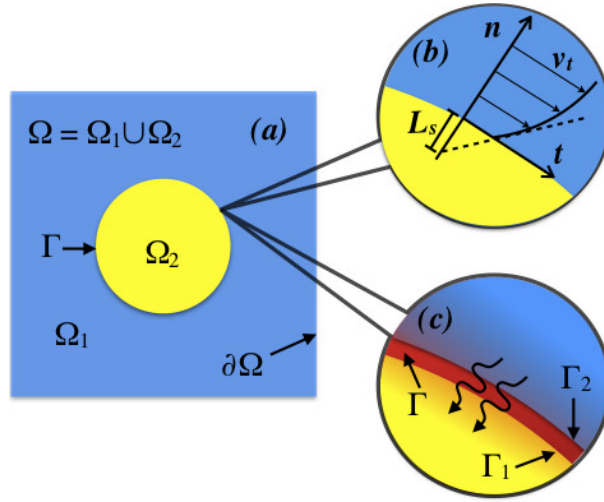


Figure 6.1: Description of the homogenization problem

We consider a periodic porous medium fulfilled by a homogeneous newtonian viscous fluid with the dynamic viscosity μ . Both the fluid and the solid are thermally conductive media with the diffusivity k_1 and k_2 respectively. By Ω , we denote the total volume of the cell, by Ω_1 and Ω_2 the volume occupied by the fluid and the solid respectively, where Ω_1 and Ω_2 are both interconnected domains. The unit cell has the dimension l along each space directions, its volume is $\Omega = l^3$. The frontier between the fluid and the solid is denoted Γ . Due to the fluid motion, the mass, momentum and energy can be transported along with the stream currents, which results in the two set of local equations:

-Fluid flow problem: the fluid motion is govern by the Stokes equation and is generated by applying the macroscopic pressure gradient \mathbf{J} . At the interface between the fluid and the solid, the slip condition is used with the slip length L_s (Fig. 6.1-b).

$$\begin{aligned}
 \mu \Delta \mathbf{v} - \nabla p &= \mathbf{J} \quad \text{in } \Omega_1, \\
 \nabla \cdot \mathbf{v} &= 0 \quad \text{in } \Omega_1, \\
 \mathbf{v} &= L_s (\mathbf{Q} \cdot \boldsymbol{\varepsilon} \cdot \mathbf{n}), \quad \mathbf{v} \cdot \mathbf{n} = 0, \quad \text{on } \Gamma.
 \end{aligned} \tag{6.1}$$

where μ is the dynamic viscosity, \mathbf{v} , it the local velocity, p is the pressure field and $\boldsymbol{\varepsilon}$ is the

strain rate tensor, \mathbf{n} is the normal unit vector taken on Γ and oriented from the solid to the fluid phase and \mathbf{Q} is the two order projector defined by:

$$\mathbf{Q} = \mathbf{I} - \mathbf{n} \otimes \mathbf{n} \quad (6.2)$$

At the macroscopic scale the flow is described by the Darcy equation:

$$\mathbf{V} = -\frac{1}{\mu} \mathbf{K}_P \cdot \mathbf{J}, \quad (6.3)$$

or, for an isotropic material:

$$\mathbf{V} = -\frac{k_P}{\mu} \mathbf{J} \quad (6.4)$$

The following change of variables is now used in the local flow equations:

$$\begin{aligned} \mathbf{v} &= \frac{|\mathbf{J}|^2}{\mu} \bar{\mathbf{v}}, & p &= |\mathbf{J}| l \bar{p}, & \mathbf{J} &= |\mathbf{J}| \bar{\mathbf{J}}, \\ L_s &= l \bar{L}_s, & \boldsymbol{\varepsilon} &= \frac{|\mathbf{J}| l}{\mu} \bar{\boldsymbol{\varepsilon}}, & \mathbf{x} &= l \bar{\mathbf{x}}. \end{aligned} \quad (6.5)$$

It leads to the following non dimensional set of equations:

$$\begin{aligned} \bar{\Delta} \bar{\mathbf{v}} - \bar{\nabla} \bar{p} &= \bar{\mathbf{J}} & \text{in } \bar{\Omega}_1, \\ \bar{\nabla} \cdot \bar{\mathbf{v}} &= 0, & \text{in } \bar{\Omega}_1 \\ \bar{\mathbf{v}} &= \bar{L}_s (\mathbf{Q} \cdot \bar{\boldsymbol{\varepsilon}} \cdot \mathbf{n}), & \bar{\mathbf{v}} \cdot \mathbf{n} = 0, & \text{on } \bar{\Gamma}. \end{aligned} \quad (6.6)$$

where $\bar{\Delta}$ and $\bar{\nabla}$ are the differential operator related to the dimensionless coordinates $\bar{x}_1, \bar{x}_2, \bar{x}_3$. These equations are solved on a cubic unit cell of dimension 1 along each space directions with the periodic conditions for $\bar{\mathbf{v}}$ and \bar{p} on the opposite sides of the cell. The above unit cell problem introduce on dimensionless parameter \bar{L}_s . Once the problem is numerically solved, the velocity field linearly depends on the applied dimensionless pressure gradient. Introducing by $\mathbf{A}(\bar{\mathbf{x}})$ the

localization tensor, the local velocity field can be reads:

$$\bar{\mathbf{v}} = -\mathbf{A}(\bar{\mathbf{x}}) \cdot \bar{\mathbf{J}} \quad (6.7)$$

The average of $\bar{\mathbf{v}}$ leads gives:

$$\langle \bar{\mathbf{v}} \rangle_{\bar{\Omega}} = -\bar{\mathbf{K}}_p \cdot \bar{\mathbf{J}}, \quad \bar{\mathbf{K}}_p = \langle \mathbf{A}(\bar{\mathbf{x}}) \rangle_{\bar{\Omega}} \quad (6.8)$$

where $\bar{\mathbf{K}}_p$ is the dimensionless permeability tensor. The relation between $\bar{\mathbf{K}}_p$ and \mathbf{K}_p is:

$$\mathbf{K}_p = l^2 \bar{\mathbf{K}}_p \quad (6.9)$$

-Heat transfer problem: Once the velocity field is determined by solving the Stokes equation, the local velocity field is used for the for convection-diffusivity problem. We assume that either the fluid and the solid are thermally conductive. The convective heat transfer equation is given by:

$$\rho C_p \frac{\partial T}{\partial t} + \mathbf{v} \cdot \nabla (\rho C_p T) = \nabla \cdot \mathbf{q} \quad \text{in } \Omega, \quad (6.10)$$

where ρ , C_p and T are the mass density, heat capacity and temperature field respectively and \mathbf{q} is the heat flux given by:

$$\mathbf{q} = k(\mathbf{x}) \nabla T \quad \text{in } \Omega \quad (6.11)$$

where $k(\mathbf{x})$ is the conductivity which takes the value k_1 in the fluid phase and k_2 in the solid.

At the interface between the fluid and the solid, the conditions are:

$$\begin{aligned} [\mathbf{q} \cdot \mathbf{n}]_{\Gamma} &= 0, \quad \text{on } \Gamma \\ [T]_{\Gamma} &= -k_t \mathbf{q} \cdot \mathbf{n} \text{ on } \Gamma. \end{aligned} \quad (6.12)$$

where k_t is Kapitza's thermal resistance coefficient. k_t is related to L_t by:

$$L_t = k_t k_1 \quad (6.13)$$

The thermal convection-diffusion is activated by applying the macroscopic temperature gradient \mathbf{E} following:

$$\langle \nabla T \rangle_{\Omega} = \mathbf{E} \quad (6.14)$$

At the boundary of the unit cell, the periodic conditions are used for the temperature field T . As already shown by Bloch and Auriault [17] and Allaire [5], the macroscopic description is:

$$\rho C_p \frac{\partial T}{\partial t} + \rho C_p \mathbf{V} \cdot \mathbf{E} = \text{div}(\mathbf{K}_D \cdot \mathbf{E}) \quad (6.15)$$

where \mathbf{K}_D is the macroscopic conductivity tensor. This tensor is determined by solving the set of local equations (6.10)-(6.14). Due to the linearity of the problem for the temperature field, there exists a uniquely zero mean local function \mathbf{g} satisfying to:

$$T = \mathbf{g} \cdot \mathbf{E} + \langle T \rangle. \quad (6.16)$$

The effective diffusivity tensor is then determined by the relation:

$$\mathbf{K}_D = \langle k \rangle \mathbf{I} + \langle k \nabla^T \mathbf{g} \rangle - \gamma \langle (\mathbf{v} - \mathbf{V}) \otimes \mathbf{g} \rangle. \quad (6.17)$$

The solution of the heat transfer problem then depends on two driving force variables, the macroscopic gradient of temperature \mathbf{E} and the gradient of pressure \mathbf{J} due to the presence of the convection term in Eq. (6.10). It must be also noted that the local temperature has a non linear dependence with the applied pressure gradient \mathbf{J} .

Note also that the above definition for the diffusivity tensor is non symmetric due to the presence of the dispersive term $\langle (\mathbf{v} - \mathbf{V}) \otimes \mathbf{g} \rangle$. However, the diffusivity tensor \mathbf{K}_D is defined

merely by its inner product with the symmetric tensor $\nabla \mathbf{E}$ in relation (6.15), so that only the symmetric part \mathbf{K}_D has a contribution at the macroscopic scale.

As for the fluid flow problem it is useful to work with dimensionless variables for the numerical integration of the local equations. To this end, let us introduce in the set of equations (6.10)-(6.14) the following change of variables:

$$L_t = l\bar{L}_t, \quad k(\mathbf{x}) = k_1\bar{k}(\bar{\mathbf{x}}), \quad T = |\mathbf{E}|l\bar{T}, \quad \mathbf{E} = |\mathbf{E}|\bar{\mathbf{E}}, \quad \mathbf{v} = \frac{|\mathbf{J}|l^2}{\mu}\bar{\mathbf{v}} \quad (6.18)$$

with:

$$\bar{k}(\mathbf{x}) = \begin{cases} 1 & \bar{\mathbf{x}} \in \bar{\Omega}_1 \\ k_2/k_1 & \bar{\mathbf{x}} \in \bar{\Omega}_2 \end{cases}. \quad (6.19)$$

We obtain:

$$\begin{aligned} -\bar{\nabla} \cdot \bar{\mathbf{q}} &= \gamma(\bar{\mathbf{v}} \cdot \bar{\nabla} \bar{T} - \bar{\mathbf{V}} \cdot \bar{\mathbf{E}}) \quad \text{in } \bar{\Omega}, \\ \bar{\mathbf{q}} &= -\bar{k}(\bar{\mathbf{x}})\bar{\nabla} \bar{T} \quad \text{in } \bar{\Omega}, \\ [\bar{\mathbf{q}} \cdot \mathbf{n}]_{\Gamma} &= 0, \quad \text{on } \bar{\Gamma} \\ [\bar{T}]_{\Gamma} &= -\bar{L}_t \bar{\mathbf{q}} \cdot \mathbf{n} \quad \text{on } \bar{\Gamma}. \end{aligned} \quad (6.20)$$

and where γ is the non dimensionless coefficient:

$$\gamma = \frac{\rho C_p |\mathbf{J}| l^3}{\mu k_1} \quad (6.21)$$

Introducing the change of variable (6.18) in relation (6.17), we deduce that:

$$\mathbf{K}_D = k_1 \left\{ \langle \bar{k}(\bar{\mathbf{x}}) \rangle \mathbf{I} + \langle \bar{k}(\bar{\mathbf{x}}) \bar{\nabla}^T \bar{\mathbf{g}} \rangle - \gamma \langle (\bar{\mathbf{v}} - \bar{\mathbf{V}}) \otimes \bar{\mathbf{g}} \rangle \right\}, \quad (6.22)$$

where $\bar{\mathbf{g}}$ is the localization tensor obtained by the resolution of the dimensionless heat transfer problem (6.20). Note that the coefficient γ is closed to the Peclet number Pe . Indeed, the

Peclet number is defined by:

$$P_e = \frac{lv_c}{\alpha} \quad (6.23)$$

where α is the diffusivity, defined by:

$$\alpha = \frac{k_1}{\rho C_p} \quad (6.24)$$

and v_c is the characteristic velocity. Consider the norm of the macroscopic velocity, $|\mathbf{V}|$ for v_c and accounting for the variable change relations (6.18), we deduce that:

$$P_e = \gamma \bar{v}_c \quad (6.25)$$

Where \bar{v}_c is the characteristic velocity computed for the dimensionless flow problem (6.6). Typically, we can use the norm of $\bar{\mathbf{V}} = \langle \bar{\mathbf{v}} \rangle_{\bar{\Omega}}$ for v_c . It can be observed that the convection-diffusion problem (6.20) depends on two parameters, \bar{L}_t that characterize the jump of the temperature across the interface and γ which is proportional to the Peclet number.

6.2 Finite elements method

In this section, we present a FEM numerical solution for the effective diffusivity coefficient. As mentioned earlier, we first compute the solution of the Stokes slip flow problem to determine the velocity field, the latter will be used in the convection-diffusivity equation. Next, the solution of the heat transfer problem is computed and the effective diffusivity is provided. In the Stokes problem, we just consider the fluid phase, and in convection problem, both the solid and fluid phase are meshed. In order to apply temperature jump conditions, we use cohesive elements at the interface.

The FEM is applied to dimensionless problem, however, for the sake of simplicity, all the bars over the dimensionless variables are now removed.

6.2.1 Weak form for the Stokes equation

Let us first consider the Stokes slip flow problem given by equations (6.6). We introduce two test functions $\mathbf{v}^*(\mathbf{x})$ and $p^*(\mathbf{x})$. Both these functions are continuous in Ω_1 and are periodic. The velocity $\mathbf{v}^*(\mathbf{x})$ is divergence free and the normal component $\mathbf{v}^*(\mathbf{x}) \cdot \mathbf{n}(\mathbf{x})$ is null on the interface Γ . Now, we multiply $\mathbf{v}^*(\mathbf{x})$ and $p^*(\mathbf{x})$ by the two first equations in (6.6) and we take the integral over the volume of the pores Ω_1 :

$$\begin{aligned} \int_{\Omega_1} \{ \mathbf{v}^*(\mathbf{x}) \cdot \Delta \mathbf{v}(\mathbf{x}) - \mathbf{v}^*(\mathbf{x}) \cdot \nabla p(\mathbf{x}) - \mathbf{v}^*(\mathbf{x}) \cdot \mathbf{J} \} dx &= 0, \\ \int_{\Omega_1} \nabla \cdot \mathbf{v}(\mathbf{x}) p^*(\mathbf{x}) dx &= 0. \end{aligned} \quad (6.26)$$

By making use of the divergence theorem and the periodicity conditions, the weak form can be written as:

$$\begin{aligned} &\int_{\Gamma} \{ -2\mathbf{v}^*(\mathbf{x}) \cdot \boldsymbol{\varepsilon}(\mathbf{v}(\mathbf{x})) \cdot \mathbf{n}(\mathbf{x}) \} dx \\ &+ \int_{\Omega_1} \{ -2\boldsymbol{\varepsilon}(\mathbf{v}^*(\mathbf{x})) : \boldsymbol{\varepsilon}(\mathbf{v}(\mathbf{x})) - \mathbf{v}^*(\mathbf{x}) \cdot \nabla p(\mathbf{x}) - \mathbf{v}^*(\mathbf{x}) \cdot \mathbf{J} \} dx = 0, \\ &\int_{\Gamma} \mathbf{v}(\mathbf{x}) \cdot \mathbf{n}(\mathbf{x}) p^*(\mathbf{x}) dx - \int_{\Omega_1} \mathbf{v}(\mathbf{x}) \cdot \nabla p^*(\mathbf{x}) dx = 0. \end{aligned} \quad (6.27)$$

Considering the slip boundary condition in Eq.(6.6), we deduce that the normal component of the velocity, $\mathbf{v}(\mathbf{x}) \cdot \mathbf{n}(\mathbf{x})$ is null on Γ . Also, \mathbf{v}^* has a null normal component on Γ . It follows that $\mathbf{v}^*(\mathbf{x}) = \mathbf{Q} \cdot \mathbf{v}^*(\mathbf{x})$ and then:

$$\mathbf{v}^*(\mathbf{x}) \cdot \boldsymbol{\varepsilon}(\mathbf{v}(\mathbf{x})) \cdot \mathbf{n}(\mathbf{x}) = \mathbf{v}^*(\mathbf{x}) \cdot \mathbf{Q} \cdot \boldsymbol{\varepsilon}(\mathbf{v}(\mathbf{x})) \cdot \mathbf{n}(\mathbf{x}) = \frac{1}{L_s} \mathbf{v}^*(\mathbf{x}) \cdot \mathbf{v}(\mathbf{x}) \quad (6.28)$$

It follows that:

$$\begin{aligned}
& \int_{\Omega_1} 2\varepsilon(\mathbf{v}^*(\mathbf{x})) : \varepsilon(\mathbf{v}(\mathbf{x}))dx + \frac{2}{L_s} \int_{\Gamma} \mathbf{v}^*(\mathbf{x}) \cdot \mathbf{v}(\mathbf{x})dx \\
& - \int_{\Omega_1} \mathbf{v}^*(\mathbf{x}) \cdot \nabla p(\mathbf{x})dx = - \int_{\Omega_1} \mathbf{v}^*(\mathbf{x}) \cdot \mathbf{J}dx, \\
& \int_{\Omega_1} \mathbf{v}(\mathbf{x}) \cdot \nabla p^*(\mathbf{x})dx = 0.
\end{aligned} \tag{6.29}$$

6.2.2 Weak form of the convection-diffusivity equation

We multiply Eq.(6.20) by the test function T^* and we integrate over the volume of the unit cell Ω . It leads to:

$$\int_{\Omega} \{-\nabla \cdot \mathbf{q}(T(\mathbf{x})) - \mathbf{v}(\mathbf{x}) \cdot \nabla T(\mathbf{x}) + \mathbf{V} \cdot \mathbf{E}\} T^*(\mathbf{x})dx = 0, \tag{6.30}$$

$\mathbf{V} \cdot \mathbf{E}$ is a constant that we denote by b . Considering the divergence theorem and the periodicity conditions, the weak form can be written as:

$$\begin{aligned}
& - \int_{\Gamma} \mathbf{q}(T(\mathbf{x})) \cdot \mathbf{n}(\mathbf{x})[T^*(\mathbf{x})]_{\Gamma}dx \\
& - \int_{\Omega} \{\mathbf{q}(T(\mathbf{x})) \cdot \nabla T^*(\mathbf{x}) + \mathbf{v}(\mathbf{x}) \nabla T(\mathbf{x})T^*(\mathbf{x})\} dx = - \int_{\Omega} bT^*(\mathbf{x})dx,
\end{aligned} \tag{6.31}$$

Considering the second and fourth equation in (6.20), we obtain:

$$\begin{aligned}
& \frac{1}{L_t} \int_{\Gamma} [T(\mathbf{x})]_{\Gamma}[T^*(\mathbf{x})]_{\Gamma}dx \\
& + \int_{\Omega} \{k(\mathbf{x})\nabla T(\mathbf{x}) \cdot \nabla T^*(\mathbf{x}) - \mathbf{v}(\mathbf{x}) \cdot \nabla T(\mathbf{x})T^*(\mathbf{x})\} dx = - \int_{\Omega} bT^*(\mathbf{x})dx.
\end{aligned} \tag{6.32}$$

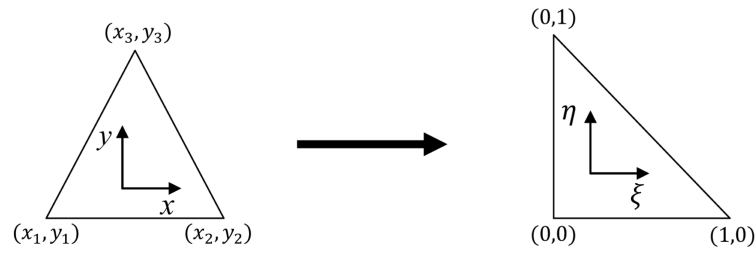


Figure 6.2: Reference element

6.2.3 Discretization and interpolation on element

We mesh each domain with triangular elements and all integrals are expressed onto the reference element. The transformation between the coordinates \mathbf{x} and the local one $\boldsymbol{\xi}$:

$$\begin{bmatrix} x \\ y \end{bmatrix} = [\mathcal{J}_e] \begin{bmatrix} \xi \\ \eta \end{bmatrix} + \begin{bmatrix} x_1 \\ y_1 \end{bmatrix}, \quad [\mathcal{J}_e] = \begin{bmatrix} x_2 - x_1 & x_3 - x_1 \\ y_2 - y_1 & y_3 - y_1 \end{bmatrix}, \quad (6.33)$$

where $[\mathcal{J}_e]$ is the jacobian matrix whose determinant is two times the area of the triangular element, $|\mathcal{J}_e| = 2A_e$. For any quantity $h(\mathbf{x})$ defined on Ω , we have:

$$\int_{\Omega_e} h(\mathbf{x}) d\mathbf{x} = \sum_e \int_{\Omega_e} h(\mathbf{x}(\boldsymbol{\xi})) |\mathcal{J}_e| d\boldsymbol{\xi}.$$

In the each element, the unknown variables are interpolated with the shape functions:

$$N_1(\boldsymbol{\xi}) = 1 - \xi - \eta, \quad N_2(\boldsymbol{\xi}) = \xi, \quad N_3(\boldsymbol{\xi}) = \eta \quad (6.34)$$

Incompressible fluid flow problems generally contain velocity and pressure as the unknown variables and fall in the category of mixed formulations [169]. It was recognized that the solutions strongly depend upon the particular pair of velocity and pressure interpolations employed. The spaces of discretization must satisfy the inf-sup condition or the Ladyhenskaya-Babuska-Brezzi known as LBB condition (this has been discussed for instance for the Stokes problem

by Babuska [10] and Brezzi [21]):

$$\mathbf{inf}_{p_h \in P_h} \mathbf{sup}_{v_h \in V_h} \frac{(\nabla \cdot v_h, p_h)}{\|\nabla v_h\| \|p_h\|} \geq \beta_0 \quad (6.35)$$

Where V_h and P_h are respectively the discrete field of velocity and pressure, β_0 is a positive constant independent from h . There are several methods to stabilize the results, one of the most common consist to use the ‘‘Bubble Function’’. This method can give stable results by adding a degree of freedom at the center of the element for velocity field. For 2D triangle element, we add the interpolation function $N_4(\xi) = 27N_1(\xi)N_2(\xi)N_3(\xi)$. $N_4(\xi)$ is null on the boundary of the element and is equal to 1 at its center.

Still in the 2d case, the elements at the interface Γ are segments. The following interpolation functions are then considered for all the quantities at the interface:

$$S_1(\xi) = 1 - \xi, \quad S_2(\xi) = \xi. \quad (6.36)$$

The determinant of the Jacobian is the length of the segment ($|\mathcal{J}_s| = \sqrt{(x_2 - x_1)^2 + (y_2 - y_1)^2}$).

The velocity \mathbf{v}_e , the pressure p_e and the temperature T_e on each element are then given by:

$$\begin{aligned} \mathbf{v}_e(\boldsymbol{\xi}) &= [N(\boldsymbol{\xi})]_{2 \times 6} [\mathbf{v}_e]_{6 \times 1} = \begin{bmatrix} N_1(\boldsymbol{\xi})\mathbf{I} & N_2(\boldsymbol{\xi})\mathbf{I} & N_3(\boldsymbol{\xi})\mathbf{I} & N_4(\boldsymbol{\xi})\mathbf{I} \end{bmatrix} \begin{bmatrix} \mathbf{v}_{e1} \\ \mathbf{v}_{e2} \\ \mathbf{v}_{e3} \\ \mathbf{v}_{e4} \end{bmatrix}, \\ p_e(\boldsymbol{\xi}) &= [N(\boldsymbol{\xi})]_{1 \times 3} [p_e]_{3 \times 1} = \begin{bmatrix} N_1(\boldsymbol{\xi}) & N_2(\boldsymbol{\xi}) & N_3(\boldsymbol{\xi}) \end{bmatrix} \begin{bmatrix} p_{e1} \\ p_{e2} \\ p_{e3} \end{bmatrix}, \\ T_e(\boldsymbol{\xi}) &= [N(\boldsymbol{\xi})]_{1 \times 3} [T_e]_{3 \times 1} = \begin{bmatrix} N_1(\boldsymbol{\xi}) & N_2(\boldsymbol{\xi}) & N_3(\boldsymbol{\xi}) \end{bmatrix} \begin{bmatrix} T_{e1} \\ T_{e2} \\ T_{e3} \end{bmatrix}. \end{aligned} \quad (6.37)$$

Where \mathbf{I} is a 2×2 unit matrix and $\mathbf{v}_{ei} = [v_{eix}, v_{eiy}]^T$. Introducing this discretization in the weak form (6.29) and (6.32), we obtain a linear system detailed below. The derivation of each matrix is detailed in Appendix.

-Stokes flow problem:

$$\begin{aligned} [V^*]^T [\mathbb{K}_s] [V] + [V^*]^T [\mathbb{K}_f] [V] + [V^*]^T [\mathbb{B}] [P] &= [V^*]^T [\mathbb{J}], \\ [P^*]^T [\mathbb{B}]^T [V] &= 0. \end{aligned} \quad (6.38)$$

The normal velocity on the solid surface is 0, and this condition will be considered into the Lagrangian boundary condition matrix.

-Heat transferring problem:

$$[T^*]^T [\mathbb{K}] [T] + [T^*]^T [\mathbb{D}] [T] + [T^*]^T [\mathbb{R}] [T] = [T^*]^T [\mathbb{N}]. \quad (6.39)$$

6.2.4 Periodic boundary condition

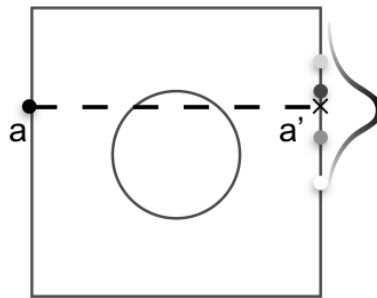


Figure 6.3: Periodic boundary condition

The periodic conditions on the boundary of the unit cell are used for the velocity, pressure and temperature fields. Consider first the problem of Stokes flow. The periodic conditions are applied for the velocity and pressure field. Let us consider a point a on the boundary of the

unit cell and let us define by a' its projection on the opposite side (see Fig. 6.3). The periodic conditions are:

$$\begin{aligned} \mathbf{v}(\mathbf{x}_a) - \mathbf{v}(\mathbf{x}_{a'}) &= \mathbf{0}, \\ p(\mathbf{x}_a) - p(\mathbf{x}_{a'}) &= 0. \end{aligned} \tag{6.40}$$

In the problem of convection-diffusion we work with the total temperature field:

$$T'(\mathbf{x}) = \mathbf{E} \cdot \mathbf{x} + T(\mathbf{x}). \tag{6.41}$$

where \mathbf{E} is the applied macroscopic gradient of temperature and $T(\mathbf{x})$ is the periodic temperature. Obviously, the term $\mathbf{E} \cdot \mathbf{x}$ is not periodic, so $T'(\mathbf{x})$ is not periodic.

It follows that:

$$\nabla T'(\mathbf{x}) = \mathbf{E} + \nabla T(\mathbf{x}). \tag{6.42}$$

The average of $\nabla T'(\mathbf{x})$ over Ω is the macroscopic temperature gradient \mathbf{E} :

$$\langle \nabla T'(\mathbf{x}) \rangle = \frac{1}{|\Omega|} \int_{\Omega} \nabla T'(\mathbf{x}) d\mathbf{x} = \mathbf{E}. \tag{6.43}$$

The periodicity condition for the temperature field is:

$$T'(\mathbf{x}_a) - T'(\mathbf{x}_{a'}) = \mathbf{E} \cdot (\mathbf{x}_a - \mathbf{x}_{a'}). \tag{6.44}$$

A simple way to apply the periodic conditions is to use a regular mesh at the boundary of the cell. This constitutes sometimes a too high constraint for meshes generators. To apply the boundary condition to arbitrary mesh, we use a method based on the Gaussian kernel to impose the periodic boundary condition. In this method, a point on the boundary is linked to all points on the opposite side with different weights. These weights can be estimated by the

Gaussian kernel. The Gaussian kernel function is given by:

$$G(\mathbf{x}_1, \mathbf{x}_0) = \exp\left(-\frac{\|\mathbf{x}_1 - \mathbf{x}_0\|^2}{2\sigma^2}\right), \quad (6.45)$$

where $\|\mathbf{x}_1 - \mathbf{x}_0\|^2$ is the squared Euclidean distance between two points \mathbf{x}_1 and \mathbf{x}_0 and σ is a parameter. The range of $G(\mathbf{x}_1, \mathbf{x}_0)$ is comprised between 0 and 1. The quantity $G(\mathbf{x}_1, \mathbf{x}_0)$ tends to 1 when \mathbf{x}_1 tends to \mathbf{x}_0 and tends to 0 otherwise. The parameter σ can adjust the decrease rate of $G(\mathbf{x}_1, \mathbf{x}_0)$. We denote the coordinates of all the opposite points by \mathbf{x}_i . The weight of every opposite points $w(\mathbf{x}_i, \mathbf{x}_{a'})$ is:

$$w(\mathbf{x}_i, \mathbf{x}_{a'}) = \frac{G(\mathbf{x}_i, \mathbf{x}_{a'})}{\sum_i G(\mathbf{x}_i, \mathbf{x}_{a'})}. \quad (6.46)$$

The periodic conditions are rewritten as:

$$\begin{aligned} \mathbf{u}(\mathbf{x}_a) - \sum_i w(\mathbf{x}_i, \mathbf{x}_{a'}) \mathbf{u}(\mathbf{x}_i) &= \mathbf{0}, \\ p(\mathbf{x}_a) - \sum_i w(\mathbf{x}_i, \mathbf{x}_{a'}) p(\mathbf{x}_i) &= 0, \\ T(\mathbf{x}_a) - \sum_i w(\mathbf{x}_i, \mathbf{x}_{a'}) T(\mathbf{x}_i) &= \mathbf{E} \cdot (\mathbf{x}_a - \mathbf{x}_{a'}). \end{aligned} \quad (6.47)$$

6.3 Results and discussion

6.3.1 Preliminary works and benchmark

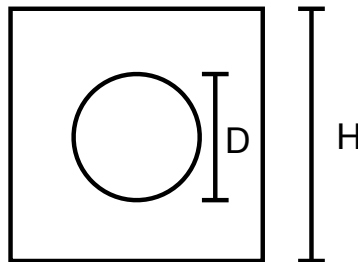


Figure 6.4: Unit cell of the periodic array of cylinders.

We consider a regular array of cylinders with the diameter D . The unit cell has the dimension 1 along each space direction. The fluid flows around the cylinders.

We determine the number of elements to obtain a good accuracy of the solution. The computation are performed with dynamic viscosity $\mu = 1$ and the thermal conductivity of the fluid $k_1 = 1$. The thermal conductivity of the solid is also $k_2 = 1$. The norm of the macroscopic pressure gradient, $|\mathbf{J}|$, is equal to 100 and the pressure gradient is applied in direction x. The macroscopic temperature gradient is equal to 1 along the x-direction and 0 along y-direction. The results are shown in Fig. 6.5. In figure a and b we provide the distribution of the velocity and temperature in the unit cell. in figure c and d we display the value of the permeability and the macroscopic diffusivity as function of the number of elements. The convergence test shows that 5000 elements is sufficient to obtain a good accuracy of the FEM solution. Validation of

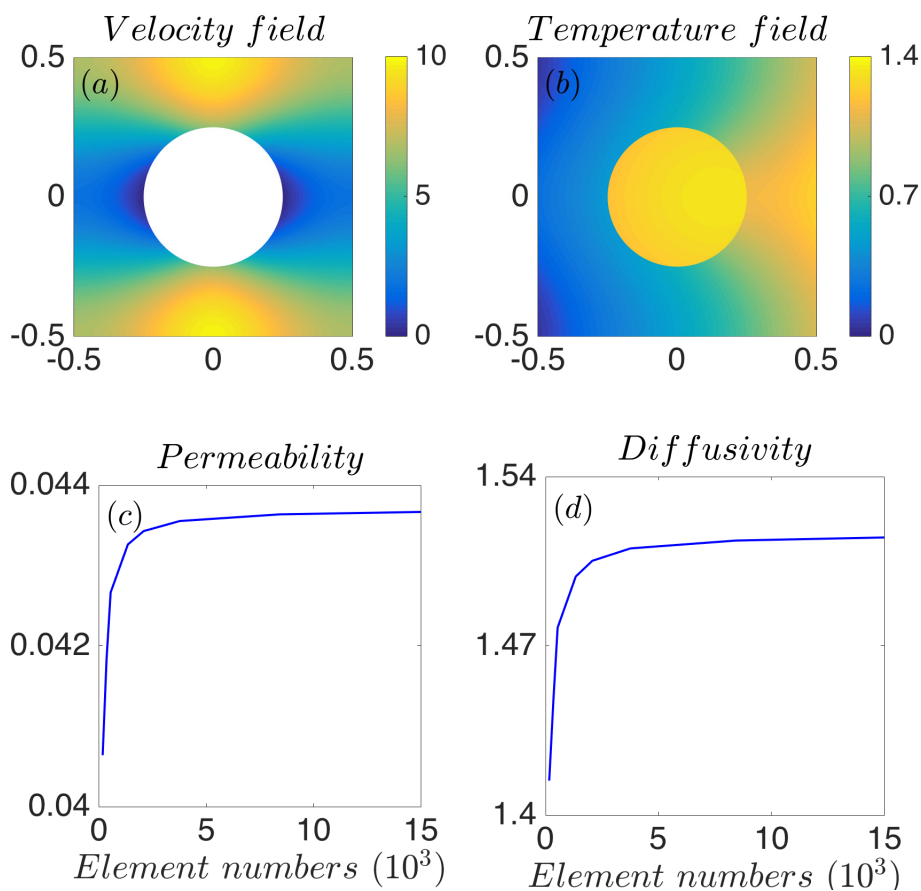


Figure 6.5: (a) the velocity distribution along x-direction, (b) the temperature distribution, (c) permeability as function of the number of elements, (d) macroscopic diffusivity as function of the number of elements.

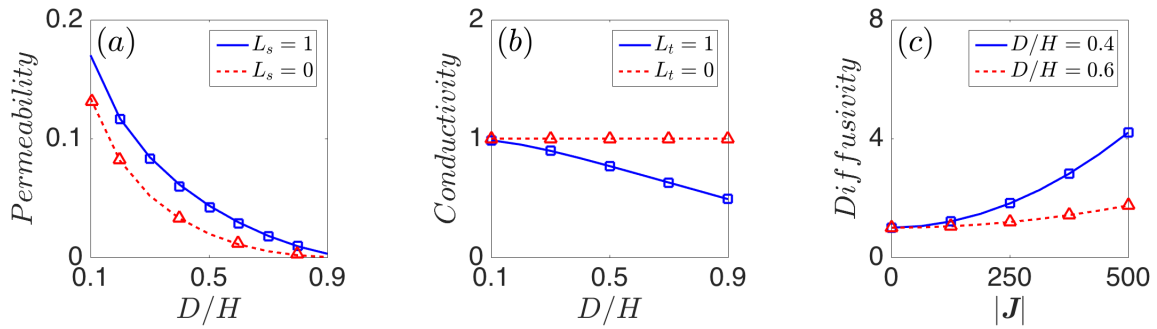


Figure 6.6: Solid line and dash line represent the FEM results, “ \square ” and “ \triangle ” discrete values represent the FFT results. (a) the permeability along x-direction under a function of the cylinder diameter, (b) conductivity along x-direction (without convection term) as a function of the cylinder diameter, (c) macroscopic diffusivity along x-direction (with convection term) as a function of the ratio the applied pressure gradient.

the FEM code is now provided by the comparison with existing results obtained with the FFT method. For instance, in [142], the no-slip Stokes flow problem and the convection-diffusivity problem with a perfect interface have been computed with the FFT method. In [94] the problem of heat transfer with an imperfect interface but no convection term has been computed with the FFT method. The FEM code is compared with some particular situations with FFT solutions in Fig. 6.6. Figure (a) gives the permeability as the function of D/H for the FFT and the FEM in the case of non-slip flow ($L_s = 0$) and in the case of a slip flow ($L_s = 1$). On figure (b), We provide the effective conductivity (without convection term) as function of D/H for a perfect inclusion ($L_t = 0$) and in the case of an imperfect inclusion ($L_t = 1$). Obviously, when in the case of a perfect inclusion, since the two medium have the same conductivity, the effective conductivity is also equal to 1 for a perfect interface. In the case of an imperfect interface, ($L_s = 1$) the conductivity depends on the size of the inclusion. In the last figure (c), we provide the effective diffusivity as a function of $|\mathbf{J}|$ for two values of the ratio D/H . On each figure, a good agreement between the FFT and the FEM solutions is observed.

p [bar]	ρ [kg/m ³]	C_p [kJ/(kg · K)]	μ [Pa · s]	C_k [W/(m · K)]
1	0.552	2.370	12.8e-6	0.0413
2	1.105	2.374	12.8e-6	0.0415
5	2.769	2.386	12.8e-6	0.0417
10	5.563	2.406	12.8e-6	0.0419

Table 6.1: Mass density ρ , heat capacity C_p , dynamic viscosity μ and thermal conductivity C_k of methane under different pressure p at 350K of CH₄ gas.

6.3.2 Determination of permeability and diffusivity for CH₄

In this subsection we determine the transport properties of CH₄ gas through a regular array of graphite fibers. We consider that the temperature in the pores is at 350 K. Through the literatures [51, 148], we determined the other constants of CH₄ gas under different pressure. These constants are presented in Tab. 6.1. From the table, we observe that only the mass density is sensitive to the value of the pressure which vary from 1 to 10 bar. The thermal conductivity of graphite fiber $k_2 = 24$ W/(m · K) in the Ref. [68], and the thermal conductivity of CH₄ flow $k_1 = C_k$ following the values in the Tab. 6.1. The interface coefficients are given by DM simulations in Ref. [84], the dimensionless friction coefficient is $\beta_1 = 0.093$ and the dimensionless thermal resistance coefficient is $\beta_2 = 0.361$. The slip length L_s and jump length L_t can be determined by following relations:

$$L_s = \frac{\mu}{\beta_1 \rho \zeta}, \quad L_t = \frac{m C_k}{2 \beta_2 \rho \zeta k_B}, \quad \zeta = \sqrt{\frac{2 k_B T}{\pi m}}. \quad (6.48)$$

We aim to determine for which value of the pore size and value of the applied pressure gradient, the slip/jump interface conditions and the convection will affect the thermal diffusivity of pore simultaneously. The wall-slip effects are starts to become dominant when the Knudsen number verify $0.01 < Kn < 0.1$ while the convection term affect the diffusivity when the Peclet number comply with $Pe > 0.5$. In our example, we fix the ratio D/H by 0.5, and we apply the pressure gradient $|\mathbf{J}| = 100$ MPa/m. The size of the unit cell vary from 1 μ m to 10 μ m. Figs. 6.7 show the variations of Kn and Pe as function of H for various values of the pressure. It is observed

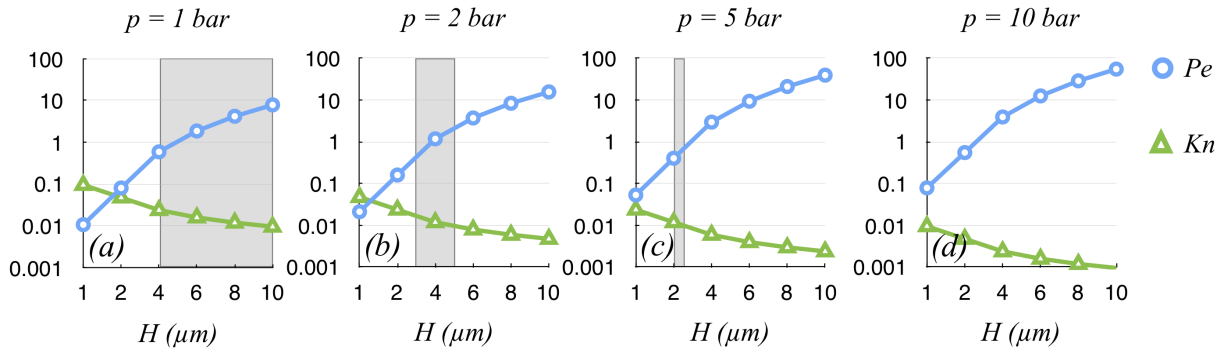


Figure 6.7: Variations of Pe and Kn with the dimension of the unit cell, H , for various values of the pressure.

that, when H increases, Pe also increases but Kn decreases. When the pressure is 1 bar, the wall-slip and convection are dominant H is comprised between 4 and 10 μm . The interval decrease when increasing the value of the pressure. For the interval is comprised between 3 and 5 μm when $p = 2$ bar, from 2 to 3 μm when $p = 5$ bar. However, when the pressure is 10 bar, it is not possible to observe simultaneously the wall-slip and the convection effects.

In the next, we take the pressure is $p = 1$ bar and the dimension of the unit cell is $H = 10\mu m$. The results are provided as a function of the porosity $\Phi = \pi D^2/(4H)$. The variations of the permeability and of the macroscopic diffusivity are shown in Fig.6.8. In Fig6.8a, we observe that the permeability increases with the porosity. Fig. 6.8c shows the ratio between the permeability with no-slip (K_P^*) and the slip condition (K_P). We observe that the permeability is strongly underestimated when the no-slip condition is used and when the porosity is low. When the value of the porosity is larger, the slip effect is less significant. This can be explained by the fact that as the porosity increases, the area of the interface decreases. However, the effect of the porosity on the macroscopic diffusivity is more complex. As shown in Fig. 6.8b, the diffusivity of the pore first decreases when increasing the porosity and then increases when the porosity is larger than 0.7. To understand how the slip and the temperature jump conditions affect the macroscopic diffusivity, we represent in Fig6.8d the ratio between the diffusivity obtained with/without slip and/or temperature jump and the macroscopic diffusivity with both slip and temperature jump. We observe that for small values of the porosity, although the no-slip

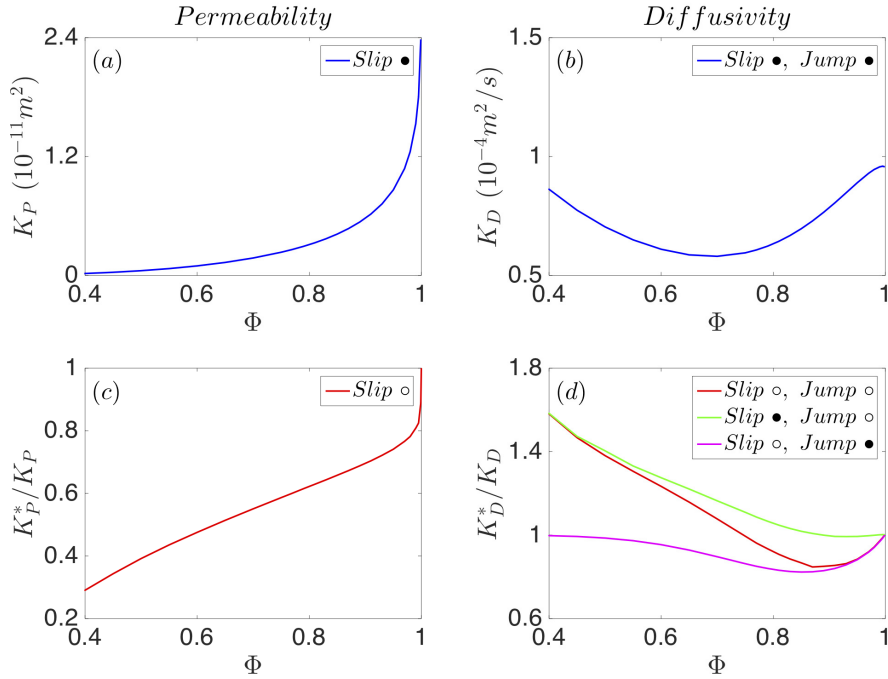


Figure 6.8: The "•" means "with" the boundary condition, the "◦" means without the boundary condition. (a) Variations of the permeability with the porosity Φ , (b) macroscopic diffusivity of a function of the porosity Φ , (c) relative permeability for no-slip/jump condition (with respect to the permeability with slip condition). (d) relative macroscopic diffusivity with no-slip/jump, slip/no jump, no slip/no jump with respect to the permeability with slip and jump condition.

condition underestimate the pore permeability, the velocity is too small to have a significant convection effect, so only the jump condition dominates in the diffusivity problem. But, as the porosity increases, the convection effect become more and more important, the impact of the jump condition on the diffusivity is relatively reduced. Therefore, the curve of no-slip/no-jump condition is closed to the curve of slip/no-jump condition at small values of the porosity but clearly differs from the curve corresponding to no-slip/jump condition. Finally, when the porosity is close to 1, all the interface effects gradually vanish. To further understand the effect of the convection term on the diffusivity, we study the variations of the macroscopic diffusivity with the applied pressure gradient for various values of the porosity. From Fig. 6.9, we find that when the macro pressure gradient along the x-direction, J_x , is small, the average velocity in the pore is close to 0 and the convection term has no significant effect on the macroscopic diffusivity. When J_x increases, the velocity increases, and the convection term becomes very significant when the porosity is large enough. Indeed, for a pressure gradient of $400 MPa/m$,

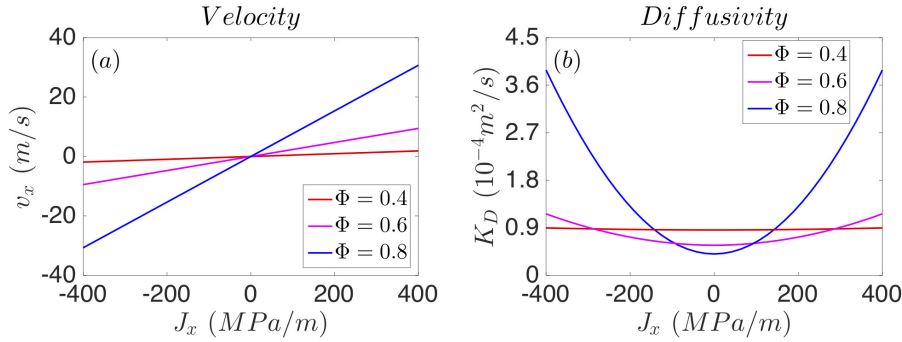


Figure 6.9: (a) Average velocity as a function of the applied macroscopic pressure gradient, (b) macroscopic diffusivity as a function of the applied macroscopic pressure gradient.

we observed that the value of the diffusivity compared to the diffusivity without convection is amplified by a factor 10 for $\Phi = 0.8$, a factor 2 times for $\Phi = 0.6$ and only 5% for $\Phi = 0.4$.

6.4 Conclusion

In this chapter we have determined the heat and mass transport properties of a regular array of cylinders. The surface effects include the wall-slip and temperature jump at the interface between the solid and the fluid has been accounted on the fluid flow and thermal conduction in a finite element simulation. It has been found that the wall-slip condition significantly increases the local velocity and then the permeability of the porous medium. The wall-slip also affects the thermal diffusivity of the saturated porous medium due to the convection term. Also, the temperature jump at the solid-liquid interface affects the thermal diffusivity. Both effects have been analyzed in the case of graphite cylinders and CH_4 gas. It have found that the wall-slip and temperature jump conditions can simultaneously affect the macroscopic thermal diffusion tensor of the porous medium pore for pores with the dimension of $10 \mu\text{m}$ and at the atmospheric pressure. When the porosity is too small (<0.6), the velocity is too small and only the jump condition significantly affects the diffusivity. For higher values of the porosity, the convection term and the wall-slip clearly affect the macroscopic diffusion. When the porosity is close to 1, both wall-slip and temperature jump condition effects vanish.

Appendix

1. Elementary matrix for 2D triangle element

-Stokes flow problem:

We note the number of element in fluid phase by N_f and the number of element at interface by N_{fs} . We compute the integrals Eq. (6.29) as following:

$$\begin{aligned}
 \int_{\Omega} 2\boldsymbol{\varepsilon}^*(\mathbf{x})\boldsymbol{\varepsilon}(\mathbf{x})d\mathbf{x} &= \sum_1^{N_f} \int_{\Omega_e} 2\boldsymbol{\varepsilon}^*(\mathbf{x})\boldsymbol{\varepsilon}(\mathbf{x})d\mathbf{x} \\
 &= \sum_1^{N_f} \int_{\Omega_r} 2\boldsymbol{\varepsilon}_e^*(\mathbf{x})\boldsymbol{\varepsilon}_e(\mathbf{x})|\mathcal{J}_e|d\boldsymbol{\xi} \\
 &= \sum_1^{N_f} [V_e^*]^T (2|\mathcal{J}_e|[E_e]^T[E_e]) [V_e] \\
 &= \sum_1^{N_f} [V_e^*]^T [\mathbb{K}_e^f][V_e], \tag{6.49}
 \end{aligned}$$

$$\begin{aligned}
 \int_{\Omega} \mathbf{v}^*(\mathbf{x})\nabla p(\mathbf{x})d\mathbf{x} &= \sum_1^{N_f} [V_e^*]^T (|\mathcal{J}_e|[N]^T[B]) [P_e] \\
 &= \sum_1^{N_f} [V_e^*]^T [\mathbb{B}_e][V_e], \tag{6.50}
 \end{aligned}$$

$$\int_{\Omega} \mathbf{v}^*(\mathbf{x}) \cdot \mathbf{J}d\mathbf{x} = \sum_1^{N_f} [V_e^*]^T [\mathbb{J}_e] \tag{6.51}$$

Where, $[\mathbb{J}_e] = (|J_s|/6)[J_x, J_y, J_x, J_y, J_x, J_y, J_x, J_y]^T$. For the integral on the interface Γ , we use interpolation on segment element:

$$\begin{aligned} \mathbf{v}_e(\xi) &= [R_v(\xi)]_{2 \times 4} [V_s]_{4 \times 1} = \begin{bmatrix} S_1(\xi) \mathbf{I} & S_2(\xi) \mathbf{I} \end{bmatrix} \begin{bmatrix} \mathbf{v}_{s1} \\ \mathbf{v}_{s2} \end{bmatrix}, \\ v_n &= [n]_{1 \times 2}^T [R_v(\xi)]_{2 \times 4} [V_s]_{4 \times 1}, \quad [n] = \begin{bmatrix} n_x \\ n_y \end{bmatrix} \end{aligned} \quad (6.52)$$

The integral over the interface is given by:

$$\int_{\Gamma} -\frac{2}{L_s} [\mathbf{v}^*(\mathbf{x}) \cdot \mathbf{v}(\mathbf{x})] d\mathbf{x} = \sum_1^{N_{fs}} [V_e^*]^T [\mathbb{K}_e^s] [V_e]. \quad (6.53)$$

-Heat transferring problem:

Let us denote by N_e the total number of element and the total segment on the boundary $\partial\Omega$ by N_s . The first integral in Eq.(6.32) reads:

$$\begin{aligned} \int_{\Omega} \mathbf{q}(\mathbf{x}) \nabla T^*(\mathbf{x}) d\mathbf{x} &= \int_{\Omega} \mathbf{k}(\mathbf{x}) \nabla T(\mathbf{x}) \nabla T^*(\mathbf{x}) d\mathbf{x} \\ &= \sum_1^{N_e} \int_{\Omega_e} \mathbf{k}(\mathbf{x}) \nabla T(\mathbf{x}) \nabla T^*(\mathbf{x}) d\mathbf{x} \\ &= \sum_1^{N_e} \int_{\Omega_r} \mathbf{k}_e \nabla T_e \nabla T_e^* |\mathcal{J}_e| d\xi \\ &= \sum_1^{N_e} [T_e^*]^T \left(\frac{1}{2} |\mathcal{J}_e| [B]^T [k_e] [B] \right) [T_e] \\ &= \sum_1^{N_e} [T_e^*]^T \left(\frac{k}{2|\mathcal{J}_e|} [B_0]^T [k_e] [B_0] \right) [T_e] \\ &= \sum_1^{N_e} [T_e^*]^T [\mathbb{K}_e] [T_e], \end{aligned} \quad (6.54)$$

where $[\mathbb{K}_e] = \left(\frac{k}{2|\mathcal{J}_e|} [B_0]^T [k_e] [B_0] \right)$, and can be computed by:

$$[B_0] = |\mathcal{J}_e| [B] = \begin{bmatrix} y_2 - y_3, & y_3 - y_1, & y_1 - y_2 \\ x_3 - x_2, & x_1 - x_3, & x_2 - x_1 \end{bmatrix}. \quad (6.55)$$

The 2nd integral become:

$$\begin{aligned} \int_{\Omega} \mathbf{v}(\mathbf{x}) \nabla T(\mathbf{x}) T^*(\mathbf{x}) d\mathbf{x} &= \sum_1^{N_e} \int_{\Omega_e} \mathbf{v}(\mathbf{x}) \nabla T(\mathbf{x}) T^*(\mathbf{x}) d\mathbf{x} \\ &= \sum_1^{N_e} \int_{\Omega_r} \mathbf{v}_e(\boldsymbol{\xi}) \nabla T_e T_e^*(\boldsymbol{\xi}) |\mathcal{J}_e| d\boldsymbol{\xi} \\ &= \sum_1^{N_e} [T_e^*]^T \left(|\mathcal{J}_e| \int_{\Omega_r} [N(\boldsymbol{\xi})]^T [V_e(\boldsymbol{\xi})]^T [B] d\boldsymbol{\xi} \right) [T_e] \\ &= \sum_1^{N_e} [T_e^*]^T \left(\int_{\Omega_r} [N(\boldsymbol{\xi})]^T [V_e(\boldsymbol{\xi})]^T [B_0] d\boldsymbol{\xi} \right) [T_e] \\ &= \sum_1^{N_e} [T_e^*]^T [\mathbb{D}_e] [T_e], \end{aligned} \quad (6.56)$$

where $[\mathbb{D}_e] = \int_{\Omega_r} [N(\boldsymbol{\xi})]^T [V_e(\boldsymbol{\xi})]^T d\boldsymbol{\xi} [B_0]$, and:

$$\int_{\Omega_r} [N(\boldsymbol{\xi})]^T [V_e(\boldsymbol{\xi})]^T d\boldsymbol{\xi} = \frac{1}{24} \begin{bmatrix} 2v_{ex1} + v_{ex2} + v_{ex3}, & 2v_{ey1} + v_{ey2} + v_{ey3} \\ v_{ex1} + 2v_{ex2} + v_{ex3}, & v_{ey1} + 2v_{ey2} + v_{ey3} \\ v_{ex1} + v_{ex2} + 2v_{ex3}, & v_{ey1} + v_{ey2} + 2v_{ey3} \end{bmatrix}. \quad (6.57)$$

In order to compute the integral over the interface Γ , we use cohesive element. the temperature jump on a segment can be expressed as:

$$[T_s(\xi)]_{\Gamma} = [R(\xi)]_{1 \times 4} [T_s^{FS}]_{4 \times 1} = \begin{bmatrix} S_1(\xi), & -S_1(\xi), & S_2(\xi), & -S_2(\xi) \end{bmatrix} \begin{bmatrix} T_{s1}^F \\ T_{s1}^S \\ T_{s2}^F \\ T_{s2}^S \end{bmatrix}. \quad (6.58)$$

The 3rd integral can then be read:

$$\begin{aligned}
\int_{\Gamma} [T(\mathbf{x})]_{\Gamma} k_t^{-1} [T^*(\mathbf{x})]_{\Gamma} d\mathbf{x} &= \sum_1^{N_s} \int_{\Gamma_s} [T(\mathbf{x})]_{\Gamma} k_t^{-1} [T^*(\mathbf{x})]_{\Gamma} d\mathbf{x} \\
&= \sum_1^{N_s} \int_{\Gamma_r} [T_s(\boldsymbol{\xi})]_{\Gamma} k_t^{-1} [T_s^*(\boldsymbol{\xi})]_{\Gamma} |\mathcal{J}_s| d\boldsymbol{\xi} \\
&= \sum_1^{N_s} [T_s^{*MI}]^T \left(k_t^{-1} |\mathcal{J}_s| \int_{\Gamma_r} [R(\boldsymbol{\xi})]^T [R(\boldsymbol{\xi})] d\boldsymbol{\xi} \right) [T_s^{MI}] \\
&= \sum_1^{N_s} [T_s^{*MI}]^T [\mathbb{R}_s] [T_s^{MI}], \tag{6.59}
\end{aligned}$$

where N_s means the number of segment at the interface and the matrix $[\mathbb{R}_s]$ is given by:

$$[\mathbb{R}_s] = \frac{|\mathcal{J}_s|}{6k_t} \begin{bmatrix} 2, & -2, & 1, & -1 \\ -2, & 2, & -1, & 1 \\ 1, & -1, & 2, & -2 \\ -1, & 1, & -2, & 2 \end{bmatrix}. \tag{6.60}$$

The 4th integral can be read:

$$\begin{aligned}
\int_{\Omega} bT^*(\mathbf{x}) d\mathbf{x} &= \sum_1^{N_e} \int_{\Omega_e} bT^*(\mathbf{x}) d\mathbf{x} \\
&= \sum_1^{N_e} \int_{\Omega_r} bT_e^*(\boldsymbol{\xi}) |\mathcal{J}_e| d\boldsymbol{\xi} \\
&= \sum_1^{N_e} [T_e^*]^T \left(b |\mathcal{J}_e| \int_{\Omega_r} [N(\boldsymbol{\xi})]^T d\boldsymbol{\xi} \right) \\
&= \sum_1^{N_e} [T_e^*]^T [\mathbb{N}_e], \tag{6.61}
\end{aligned}$$

where $[\mathbb{N}_e] = b|\mathcal{J}_e| \int_{\Omega_r} [N(\boldsymbol{\xi})]^T d\boldsymbol{\xi}$, and the integral of $[N(\boldsymbol{\xi})]^T$ is:

$$\int_{\Omega_r} [N(\boldsymbol{\xi})]^T d\boldsymbol{\xi} = \begin{bmatrix} \frac{1}{6} \\ \frac{1}{6} \\ \frac{1}{6} \end{bmatrix}. \quad (6.62)$$

Chapter 7

Conclusions and perspectives

The goal of this thesis is to study the origin of the velocity slip and temperature jump phenomena from the fluid-solid interaction at the atomic scale and their effects on the fluid transport in micro/nanoporous media. The contribution of the thesis can be attributed to the three following aspects: **I.** Understanding the friction of molecular liquids in nanochannel composed of graphite. **II.** Modeling collisions between gas and solid wall and investigating the relation with the slip and jump phenomena. **III.** Numerical simulations and homogenization of heat and mass transports of fluid in micropore under slip/jump conditions. The different conclusions are developed below for each contribution.

Orientation dependence friction in strained graphene/graphite system. Due to the considerable slippage of fluid confined in graphite nanopores, the permeability of nano and micropores can be enhanced significantly. Using molecular dynamics simulations, we investigated the friction of three molecular fluids, namely water, carbon dioxide and methane, confined between two graphene layers. The friction tensor was determined via Green-Kubo formula, a time correlation integral.

Our simulation results show that the friction coefficients strongly depend on the strain magni-

tude and direction of the graphene. Numerical evidences also show that the anisotropy effect is more remarkable for the aspherical shape molecules like H_2O and CO_2 . Investigation on the structure and dynamics of those liquids revealed that the relaxation time increases considerably with strain and contributes to an important part in the increase of the friction. The contribution of the present work helps better understanding and modeling the friction between liquids and anisotropic surfaces.

Stochastic modeling of gas-wall interaction. Different from the liquids confined in nanochannel, the velocity slip and the temperature jump of gas flow on solid wall are due to the rarefaction of the gas. Based on MD simulations, we investigated following four systems: CH_4 -C, CO_2 -C, Ar-Au, He-Au. From independent simulations of collisions, we collected pre- and post-collision velocity data of gas molecules. The simulation results show that the reflection of CH_4 , CO_2 on graphite and of Ar on gold varies from specular to diffusive when the roughness increases. In contrast, He gas atoms reflect on the gold surface in a nearly elastic manner.

We investigated different methods to compute the friction coefficient and thermal resistance coefficients from the incident-reflective velocity of gas molecules. Since conventional scattering kernels, like Maxwell or CL, cannot guarantee the accuracy in determining these coefficients, we proposed the use of NP and GM kernels. The friction and thermal resistance coefficients obtained by the correlation methods, by the CL, NP and GM kernels are consistent with the results of MD simulations. In particular, we found the GM kernel has the best performance.

Homogenization of heat and mass transports of fluid in micropores. In the study of the surface effect including the velocity slip and the temperature jump on the heat and mass transports of fluid in porous media. Due to the slip condition, the permeability of nano and micropores can be enhanced several times or even several hundred times. This condition can fundamentally affect the thermal diffusivity of saturated porous media by means of convection. On the other hand, the temperature discontinuity at the solid-liquid boundary also profoundly

affects the thermal conductivity of porous media. With reference to the results of the fast Fourier transform method, we have developed a finite element code to compute the permeability and the diffusivity of an array of cylinder with the wall-slip and the temperature jump.

Using the parameters obtained in the MD study and literatures, we investigated the transport of methane gas in the graphite pores. With the pressure and the pressure gradient unchanged, as the characterized size of pore increases, the Peclet number increases but the Knudsen number decreases. Finally, we found that the slip/jump conditions and the convection can simultaneously and significantly affect the thermal diffusion of CH_4 in graphite pores of about $10 \mu\text{m}$ under one atmospheric pressure. Numerical evidences show that at a characterized size of $10 \mu\text{m}$, when the porosity is too small (<0.6) and because the average speed is too small, the jump condition is the main factor affecting the diffusivity. As the porosity increases, the convection begins to affect the diffusion, so the slip condition becomes important. But when the porosity is too large (close to 1), both slip and jump conditions are gradually losing the influence on the diffusivity. The contribution of this part of work helps better understanding and modeling the fluid in nano and micropores whose fluid-solid interface condition is very different from macroporous media.

Perspectives. From the outcome of the thesis, there are numerous directions to pursuit in future works. **I.** The surface of a pore is usually rough and random. Using fractal surface and one of the scattering kernel that we proposed, we could simulate gas-solid collisions at the mesoscale. By this way, we can study how a realistic surface can affect the interfacial slip/jump coefficients. **II.** We could implement the scattering kernel in a simulation code to study heat and mass transfers in channels and porous media. The accuracy of the kernel will guarantee the accuracy of the simulation results and will promise new interesting results. **III.** Another aspect to explore is the adsorption of gas atoms at a solid surface. In this case, the collisions are no longer independent and the residential time must be considered. Developing statistical models via learning methods to capture this issues is vital for a better understanding of the physical phenomena. **IV.** Based on the current FE simulations with slip/jump conditions, in

the future, people could use topological optimizations to design better nanothermal devices.

Bibliography

- [1] J. L. Abascal and C. Vega. A general purpose model for the condensed phases of water: Tip4p/2005. *J. Chem. Phys.*, 123(23):234505, 2005.
- [2] F. Alcocer, V. Kumar, and P. Singh. Permeability of periodic porous media. *Phys. Rev. E*, 59(1):711, 1999.
- [3] F. Alcocer and P. Singh. Permeability of periodic arrays of cylinders for viscoelastic flows. *Phys. Fluids*, 14(7):2578–2581, 2002.
- [4] B. J. Alder and T. E. Wainwright. Studies in molecular dynamics. i. general method. *J. Chem. Phys.*, 31(2):459–466, 1959.
- [5] G. Allaire. *Numerical analysis and optimization: an introduction to mathematical modelling and numerical simulation*. Oxford university press, 2007.
- [6] M. Allen and D. Tildesley. *Computer Simulation of Liquids*. Oxford University Press, 1989.
- [7] J.-L. Auriault. Upscaling heterogeneous media by asymptotic expansions. *J. Eng. Mech.*, 128(8):817–822, 2002.
- [8] J.-L. Auriault, C. Boutin, and C. Geindreau. *Homogenization of coupled phenomena in heterogenous media*, volume 149. John Wiley & Sons, 2010.
- [9] J.-L. Auriault and E. Sanchez-Palencia. Etude du comportement macroscopique d’un milieu poreux saturé déformable. *J. méc.*, 16(4):575–603, 1977.

- [10] I. Babuška. Error-bounds for finite element method. *Numer. Math.*, 16(4):322–333, 1971.
- [11] J.-L. Barrat and L. Bocquet. Large slip effect at a nonwetting fluid-solid interface. *Phys. Rev. Lett.*, 82(23):4671–4674, 1999.
- [12] J.-L. Barrat et al. Influence of wetting properties on hydrodynamic boundary conditions at a fluid/solid interface. *Faraday Discuss.*, 112:119–128, 1999.
- [13] M. Bazant and O. Vinogradova. Tensorial hydrodynamic slip. *J. Fluid Mech.*, 613:125–134, 2008.
- [14] A. Bensoussan, J.-L. Lions, and G. Papanicolaou. *Asymptotic analysis for periodic structures*, volume 374. American Mathematical Soc., 2011.
- [15] A. L. Berdichevsky and Z. Cai. Preform permeability predictions by self-consistent method and finite element simulation. *Polym. Compos.*, 14(2):132–143, 1993.
- [16] G. A. Bird. Molecular gas dynamics. *NASA STI/Recon Technical Report A*, 76, 1976.
- [17] J.-F. Bloch and J.-L. Auriault. Heat transfer in nonsaturated porous media. modelling by homogenisation. *Transp. Porous Media*, 30(3):301–321, 1998.
- [18] P. E. Blöchl. Projector augmented-wave method. *Phys. Rev. B*, 50:17953–17979, Dec 1994.
- [19] L. Bocquet and J.-L. Barrat. Hydrodynamic boundary conditions, correlation functions, and kubo relations for confined fluids. *Phys. Rev. E*, 49:3079–3092, Apr 1994.
- [20] L. Bocquet and J.-L. Barrat. On the green-kubo relationship for the liquid-solid friction coefficient. *J. Chem. Phys.*, 139(4):–, 2013.
- [21] F. Brezzi. On the existence, uniqueness and approximation of saddle-point problems arising from lagrangian multipliers. *Rev. fr. autom. inform. rech. opér. , Anal. numér.*, 8(R2):129–151, 1974.

- [22] S. Brull, P. Charrier, and L. Mieussens. Gas-surface interaction and boundary conditions for the boltzmann equation. *Kin. Rel. Mod.*, 38(7):219–251, 2014.
- [23] S. Calinon. *Robot Programming by Demonstration: A Probabilistic Approach*. EPFL/CRC Press, 2009. EPFL Press ISBN 978-2-940222-31-5, CRC Press ISBN 978-1-4398-0867-2.
- [24] B.-Y. Cao, J. Sun, M. Chen, and Z.-Y. Guo. Molecular momentum transport at fluid-solid interfaces in mems/nems: a review. *Int. J. Mol. Sci.*, 10(11):4638–4706, 2009.
- [25] C. Cercignani. *Theory and application of the Boltzmann equation*. Scottish Academic Press, 1975.
- [26] C. Cercignani. *Rarefied gas dynamics: from basic concepts to actual calculations*, volume 21. Cambridge University Press, 2000.
- [27] C. Cercignani and M. Lampis. Kinetic models for gas-surface interaction. *Transport Theory Stat. Phys.*, 1(9):101–114, 1971.
- [28] D. Chandler. *Introduction to Modern Statistical Mechanics*. Oxford University Press, 1987.
- [29] S. Chapman and T. Cowling. *The mathematical theory of non-uniform gases: an account of the kinetic theory of viscosity, thermal conduction, and diffusion in gases*. Cambridge University Press, 1970.
- [30] A. Chizmeshya and E. Zaremba. Interaction of rare gas atoms with metal surface: a pseudo-potential approach. *Surf. Sci.*, 220:443–470, 1989.
- [31] A. Chizmeshya and E. Zaremba. The interaction of rare gas atoms with metal surfaces: a scattering theory approach. *Surf. Sci.*, 268:432–456, 1992.
- [32] F. G. Collins and E. Knox. Parameters of nocilla gas/surface interaction model from measured accommodation coefficients. *AIAA J.*, 32(4):765–773, 1994.

- [33] S. K. Dadzie and J. G. Méolans. Anisotropic scattering kernel: Generalized and modified maxwell boundary conditions. *J. Math. Phys.*, 45(5):1804–1819, 2004.
- [34] S. K. Dadzie and J. G. Méolans. Temperature jump and slip velocity calculations from an anisotropic scattering kernel. *Physica A*, 358(2–4):328 – 346, 2005.
- [35] M. P. de Lara-Castells, M. Bartolomei, A. O. Mitrushchenkov, and H. Stoll. Transferability and accuracy by combining dispersionless density functional and incremental post-hartree-fock theories: noble gases adsorption on coronene/graphene/graphite surfaces. *J. Chem. Phys.*, 143:194701, 2015.
- [36] M. P. de Lara-Castells, H. Stoll, B. Civalleri, M. Causà, E. Voloshina, A. O. Mitrushchenkov, and M. Pi. Communication: a combined periodic density functional and incremental wave-function-based approach for the dispersion-accounting time-resolved dynamics of ^4he nanodroplets on surfaces: ^4he /graphene. *J. Chem. Phys.*, 141(15):151102, oct 2014.
- [37] M. P. de Lara-Castells, H. Stoll, and A. O. Mitrushchenkov. Assessing the performance of dispersionless and dispersion-accounting methods: helium interaction with cluster models of the $\text{tio}_2(110)$ surface. *J. Phys. Chem. A*, 118(33):6367–6384, aug 2014.
- [38] F. Della Sala and A. Görling. Efficient localized hartree–fock methods as effective exact-exchange kohn–sham methods for molecules. *J. Chem. Phys.*, 115(13):5718–5732, 2001.
- [39] A. P. Dempster, N. M. Laird, and D. B. Rubin. Maximum likelihood from incomplete data via the em algorithm. *J. Royal Stat. Soc. Series B*, pages 1–38, 1977.
- [40] K. Doll, P. Pyykkö, and H. Stoll. Closed-shell interaction in silver and gold chlorides. *J. Chem. Phys.*, 109, 1998.
- [41] R. Dovesi, R. Orlando, A. Erba, C. M. Zicovich-Wilson, B. Civalleri, S. Casassa, L. Maschio, M. Ferrabone, M. De La Pierre, P. D’Arco, et al. Crystal14: A program for the

- ab initio investigation of crystalline solids. *Int. J. Quantum Chem.*, 114(19):1287–1317, 2014.
- [42] R. Dovesi, V. R. Saunders, C. Roetti, R. Orlando, C. M. Zicovich-Wilson, F. Pascale, B. Civalleri, K. Doll, N. M. Harrison, I. J. Bush, P. D’Arco, M. Llunel, M. Causà, and Y. Noël. CRYSTAL14 User’s Manual, Università Torino, Torino, 2014. <http://www.crystal.unito.it> (accessed May 20, 2018).
- [43] J. C. Eijkel and A. Van Den Berg. Nanofluidics: what is it and what can we expect from it? *Microfluid. Nanofluid.*, 1(3):249–267, 2005.
- [44] D. Evans and G. Morriss. *Statistical mechanics of nonequilibrium liquids*. Cambridge University Press, 2008.
- [45] K. Falk, F. Sedlmeier, L. Joly, R. R. Netz, and L. Bocquet. Molecular origin of fast water transport in carbon nanotube membranes: Superlubricity versus curvature dependent friction. *Nano Lett.*, 10(10):4067–4073, 2010.
- [46] K. Falk, F. Sedlmeier, L. Joly, R. R. Netz, and L. Bocquet. Ultralow liquid/solid friction in carbon nanotubes: Comprehensive theory for alcohols, alkanes, omcts, and water. *Langmuir*, 40(28):14261–14272, 2012.
- [47] D. Figgen, G. Rauhut, M. Dolg, and H. Stoll. Energy-consistent pseudopotentials for group 11 and 12 atoms: adjustment to multi-configuration dirac–hartree–fock data. *Chem. Phys.*, 311(1-2):227–244, 2005.
- [48] D. Frenkel and B. Smit. *Understanding Molecular Simulation: From Algorithms to Applications*. Academic Press, 2002.
- [49] A. L. Garcia and B. J. Alder. Generation of the chapman–enskog distribution. *J. Comput. Phys.*, 140(1):66–70, 1998.

- [50] A. M. Gardner, R. J. Plowright, M. J. Watkins, T. G. Wright, and W. Breckenridge. Theoretical study of the $x \sigma 2+$ states of the neutral cm–rg complexes (cm= coinage metal, cu, ag, and au and rg= rare gas, he–rn). *J. Chem. Phys.*, 132(18):184301, 2010.
- [51] I. Golubev. A bicalorimeter for determining the thermal conductivity of gases and liquids at high pressures and different temperatures. *Teploenergetika*, (12):78–82, 1963.
- [52] M. A. Gonzalez and J. L. F. Abascal. The shear viscosity of rigid water models. *J. Chem. Phys.*, 132, 2010.
- [53] H. Grad. Principles of the kinetic theory of gases. In *Thermodynamik der Gase/Thermodynamics of Gases*, pages 205–294. Springer, 1958.
- [54] R. Grenier, Q.-D. To, M. P. de Lara Castells, and C. Léonard. Argon interaction with gold surfaces: ab initio-assisted determination of pair Ar-Au potentials for molecular dynamics simulations. *J. Phys. Chem. A*, 119:6897–6908, 2015.
- [55] M. Hadj Nacer, I. Graur, and P. Perrier. Mass flow measurement through rectangular microchannel from hydrodynamic to near free molecular regimes. *Houille Blanche*, 4:49–54, 2011.
- [56] M. Hadj Nacer, I. Graur, P. Perrier, J. G. Méolans, and M. Wuest. Gas flow through microtubes with different internal surface coatings. *J. Vac. Sci. Technol. A*, 32:021601, 2014.
- [57] J. Hansen and I. McDonald. *Theory of simple liquids*. Academic Press, 2006.
- [58] J. G. Harris and K. H. Yung. Carbon dioxide’s liquid-vapor coexistence curve and critical properties as predicted by a simple molecular model. *J. Phys. Chem.*, 99(31):12021–12024, 1995.
- [59] T. Hastie, R. Tibshirani, and J. Friedman. The em algorithm. *The elements of statistical learning*, pages 236–243, 2001.

- [60] H. Helmholtz and G. v. Piotrowski. Üeber die reibung tropfbarer flüssigkeiten. *Sitz.-Ber. der k. Akad. d. Wiss. in Wien. Math. nat. Kl*, pages 607–658, 1860.
- [61] M. Hollander, D. A. Wolfe, and E. Chicken. *Nonparametric statistical methods*, volume 751. John Wiley & Sons, 2013.
- [62] J. K. Holt, H. G. Park, Y. Wang, M. Stadermann, A. B. Artyukhin, C. P. Grigoropoulos, A. Noy, and O. Bakajin. Fast mass transport through sub-2-nanometer carbon nanotubes. *Science*, 312(5776):1034–1037, 2006.
- [63] K. Hooman. Heat and fluid flow in a rectangular microchannel filled with a porous medium. *Int. J. Heat Mass Transf.*, 51(25-26):5804–5810, 2008.
- [64] K. Hooman. Slip flow forced convection in a microporous duct of rectangular cross-section. *Appl. Therm. Eng.*, 29(5-6):1012–1019, 2009.
- [65] M. Hossein Gorji and P. Jenny. A gas-surface interaction kernel for diatomic rarefied gas flows based on the cercignani-lampis-lord model. *Phys. Fluids*, 26(12):122004, 2014.
- [66] Z. E. Hughes, S. M. Tomasio, and T. R. Walsh. Efficient simulations of the aqueous bio-interface of graphitic nanostructures with a polarisable model. *Nanoscale*, 6:5438, 2014.
- [67] G. Hummer, J. C. Rasaiah, and J. P. Noworyta. Water conduction through the hydrophobic channel of a carbon nanotube. *Nature*, 414(6860):188, 2001.
- [68] R. Joven, R. Das, A. Ahmed, P. Roozbehjavan, and B. Minaie. Thermal properties of carbon fiber-epoxy composites with different fabric weaves. *SAMPE, Charleston, SC*, 2012.
- [69] S. K. Kannam, B. Todd, J. S. Hansen, and P. J. Daivis. How fast does water flow in carbon nanotubes? *J. Chem. Phys.*, 138(9):094701, 2013.
- [70] S. K. Kannam, B. D. Todd, J. S. Hansen, and P. J. Daivis. Slip flow in graphene nanochannels. *J. Chem. Phys.*, 135(14), 2011.

- [71] P. Kapitza. Heat transfer and superfluidity of helium ii. *Phys. Rev.*, 60(4):354, 1941.
- [72] G. Karniadakis, A. Beskok, and N. Aluru. *Microflows and nanoflows: fundamentals and simulation*, volume 29. Springer Science & Business Media, 2006.
- [73] L. Klinkenberg et al. The permeability of porous media to liquids and gases. In *Drilling and production practice*. American Petroleum Institute, 1941.
- [74] G. Kresse and D. Joubert. From ultrasoft pseudopotentials to the projector augmented-wave method. *Phys. Rev. B*, 59:1758–1775, 1999.
- [75] G. Kresse and J. Furthmüller. Efficient iterative schemes for ab initio total-energy calculations using a plane-wave basis set. *Phys. Rev. B*, 54:11169, 1996.
- [76] R. Kubo. Statistical-mechanical theory of irreversible processes. i. general theory and simple applications to magnetic and conduction problems. *J. Phys. Soc. Jpn.*, 12(6):570–586, 1957.
- [77] S. Kullback and R. A. Leibler. On information and sufficiency. *Ann. Math. Stat.*, 22(1):79–86, 1951.
- [78] F. Kuwahara, A. Nakayama, and H. Koyama. A numerical study of thermal dispersion in porous media. *J. Heat. Transf.*, 118(3):756–761, 1996.
- [79] F. Kuwahara, T. Yamane, and A. Nakayama. Large eddy simulation of turbulent flow in porous media. *Int. Commun. Heat Mass Transf.*, 33(4):411–418, 2006.
- [80] K. Lee, É. D. Murray, L. Kong, B. I. Lundqvist, and D. C. Langreth. Higher-accuracy van der waals density functional. *Phys. Rev. B*, 82(8):081101, 2010.
- [81] C. Léonard, V. Brites, T. Pham, Q.-D. To, and G. Lauriat. Influence of the pairwise potential on the tangential momentum accommodation coefficient: a multi-scale study applied to the argon on pt(111) system. *Eur. Phys. J. B*, 86(4):1–11, 2013.

- [82] T. Liang, Q. Li, and W. Ye. A physical-based gas–surface interaction model for rarefied gas flow simulation. *J. Comput. Phys.*, 352:105–122, 2017.
- [83] M. Liao, R. Grenier, Q.-D. To, M. P. de Lara-Castells, and C. Léonard. Helium and argon interactions with gold surfaces: *ab initio*-assisted determination of the he-au pairwise potential. application to accommodation coefficients determination. *J. Phys. Chem. C*, 122(26):14606–14614, 2018.
- [84] M. Liao, Q.-D. To, C. Léonard, and V. Monchiet. Non-parametric wall model and methods of identifying boundary conditions for moments in gas flow equations. *Phys. Fluids*, 30(3):032008, 2018.
- [85] M. Liao, Q. D. To, C. Léonard, V. Monchiet, and V. H. Vo. Strain-induced friction anisotropy between graphene and molecular liquids. *J. Chem. Phys.*, 146(1):014707, 2017.
- [86] P. J. Linstrom and M. W. G. *NIST Chemistry WebBook; NIST Standard Reference Database No. 69*, 2017.
- [87] J. Liu, Y. Sano, and A. Nakayama. A simple mathematical model for determining the equivalent permeability of fractured porous media. *Int. Commun Heat Mass Transf.*, 36(3):220–224, 2009.
- [88] D. A. Lockerby and J. M. Reese. On the modelling of isothermal gas flows at the microscale. *J. Fluid Mech.*, 604:235–261, 2008.
- [89] R. Lord. Some extensions to the cercignani–lampis gas–surface scattering kernel. *Phys. Fluids A*, 3(4):706–710, 1991.
- [90] M. Majumder, N. Chopra, R. Andrews, and B. J. Hinds. Nanoscale hydrodynamics: enhanced flow in carbon nanotubes. *Nature*, 438(7064):44–44, 2005.
- [91] M. G. Martin and J. I. Siepmann. Transferable potentials for phase equilibria. 1. united-atom description of n-alkanes. *J. Phys. Chem. B*, 102(14):2569–2577, 1998.

- [92] J. Maxwell. On stresses in rarified gases arising from inequalities of temperature. *Philos. T R. Soc. A*, 170:231–256, 1879.
- [93] A. Heßelmann. Improved supermolecular second order Möller-pleeset intermolecular interaction energies using time-dependent density functional response theory. *J. Chem. Phys.*, 128:144112, 2008.
- [94] V. Monchiet. Fft based iterative schemes for composites conductors with non-overlapping fibers and kapitza interface resistance. *J. Mech. Mater. Struct.*, 2017.
- [95] V. Monchiet, G. Bonnet, and G. Lauriat. A fft-based method to compute the permeability induced by a stokes slip flow through a porous medium. *Comptes rendus. Mécanique*, 337(4):192–197, 2009.
- [96] T. G. Myers. Why are slip lengths so large in carbon nanotubes? *Microfluid. Nanofluid.*, 10:1141–1145, 2011.
- [97] C. Neto, D. R. Evans, E. Bonaccorso, H.-J. Butt, and V. S. Craig. Boundary slip in newtonian liquids: a review of experimental studies. *Rep. Prog. Phys.*, 68(12):2859, 2005.
- [98] K. Pernal, R. Podeszwa, K. Patkowski, and K. Szalewicz. Dispersionless density functional theory. *Phys. Rev. Lett.*, 103:263201, 2009.
- [99] K. A. Peterson and C. Puzzarini. Systematically convergent basis sets for transition metals. ii. pseudopotential-based correlation consistent basis sets for the group 11 (cu, ag, au) and 12 (zn, cd, hg) elements. *Theor. Chem. Acc.*, 114(4-5):283–296, 2005.
- [100] T. Pham, Q.-D. To, G. Lauriat, and C. Léonard. Tensorial slip theory for gas flows and comparison with molecular dynamics simulations using an anisotropic gas-wall collision mechanism. *Phys. Rev. E*, 87:053012, May 2013.
- [101] T. T. Pham, Q. D. To, G. Lauriat, C. Léonard, and V. Van Hoang. Effects of surface morphology and anisotropy on the tangential-momentum accommodation coefficient between Pt(100) and Ar. *Phys. Rev. E*, 86:051201, Nov 2012.

- [102] S. Plimpton. Fast parallel algorithms for short-range molecular dynamics. *J. Comput. Phys.*, 117(1):1–19, 1995.
- [103] S. Plimpton, P. Crozier, and A. Thompson. Lammmps-large-scale atomic/molecular massively parallel simulator. *Sandia National Laboratories*, 18:43, 2007.
- [104] R. Podaszwa, K. Pernal, K. Patkowski, and K. Szalewicz. Extension of the hartree-fock plus dispersion method by first-order correlation effects. *J. Phys. Chem. Lett.*, 1:550–555, 2010.
- [105] R. Podaszwa and K. Szalewicz. Density functional theory overcomes the failure of predicting intermolecular interaction energies. *J. Chem. Phys.*, 136:161102, 2012.
- [106] D. Rapaport. *The Art of Molecular Dynamics Simulation*. Cambridge University Press, 2004.
- [107] C. E. Rasmussen and C. K. Williams. Gaussian processes for machine learning. 2006. *The MIT Press, Cambridge, MA, USA*, 38:715–719, 2006.
- [108] M. Rubeš, J. Kysilka, P. Nachtigall, and O. Bludský. Dft/cc investigation of physical adsorption on a graphite (0001) surface. *Phys. Chem. Chem. Phys.*, 12(24):6438–6444, 2010.
- [109] J.-P. Ryckaert, G. Ciccotti, and H. J. Berendsen. Numerical integration of the cartesian equations of motion of a system with constraints: molecular dynamics of n-alkanes. *J. Comput. Phys.*, 23(3):327–341, 1977.
- [110] E. Sanchez-Palencia. Homogenization of second order equations. *Non-Homogeneous Media and Vibration Theory*, pages 45–83, 1980.
- [111] E. Sanchez-Palencia. General introduction to asymptotic methods. In *Homogenization techniques for composite media*, pages 121–136. Springer, 1987.
- [112] A. Sangani and A. Acrivos. Slow flow past periodic arrays of cylinders with application to heat transfer. *Int. J. Multiphase Flow*, 8(3):193–206, 1982.

- [113] A. Sangani and A. Acrivos. Slow flow through a periodic array of spheres. *Int. J. Multiphase Flow*, 8(4):343–360, 1982.
- [114] Y. Sano, F. Kuwahara, M. Mobedi, and A. Nakayama. Effects of thermal dispersion on heat transfer in cross-flow tubular heat exchangers. *Heat Mass Transf.*, 48(1):183–189, 2012.
- [115] R. B. Schoch, J. Han, and P. Renaud. Transport phenomena in nanofluidics. *Rev. Mod. Phys.*, 80(3):839, 2008.
- [116] E. Secchi, S. Marbach, A. Nigues, D. Stein, A. Siria, and L. Bocquet. Massive radius-dependent flow slippage in carbon nanotubes. *Nature*, 537:210–213, 2016.
- [117] F. Sharipov. Application of the cercignani–lampis scattering kernel to calculations of rarefied gas flows. ii. slip and jump coefficients. *Eur. J. Mech. B Fluids*, 22(2):133–143, 2003.
- [118] F. Sharipov. Application of the cercignani–lampis scattering kernel to calculations of rarefied gas flows. iii. poiseuille flow and thermal creep through a long tube. *Eur. J. Mech. B Fluids*, 22(2):145–154, 2003.
- [119] H. W. Sheng, M. J. Kramer, A. Cadien, T. Fujita, and M. W. Chen. Highly optimized embedded-atom-method potentials for fourteen fcc metals. *Phys. Rev. B*, 83:134118, 2011.
- [120] N. Shenogina, R. Godawat, P. Keblinski, and S. Garde. How wetting and adhesion affect thermal conductance of a range of hydrophobic to hydrophilic aqueous interfaces. *Phys. Rev. Lett.*, 102(15):156101, 2009.
- [121] H. Shokouhmand, A. M. Isfahani, and E. Shirani. Friction and heat transfer coefficient in micro and nano channels filled with porous media for wide range of knudsen number. *Int. Commun. Heat Mass Transf.*, 37(7):890–894, 2010.
- [122] J.-J. Shu, J. B. M. Teo, and W. K. Chan. Fluid velocity slip and temperature jump at a solid surface. *Appl. Mech. Rev.*, 69(2):020801, 2017.

- [123] E. Skjetne and J.-L. Auriault. Homogenization of wall-slip gas flow through porous media. *Transport Porous Med.*, 36(3):293–306, 1999.
- [124] M. Smoluchowski von Smolan. Über wärmeleitung in verdünnten gasen. *Annalen der Physik*, 300(1):101–130, 1898.
- [125] P. Spijker, A. J. Markvoort, S. V. Nedeia, and P. A. J. Hilbers. Computation of accommodation coefficients and the use of velocity correlation profiles in molecular dynamics simulations. *Phys. Rev. E*, 81(1):011203, Jan 2010.
- [126] H. Struchtrup. Failures of the burnett and super-burnett equations in steady state processes. *Continuum Mech. Therm.*, 17(1):43–50, 2005.
- [127] H. Struchtrup. *Macroscopic Transport Equations for Rarefied Gas Flows: Approximation Methods in Kinetic Theory*. Springer, 2005.
- [128] H. Struchtrup. Maxwell boundary condition and velocity dependent accommodation coefficient. *Phys. Fluids*, 25(11):112001, 2013.
- [129] H. Struchtrup and M. Torrilhon. Regularization of grad’s 13 moment equations: derivation and linear analysis. *Phys. Fluids*, 15(9):2668–2680, 2003.
- [130] S. J. Stuart, A. B. Tutein, and J. A. Harrison. A reactive potential for hydrocarbons with intermolecular interactions. *J. Chem. Phys.*, 112(14):6472–6486, 2000.
- [131] H. G. Sung. *Gaussian mixture regression and classification*. PhD thesis, Rice University, 2004.
- [132] E. T. Swartz and R. O. Pohl. Thermal boundary resistance. *Rev. Mod. Phys.*, 61(3):605, 1989.
- [133] K. T. Tang and J. P. Toennies. An improved simple-model for the van der waals potential based on universal damping functions for the dispersion coefficients. *J. Chem. Phys.*, 80:3726–3741, 1984.

- [134] K. T. Tang and J. P. Toennies. Recalculation of physisorption potentials of rare gases on noble metals. *Surf. Sci. Lett.*, 279:L203–L206, 1992.
- [135] J. A. Thomas and A. J. McGaughey. Reassessing fast water transport through carbon nanotubes. *Nano Lett.*, 8(9):2788–2793, 2008.
- [136] L. B. Thomas and E. B. Schofield. Thermal accommodation coefficient of helium on a bare tungsten surface. *J. Chem. Phys.*, 23(5):861–866, 1955.
- [137] P. Thompson and S. Troian. A general boundary condition for liquid flow at solid surfaces. *Nature*, 389(6649):360–361, 1997.
- [138] Q. D. To, C. Léonard, and G. Lauriat. Free-path distribution and knudsen-layer modeling for gaseous flows in the transition regime. *Physical Review E*, 91(2):023015, 2015.
- [139] Q.-D. To, T. Pham, V. Brites, C. Léonard, and G. Lauriat. Multiscale study of gas slip flows in nanochannels. *J. Heat Transfer*, 137:091002, 2015.
- [140] Q.-D. To, V.-H. Vu, G. Lauriat, and C. Léonard. Boundary conditions for gas flow problems from anisotropic scattering kernels. *J. Math. Phys.*, 56(10):103101, 2015.
- [141] Q. D. To, V. H. Vu, G. Lauriat, and C. Léonard. Velocity slip and temperature jump for gas flows past anisotropic surfaces: Analytical derivation and numerical simulation. In *ASME 2016 14th International Conference on Nanochannels, Microchannels, and Minichannels collocated with the ASME 2016 Heat Transfer Summer Conference and the ASME 2016 Fluids Engineering Division Summer Meeting*, pages V001T01A002–V001T01A002. American Society of Mechanical Engineers, 2016.
- [142] V.-T. To, V. Monchiet, and Q. D. To. An fft method for the computation of thermal diffusivity of porous periodic media. *Acta Mech.*, pages 1–19, 2017.
- [143] M. Torrilhon. Modeling nonequilibrium gas flow based on moment equations. *Annu. Rev. Fluid Mech.*, 48:429–458, 2016.

- [144] M. Torrilhon and H. Struchtrup. Boundary conditions for regularized 13-moment-equations for micro-channel-flows. *J. Comput. Phys.*, 227(3):1982–2011, 2008.
- [145] W. M. Trott, J. N. Castañeda, J. R. Torczynski, M. A. Gallis, and D. J. Rader. An experimental assembly for precise measurement of thermal accommodation coefficients. *Rev. Sci. Instrum.*, 82:035120, 2011.
- [146] J. C. Tully. Washboard model of gas–surface scattering. *J. Chem. Phys.*, 92(1):680–686, 1990.
- [147] M. Vandamme, L. Brochard, B. Lecampion, and O. Coussy. Adsorption and strain: The co₂-induced swelling of coal. *J. Mech. Phys. Solids*, 58:1489–1505, 2010.
- [148] V. Vdi. Heat atlas, 2010.
- [149] G. Vidali, G. Ihm, H.-Y. Kim, and M. W. Cole. Potentials of physical adsorption. *Surf. Sci. Rep.*, 12:133–181, 1991.
- [150] T. Vu, G. Lauriat, and O. Manca. Forced convection of air through networks of square rods or cylinders embedded in microchannels. *Microfluid. nanofluid.*, 16(1-2):287–304, 2014.
- [151] C. Wang. Stokes flow through a tube with annular fins. *Eur. J. Mech. B/Fluids*, 15(6):781–789, 1996.
- [152] C. Wang. Stokes flow through a periodically constricted tube and the resistance due to a contraction. *Acta Mech.*, 148(1-4):55–61, 2001.
- [153] C. Wang. Flow due to a stretching boundary with partial slip—an exact solution of the navier–stokes equations. *Chem. Eng. Sci.*, 57(17):3745–3747, 2002.
- [154] C. Wang. Stagnation flows with slip: exact solutions of the navier-stokes equations. *Z. Angew. Math. Phys.*, 54(1):184–189, 2003.

- [155] M. Watari. Relationship between accuracy and number of velocity particles of the finite-difference lattice boltzmann method in velocity slip simulations. *J. Fluid. Eng.*, 132(10):101401, 2010.
- [156] H. J. Werner, P. J. Knowles, G. Knizia, F. R. Manby, M. Schütz, P. Celani, T. Korona, R. Lindh, A. O. Mitrushchenkov, G. Rauhut, and et al. Molpro, version 2012.1, a package of *ab initio* programs, <http://www.molpro.net> (accessed may 20, 2018).
- [157] S. Whitaker. Diffusion and dispersion in porous media. *AIChE J.*, 13(3):420–427, 1967.
- [158] M. Whitby, L. Cagnon, M. Thanou, and N. Quirke. Enhanced fluid flow through nanoscale carbon pipes. *Nano Lett.*, 8(9):2632–2637, 2008.
- [159] D. E. Woon and T. H. Dunning. Gaussian basis sets for use in correlated molecular calculations. iv. calculation of static electrical response properties. *J. Chem. Phys.*, 100(4):2975–2988, 1994.
- [160] W. Xiong, J. Z. Liu, M. Ma, Z. Xu, J. Sheridan, and Q. Zheng. Strain engineering water transport in graphene nanochannels. *Phys. Rev. E*, 84(5):056329, 2011.
- [161] H. Xu, W. Chu, X. Huang, W. Sun, C. Jiang, and Z. Liu. CO₂ adsorption-assisted CH₄ desorption on carbon models of coal surface: A dft study. *Appl. Surf. Sci.*, 375:196–206, 2016.
- [162] L. Xue, P. Keblinski, S. Phillpot, S.-S. Choi, and J. Eastman. Two regimes of thermal resistance at a liquid–solid interface. *J. Chem. Phys.*, 118(1):337–339, 2003.
- [163] K. Yamamoto, H. Takeuchi, and T. Hyakutake. Characteristics of reflected gas molecules at a solid surface. *Phys. Fluids*, 18:046103, 2006.
- [164] T. Yan, W. L. Hase, and J. C. Tully. A washboard with moment of inertia model of gas-surface scattering. *J. Chem. Phys.*, 120(2):1031–1043, 2004.
- [165] E. Zaremba and W. Kohn. Van der Waals interaction between an atom and a solid surface. *Phys. Rev. B*, 13:2270–2285, 1976.

-
- [166] W.-M. Zhang, G. Meng, and X. Wei. A review on slip models for gas microflows. *Microfluid. Nanofluid.*, 13(6):845–882, 2012.
- [167] Z. Zhang and S. C. Glotzer. Self-assembly of patchy particles. *Nano Lett.*, 4(8):1407–1413, 2004.
- [168] A. S. Ziarani and R. Aguilera. Knudsen’s permeability correction for tight porous media. *Transport Porous Med.*, 91(1):239–260, 2012.
- [169] O. Zienkiewicz, R. Gallagher, and P. Hood. Newtonian and non-newtonian viscous incompressible flow. temperature induced flows. finite element solutions. *The mathematics of finite elements and applications*, 2:235–267, 1975.